

**SINGLE-PHASE FLOW AND FLOW BOILING  
OF WATER IN HORIZONTAL  
RECTANGULAR MICROCHANNELS**

A thesis submitted for the degree of Doctor of Philosophy

By

**Mirmanto**

School of Engineering and Design  
Brunel University London  
Uxbridge, UB8 3PH, United Kingdom

2013

## Abstract

The current study is part of a long term experimental project devoted to investigating single-phase flow pressure drop and heat transfer, flow boiling pressure drop and heat transfer, flow boiling instability and flow visualization of de-ionized water flow in microchannels. The experimental facility was first designed and constructed by S. Gedupudi (2009) and in the present study; the experimental facility was upgraded by changing the piping and pre-heaters so as to accommodate the objectives of the research. These objectives include (i) modifying the test rig, to be used for conducting experiments in microchannels in single and two-phase flow boiling heat transfer, pressure drop and visualization, (ii) redesign metallic single microchannels using copper as the material. The purpose of the redesign is to provide microchannels with strong heaters, high insulation performance and with test sections easy to dismantle and reassemble, (iii) obtaining the effect of hydraulic diameter on single-phase flow, flow pattern, heat transfer and pressure drop, (iv) studying the effects of heat flux, mass flux, and vapour quality on flow pattern, flow boiling heat transfer and pressure drop, (v) comparing experimental results with existing correlations. However, the main focus in this present study is to investigate the effects of hydraulic diameter, heat flux, mass flux and vapour quality on flow pattern, flow boiling heat transfer coefficient and pressure drop.

In addressing (iii) many possible reasons exist for the discrepancies between published results and conventional theory and for the scatter of data in published flow boiling heat transfer results:

1. Accuracy in measuring the dimensions of the test section, namely the width, depth and length and in the tested variables of temperature, pressure, heat flux and mass flux.
2. Variations in hydraulic diameter and geometry between different studies.
3. Differences in working fluids.
4. Effects of hydrodynamic and thermal flow development
5. Inner surface characteristics of the channels.

Three different hydraulic diameters of copper microchannels were investigated: 0.438 mm, 0.561 mm and 0.635 mm. For single-phase flow the experimental conditions included mass fluxes ranging from 278 – 5163 kg/m<sup>2</sup> s, heat fluxes from 0 - 537 kW/m<sup>2</sup>, and inlet temperatures of 30, 60 and 90°C. In the flow boiling experiments the conditions comprised of an inlet pressure of 125 kPa (abs), inlet temperature of 98°C (inlet sub-cooling of 7 K), mass fluxes ranging from 200 to 1100 kg/m<sup>2</sup>s, heat fluxes ranging from 0 to 793 kW/m<sup>2</sup> and qualities up to 0.41. All measurements were recorded after the system attained steady states.

The single-phase fluid flow results showed that no deviation of friction factors was found from the three different hydraulic diameters. The effect of fluid temperature on friction factor was insignificant and the friction factors themselves were in reasonable agreement with developing flow theory. The typical flow patterns observed in all three test sections were bubbly, slug/confined churn and annular, however, based on the observation performed near the outlet, the bubbly flow was not detected. The effects of mass flow and hydraulic diameter on flow pattern for the three test sections investigated in the range of experimental conditions were not clear.

The single-phase heat transfer results demonstrated that smaller test sections result in higher heat transfer coefficients. However, for heat transfer trends presented in the form of Nusselt number versus Reynolds number, the effect of hydraulic diameter was insignificant.

The flow boiling experiments gave similar heat transfer results; they exhibited that the smaller hydraulic diameter channels resulted in higher heat transfer coefficients. The nucleate boiling mechanism was found for all three test sections, evidenced by the significant effect of heat flux on the local heat transfer coefficient. Moreover, the heat flux had a clear effect on average heat transfer coefficient for the 0.561 mm and 0.635 mm test sections, whilst for the 0.438 mm test section, there was no discernible effect. At the same heat flux, increases in mass flux caused heat transfer coefficients to decrease. This could be due to the decrease of pressure inside the test section. When a higher mass flux was tested, the inlet pressure increased, and in reducing the inlet pressure to the original value, a decrease in system pressure resulted. Consequently, the outlet pressure and local pressure became lower.

Existing flow pattern maps, flow boiling heat transfer and pressure drop correlations were compared with the experimental results obtained for all three test sections. The comparison showed that the flow pattern map proposed by Sobierska et al. (2006) was the most successful in predicting the experimental data. The local heat transfer coefficient data were compared with existing published correlations. The correlations of Yu et al. (2002), Qu and Mudawar (2003) and Li and Wu (2010) are found to predict the current local heat transfer coefficient better than other correlations tested.

Pressure drop results showed that as the heat flux and mass flux were increased, the two-phase pressure drop increased too. These were due to the increase in bubble generations and the inertia momentum effect. As the channel was reduced, the two-phase pressure drop increased because the pressure drop related inversely with the channel hydraulic diameter.

The pressure and pressure drop fluctuations were indentified in this project, however, the maximum pressure fluctuation was found in the 0.438 mm channel whilst the minimum fluctuation was attained in the 0.561 mm channel. This indicated that the effect of decreasing in hydraulic diameter on pressure and pressure drop fluctuations is not clear and needs to be investigated further. The two-phase pressure drop data were compared with selected correlations. The Mishima and Hibiki (1996)'s correlation was found to predict the current two-phase pressure drop better than the other correlations examined in this study.

## **Declaration**

The research presented in this thesis is the original work of the author except where otherwise specified, or where acknowledgements are made by references. This project was carried out at the School of Engineering and Design, Brunel University, under the supervision of Prof. T. G. Karayiannis, Dr. J.S. Lewis and Prof. D.B.R. Kenning.

The work has not been submitted for another degree or award to any other institution.

## **Acknowledgements**

I would like to express my gratitude to my supervisors Prof. T.G. Karayiannis, Dr. J.S. Lewis and Prof. D.B.R. Kenning for all their support, guidance and encouragement throughout this work. Without their productive discussions and constructive comments through regular research meetings, this work would not have been possible.

I would also like to thank Dr. S. Gedupudi for the experimental facility, Prof. M. Collins, Mrs. Beatriz Lopez, Mrs. Lin Wilding for all their helps, supports, guidance and encouragements to this work.

I am grateful to the technician Mr. C. Xanthos, Mr. P. Yates and Mr. Kliff for their support and help in the preparation and manufacture of the investigated test sections.

I would like to acknowledge the Indonesian Ministry of Higher Education for granting me the scholarship.

I would like to thank my lovely family for their constant patience, financial support and encouragement all the time.

Above all, I would like to thank “Allah” the Almighty God for granting me the power to accomplish this work. Without the willing of Allah, nothing is possible.

# Contents

<b>Abstract</b>	<b>ii</b>
<b>Declaration</b>	<b>v</b>
<b>Acknowledgments</b>	<b>vi</b>
<b>List of Figures</b>	<b>xi</b>
<b>List of Tables</b>	<b>xx</b>
<b>Nomenclature</b>	<b>xxii</b>

## **1. Introduction**

1.1	What is a microchannel?	1
1.2	Background	1
1.3	Research motivation	3
1.3.1	Issues in single-phase flow	4
1.3.2	Issues in flow boiling	6
1.4	Research objectives	8
1.5	Structure of the thesis	9
1.6	Research contribution	11

## **2. Literature Review**

2.1	Introduction	12
2.2	Definition of a microchannel	12
2.3	Single-phase pressure drop and heat transfer in microchannels	15
2.3.1	Single-phase pressure drop	16
2.3.2	Single-phase heat transfer	22
2.4	Flow boiling	27
2.4.1	Flow patterns in microchannels	27
2.4.2	Flow pattern maps	37
2.4.3	Flow boiling heat transfer	47
2.4.4	Heat transfer correlations	60
2.4.5	Flow boiling pressure drop	63
2.4.6	Pressure drop correlations	64
2.4.7	Flow boiling instability	65

2.5	Summary of the findings	67
2.5.1	Single-phase flow	67
2.5.2	Two-phase flow	68
2.5.3	Two-phase pressure drop	70
2.5.4	Flow boiling instability	70
<b>3.</b>	<b>Experimental Facility and Method</b>	
3.1	Introduction	71
3.2	Water flow loop system	75
3.2.1	Main reservoir	75
3.2.2	Subcooler	76
3.2.3	Gear pump	76
3.2.4	Purging system	77
3.2.5	Coriolis flowmeter	77
3.2.6	Electric pre-heaters	78
3.2.7	Cooler-condenser and reflux condenser	79
3.2.8	Water manometer	79
3.3	Microchannel test sections	79
3.4	Visualisation system	87
3.5	Data acquisition system	88
3.6	Chiller system	89
3.7	Running the test rig: experimental procedures	90
3.7.1	Degassing procedure	90
3.7.2	Sequence of steps for running an experiment	91
3.8	Heat loss measurement procedures	95
3.9	Calibration procedures	96
3.9.1	Precision thermometer and PRT	96
3.9.2	Digital electronic balance	97
3.9.3	Digital electronic stop watch	97
3.9.4	Gravitational acceleration	98
3.9.5	Digital barometer	99
3.9.6	Sensor calibrations	100

3.10	Data reduction	105
3.10.1	Single-phase data reduction	105
3.10.2	Flow boiling data reduction	109
3.11	Summary	113
<b>4.</b>	<b>Single-phase flow: Experimental Results and Discussions</b>	
4.1	Introduction	114
4.2	Pressure drops	114
4.3	Single-phase heat transfer	126
4.3.1	Heat removal and heat loss	126
4.3.2	Wall and fluid temperature distribution	128
4.3.3	Heat transfer coefficient and the Nusselt number	129
4.4	Comparison with existing Nusselt number correlations	133
4.5	Repeatability of measurements	136
4.6	Summary	138
<b>5.</b>	<b>Flow Patterns &amp; Heat Transfer: Results &amp; Discussions</b>	
5.1	Introduction	141
5.2	Flow pattern results	141
5.2.1	Effect of hydraulic diameter on flow patterns	142
5.2.2	Effect of heat flux on flow patterns	147
5.2.3	Effect of mass flux on flow patterns	150
5.2.4	Comparison with flow pattern maps	152
5.3	Flow boiling heat transfer results	157
5.3.1	Effect of hydraulic diameter	160
5.3.2	Effect of heat flux	161
5.3.3	Effect of mass flux	169
5.3.4	Flow boiling curve	171
5.4	Heat transfer fluctuation	174
5.5	Repeatability of measurements	176
5.6	Comparison with flow boiling correlations	178
5.6.1	Evaluation of macroscale correlations	178
5.6.2	Evaluation of small to microscale correlations	183

5.7	Summary	194
5.7.1	Flow patterns and flow pattern maps	194
5.7.2	Heat transfer characteristics	194
5.7.3	Comparison with existing heat transfer coefficient correlations	195
<b>6.</b>	<b>Flow Boiling Pressure Drop: Results and Discussion</b>	
6.1	Introduction	196
6.2	Two-phase pressure drop	196
6.2.1	Effect of hydraulic diameter on two-phase pressure drop	197
6.2.2	Effect of heat flux and mass flux on two-phase pressure drop	201
6.3	Pressure and pressure drop fluctuation	209
6.4	Comparison with existing correlations	218
6.5	Summary	224
<b>7.</b>	<b>Conclusions and Recommendations</b>	
7.1	Conclusions	225
7.1.1	Single-phase pressure drop and heat transfer	225
7.1.2	Flow patterns	226
7.1.3	Heat transfer characteristics	227
7.1.4	Pressure drop	228
7.2	Recommendations	228
	<b>References</b>	230
<b>Appendix A</b>	<b>Selected correlations for the study</b>	249
<b>Appendix B</b>	<b>Sensor calibration results</b>	261
<b>Appendix C</b>	<b>Test section design</b>	270
<b>Appendix D</b>	<b>Uncertainty analysis</b>	280
	<b>Publications</b>	294

## List of Figures

Fig.		Page
2.1	Sketch of the air-water flow patterns in vertical tubes of diameter 1.05 – 4.08 mm Mishima and Hibiki, (1996).	30
2.2	Effect of channel diameter on the flow pattern transition boundaries, Coleman and Garimella (1999).	31
2.3	Flow pattern and pressure fluctuation in a vertical triangular channel with a hydraulic diameter of 0.866 mm; (a) capillary bubble, (b) and (c) slug, (d) churn, (e) and (f) annular, Zhao and Bi (2001).	33
2.4	Flow patterns observed in the 1.1 mm internal diameter at 10 bar, taken from Chen et al. (2006).	36
2.5	Flow pattern map for the 1.096 mm tube diameter, redrawn from Triplett et al. (1999). The line boundary data were taken using the Digitizelts software.	38
2.6	Universal flow pattern map for flow boiling in horizontal microchannels, Hassan et al. (2005).	39
2.7	Flow pattern map for single side heated narrow rectangular channel, Wang et al. (2011).	40
2.8	Flow patterns observed and pattern map proposed by Sobierska et al. (2006).	41
2.9	Flow boiling pattern maps of R134a at $p = 10$ bar for the 1.1 mm tube in superficial gas/liquid velocity and Webber number planes, Chen et al. (2006).	42
3.1	Schematic diagram of the test rig (Gedupudi et al. 2009).	73
3.2	Photograph of experimental facility.	74
3.3	Micropump GA-T23 performance with water at 1 cP.	77
3.4	Accuracy levels of the Coriolis flowmeter given by the manufacturer.	78
3.5	Width measurements using a Zeiss Supra 35 VP electron microscope: (a) Test section 1, (b) Test section 2, (c) Test section 3.	80

3.6	Test section construction showing the main parts (all dimensions in mm).	82
3.7	Photographs showing the top view of the three microchannel test sections.	83
3.8	SEM images of microchannel base surfaces: (a) Test section 1, (b) Test section 2 and (c) Test section 3.	85
3.9	Surface roughness measurements; (a) Test section 1, (b) Test section 2 and (c) Test section 3. The measurements shown were taken at a location near the middle of each microchannel for a sample test area of 0.265 x 0.199 mm <sup>2</sup> .	86
3.10	Visualisation system.	88
3.11	Data acquisition system.	89
3.12	Schematic diagram of chiller system.	90
4.1	Experimental friction factors for fully developed flows in a stainless steel tube.	115
4.2	Channel pressure drops: (a) effect of inlet temperature and (b) effect of hydraulic diameter.	117
4.3	Effect of temperature on water properties; density and viscosity, obtained using EES software.	117
4.4	Effect of inlet temperature on friction factor: (a) test section one, (b) test section two, (c) test section three.	121
4.5	Effect of hydraulic diameter on the friction factor at the same inlet temperature of 30°C.	122
4.6	Effect of inlet temperature on the Poiseuille number for the 0.635 mm channel.	125
4.7	Pressure distributions along the channel at inlet temperature of 30°C for the 0.438 mm channel.	125
4.8	Heat removal and heat loss versus Reynolds number at several given power for the 0.635 mm channel test section.	126
4.9	Variation of channel wall and fluid temperatures with distance from the entry for the 0.635 mm channel at a heat flux of 154 kW/m <sup>2</sup> . Note: wall temperatures are at the thermocouple locations.	128
4.10	Variation of heat transfer coefficient with Reynolds number for the	129

- 0.635 mm channel, and for a range of heat fluxes.
- 4.11 Variation of heat transfer coefficient with Reynolds number for almost constant heat flux and 30°C inlet temperature. 131
- 4.12 Variation of Nusselt number with Reynolds numbers at almost constant heat flux and inlet temperature of 30°C and comparisons with conventional correlations and results obtained by Harms et al. (1999). 132
- 4.13 Comparison of experimental Nusselt numbers with published macroscale correlations at Reynolds numbers ranging from 244 to 4110. 135
- 4.14 Comparison of experimental Nusselt number data with the new correlations for the 0.438 mm, 0.561 mm, and 0.635 mm channels: (a) developing laminar flow, (b) developing turbulent flow. 136
- 4.15 Repeatability of friction factor measurements at temperature of 60°C: (a)  $D_h = 0.438$  mm, (b)  $D_h = 0.561$  mm, (c)  $D_h = 0.635$  mm. 137
- 4.16 Repeatability of Nusselt number measurements at inlet temperature of 30°C: (a)  $D_h = 0.438$  mm, (b)  $D_h = 0.561$  mm, (c)  $D_h = 0.635$  mm. 138
- 5.1 Flow patterns observed in the 0.438 mm channel at mass flux of 601 kg/m<sup>2</sup>s, inlet pressure and temperature of 125 kPa (abs) and 98°C: (a) at several heat fluxes, (b) at 175 kW/m<sup>2</sup>. 142
- 5.2 Flow patterns observed in the 0.561 mm channel at mass flux of 600 kg/m<sup>2</sup>s, inlet pressure and temperature of 125 kPa (abs) and 98°C: (a) at several heat fluxes, (b) at 445 kW/m<sup>2</sup>. 144
- 5.3 Flow patterns observed in the 0.635 mm channel at mass flux of 602 kg/m<sup>2</sup>s, inlet pressure and temperature of 125 kPa (abs) and 98°C: (a) at several heat fluxes, (b) at 290 kW/m<sup>2</sup>. 145
- 5.4 Comparison with three published flow pattern maps: (a)  $D_h = 0.438$  mm, (b)  $D_h = 0.561$  mm and (c)  $D_h = 0.635$  mm channels. IT: intermittent (slug and slug-annular). 154
- 5.5 Comparison with the flow pattern map proposed by Sobierska et al. (2006): (a)  $D_h = 0.438$  mm, (b)  $D_h = 0.561$  mm, (c)  $D_h = 0.635$  mm channels. 155

5.6	Comparison with the flow pattern map proposed by Chen et al. (2006) based on the data for the 1.1 mm diameter tube in the form of Webber number plane.	156
5.7	Oscillations of variables as a function of time at heat flux of 222 kW/m <sup>2</sup> , mass flux of 601 kg/m <sup>2</sup> s, inlet temperature and pressure of 98°C and 125 kPa (abs) for the 0.438 mm channel.	157
5.8	Effect of hydraulic diameter and local thermodynamic quality on the local heat transfer coefficient for the three test sections at a nominal mass flux of 600 kg/m <sup>2</sup> s, inlet temperature of 98°C and inlet pressure of 125 kPa (abs).	159
5.9	Effect of hydraulic diameter and heat flux on the average heat transfer coefficient for the three test sections at a nominal mass flux of 600 kg/m <sup>2</sup> s, inlet temperature of 98°C, and inlet pressure of 125 kPa (abs).	160
5.10	Effect of heat flux and local thermodynamic quality on the local heat transfer coefficient for 0.438 mm channel at 601 kg/m <sup>2</sup> s and inlet pressure of 125 kPa (abs).	161
5.11	Saturation temperature distributions along the test section for the 0.438 mm channel, for a range of heat fluxes and at the mass flux of 601 kg/m <sup>2</sup> s.	162
5.12	Effect of heat flux and dimensionless distance from entry on the local heat transfer coefficient, for 0.438 mm channel at a mass flux of 601 kg/m <sup>2</sup> s.	163
5.13	Effect of heat flux and local thermodynamic quality on the local heat transfer coefficient for 0.561 mm channel at 600 kg/m <sup>2</sup> s, inlet temperature of 98°C and inlet pressure of 125 kPa (abs).	164
5.14	Effect of heat flux and dimensionless distance from entry on the local heat transfer coefficient for 0.561 mm channel at 600 kg/m <sup>2</sup> s, inlet temperature of 98°C and inlet pressure of 125 kPa (abs).	164
5.15	Effect of heat flux and local thermodynamic quality on the local heat transfer coefficient for 0.635 mm channel at inlet temperature of 98°C and inlet pressure of 125 kPa (abs): (a) $G = 202$ kg/m <sup>2</sup> s, (b) $G = 602$ kg/m <sup>2</sup> s.	166
5.16	Effect of heat flux and dimensionless distance from entry on the local heat transfer coefficient for 0.635 mm channel at 602 kg/m <sup>2</sup> s,	167

- inlet pressure of 125 kPa (abs) and inlet temperature of 98°C.
- 5.17 Effect of heat flux on the local heat transfer coefficient for 0.635 mm 167  
channel at 602 kg/m<sup>2</sup>s, inlet temperature of 98°C and inlet pressure  
of 125 kPa (abs) at two different locations.
- 5.18 Effect of mass flux and local thermodynamic quality on the local 169  
heat transfer coefficient at the heat flux of 441 kW/m<sup>2</sup>, inlet  
temperature of 98°C and inlet pressure of 125 kPa (abs) for the 0.438  
mm channel.
- 5.19 Effect of mass flux and local thermodynamic quality on the local 170  
heat transfer coefficient at the heat flux of 445 kW/m<sup>2</sup>, inlet  
temperature of 98°C and inlet pressure of 125 kPa (abs) for the 0.561  
mm channel.
- 5.20 Effect of mass flux and local thermodynamic quality on the local 170  
heat transfer coefficient at the heat flux of 441 kW/m<sup>2</sup>, inlet  
temperature of 98°C and inlet pressure of 125 kPa (abs) for the 0.635  
mm channel.
- 5.21 Effect of heat flux on the boiling curve at inlet temperature of 98°C 172  
and inlet pressure of 125 kPa (abs): (a)  $D_h = 0.438$  mm, (b)  $D_h =$   
0.561 mm, (c)  $D_h = 0.635$  mm.
- 5.22 Fluctuation of local heat transfer coefficient at nominal mass flux of 174  
600 kg/m<sup>2</sup>s, inlet temperature and pressure of 98°C and 125 kPa  
(abs): (a)  $D_h = 0.438$  mm, (b)  $D_h = 0.561$  mm, (c)  $D_h = 0.635$  mm.
- 5.23 Repeatability of the local heat transfer measurement at a nominal 176  
mass flux of 600 kg/m<sup>2</sup>s, inlet pressure of 125 kPa(abs) and inlet  
temperature of 98°C at  $z/L = 1$ : (a)  $D_h = 0.438$  mm, (b)  $D_h = 0.561$   
mm and (c)  $D_h = 0.635$  mm.
- 5.24 Experimental local heat transfer coefficient compared with 178  
macroscale predictions at a nominal mass flux of 602 kg/m<sup>2</sup>s, inlet  
temperature of 98°C and inlet pressure of 125 kPa (abs): (a)  $D_h =$   
0.438 mm, (b)  $D_h = 0.561$  mm and (c)  $D_h = 0.635$  mm.
- 5.25 Comparison of experimental data with the correlation of Shah 179  
(1982): (a)  $D_h = 0.438$  mm, (b)  $D_h = 0.561$  mm and (c)  $D_h = 0.635$   
mm channels.

- 5.26 Comparison of experimental data with the correlation of Gungor and Winterton (1987): (a)  $D_h = 0.438$  mm, (b)  $D_h = 0.561$  mm and (c)  $D_h = 0.635$  mm channels. 180
- 5.27 Comparison of experimental data with the correlation of Kandlikar (1990): (a)  $D_h = 0.438$  mm, (b)  $D_h = 0.561$  mm and (c)  $D_h = 0.635$  mm channels. 181
- 5.28 Experimental local heat transfer coefficient compared with small to microscale predictions at a nominal mass flux of  $600 \text{ kg/m}^2\text{s}$ , inlet temperature of  $98^\circ\text{C}$  and inlet pressure of  $125 \text{ kPa}$  (abs): (a)  $D_h = 0.438$  mm, (b)  $D_h = 0.561$  mm and (c)  $D_h = 0.635$  mm. 184
- 5.29 Comparison of experimental data with the correlation of Lazarek and Black (1982): (a)  $D_h = 0.438$  mm, (b)  $D_h = 0.561$  mm and (c)  $D_h = 0.635$  mm channels. 185
- 5.30 Comparison of experimental data with the correlation of Kew and Cornwell (1997): (a)  $D_h = 0.438$  mm, (b)  $D_h = 0.561$  mm and (c)  $D_h = 0.635$  mm channels. 186
- 5.31 Comparison of experimental data with the correlation of Yu et al. (2002): (a)  $D_h = 0.438$  mm, (b)  $D_h = 0.561$  mm and (c)  $D_h = 0.635$  mm channels. 187
- 5.32 Comparison of experimental data with the correlation of Warriier et al. (2002): (a)  $D_h = 0.438$  mm, (b)  $D_h = 0.561$  mm and (c)  $D_h = 0.635$  mm channels. 188
- 5.33 Comparison of experimental data with the correlation of Lee and Mudawar (2005): (a)  $D_h = 0.438$  mm, (b)  $D_h = 0.561$  mm and (c)  $D_h = 0.635$  mm channels. 189
- 5.34 Comparison of experimental data with the correlation of Sun and Mishima (2009): (a)  $D_h = 0.438$  mm, (b)  $D_h = 0.561$  mm and (c)  $D_h = 0.635$  mm channels. 190
- 5.35 Comparison of experimental data with the correlation of Li and Wu (2010): (a)  $D_h = 0.438$  mm, (b)  $D_h = 0.561$  mm and (c)  $D_h = 0.635$  mm channels. 191
- 6.1 Two-phase pressure drop versus heat flux at almost the same mass flux for the  $0.438$  mm,  $0.561$  mm and  $0.635$  mm channels. 198

6.2	Accelerational and frictional pressure drops based on Eq. (6.5) at a nominal mass flux of 600 kg/m <sup>2</sup> s for the 0.438 mm, 0.561 mm and 0.635 mm channels.	200
6.3	Total channel pressure drop of flow boiling in the 0.438 mm channel, showing effect of heat flux and mass flux.	201
6.4	Effect of mass flux and heat flux on the two-phase pressure drop for the (a) 0.438 mm, (b) 0.561 mm and (c) 0.635 mm channels.	202
6.5	Channel and two-phase pressure drops at two different mass fluxes for the 0.438 mm channel.	203
6.6	Subcooled and saturation lengths at the mass flux of 601 kg/m <sup>2</sup> s, inlet temperature of 98°C and inlet pressure of 125 kPa (abs) for the 0.438 mm channel.	204
6.7	Two-phase pressure drop versus exit quality at the nominal mass flux of 600 kg/m <sup>2</sup> s, inlet temperature of 98°C and inlet pressure of 125 kPa obtained for the (a) 0.438 mm, (b) 0.561 mm and (c) 0.635 mm channels.	205
6.8	Experimental two-phase pressure drop multiplier for the 0.438 mm channel compared to predictions using correlations of: (a) Lockhart–Martinelli (1949) (b) Mishima & Hibiki (1996).	206
6.9	Two-phase pressure drops versus superficial velocity at inlet temperature and pressure of 98°C and 125 kPa (abs) for the (a) 0.438 mm, (b) 0.561 mm and (c) 0.635 mm channels. The corresponding flow patterns given on the graphs were flow patterns observed near the outlet.	208
6.10	Pressure distribution along the test section based on the linear pressure distribution assumption and measurement, at a mass flux of 601 kg/m <sup>2</sup> s and several heat fluxes, for the 0.438 mm channel.	210
6.11	Pressure fluctuation at the mass flux of 601 kg/m <sup>2</sup> s, heat flux of 161 kW/m <sup>2</sup> , inlet temperature of 98°C and inlet pressure of 125 kPa (abs), for the 0.438 mm channel.	211
6.12	Pressure drop fluctuation and frequency at a mass flux of 601 kg/m <sup>2</sup> s and heat flux of 161 kW/m <sup>2</sup> , inlet temperature and pressure of 98°C and 125 kPa (abs) for the 0.438 mm channel.	212

6.13	Pressure fluctuation at a mass flux of 601 kg/m <sup>2</sup> s and heat flux of 222 kW/m <sup>2</sup> , inlet temperature of 98°C and inlet pressure of 125 kPa (abs), for the 0.438 mm channel.	213
6.14	Pressure drop fluctuation and frequency at a mass flux of 601 kg/m <sup>2</sup> s and heat flux of 222 kW/m <sup>2</sup> , for the 0.438 mm channel.	213
6.15	Pressure fluctuation at a mass flux of 601 kg/m <sup>2</sup> s and heat flux of 646 kW/m <sup>2</sup> and for the 0.438 mm channel.	215
6.16	Pressure drop fluctuation and frequency at heat flux of 646 kW/m <sup>2</sup> and mass flux of 601 kg/m <sup>2</sup> s for the 0.438 mm channel.	215
6.17	Pressure drop fluctuation and frequency obtained for the 0.635 mm at a mass flux of 202 kg/m <sup>2</sup> s and heat flux of 226 kW/m <sup>2</sup> .	216
6.18	Pressure drop fluctuation and frequency at a nominal mass flux of 700 kg/m <sup>2</sup> s and heat flux of 172 kW/m <sup>2</sup> , inlet temperature and pressure of 98°C and 125 kPa (abs) for the (a) 0.438 mm, (b) 0.561 mm and (c) 0.635 mm channels.	217
6.19	Comparison of the experimental data with selected correlations for the (a) 0.438 mm, (b) 0.561 mm and (c) 0.635 mm channels.	219
6.20	Comparison with correlations for the 0.438 mm.	220
6.21	Comparison with correlations for the 0.561 mm.	221
6.22	Comparison with correlations for the 0.635 mm.	222
B.1	A photograph of the reference pressure sensor.	261
B.2	Reference pressure (Druck pressure transducer) calibration results.	262
B.3	Local pressure sensors.	263
B.4	Local pressure transducer calibration results.	264
B.5	Local pressure transducer (Pi6010P) calibration results.	265
B.6	Comparison of Cole Parmer digital barometer reading with the corrected Fortin mercury barometer (kPa).	265
B.7	Coriolis flowmeter calibration results.	266
B.8	Power meter calibration curves.	267
B.9a	Thermocouple calibration results.	268
B.9b	Thermocouple calibration results.	269
B.9c	Thermocouple calibration results.	270
C.1	Model of the test section.	272

C.2	Contours of temperature distribution on the copper body of the test section, isometric view.	272
C.3	Contours of temperature distribution, cross section view and in the middle of body.	273
C.4	Contour of temperature distribution along the body of the test section.	273
C.5	Model for the rectangular copper block: (a) 25 mm high, (b) 50 mm high.	275
C.6	Model for the cone copper block: (a) before insulated, (b) after insulated.	275
C.7	Contours of wall temperatures (cross section view) for the 25 mm high and 50 mm high copper blocks at the fluid velocity of 1 m/s.	276
C.8	Contours of wall temperatures (cross section view) for the cone copper block; (a) without flow, (b) at the fluid velocity of 1 m/s.	276
C.9	Test section with a width of 0.5 mm.	278
C.10	Test section with a width of 1 mm.	279
C.11	Test section with a width of 1.7 mm.	280

## List of Tables

Table		Page
2.1	Hydraulic diameter of microchannels based on published criteria at the above conditions.	15
2.2	Literature for experimental Poiseuille numbers of single-phase flow of water in non circular microchannel passages.	19
2.3	Literature for experimental Nusselt numbers for single-phase flow of water in non circular microchannel passages.	25
2.4	Flow patterns observed in several hydraulic diameter channels.	43
2.5	Effect of decreasing hydraulic diameter on heat transfer coefficient.	50
2.6	Summary of the findings of heat transfer mechanisms in the previous studies.	58
3.1	Details of test section dimensions.	81
3.2	Local surface roughness (Ra) measurements and averaged values for each microchannel.	87
3.3	Comparison of applied weights and balance readings.	97
3.4	Comparison of times indicated by Lonsdale and RS stop watches.	98
3.5	Comparison of atmospheric pressure readings from the three instruments at corresponding times.	99
3.6	Standard deviations of thermocouple calibration.	101
3.7	Standard deviations of calibration data for the local pressure transducers.	104
3.8	Values of Poiseuille number, constant $C$ and the incremental pressure drop.	111
4.1	$K_c$ and $K_e$ values for the three test sections.	116
4.2	Effect of hydraulic diameter on pressure drop.	119
4.3	Calculated hydrodynamically entrance length for laminar flow.	123
4.4	Calculated thermal entrance lengths for all test sections, for a range of Reynolds numbers and at almost the same heat flux.	130
5.1	Effect of heat flux on the flow pattern in different channels at a nominal	147

mass flux of 600 kg/m<sup>2</sup>s, inlet temperature of 98°C (inlet subcooled 7 K) and inlet pressure of 125 kPa (abs).

5.2	Effect of mass flux on flow pattern at two fixed heat fluxes, inlet temperature and pressure of 98°C and 125 kPa (abs) respectively for the 0.635 mm channel.	150
5.3	Standard and percentage deviations of parameter for 1800 data point samples.	158
5.4	Mean absolute error (MAE) and the percentage of data within the $\pm 30$ % error bands for all evaluated correlations.	193
6.1	MAE values of comparison with the existing correlations.	223
A.1	Selected friction factor theory and correlations.	249
A.2	Selected Nusselt number correlations.	250
A.3	Selected flow boiling heat transfer correlations.	252
A.4	Selected two-phase pressure drop correlations.	257
C.1	Comparison of heat losses estimated using Fluent with the calculation.	277
D.1	Uncertainties of experimental measurements.	283
D.2	Experimental conditions and uncertainties for single-phase experiments.	292
D.3	Experimental conditions and uncertainties for flow boiling experiments.	293

## Nomenclature

$A_c$	Cross section area	$m^2$
$A_{ht}$	Heat transfer area	$m^2$
$Bo$	Boiling number, $Bo = q / Gh_{fg}$	
$Bd$	Bond number, $Bd = g\Delta\rho D_h^2 / \sigma$	
$b_r$	Systematic uncertainty in a measured parameter $X$	
$C$	Constant	
$Co$	Convective number,	
	$Co = \left( \frac{1-x}{x} \right)^{0.8} \left( \frac{\rho_g}{\rho_l} \right)^{0.5}$	
$Cof$	Confinement number,	
	$Cof = \left( \frac{\sigma}{g(\rho_l - \rho_g)} \right)^{0.5} / D$	
$c_p$	Specific heat	J/kg K
$D$	Circular tube diameter	m
$D_h$	Hydraulic diameter	m
$D_o$	Outer diameter	m
$E\ddot{o}$	Eötvös number, $4\pi^2\sigma / D^2\Delta\rho g$	
$f_{ch}$	Channel Fanning friction factor	
$Fr$	Froude number, $Fr_l = G^2 / gD\rho_l^2$	
$f_{Re}$	Poiseuille number	
$f_{FD}Re$	Poiseuille number for fully developed flow	
$G$	Mass flux	$kg/m^2 s$
$g$	Gravitational acceleration	$m/s^2$
$H$	Channel depth	m
$\bar{h}$	Average heat transfer coefficient	$W/m^2 K$
$h(z)$	Local heat transfer coefficient	$W/m^2 K$
$I$	Current	A
$i$	Enthalpy	J/kg
$i_{lg}$	Enthalpy for evaporation	J/kg

$J$	Superficial velocity	m/s
$K$	Loss coefficient	
$K(\infty)$	Pressure drop incremental	
$k$	Thermal conductivity	W/m K
$L$	Channel length	m
$L_{sat}$	Saturation region length	m
$L_{sub}$	Subcooled region length	m
$L^*$	Dimensionless length	
$\dot{m}$	Mass flow rate	kg/s
$N_c$	Conduction number, Eq. (1.1)	
$\bar{Nu}$	Average Nusselt number, $\bar{Nu} = \bar{h}D_h / k$	
$p$	Pressure	Pa
$P$	Power, $VI$	W
Po	Poiseuille number, $fRe$	
Pr	Prandtl number, $Pr = c_p\mu / k$	
$q$	Heat rate	W
$q_{loss}$	Heat loss rate	W
$q_{rem}$	Heat removal rate	W
$q''$	Heat flux	W/m <sup>2</sup>
Re	Reynolds number, $Re = GD_h / \mu$	
$S$	Standard deviation	
$S_x$	Standard deviation of $x$ variable	
$T$	Temperature	°C
$T_{ma}$	Temperature difference between wall temperature and ambient temperature	K
$t$	Distance between thermocouple location and channel base	m
$U$	Uncertainty	
$V$	Voltage	V
$\bar{V}$	Average velocity	m/s
$v$	Specific volume	m <sup>3</sup> /kg
$W$	Channel width	m

$We$	Weber number, $We = \rho \bar{V}^2 D_h / \sigma$	
$X^2$	Martinelli parameter	
$x$	Thermodynamic quality	
$x_e$	Thermodynamic quality at the exit	
$z$	Distance measured from inlet end of channel	m

### Greek

$\alpha$	Void fraction	
$\beta$	Aspect ratio, $\beta = H / W$	
	Surface area density	m <sup>2</sup> /m <sup>3</sup>
	Percentage of data within $\pm 30\%$	
$\Delta p$	Pressure drop	Pa
$\Delta T$	Temperature difference	K
$\Delta T_{lm}$	Log mean temperature difference	
$\phi$	Two-phase multiplier, $\phi^2 = 1 + \frac{C}{X} + \frac{1}{X^2}$	
$\mu$	Viscosity	kg/m s
$\rho$	Density	Kg/m <sup>3</sup>
$\sigma$	Surface tension	N/m

### Subscripts

3	Three heated walls
4	Four heated walls
$a$	Ambient
$app$	Apparent
$c$	Contraction
$c_u$	Copper
$e$	Enlargement, exit
$f$	Fluid
$g$	Gas, vapour
$i$	Inlet
$l$	liquid

<i>o</i>	Outlet
<i>s</i>	Surface
<i>sat</i>	Saturation
<i>sp</i>	Single-phase
<i>sub</i>	Subcooling
<i>tp</i>	Two-phase
<i>vv</i>	Laminar liquid – laminar vapour
<i>vt</i>	Laminar liquid – turbulent vapour
<i>w</i>	Wall

### **Abbreviations**

AC	Alternating current
CPU	Computer processing unit
DC	Direct current
EDL	Electric double layer
ONB	Onset of nucleate boiling
UWH	Uniform wall heat flux
UWT	Uniform wall temperature

# Chapter 1

## Introduction

### 1.1 What is a microchannel?

Despite the importance of microstructure devices in applications involving the intensification of heat exchange and the continued interest in thermofluids research on microscale processes, until recently there has been no general agreement on the definition of a microchannel. The term microchannel obviously refers to the size of channel cross-section, normally expressed by the hydraulic diameter,  $D_h$ , which is inversely related to the ratio of the wetted surface area to the volume of the channel. Shah and Sekulic (2003) classified heat transfer surfaces in terms of the surface area density,  $\beta$ , which is the heat transfer area per unit volume or compactness, to differentiate between conventional, compact, meso and micro heat exchangers. More specifically, heat exchangers were regarded as compact when  $\beta \geq 700 \text{ m}^2/\text{m}^3$  ( $D_h \leq 6 \text{ mm}$ ) for gas-side operation or  $\beta \geq 400 \text{ m}^2/\text{m}^3$  for liquid-side or two-phase operation, meso when  $\beta \geq 3000 \text{ m}^2/\text{m}^3$  ( $100 \mu\text{m} \leq D_h \leq 1 \text{ mm}$ ) and micro when  $\beta \geq 15000 \text{ m}^2/\text{m}^3$  ( $1 \mu\text{m} \leq D_h \leq 100 \mu\text{m}$ ). Mehendale et al. (2000) and Kandlikar and Grande (2003) classified small channels based on the size of flow passages. Their classifications in terms of hydraulic diameters are given in Chapter 2.

### 1.2 Background

Heat transfer devices incorporating microchannels have been developed relatively recently for single and two-phase operations and used in many application areas because they offer advantages such as high heat flux removal and compactness. Moreover, the use of microchannels is not restricted to heat transfer duties. In the chemical, biochemical and medical sectors, for instance, microchannel structures are used as micro-fluidics. In other sectors, microchannel heat exchangers in air conditioning and refrigeration equipment and microchannels are also widely utilized in cooling systems for microprocessors and other electronic components, laser diodes, gas turbine blades, bearings and cutting tools. Mudawar (2001) classified the applications of

microchannel, into two groups, based on the magnitude of the cooling requirements, namely those high and ultra-high heat fluxes. Respective examples include those generating high heat fluxes of the order of 1–10 MW/m<sup>2</sup> encountered in high performance supercomputers, power devices, electric vehicles and advanced military avionics, and applications producing ultra-high heat fluxes of 10– 10<sup>3</sup> MW/m<sup>2</sup>, such as fusion reactors, laser and radar devices and microwave weapons.

Generalising, the advantages that microchannels have over macrochannels and the consequent benefits include the following:

1. Extremely compact heat exchange equipments (overall reduction in plant size).
2. Smaller coolant fluid charge (cost, safety and environmental benefits).
3. Lower weight (important in mobile and airborne applications).
4. Higher heat transfer capability and plant efficiency.
5. Low waste production (environmental impact benefits).

From the heat transport point of view, the benefits of using microchannels are:

1. Higher ratio of heat transfer area to unit volume.
2. Higher heat transfer coefficients for both laminar and turbulent single-phase flows (as reported by Tukerman and Pease (1981), Wu and Little (1983), Jiang et al. (2001)).
3. Much higher heat transfer coefficients in flow boiling (as demonstrated by Saitoh et al. (2005), Consolini and Thome (2009) and Karayiannis et al. (2010)).
4. A smaller rise in fluid temperature difference owing to the very short channel length. This will increase the plant efficiency which in the long term will benefit environmental protection and efficient use of energy resources.

However, the practical application of microchannels does have some limitations. Higher pressure drops, flow boiling instabilities and dry-out are often encountered. Higher pressure drops result in higher pumping power, while flow instability and dry-out can greatly deteriorate microchannel performance. Focusing on the former, pressure drop can be quantified by using the Poiseuille

number,  $fRe$ , in the case of laminar single-phase flow. A higher  $fRe$  represents a higher pressure drop. The range of  $fRe$  found by Pfahler et al. (1990) in their microchannel experiments was 23.45 – 23.75, substantially higher than the theoretical fully developed values of 16 for a circular or 13.56 for a rectangular channel.

Although the literature on flow and heat transfer in microchannels shows an increase in the number of studies every year, inconsistencies in results are still encountered. The mechanisms of flow boiling heat transfer in microchannels are still unclear and researchers often reach contradictory conclusions. Results from investigations now cover a wide range of experimental conditions, working fluids and channel geometries. Therefore, no model or correlation has been developed which is able to systematise the data. Many researchers found that experimental data collected from small to micro diameter channels were poorly predicted by established macroscale correlations. Even predictions made using recently developed microscale correlations based on a single set of experimental data, compared poorly with data obtained by different researchers. The consequent lack of validated design correlations, represents a major barrier to the wide spread adoption of compact microchannel evaporators in equipment for commercial applications. This was recognised by Watel et al. (2003) who pointed out that current advances in microchannel design have been limited by direct experience and experimentation on prototypes. The generation of accurate design correlations requires a correspondingly more accurate experimental database covering a range of flow regimes and heat transfer mechanisms.

### **1.3 Research motivation**

It is clear from the discussion above that single-phase liquid flows and flow boiling in microchannels have considerable potential for use in a wide range of heat transfer application areas, including refrigeration and air conditioning systems, cooling of electronic devices, mechanical component cooling systems and microheat exchangers. However, several fundamental issues regarding heat transfer and fluid flow at the microscale have arisen within the research community. These issues are briefly and separately discussed in the following section for single and two-phase flows.

### 1.3.1 Issues in single-phase flow

In the thermal hydraulic design of heat exchange equipment, internal flow, single-phase heat transfer coefficients and friction factors are commonly calculated from analytical solutions or empirical correlations, established for conventional size channels, such as those given by Shah and London (1978), Dittus and Boelter and Gnielinski. There is a relevant question in the context of microchannels, about whether there is an effect of size and the applicability of single-phase fluid flow and heat transfer equations used at the macroscale. Some single-phase experimental studies have reported size effects, e.g. Tukerman and Pease (1981), Papautsky et al. (1999), Qu et al. (2000), Jiang et al. (2008), suggesting that single-phase correlations originally developed using data from experiments with conventional size channels, should be used with caution at the microscale. On the other hand, a substantial number of other investigators have not found any size effects, e.g. Agostini et al. (2002), Li and Cui (2003), Lelea et al. (2004), Hwang and Kim (2006) and Li et al. (2007). From the above literature, it can be noted that different conclusions have been reached by different group of researchers regarding single-phase flow and heat transfer in microchannels. The following issues may be identified as requiring clarification:

1. Dependence of the Poiseuille number ( $Po = fRe$ ) on Reynolds number, especially in laminar flow regimes, see Jiang et al. (1995), Mala and Li (1999) and Xu et al. (2000).
2. Higher experimental values of friction factor than predicted by conventional theory, see Papautsky et al. (1999), Qu et al. (2000) and Pfund et al. (2000). Papautsky et al. (1999) did not reveal the cause of it, whilst Qu et al. (2000) explained that the high friction factor was due to the relative surface roughness (3.5 to 5.7%). However, Pfund et al. (2000) elucidated that although experimental uncertainties and systematic error had been considered, their friction factor data were still higher than conventional theory.
3. In contrast to issue 2, lower values of friction factor than predicted by theory, see Pfahler et al. (1990), Jiang et al. (1997) and Jiang et al. (2008). Pfahler et al. (1990) addressed the lower friction factor obtained in the channel with a depth of 17  $\mu\text{m}$  to the thermophysical properties of the fluid. Jang et al. (1997) found lower friction factors than conventional theory. They did not explained the causes, however, they elucidated that the lower friction factors were obtained in the trapezoidal channel whilst in the circular channel the friction

factors were in good agreement with conventional theory. Meanwhile, Jiang et al. (2008) did not explain the causes of the friction factor being lower than conventional theory.

4. Early transition from laminar to turbulent flow, see Harms et al. (1999), Jiang et al. (2001) and Jiang et al. (2008).
5. Dependence of the Nusselt number on Reynolds number in fully developed laminar flow; see Choi et al. (1991) and Lee et al. (2005).
6. Effects of surface roughness in laminar flow, e.g. Mala and Li (1999), Qu et al. (2000), Kandlikar et al. (2001) and Wang and Wang (2007).

Researchers reporting channel size effects on friction factor and Nusselt number at the microscale have identified the following possible causes; surface roughness, the effect of ionic concentration in the fluid, viscous heat dissipation and axial heat conduction. Mala et al. (1997) analyzed the effects of the electric double layer (EDL) on liquid flow and heat transfer through a microchannel. They introduced the friction constant ( $f/Re$ ) as a function of the surface potential. They concluded that, as the surface potential increases, e.g. the electrostatic charge at the surface increases, the friction constant rises above the conventional value of 24 for laminar flow between parallel plates. Maranzana et al. (2004) developed an analytical model for the conjugate problem of heat transfer in a channel flow between parallel plates with axial conduction in the walls. They introduced a dimensionless number comparing the axial wall conduction to the convection heat transfer in the flow. The axial wall conduction could be neglected when the ratio of axial wall conduction was less than 0.01. Li et al. (2007) simulated the effect of axial wall conduction on heat transfer in microtubes. They found that the effect of axial heat conduction should be neglected when the ratio of axial conduction was less than  $10^{-5}$ . Recently, Rosa et al. (2009) carried out a review of single-phase heat transfer in microchannels and the importance of scaling effects. They concluded that standard theories and correlations were suitable to describe heat transfer in microchannels, once cross-section geometry, scaling effects and measurement uncertainties were carefully considered. The influences of following scaling effects on heat transfer were considered important: entrance effects, temperature dependence of the fluid properties, conjugate heat transfer and viscous heating effects. Finally, another important

consideration that can contribute to apparent inconsistency of experimental results with conventional theory is the accuracy of measuring the channel dimensions. For example, in the case of a circular tube, the Fanning friction factor depends on  $D^5$ , which means that a small error in measurement of the tube diameter could lead to a large uncertainty in the measured friction factor.

### **1.3.2 Issues in flow boiling**

The classification of flow passages in terms of size and the definition of a microchannel has already been noted. Even when the size issue is set aside, the mechanisms of heat transfer in flow boiling inside mini and microchannels remain unclear. These uncertainties are evidenced by the many contradictory conclusions reached in studies to be found in the literature and examples of these are mentioned below. Lazarek and Black (1982), Tran et al. (1996), Bao et al. (2000), Huo et al. (2007) and Wen et al. (2004) reported that flow boiling heat transfer coefficients were more or less independent of vapour quality and mass flux, but strongly dependent on the heat flux and working system pressure. This was interpreted as indicating that in their experiments, the heat transfer mechanism was dominated by nucleate boiling. However, Wambsganss et al. (1993) found that their heat transfer coefficient measurements depended on quality, mass flux and heat flux, and Agostini et al. (2008) concluded that at low heat fluxes, the heat transfer coefficient increased with vapour quality but was independent of heat flux and mass velocity. Furthermore, the ability of available correlations and models to predict the experimental data in flow boiling was found to be inadequate.

The study of two-phase flow patterns can be useful in explaining the prevailing heat transfer mechanisms in flow boiling. In bubbly flow and slug flow regimes, heat transfer mechanism is dominated by nucleate boiling, whilst in annular and mist flow regimes the heat transfer mechanism is governed by convective boiling. Again, researchers have given different descriptions based on their observation of flow patterns. For example Hetsroni et al. (2009) observed bubbly, slug, and annular flow with either a thin or thick liquid film for gas-liquid flow in parallel microchannels; Harirchian and Garimella (2009b) concluded that the flow patterns

observed in their experiment were slug and annular only, when the hydraulic diameter used was 100  $\mu\text{m}$ ; whilst Karayiannis et al. (2010) reported that the flow boiling patterns observed in small to micro diameter tubes were dispersed bubble, bubbly, confined bubble, slug, churn, annular and mist flows.

Instabilities in flow boiling have attracted considerable interest among researchers. Flow reversal and pressure fluctuations associated with flow boiling instabilities are important to understand because they can result in a decrease of heat transfer performance of microchannels or even damage the channels. The literature on these topics is extensive. Kenning et al. (2006), Gedupudi et al. (2009) and Zu et al. (2009) reported that pressure fluctuations and instabilities were caused by factors such as bubble generation, upstream and downstream compressible volumes, inlet and outlet plenum geometries and trapped gas in the tubing and fittings. Wu et al. (2006), on the other hand, explained the occurrence of large amplitude, long period, oscillations of pressure and temperature measurements, could be attributed to alternation between incoming liquid and reversed flow of the vapour core, caused by the limited bubble expansion space in the microchannels. Further, it was suggested that the out of phase reversed flow of vapour in neighboring microchannels might be due to non-uniform flow distribution or bubble nucleation. Qu and Mudawar (2003a) found that fairly periodic, large amplitude, flow oscillations produced by pressure drop oscillation in microchannel heat sinks, were the result of interaction between vapour generation in the channels and upstream compressible volume in the flow loop. Turning to flow reversal, Zu et al. (2009) revealed that flow reversal could only occur at the inlet of a single channel if compressibility existed in the upstream circuit. Mukherjee and Kandlikar (2009) suggested that movement of the upstream interface of vapour plug towards the inlet in some channels could be due to the rate of vapour generation at the upstream interface exceeding the rate of liquid supplied to the channel from the inlet header. Furthermore, rapid vapour plug growth may cause high pressure build-up near the upstream interface pushing the liquid back into the inlet header. Finally, it is noted that flow boiling instabilities in microchannels are affected by the inlet and outlet header configurations. Wang et al. (2008) investigated different plenum geometries and found that when the inlet area restriction was introduced for each channel, no

temperature or pressure oscillation occurred and reverse flow of vapour bubbles was not observed.

#### **1.4 Research objectives**

The main objectives of this study are as follows:

1. To modify a pre-existing test rig to be used for conducting heat transfer experiments in microchannels single-phase flow and flow boiling, pressure drop tests and two-phase flow pattern visualization.
2. To clarify the applicability of theory and the discrepancy published results.
3. To know the effect of hydraulic diameter on flow pattern, heat transfer and pressure drop.
4. To investigate the effects of heat flux, mass flux, and vapour quality on flow pattern, heat transfer and pressure drop.
5. To compare the experimental results with existing flow pattern maps, heat transfer and pressure drop correlations.

The necessity for redesigning the test sections was because of problems encountered with those used in previous microchannel research of Brunel University, particularly leakages and heater failures. Leakage occurred because there was no proper seal around the channel slot and due to holes drilled through the inlet and exit plenums. The heater used previously was fragile as it was made of a very thin resistance wire and was subject to stress because the rear surface of the test section on which it was mounted was not flat. To avoid similar problems in this project, the new test sections include: (i) an O-ring seal around the edge of the microchannel, (ii) redesigned plenums to prevent leakage, and (iii) a robust and powerful electrical cartridge heater house in the main body of the test section.

## 1.5 Structure of the thesis

The thesis contains seven chapters arranged as follows:

1. **Chapter 1 – Introduction:** This chapter discusses the background and motivation for the study and sets out the research objectives, the structure of the thesis and the contributions made by this work.
2. **Chapter 2 – Literature Review:** In this chapter a detailed review of publications from studies of single-phase flow and flow boiling in small channels is presented with the following objectives:
  - a). To clarify the aims of the study and to assist the test section design and modifications of the experimental facility.
  - b). To understand the effects of the main parameters on the thermal-hydraulic flow behaviour of single-phase flow and flow boiling in microchannels, including inlet temperature, mass flux and heat flux, system working pressure and hydraulic diameter.
  - c). To identify the reason for discrepancies between experimental results obtained for microchannel flows and theory and correlations established for conventional-size channels.
  - d). To understand the fundamental issues of flows in microchannels and how they may be successfully addressed.

A final summary is given of the findings of the review.

3. **Chapter 3 – Experimental Facility and Research Method:** This chapter describes the experimental facility, including the flow loop, test sections and measurement and equipment, the experimental procedures employed, the data reduction method and analysis of experimental uncertainties, together with the sensor calibration results. The experimental facility comprises the following systems:
  1. Water flow loop system,
  2. Chiller cooling system,
  3. Visualization system and
  4. Data acquisition system.

Modifications made to the test rig and the redesigned microchannel test sections are fully described in order to clarify the differences between the previous and current test rigs and to understand the beneficial effects of modification and redesign.

4. **Chapter 4 – Single-phase Flow Experimental Results and Discussion:** This chapter presents and discusses the experimental results obtained from the single-phase flow and heat transfer experiments, including pressure drop data, friction factors, heat transfer coefficients and Nusselt numbers. These results are compared with analytical solutions and empirical equations from other sources. In addition, the experimental results are used to provide validation of the experimental set-up and measuring instruments, including pressure sensors, thermocouples and a Coriolis mass flowmeter and the data acquisition system.
5. **Chapter 5 – Flow Boiling Heat Transfer Results and Discussion:** This chapter presents and discusses the experimental results obtained from the flow boiling investigation, including the heat transfer characteristics and comparisons of the measured data with published heat transfer correlations for flow boiling. In addition, results from the visualization study providing high-speed capture of flow boiling patterns are discussed and presented in flow pattern regime maps.
6. **Chapter 6 – Flow Boiling Pressure Drop Results and Discussion:** This chapter reports on the experimental results obtained for two-phase pressure drop as well as pressure drop fluctuations under flow boiling conditions. Comparisons of the experimental data with existing correlations are presented.
7. **Chapter 7 – Conclusions:** The final chapter presents the conclusions which can be drawn from this study, together with recommendations for further research to clarify outstanding issues.

## **1.6 Research contribution**

The research reported in this present study provides the following contributions to knowledge:

1. Identification and verification of discrepancies between published experimental data for single-phase flow and heat transfer in microchannels and correlations established for macroscale channel flows and hence the issues of applicability of such correlations to

microchannels. This output, therefore, is given in the form of answers to specific questions about whether and how existing theory and correlations developed for conventional-size ducts should be applied to micro passages.

2. Gaining of an in-depth understanding of the reasons behind the wide scatter and apparent different trends exhibited by published flow boiling heat transfer results for microchannels. This study examines possible reasons which may cause such deviations. This enables the varied and contradictory findings and conclusions of experimental works in the literature to be clearly explained.
3. An increased knowledge of the fundamentals of flow and heat transfer in microchannels. Such knowledge is urgently needed in order to improve the design process for devices incorporating microchannels.
4. Evaluation of existing heat transfer and pressure drop prediction methods leading to a full clarification of their capability. This will enable correlations to be improved to give better quantitative reliability in predicting pressure drop and heat transfer correlations.
5. Generation of new experimental data to add to the existing literature on heat transfer and fluid flow in microchannels. This research is aimed at providing reference data to aid engineering design at the microscale.

# Chapter 2

## Literature Review

### 2.1 Introduction

In this chapter the topics of single-phase flow and flow boiling in microchannels are reviewed. The lack of agreement on the strict definition of a microchannel has already been noted. Qualitatively it is to do with size. The term “macrochannel” or “macroscale” is used for conventional large diameter channels, whereas “microchannel” or “microscale” is simply used for small to micro sized channels. In this review, the hydraulic diameter  $D_h$  is used as a criterion, with channels of greater than or equal to 1 mm classified as macro or conventional, and those with less than 1 mm as microchannels.

The chapter is organized as follows: section 2.1 Introduction; section 2.2 Definition of a microchannel; section 2.3 Single-phase pressure drop and heat transfer in microchannels; section 2.4 Flow boiling and section 2.5 Summary of the findings.

### 2.2 Definition of a microchannel

In recent years, due to the rapid development of small thermofluid devices, the need for studies of heat transfer and flow in the correspondingly small constituent passages has been highlighted. Because of the significant differences in the transport phenomena for such passages (“microchannels”) as compared with those of conventional size (“macrochannels”) a key introductory issue which needs clarifying is the distinction between the two classes. Despite its importance, however, there is no universal agreement on this distinction in the relevant literature.

The first attempt at establishing a criterion for the microchannel was made by Brauner and Moalem-Maron (1992). Based on an analysis of linear stability of stratified flow, and the argument that neutral stability should involve a disturbance wavelength of the order of channel

diameter, they derived the Eotvös number (Eö) criterion for the dominance of surface tension in a microscale channel,

$$E\ddot{o} = \frac{4\pi^2\sigma}{D_h^2 g(\rho_l - \rho_g)} > 1 \quad (2.1)$$

where  $\sigma$  is the surface tension,  $D_h$  refers to the hydraulic diameter of the channel,  $g$  represents the gravitational acceleration,  $\rho_l$  and  $\rho_g$  are liquid and gas/vapour densities respectively. This was followed by Kew and Cornwell (1997), who proposed a confinement number  $Co$  to distinguish between macro and microscale channels. The authors stated that confinement effects are significant for values of  $Co$  above 0.5, expressed algebraically as:

$$Co = \frac{1}{D_h} \left( \frac{4\sigma}{g(\rho_l - \rho_g)} \right)^{1/2} > 0.5 \quad (2.2)$$

There is a commonality of expression for Eö and  $Co$  in Eq. (2.1) and (2.2) and  $Co$  in particular is actually based on the definition of the Laplace constant  $L_c$ , where

$$L_c = \left( \frac{\sigma}{g(\rho_l - \rho_g)} \right)^{1/2} \quad (2.3)$$

Therefore, the hydraulic diameter of a channel based on the Eotvös number and confinement number can be expressed in the term of Laplace number,  $D_h < 2\pi L_c$  and  $D_h < 4L_c$  respectively.

A related criterion proposed by Peng and Wang (1998) was based on the initiation of nucleation. They found that nucleate boiling in channels with diameters less than 1 mm was much more difficult to achieve than in conventional channels, with its initiation requiring extremely high heat fluxes. Their criterion, expressed in terms of the nucleation characteristic  $N_{nb}$ , is given by:

$$N_{nb} = \frac{h_{lg} \alpha_g}{c \pi (v_g - v_l) q'' D_h} \leq 1 \quad (2.4)$$

where  $h_{lg}$  is the energy of evaporation,  $\alpha_g$  is the thermal diffusivity of gas/vapour,  $q''$  is the heat flux,  $v_l$  and  $v_g$  are the specific volumes of liquid and gas/vapour respectively and  $c$  is an experimental constant of value 1 for water, acetone and R12. Peng and Wang (1998) concluded that the condition for liquid nucleation in channels with diameters less than 1 mm could be expressed with a nucleate characteristic less than or equal to 1.

As mentioned above, the hydraulic diameter  $D_h$  and the Laplace constant  $L_c$ , have already been introduced. In fact  $L_c$  itself is an important dimensionless number, which can be used to represent the nature of fluid flow in microchannels, therefore, Triplett et al. (1999) defined channels with a hydraulic diameter  $D_h$  of the order of, or smaller than,  $L_c$ , as microchannels.

Meanwhile,  $D_h$  has also been on its own to distinguish microchannels from macrochannels and Mehendale et al. (2000) classified heat exchangers in general, in terms of  $D_h$ :

- (a) Micro heat exchanger:  $D_h = 1 - 100 \mu\text{m}$ .
- (b) Meso heat exchanger:  $D_h = 100 \mu\text{m} - 1 \text{ mm}$ .
- (c) Compact/macro heat exchanger:  $D_h = 1 - 6 \text{ mm}$ .
- (d) Conventional heat exchanger:  $D_h > 6 \text{ m}$ .

Finally, based on engineering practice and application areas, such as refrigeration industry in small tonnage units, compact evaporators, cryogenic industries, cooling elements of microelectronics and microelectromechanical systems (MEMS), Kandlikar (2002) subdivided channels into three groups in terms of  $D_h$ , as follows:

- (a) Conventional channels:  $D_h > 3 \text{ mm}$ .
- (b) Minichannels:  $D_h = 200 \mu\text{m} - 3 \text{ mm}$ .
- (c) Microchannels:  $D_h = 10 - 200 \mu\text{m}$ .

To understand the above criteria for distinguishing the microchannel from macrochannel, let's consider Table 2.1. Data in Table 2.1 were obtained using an assumption that flow boiling occurred for conditions as follows:

1. System pressure: 125 kPa (abs).
2. Heat flux: 100 kW/m<sup>2</sup>.
3. Saturated flow boiling.
4. Working fluid: water.

From the above conditions the diameter of channels can be determined, see Table 2.1. It can be seen in the Table that the definition of a microchannel is not clear. A diameter of channels based on Eotvös number, Confinement number and Laplace number criteria is bigger than that based on Nucleation characteristic and hydraulic diameter criteria.

Table 2.1 Hydraulic diameter of microchannels based on published criteria at the above conditions.

Reference	Criterion	$D_h$ [mm]
Brauner and Moalem-Maron (1992)	Eotvös number ( $Eö$ )	$D_h < 15.6$
Kew and Cornwell (1997)	Confinement number ( $C_o$ )	$D_h < 9.94$
Peng and Wang (1998)	Nucleation characteristic ( $N_{nb}$ )	$D_h \leq 0.09$
Triplett et al. (1999)	Laplace number ( $L_c$ )	$D_h < 2.5$
Mehendale et al. (2000)		$0.001 < D_h < 0.1$
Kandlikar (2002)		$0.01 < D_h < 0.2$

### 2.3 Single-phase Pressure Drop and Heat Transfer in Microchannels

Here two recent comprehensive reviews of single-phase flow in microchannels, those of Morini (2004) and of Rosa et al. (2009) are noted. Morini (2004) examined over 90 papers on single-phase fluid flow and convective heat transfer. From the available experimental data he concluded that further systematic studies were required to generate a sufficient body of knowledge of flow in microchannels. Rosa et al. (2009) studied the scaling effects; including entrance effect,

geometry configuration, wall roughness, temperature dependence, EDL effect, and compressibility. The uncertainty of measured data was also highlighted as an important parameter in microchannel studies.

### **2.3.1 Single-phase pressure drop**

The concept of a microchannel was introduced by Tukerman and Pease in the early 1980s. They proposed a microchannel heat sink cooling device made of silicon with a total surface area of 1 cm<sup>2</sup> (50 μm wide, 302 μm deep and a fin 50 μm thick) and stated that higher heat transfer coefficients could be obtained by decreasing hydraulic diameter (Tukerman and Pease, 1981).

Subsequently, many studies on microchannels have been reported. A wide range of authors concluded that single-phase pressure drop in a microchannel still obeyed conventional theory and macroscale correlations; see Wilding et al. (1994), Jiang et al. (1995), Harms et al. (1999), Xu et al. (2000), Gao et al. (2002), Judy et al. (2002), Yu et al. (2004) and Baviere et al. (2004). In addition, Kohl et al. (2005) conducted an investigation on discrepancies in previously published data using water as the working fluid and straight channel test sections made of silicon with hydraulic diameters ranging from 25 μm to 100 μm. They suggested that friction factors for microchannels could be accurately determined from data for standard large channels. By about that time the published data were sufficient (150 papers relating to 500 data sets) to warrant the review of Steinke and Kandlikar (2006). The data covered wide ranges of hydraulic diameters 8 μm to 990 μm and of Reynolds numbers 0.002 to 5000. They concluded that in general, conventional theory was applicable to microchannels.

Costaschuk et al. (2007) investigated water flowing in an aluminium rectangular microchannel with a hydraulic diameter of 169 μm and over a Reynolds number range of 230 to 4740. Their experimental Poiseuille numbers agreed with conventional theory. A similar conclusion was reached by Caney et al. (2007), who studied friction losses and heat transfer for water flowing in a 1 mm square minichannel, and Silverio and Moreira (2008), who investigated convection and pressure drop for fully-developed laminar flow of distilled water in microchannels of diverse

cross-sections using channels with hydraulic diameters ranging from 200  $\mu\text{m}$  to 500  $\mu\text{m}$ . They all stated that conventional theory agreed with their experimental data.

In contrast to the above literature, other experimental studies provided evidence that conventional theory was not applicable to microchannels; see Papautsky et al. (1999), Pfund et al. (2000) and Ren et al. (2001). Jiang et al. (2008) studied fluid flow and heat transfer characteristics for water flowing in rectangular microchannels. Their experimental friction factors were only 20% to 30% of conventional theory,  $16/\text{Re}$ . The transitional Reynolds number found was 1100 which was lower than conventional theory. Akbari et al. (2009) examined pressure drops of deionized water flowing in a rectangular microchannel with aspect ratios ranging from 0.13 to 0.76 and Reynolds numbers from 1 to 35. According to their experimental data and an accompanying analytical model, the Poiseuille numbers were found to be a function of microchannel geometry over the above range of tested Reynolds numbers. Their friction factors, therefore, were different with conventional theory.

Due to the small size, small roughness can greatly affect flow measurements. Qu et al. (2000) demonstrated relatively high friction factors from conventional theory when they measured pressure drops of water flowing in trapezoidal silicon microchannels with hydraulic diameters ranging from 51  $\mu\text{m}$  to 169  $\mu\text{m}$ . Their friction factors were about 8% to 38% higher than conventional theory. However, they justified the deviation as being the result of the high relative roughness (3.5% to 5.7%). Jiang et al. (2001), who used a microchannel with a hydraulic diameter of 300  $\mu\text{m}$ , and Kandlikar et al. (2003), who employed diameters of 1.06 mm and 0.62 mm tubes, elucidated that because of the channel roughness, their friction factors were higher than conventional theory. However, Kandlikar et al. (2003) specified that the effect of surface roughness (relative roughness of 0.36%) was significant only for the smallest diameter test section (0.62 mm). Shen et al. (2006) studied flow and heat transfer of deionized water flowing in rough-walled copper microchannels assembled in a 26-channel arrays. The rectangular channels were 300  $\mu\text{m}$  wide and 800  $\mu\text{m}$  deep. They applied three different inlet temperatures; 30°C, 50°C and 70°C and their Reynolds numbers varied from 162 to 1257. They found that the effect of

surface roughness (relative roughness 4 - 6%) on laminar flow was significant and higher inlet temperatures decreased the pressure drop. However, they did not explain the effect of fluid temperature on the friction factor.

Fluid temperatures may affect the friction factor in microchannels. Urbanek et al. (1993) investigated the influence of temperature on the Poiseuille number of flow of propanol, pentanol and water in trapezoidal and triangular microchannels with hydraulic diameters of 5  $\mu\text{m}$ , 12  $\mu\text{m}$  and 25  $\mu\text{m}$ . They claimed that as the temperature increased from 0°C to 80°C, the Poiseuille numbers also increased by as much as 25% and 10% for the 12  $\mu\text{m}$  and 25  $\mu\text{m}$  channels, respectively. In contrast, Toh et al. (2002), who performed an experimental investigation of water flowing in parallel silicon channels with widths and depths ranging from 50 to 64  $\mu\text{m}$  and 280 to 320  $\mu\text{m}$  respectively, stated that as the temperature was increased, the friction factor decreased.

Table 2.2 is the summary of review on the papers showing the discrepancy between the published experimental results of water single-phase flow in non-circular conduits and conventional theory. From Table 2.2, it can be noted that in the basis of friction factor from 21 selected papers, authors in 13 papers stated that their results were in good agreement with conventional theory, authors in 7 papers claimed that their findings did not agree and authors in one paper did not compare their results with conventional theory. However, based on the hydraulic diameter used by the authors in the papers, it can be concluded that the effect of diameter on the agreement with conventional theory needs further investigations. In addition, the friction factor results are compared with fully developed flow theory and correlations, e.g. fully developed flow proposed by Shah and London (1978), developing laminar flow correlation proposed by Shah (1978), fully developed turbulent flow proposed by Blasius (Hager, 2003) and developing turbulent flow correlation due to Phillips (1987). All correlations used in the comparison are given in Table A.1 in Appendix A.

Table 2.2 Literature for experimental Poiseuille numbers of single-phase flow of water in non circular microchannel passages.

Author	Fluid/ Shape and Channel material	$D_h$ ( $\mu\text{m}$ )	$W(\mu\text{m})$	$H(\mu\text{m})$	$\beta=W/H$	Number of channel	Re	$fRe$	$L(\text{mm})$	Agree or not with the classical theory
Urbanek et al. (1993)	Propanol, water/TP, TR, silicon	5, 12, 25	-	-	-	2	-	-	-	N/higher
Wilding et al. (1994)	Water, blood, serum/R, silicon.	26.7- 63.16	40-150	20-40	2-3.75	1	-	-	11.7	Y
Jiang et al. (1995)	Deionized water/R, silicon.	47, 88.89, 160	25,50, 100	400	0.0625; 0.125; 0.250	1	-	-	2.5; 5; 10	Y
Harms et al. (1999)	Deionized water/R, Silicon	401.3	251	1000	0.251	1 and 68	173- 12900	-	25	Y
Papautsky et al. (1999)	Water/R, nickel channel.	28.57- 57.14	50-600	20-30	2.5-20	5, 7	1-20	51.84	12.75	N/65.5, higher
Pfund et al. (2000)	Water/R, Polyimide	252.76- 990.4	10000	128- 521	78.125- 19.19	1	60- 3450	24.2	100	N/22.4, higher

Table 2.2 Continued

Xu et al. (2000)	Water/R, aluminum	288.15-29.56	228-377.8	391.3-15.4	1.716-0.041	1	-	-	10-50	Y
Qu et al. (2000)	Deionized water/TP, silicon	51-169	-	-	-	5	Up to 1500	85-65	28	N/higher 8 to 38%
Jiang et al. (2001)	Water/R, pure copper plate.	300	200	600	0.333	38	60-3000	-	15	N/higher
Ren et al. (2001)	KCL, water/R, silicon	28.1, 56.1, 80.3	5000	14.1, 28.2, 40.5	0.0028, 0.0056, 0.0081	1	60	-	30	-
Gao et al. (2002)	Water/R, brass	199 - 1923	25000	100 - 1000	0.004 - 0.04	1	Up to 8000	24	82	Y
Baviere et al. (2004)	Water/R, Silicon	43.98	500	23	21.74	1	Up to 300	23.44	20.5 and 36.5	Y
Kohl et al. (2005)	Water/R, silicon	25-100	25.6-101.3	24.4-98.4	1-0.987	1	4.9-2068	-	10-22	Y
Shen et al. (2006)	Deionized water/R, copper	436.36	300	800	0.375	26	162-1257	-	50	N/higher

Table 2.2 Continued

Costaschuk et al. (2007)	Water/R, Aluminum channel	169.3	1161.5	91.3	12.72	1	230- 4740	86.4	57.1	Y/86.9
Jiang et al. (2008)	Water/R, oxygen free copper.	504	900	350	2.57	13	Up to 6000	-	80	N/lower
Silverio and Moreira (2008)	Water or HFE7100/R, Borosilicate glass	200	200	200	1	1	20- 800	-	-	Y
Akbari et al. (2009)	Water/R, Polydimethyl silocane	96.4- 58.24	390-67	55-51.5	0.13- 0.76	1	1-35	13.16	50	Y

Note: R-rectangular channel, S-square channel, TP- trapezoidal channel and TR- triangular channel.

### 2.3.2 Single-phase heat transfer

Single-phase heat transfer in microchannels was investigated and reported by several researchers. Some researchers claimed that the heat transfer coefficient in micro passages was different from that of macro passages; see Tukerman & Pease (1981), Gao et al. (2002) and Silverio and Moreire (2008), whilst other researchers reported that conventional theory was still applicable for predicting the data for micro passages, e.g. Harms et al. (1999), lelea et al. (2004) and lee et al. (2005). In contrast, Wang and Peng (1994) studied experimentally forced convective flow and heat transfer in rectangular stainless steel microchannels with hydraulic diameters ranging from 0.31 to 0.747 mm using water as the working fluid. They found that in turbulent flow the trends of heat transfer coefficient could be predicted using Dittus-Boelter's correlation. However, the values of the Nusselt number obtained were lower than those calculated using Dittus-Boelter's correlation. This was indicated by the coefficient of their correlation, 0.00805, see Eq. (2.5):

$$\text{Nu} = 0.00805 \text{ Re}^{0.8} \text{ Pr}^{0.33} \quad (2.5)$$

In addition, they revealed that the laminar and transition heat transfer behaviour in microchannels were unusual and complex and were strongly influenced by the liquid temperature, velocity and microchannel size.

The dependence of Nusselt number on the Reynolds number was found by Steinke et al. (2006). They investigated single-phase liquid heat transfer and pressure drop in various microchannel geometries. They used water as the working fluid and the microchannels were made of silicon substrate with a width of 100  $\mu\text{m}$  and a height of 200  $\mu\text{m}$  ( $D_h = 133.3 \mu\text{m}$ ). They expressed the heat transfer performance in terms of thermal resistance. The thermal resistance depended on the Reynolds number for low mass fluxes but was independent of the Reynolds number for high mass fluxes. Similarly, Mishan et al. (2007), who studied experimentally the effect of developing thermal region on heat transfer performance of flow in microchannels made of aluminium with a hydraulic diameter of 440  $\mu\text{m}$ , explained that the Nusselt number was not constant but increased with Reynolds number. Furthermore, the average Nusselt number increased from 5 to 7 with Reynolds numbers ranging from 40 to 560.

The lower Nusselt number than conventional theory was found by Jiang et al. (2008), who studied water flowing in a parallel rectangular microchannel made of copper with a height and width of 350  $\mu\text{m}$  and 900  $\mu\text{m}$  respectively. They elucidated that the Nusselt number remained constant when the flow rate was small, however, as the flow rate was increased, the Nusselt number significantly increased and exceeded the value of the Nusselt number for fully developed flow in conventional channels. Furthermore, the Nusselt number was affected by the heat flux when the mass flow rate was large. They stated that the Nusselt number of flows in microchannels was smaller than that in macrochannels at a flow rate of  $1.8 \times 10^{-5} \text{ m}^3/\text{s}$  (1080 ml/min). The Nusselt number was constant at approximately two in the laminar regime for  $\Delta T_{lm}$  ranging from 10 to 100. However, at a flow rate of  $2.77 \times 10^{-5} \text{ m}^3/\text{s}$  (1660 ml/min), the Nusselt number increased with  $\Delta T_{lm}$  ranging from 10 to 60. In transition regimes they found that the Nusselt number increased slightly, whilst in turbulent regimes the Nusselt number increased sharply with the Reynolds number.

Jung and Kwak (2008) measured the heat transfer coefficient and friction factor of water flowing in a microchannel with a hydraulic diameter of 100  $\mu\text{m}$ . They concluded that the Nusselt number differed from conventional theory and could be correlated as

$$\text{Nu} = 0.00058 \text{Re}^{1.15} \text{Pr}^{1/3} (\mu(T_w) / \mu(T_\infty))^{2.76} (W / H)^{0.3} \quad (2.6)$$

where  $T_w$  is the wall temperature,  $T_\infty$  the fluid temperature in the core,  $\mu$  the dynamic viscosity,  $W$  the channel width and  $H$  the channel height.

Finally, to know the effect of hydraulic diameter on the Nusselt number, Table 2.3 is presented. From Table 2.3, it can be noted that the effect of hydraulic diameter on the Nusselt number is not clear. It is shown by the scattered and discrepancy results. For example, Jung and Kwak (2006) used a microchannel with a hydraulic diameter of 100  $\mu\text{m}$  found that the Nusselt number was lower than conventional theory, whilst Mishan et al. (2007) employed a microchannel with a hydraulic diameter 440  $\mu\text{m}$  obtained a higher Nusselt number than conventional theory. Meanwhile, Tukerman and Pease (1981), who used microchannels with hydraulic diameters of

85.8, 92.3 and 95.3  $\mu\text{m}$ , revealed that their experimental Nusselt numbers were higher than conventional theory. Therefore, the Nusselt number of flow in microchannels needs to be investigated more precisely.

Similar to friction factor results, the experimental Nusselt numbers are also compared with several correlations. The correlations used in the comparison are fully developed laminar flow for three heated walls and uniform wall temperature proposed by Shah and London (1978), thermally developing laminar flow proposed by Shah and London (1978), thermally developing laminar flow for non-circular conduits proposed by Bejan (2004), fully developed turbulent flow correlations proposed by Dittus-Boelter, Gnielinski and Seider-Tate (Incropera et al. 2006), and a correlation proposed by Choi et al. (1991). All correlations mentioned here are listed in Table A.2 in appendix A. The equation proposed by Shah and London (1978) is used for a comparison because the correlation was created for three heated walls and uniform wall temperature. Thus, the correlation does meet the experimental conditions in this study. Also, the correlation was proposed for laminar fully developed flow and thermally developing flow as well as for non-circular conduits. The correlation proposed by Bejan (2004) is also suitable to be compared because the correlation was used for developing flow and non-circular conduits. Meanwhile, correlations proposed by Dittus-Boelter, Gnielinski, Seider-Tate are used because they are for general purposes and macroscale. Thus, they are used for checking the heat transfer characteristics in this study to see if there is discrepancy of thermal behavior in the study with macroscale correlations. Choi et al (1991) performed experiments to investigate the Nusselt numbers for Reynolds numbers ranging between 50 and 20000. Both laminar and turbulent regimes are studied. They found that the Nusselt number depended on the Reynolds number and Prandtl number in laminar regimes. They proposed two new correlations for the average Nusselt number in laminar and turbulent regimes.

Table 2.3 Literature for experimental Nusselt numbers for single-phase flow of water in non-circular microchannel passages.

Author	Fluid/ Shape and Channel material	$D_h$ ( $\mu\text{m}$ )	$W(\mu\text{m})$	$H(\mu\text{m})$	$\beta=H/W$	Number of channel	Re	Nu	$L(\text{mm})$	Agree or not with the classical theory
Tukerman and Pease (1981)	Water/R, Silicon.	95.3 92.3 85.8	56 55 50	320 287 302	5.7 5.2 6	Not stated	Not stated	3 - 9	10	N/higher
Wang and Peng (1994)	Water/R, Stainless Steel.	310 - 747	200 - 800	700	3.5 - 0.875	4 - 6	100 - 1500	0.00805 $\text{Re}^{0.8}$ $\text{Pr}^{0.33}$	45	N/lower
Harms et al. (1999)	Deionized water/R, Silicon.	401.3	251	1000	0.251	1 and 68	173- 12900	Various	25	Y
Gao et al. (2002)	Water/R, Brass.	199 - 1923	25000	100 - 1000	0.004 - 0.04	1	200 - 6000	Various	82	N/lower
Lelea et al. (2004)	Water/C, Stainless steel tubes.	100, 300, 500	-	-	-	1	- 800	$\sim 4.36$	250	Y

Table 2.3 Continued

Lee et al. (2005)	Water/R, Copper.	318 - 903	194 - 534	884 - 2910	4.56 – 5.45	10	300 - 3500	-	25.4	Y
Steinke et al. (2006)	Water/R, Silicon.	133.33	100	200	2	18 - 100	61 - 364	Not stated	10	-
Mishan et al. (2007)	Water/R, Aluminum.	440	320	750	2.34	Not sated	40 - 560	5 - 7	82	Y
Jiang et al. (2008)	Water/R, Copper.	504	900	350	0.39	13	300 - 6000	2	80	N/lower
Silverio and Moreira (2008)	Water and HFE 7100/C, R. Borosilicate tubes.	200, 500	200	200	1	1	- 800	Lower	60	N/lower
Jung and Kwak (2008)	Water/R, Silicon.	100	100	100	1	5	- 330	Lower	15	N/higher

## **2.4 Flow boiling**

When liquid is exposed to a surface heated above the liquid saturation temperature then the liquid will boil. Boiling can be divided into two categories: pool boiling and flow boiling. When stationary liquid is boiling, it is called pool boiling and if the boiling liquid has a relative velocity to the heated surface then it is termed flow boiling. Flow boiling is the focus of this thesis and therefore will be discussed in detail.

Basically flow boiling itself has two categories: subcooled boiling and saturated boiling. Subcooled flow boiling occurs when the bulk liquid temperature is subcooled below the liquid saturation temperature at corresponding pressure, and the heated surface temperature is above that temperature. The bubbles formed on the heated surface may not grow further and even may collapse due to the subcooled liquid. In the case of saturated flow boiling, the bulk liquid temperature is in saturated conditions and the bubble formed can grow depending on heat input to the heating surface. Saturated flow boiling is classified into two different mechanisms, i.e. nucleate boiling and convective boiling. In fact, it may be possible that both mechanisms can happen together. In nucleate boiling, heat is transferred through bubbles formed at the nucleation sites on the heated surface. In convective boiling, heat is transferred through a thin liquid film between vapour and heated surface and evaporation takes place without bubble nucleation at the liquid vapour interface. In addition, in dominant nucleate flow boiling, the heat transfer coefficient is expected to increase with increasing heat flux, whilst in convective flow boiling it is expected to increase with increasing mass flux and vapour quality. The dependence of nucleate boiling and convective boiling on heat flux and mass flux has been used by most authors in the literature to determine the dominant mechanism, even though some tests were done with glass tubes, so that the actual nucleation of bubbles was visible and the corresponding type of boiling mechanism could be found correctly.

### **2.4.1 Flow patterns in microchannels**

As mentioned above, flow patterns in flow boiling correlate with heat transfer mechanisms and even the heat transfer coefficients. This correlation becomes very important in studying flow

patterns of flow boiling. In microchannels, the flow patterns vary considerably, as observed by different researchers. Because there is no specific standard for naming and assessing flow patterns, researchers have often adopted their own definitions/names. Further, the observational length and location have not yet been standardized and explained in the literature. This might be the cause of discrepancies in results reported from previous studies. As the heat transfer mechanisms are strictly linked to flow patterns, the nature of flow patterns are required for a fundamental understanding of heat transfer in small passages, particularly in micro passages.

#### 2.4.1.1 Adiabatic flow patterns

There is disagreement on whether adiabatic flow patterns can explain flow boiling heat transfer and pressure drop characteristics. This is the reason for distinguishing between adiabatic studies and flow boiling studies. Nevertheless, in this work, the literature for adiabatic flow patterns is used to clarify whether there is any difference with diabatic (flow boiling) patterns. As channel size decreases, surface tension forces dominate over gravity forces and so the effect of channel orientation becomes insignificant, see Chen et al. (2002) and Akbar et al. (2003). As a consequence, new flow patterns/features may appear or some of conventional patterns may collapse. For instance, the conventional stratified flow pattern diminishes in microchannels: see Triplett et al. (1999), Chen et al. (2002), and Saisorn and Wongwises (2010). Bubbly and churn flows were not observed in the studies of Kawahara et al. (2002), Hayashi et al. (2007) and Xiong and Chung (2007). It should be noted that the adiabatic two-phase flow presented here is only of co-current flow.

The effect of channel aspect ratio on flow pattern was investigated by Wambsganss et al. (1991). They studied adiabatic air-water horizontal two-phase flow patterns in a rectangular Plexiglas mini-channel, 3.18 mm deep and 19.05 mm wide (or 5.45 mm of hydraulic diameter) and 1.14 m long. They identified flow patterns at mass fluxes ranging from 100 to 1000 kg/m<sup>2</sup>s in the two channels with different aspect ratios. The aspect ratio used in their study was defined as the channel height divided by the channel width. The flow patterns observed in a channel of aspect ratio 6 with the photographs being taken from a horizontal position were bubble, plug, slug, stratified, wave and annular, whilst those observed in a channel of aspect ratio 1/6 with

photographs taken from above the channel or in a vertical position were bubble, plug, slug and annular. The two flow patterns, stratified and wave were not observed in the channel with an aspect ratio of 1/6. For the large aspect ratio, the flow has a bigger and longer size of bubbles than those for the smaller aspect ratio. The authors explained that this phenomenon could be due to the small vertical gap which did not allow the existence of a finite thickness film. Waves on such a film could easily reach the upper surface, giving rise to other flow patterns. Overall, these findings indicated that the aspect ratio gave a more significant influence than the diameter. A similar study was performed by Mishima et al. (1993) to observe adiabatic air-water vertical up flow in three rectangular mini-channels 1.0, 2.4, and 5.0 mm deep, and 40 mm wide, giving hydraulic diameters of 1.95 mm, 4.528 mm and 8.89 mm made of acrylic resin. Four flow patterns (bubbly, slug, churn, and annular) were found, but churn flow was never observed in the channel 1.0 mm deep. The authors questioned whether the diminishing churn flow was eliminated by the depth (aspect ratio) or by the smaller hydraulic diameter.

The observations of Wilmarth and Ishii (1994) were for an adiabatic air-water two-phase flow vertically and horizontally in two stainless steel rectangular minichannels with hydraulic diameters of 1.9 mm and 3.53 mm and adjustable gaps. In the vertical channels, the flow patterns observed were bubbly, cap bubbly, slug, slug-churn, churn and annular, whilst in the horizontal channels were stratified, plug, slug, dispersed and wavy annular. Three transition regions namely elongated plug, elongated slug, cap bubbly were identified for horizontal flow. Comparing the two sets of flow patterns shows that channel orientation plays the dominant role. In contrast, Mishima and Hibiki (1996) investigated air/de-ionized water flow in four Pyrex glass tubes of diameters 1.05, 2.05, 3.12, 4.08 mm and in four aluminium tubes of diameters 1.09, 2.1, 3.08, 3.9 mm. They found that the flow patterns observed were the same as those in conventional channels; bubbly, slug, churn, annular and annular-mist flow. However, the capillary tube demonstrated the following new features, see Fig. 2.1.

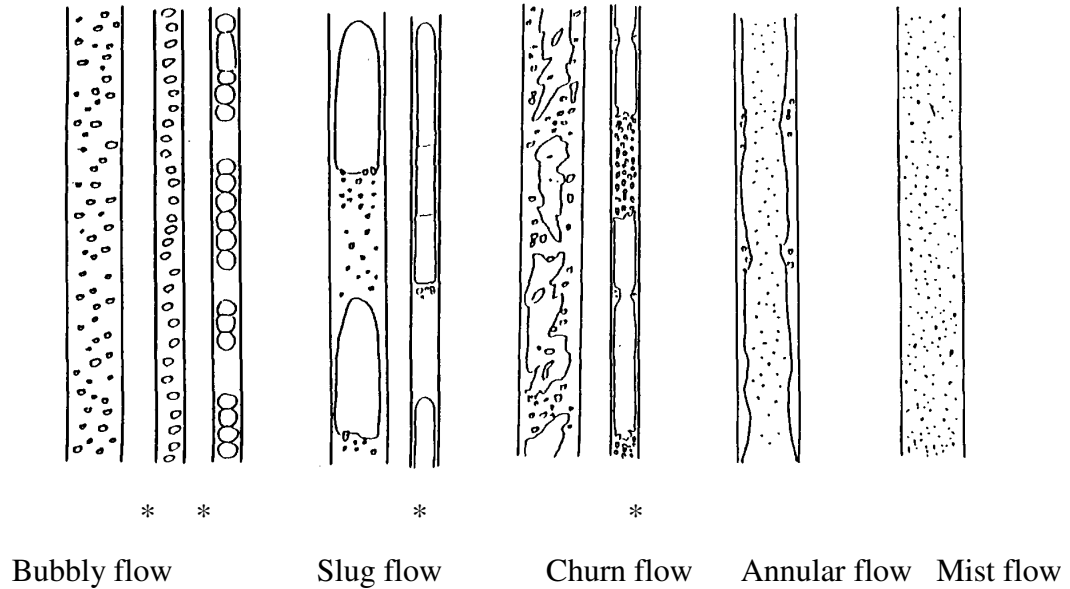


Figure 2.1 Sketch of the air-water flow patterns in vertical tubes of diameter 1.05 – 4.08 mm Mishima and Hibiki, (1996).

The authors stated that the asterisks denoted flow regimes which were specific for a capillary tube, whereas the other sketches showed flow regimes observed in both larger diameter and capillary tubes.

The presence of the edges or corners in non-circular channels may keep the channel wall covered with liquid all the time and consequently influence the features of the gas-liquid interface. This was investigated by Xu et al. (1999). They performed an adiabatic air-water vertical up flow in three rectangular mini/microchannels (12 mm in width, 0.3, 0.6, and 1.0 mm in depth, with hydraulic diameters of 0.585, 1.143 and 1.846 mm) made of Pyrex glass. Four flow patterns (bubbly, slug, churn, annular) and two transition regions (cap-bubbly, slug-churn) were identified in the 0.6 and 1.0 mm channels, but only four patterns (cap-bubbly, slug-droplet, churn, and annular-droplet) in the 0.3 mm channel. They explained that with decreasing channel depth, the transition boundaries for bubbly-slug, slug-churn, and churn-annular flow shifted to lower values of superficial gas velocity.

The effect of diameter on flow patterns of air-water was investigated by Coleman and Garimella (1999). They performed experiments using horizontal circular tubes made of Pyrex glass and a rectangular channel made of transparent plastic with diameters ranging from 1.3 to 5.5 mm and a hydraulic diameter of 5.36 mm respectively. They reported that the channel diameter had a significant effect on intermittent/bubbly, intermittent/dispersed and intermittent/annular transition boundaries. Note that intermittent meant the flow was characterized by discontinuous liquid and gas flow. These are shown in Fig. 2.2. As the channel diameter decreased, the transition from intermittent to dispersed bubbly or bubbly flow occurred at progressively higher liquid superficial velocities and almost constant superficial gas velocities. This was attributed to the predominance of surface tension.

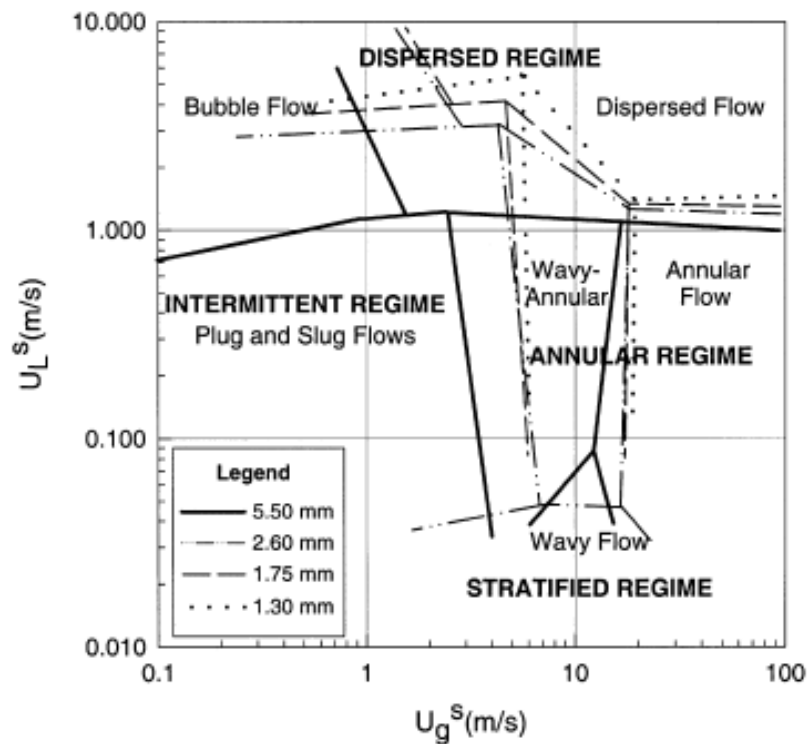


Figure 2.2 Effect of channel diameter on the flow pattern transition boundaries, Coleman and Garimella (1999).

Different with those observed by Coleman and Garimella (1999), Triplett et al. (1999), who studied two-phase flow of air-water in horizontal circular and semi triangular tubes with

diameters of 1.097 and 1.447 mm and 1.088 and 1.493 mm, did not observe the effect of diameter on flow pattern. They employed circular tubes made of Pyrex glass, small semi triangular channel made of Acrylic and the big semi triangular made of Polycarbonate. They revealed that the flow patterns observed were the same for all test sections, namely bubbly, slug, churn, slug-annular and annular.

Characteristics of upward air-water two-phase flow patterns in vertical triangular channels with hydraulic diameters of 2.886 mm, 1.433 mm and 0.866 mm were investigated by Zhao and Bi (2001). The test section was made of Lucite material (Plexiglas/acrylic) with a length of 270 mm. As shown in Fig. 2.3, they found that for the two larger diameters the flow patterns observed were dispersed bubbly, slug, churn and annular, whilst for the smallest channel the patterns observed were capillary bubbly, slug, churn and annular. Thus, the differences of flow patterns among those three different hydraulic diameters are dispersed bubbly (for the two larger channels) and capillary bubbly flow (for the smallest channel). For the 1.433 and 2.866 mm tubes, they found that the flow patterns observed were dispersed bubbly, slug, churn and annular.

Hetsroni et al. (2003) observed air-water flows in parallel triangular microchannels made of fabricated silicon substrate 15 x 15 mm, 530  $\mu\text{m}$  thick. They used three types of test modules: Type 1 consisting of 21 channels with hydraulic diameter 0.129 mm, Type 2 of 26 channels with hydraulic diameter 0.103 mm, and Type 3 of 17 channels with hydraulic diameter 0.161 mm. At low heat fluxes, bubble nucleation was observed on the wall of the test section. The size of the smallest bubble was found to be approximately 30  $\mu\text{m}$ . Then the bubble grew and flowed downstream. As the flow rate of gas was increased, different flow patterns were observed, namely capillary bubble flow, slug and annular flow. Nevertheless, the authors did not specify nor present the difference of the flow patterns observed in the three test sections (0.129 mm, 0.103 mm and 0.161 mm channels).

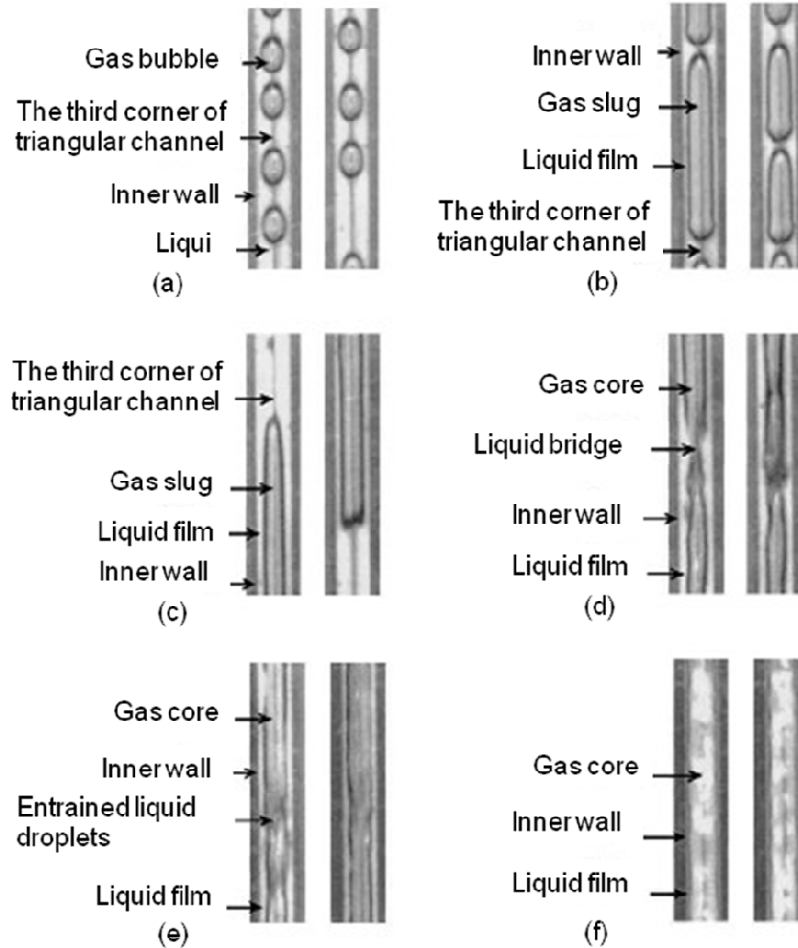


Figure 2.3 Flow pattern and pressure fluctuation in a vertical triangular channel with a hydraulic diameter of 0.866 mm; (a) capillary bubble, (b) and (c) slug, (d) churn, (e) and (f) annular, Zhao and Bi (2001).

Similar to that revealed by Chen et al. (2002) and Saisoron and Wongwises (2010), the experiments of Qu et al. (2004) which involved adiabatic nitrogen-water two-phase flow in a horizontal Acrylic rectangular microchannel of  $0.406 \times 2.032 \text{ mm}^2$  cross section, hydraulic diameter of 0.677 mm and length of 120 mm, demonstrated diminishing some flow patterns. In their experiments, they employed superficial velocities of nitrogen and water ranging from 0.08 to 81.92 m/s and 0.04 to 10.24 m/s. They found that the dominant flow patterns were slug and annular, with bubbly flow occurring occasionally. Stratified and churn flow were never observed, there were no water droplets present in the nitrogen bubble, nor were any nitrogen bubbles

present in the water slugs. Venkatesan et al. (2010) also studied the same subject as Qu et al. (2004). They used horizontal tubes made of borosilicate glass with inner diameters of 0.6, 1.2, 1.7, 2.6 and 3.4 mm. They applied gas and liquid superficial velocities ranging from 0.01 to 50 m/s and 0.01 to 3 m/s. The flow patterns observed for the 3.6 mm tube were dispersed bubbly, bubbly, slug, slug-annular and wavy annular, whilst those for the 2.6 mm tube were dispersed bubbly, bubbly, slug, slug-annular, wavy annular and stratified. However, for the smaller test sections, 1.2 and 1.7 mm tubes, the flow patterns found were dispersed bubbly, bubbly, slug, slug-annular, annular and for the 0.6 mm tube were dispersed bubbly, bubbly, slug and slug-annular.

#### 2.4.1.2 Flow boiling patterns

As mentioned before, flow boiling patterns are linked to two-phase flow heat transfer coefficients and mechanisms. Knowledge of the flow patterns means the heat transfer mechanism can be identified as to whether it is dominated by nucleation or convection or even both. In macrochannels, the commonly observed flow boiling patterns are bubbly, slug, churn, annular and mist flow as explained by Collier and Thome (1994), whilst Kandlikar (2002) reported that isolated bubble, confined bubble/slug and annular flow are patterns prevalent in microchannels. Some researchers, namely Sobierska et al. (2006) and Revellin et al. (2006), claimed that the churn pattern diminished in microchannels. Using confinement number criterion, Sobierska et al. (2006) explained that the channel having a hydraulic diameter of 1.2 mm was classified as a microchannel because the confinement number obtained was 2.2. They used water as the working fluid and the channel was made of copper. Only three basic flow patterns were found (bubbly, slug and annular). Unlike the behaviour in adiabatic two-phase flow, the flow pattern and the associated vapour quality changed along the channel axis. During heating the fluid temperature close to the wall reached the saturation condition and bubble generation started, even if the bulk volume of water were subcooled. For negative quality (in the subcooled region), the dominant flow pattern was bubbly.

As there is no standard for naming the flow patterns, in this study, the flow pattern definition used by Chen et al. (2006) is used to classify the observed flow patterns. In Chen et al (2006), the

flow boiling patterns of refrigerant R134a in 1.1 mm, 2.01 mm, 2.88 mm and 4.26 mm stainless steel tubes were dispersed bubble, bubbly, confined, slug, churn, annular and mist. Of these, dispersed bubble, bubbly, slug, churn and annular flow were observed in all the tubes. Occasionally mist flow was observed in the larger tubes at very high vapour velocity whilst confined bubble flow was found in smaller tubes at lower vapour and liquid velocities. A set of typical flow patterns can be seen in Fig. 2.4 for the 1.1 mm diameter tube. They defined the above-mentioned seven flow patterns as follows:

- (a) Dispersed bubble: numerous small bubbles float in a continuous liquid phase.
- (b) Bubbly: bubble size is comparable to but not as large as the tube diameter.
- (c) Confined bubble: bubble size reaches the diameter of the tube and is confined by the tube wall. They have regular vapour-liquid interfaces and spherical caps and bottoms.
- (d) Slug: bubbles develop into a bullet shape due to the tube wall restriction. Sometimes the bullet bubble is followed by a stream of small bubbles creating a trail.
- (e) Churn: bullet bubbles start to distort and small bubbles in liquid slug coalesce into gas clump with increase of gas velocity - a highly oscillatory flow with chaotic interface.
- (f) Annular: gas phase becomes a continuous flow in the core of the tube.
- (g) Mist: liquid film is blown away from the tube wall and numerous liquid droplets float in high-speed vapour flow.

Flow patterns in stable and unstable conditions of flow boiling were investigated by Wang et al. (2007) using eight parallel channels with a hydraulic diameter of 186  $\mu\text{m}$  at inlet temperature of 35°C. The flow patterns observed were bubbly, transition between bubbly to annular/mist, annular/mist, transition between annular/mist to bubbly. The same subject was investigated by Wang et al. (2008) using three type configurations of inlet and outlet plenums. The flow patterns observed generally were the same, irrespective of configuration: alternating bubbly-slug, alternating bubbly annular and alternating annular-mist.

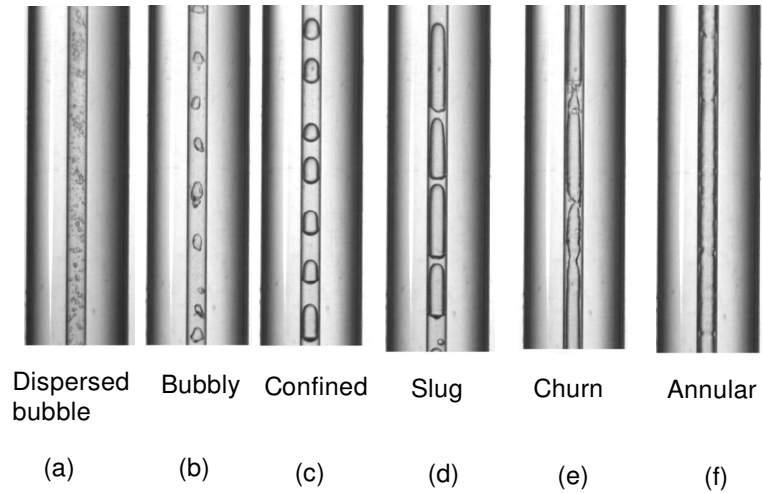


Figure 2.4 Flow patterns observed in the 1.1 mm internal diameter at 10 bar, taken from Chen et al. (2006).

Similar to that observed by Sobierska et al. (2006), Singh et al. (2009) also observed three basic flow patterns, namely bubbly, slug and annular. They used a trapezoidal silicon microchannel with a hydraulic diameter of  $109 \mu\text{m}$  with water as the working fluid at a saturation inlet temperature of  $100^\circ\text{C}$ . However at low mass fluxes and heat fluxes, the bubbly flow regime diminished. This behaviour was attributed to the bubbles having a short lifespan or growing rapidly to the channel size.

Wang et al. (2011) performed a photographic study on two-phase flow patterns of water in a single side heated narrow rectangular channel of cross section  $40 \times 3 \text{ mm}^2$  with a hydraulic diameter of  $5.58 \text{ mm}$  and an aspect ratio of 13.33. The channel was installed vertically and made of quartz glass, whilst the heated plate was made of stainless steel. Four discernible flow patterns, entitled dispersed bubbly, coalesced bubbly, churn flow, and annular flow were observed. The dominant flow patterns observed for upward flow boiling were dispersed bubbly, churn and annular.

### 2.4.2 Flow pattern maps

Flow-pattern maps may be classified primarily into two types: empirical flow-pattern maps, which are generally fitted to the observed flow-pattern database, and theoretical or semitheoretical flow-pattern maps whose transitions are predicted from physical models of the flow phenomena. Theoretical or semitheoretical flow-pattern maps are developed according to the flow structure and are sometimes related to heat transfer mechanisms and diabatic characteristics. Usually, only two flow parameters are used to define a coordinate system on which the boundaries between the different flow patterns are charted, such as the superficial gas and liquid velocities. Transition boundaries are then proposed to distinguish the location of the various flow regimes as in a classical map. Most flow maps are only valid for a specific set of conditions and/or fluids, although efforts are made to propose generalized flow maps.

Adiabatic two-phase flow patterns were studied experimentally by Triplett et al. (1999) in circular channels 1.1 mm and 1.45 mm in diameter, and in semi-triangular channels 1.09 mm and 1.49 mm in hydraulic diameter. They constructed flow pattern maps by plotting gas superficial velocity against liquid superficial velocity. As shown in Fig. 2.5 for the 1.09 mm hydraulic diameter semi triangular microchannel there were five regions: bubbly, slug, churn, slug-annular and annular. They concluded that for all test sections the flow pattern map suitably demonstrated the flow patterns, thus indicating that there was no effect of hydraulic diameter on flow pattern. However, the flow pattern map as taken from Triplett et al. (1999) was not clear, so the map has been redrawn to give the clear graph of Fig. 2.5.

Zhao and Bi (2001) presented flow regime maps based on observations on three triangular channels having hydraulic diameters of 2.89, 1.44 and 0.87 mm. They found that the patterns in the two larger channels were similar to typical flow patterns encountered in conventional, large-sized vertical tubes, such as bubbly flow, slug flow, churn flow and annular flow. Dispersed bubble flow was also observed for these two channels. However, in the smallest channel (0.87 mm), the dispersed bubble vanished from the flow regime map. This indicated that reducing the channel size causes the number of flow regimes to collapse.

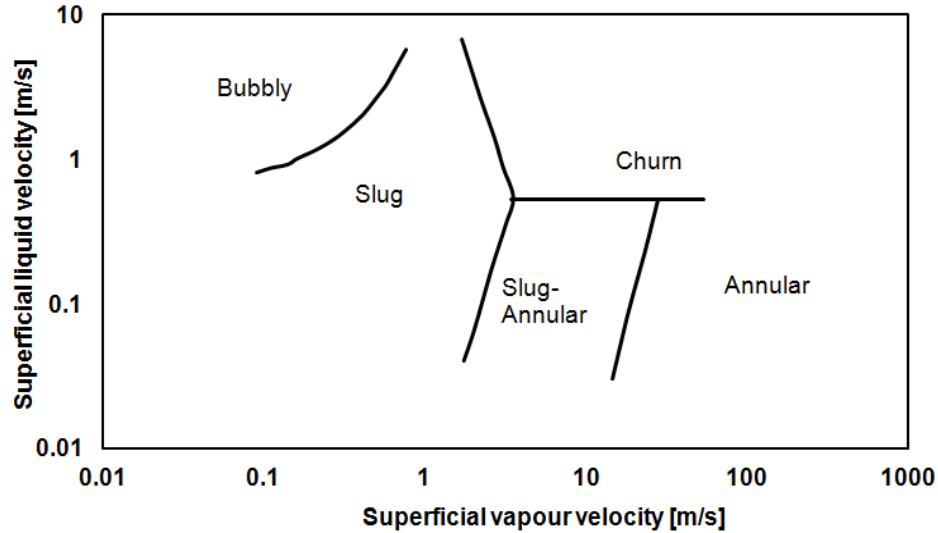


Figure 2.5 Flow pattern map for the 1.096 mm tube diameter, redrawn from Triplett et al. (1999). The line boundary data were taken using the Digitizelts software.

The adiabatic flow pattern map created by Qu et al. (2004) for air-water flow in a horizontal rectangular microchannel. It consists of bubbly-slug, liquid-slug, slug, liquid-annular and annular regimes. The hydraulic diameter used was smaller at 0.668 mm than that of the channel tested by Zhao and Bi (2001). However, capillary bubble flow was not observed but appeared as bubbly-slug flow consisting of bubble and slug flowing intermittently. The lines of transition flow pattern differ from those of Zhao and Bi (2001), indicating that channel orientation (horizontal/vertical) strongly affects the flow pattern maps for microchannels.

A general flow pattern map has been created by Hassan et al. (2005), based on experimental flow patterns of flow boiling in horizontal rectangular microchannels. The fluids used were commonly water. This universal flow pattern map is shown in Fig. 2.6 and holds for hydraulic diameters less than 1 mm. In formulating the map they grouped the maps into two categories: the surface tension dominated regime and the inertia dominated flow regime. Four general regimes were chosen as identifiers: bubbly, intermittent, churn and annular flows. The flow regimes mainly dominated by surface tension are characterized by large and elongated bubbles of gas and regroup flows such as bubbly, intermittent flow, churn flow and annular flow. The regimes for

inertia dominated flows include annular and dispersed flows. Intermittent indicates that the patterns consisted of slug and slug/annular, therefore, in Fig. 2.6, the transition line separating the slug and slug-annular areas, alike shown in Fig. 2.5, disappears.

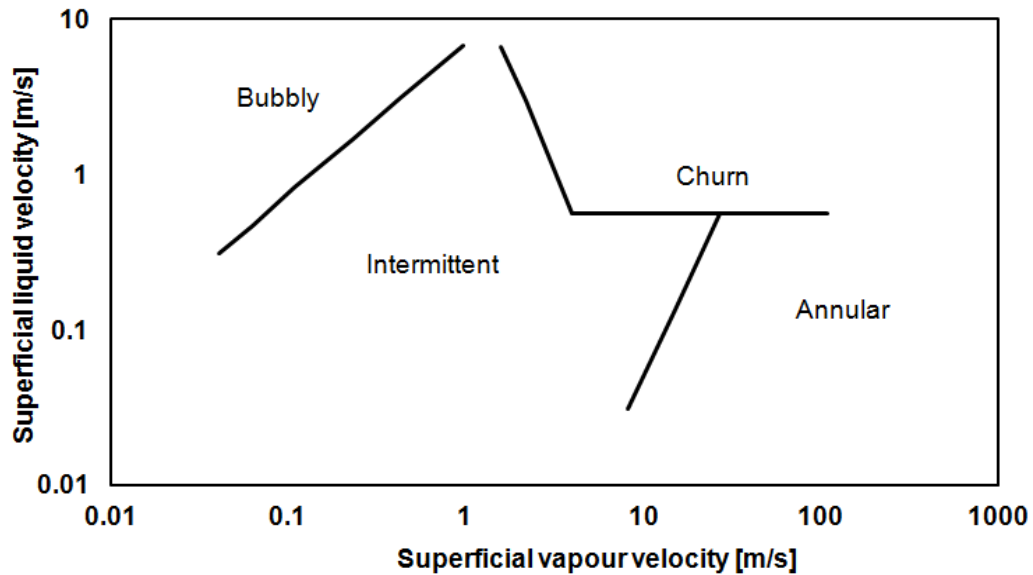


Figure 2.6 Universal flow pattern map for flow boiling in horizontal microchannels, Hassan et al. (2005).

In the same way as Zhao and Bi (2001), Sowinski and Dziubinski (2008) performed experiments on gas-water flow in vertical microchannels made of polycarbonate with hydraulic diameters of 1.25 and 1.13 mm. However, the map created by Sowinski and Dzibinski (2008), which consisted of bubble, cap bubble, slug, slug-churn, and annular flows, indicated that decreasing hydraulic diameter had an inconsistent effect on the pattern map.

Another flow boiling pattern map was created by Wang et al. (2011), as shown in Fig. 2.7. They used water as the working fluid. The channel was made of quartz glass and the heated part of stainless steel. Since the hydraulic diameter was 5.58 mm, it was considered to be a minichannel. Their map consisted of dispersed bubbly, coalescent bubbly, churn flow and annular flow. The transition flow pattern lines differ from those of the universal map of Hassan et al. (2005). For

example, the transition line between churn flow and annular flow is a straight vertical line, whilst in Hassan et al. (2005) is horizontal.

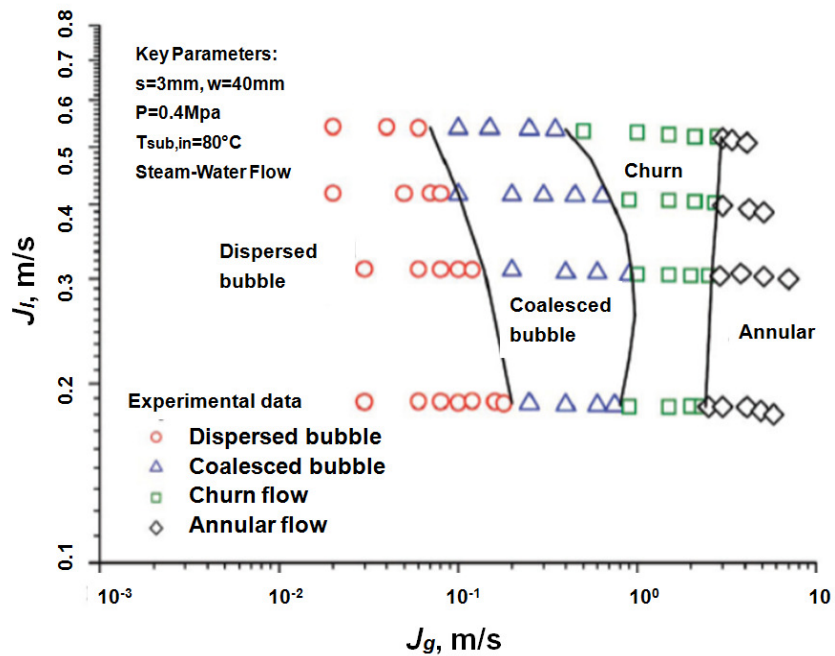


Figure 2.7 Flow pattern map for single side heated narrow rectangular channel, Wang et al. (2011).

Differing from other maps, the flow pattern map proposed by Sobierska et al. (2006) shown in Fig. 2.8, has the quality as the horizontal axis and the mass flux as the vertical axis. Bubbly flow occupies the area near to below zero qualities and slug flow dwells the area in the middle, whilst annular flow is on the right side of the second transition line.

Chen et al. (2006) investigated the effects of diameter on flow boiling patterns of R134a in four vertical tubes of inner diameter 4.26, 2.88, 2.01 and 1.1 mm. Fig. 2.9 (a) and (b) shows these effects in terms of superficial velocity and Weber number respectively. Fig. 2.21(a) shows that a decrease in tube diameter shifted the transition boundaries of slug/churn and churn/annular to higher vapour velocities and the dispersed bubble/bubbly boundary to higher liquid velocities. However, the dispersed bubble/churn and bubbly/slug boundaries were not significantly influenced by the diameter. Whilst their additional flow maps, using liquid and gas Weber

numbers as coordinates (Fig 2.9(b)), showed some effect of tube diameter, by using the Weber number map the transition boundaries collapsed onto one line. This led them to conclude that Weber number may be the right parameter for representing the effect of tube diameter on flow transition boundaries.

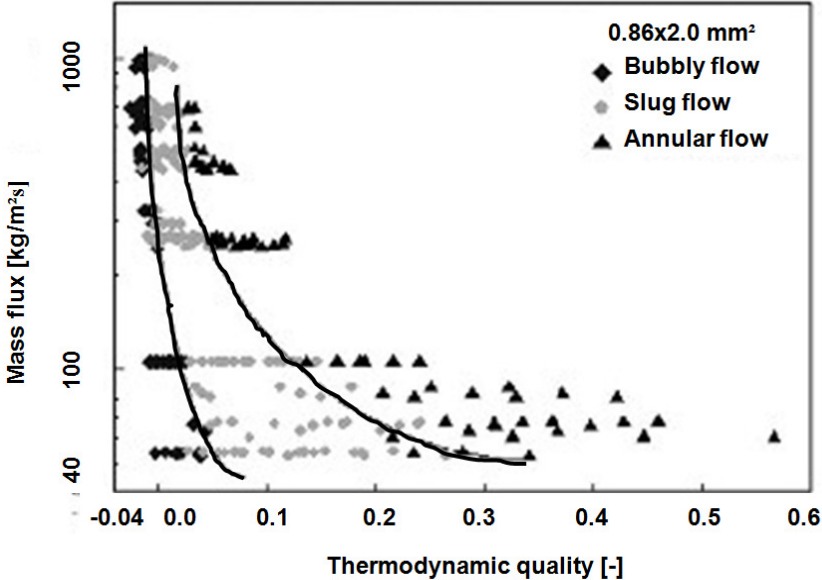


Figure 2.8 Flow patterns observed and pattern map proposed by Sobierska et al. (2006).

In order to see clearly the difference of the flow pattern observed in several hydraulic diameter channels, Table 2.1 is presented. As stated in the above literature, some authors found that as the hydraulic diameter decreased the number of conventional patterns diminished and new flow patterns appeared. Also, it was reported that in smaller channels, the transitional boundaries shifted to higher/lower liquid or gas velocity. Nevertheless, when all findings are listed in a table, it is not worth concluding the flow patterns observed relating to the decrease in hydraulic diameter, as the findings are very scattered and they contradict each other. There is no consistency finding of flow patterns for test sections with hydraulic diameters less than 1 mm.

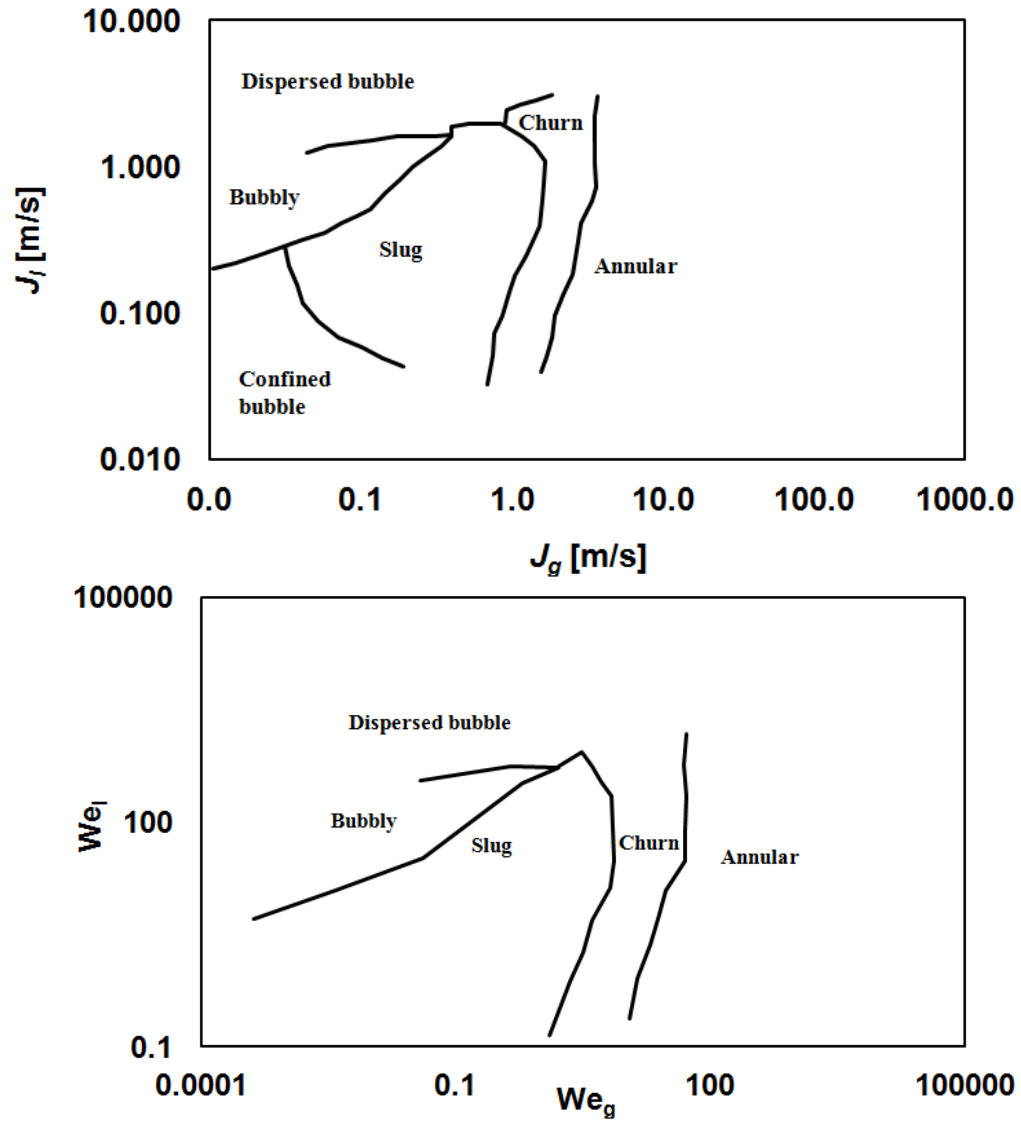


Figure 2.9 Flow boiling pattern maps of R134a at  $p = 10$  bar for the 1.1 mm tube in superficial gas/liquid velocity and Webber number planes, Chen et al. (2006).

Table 2.4 Flow patterns observed in several hydraulic diameter channels.

Reference	Fluid	Geometry/ position/ material	Hydraulic diameter (mm)	Flow pattern observed
Wambsganss et al. (1991)	Air-water	Rectangular/ horizontal/ Plexiglas	5.45	B, P, S, A
Mishima et al. (1993)	Air-water	Rectangular/ vertical/ acrylic resin	1.95 4.528, 8.89	B, S, A B, S, C, A
Wilmarth and Ishii (1994)	Air-water	Rectangular/ vertical and horizontal/ stainless steel	1.9, 3.53 3.53	B, CaB, S, S-C, C, A St, P, S, D, WA
Mishima and Hibiki (1996)	Air-water	Circular tube/ vertical/ glass and aluminum	Glass: 1.05, 2.05, 3.12, 4.08 Al: 1.09, 2.1, 3.08, 3.9	B, S, C, A, A-M B, S, C, A, A-M
Xu et al. (1999)	Air-water	Rectangular/ vertical/ pyrex glass	0.585  1.143, 1.846	S, C, A Boundary transition shifted to lower superficial gas velocity. CaB, S, C, A

Table 2.4 Continued.

Coleman and Garimella (1999)	Air-water	Circular and rectangular/ horizontal/ Pyrex glass for circular and transparent plastic for rectangular	Cir: 1.3 – 5.5 Rect: 5.36	St, EB, S, WA, A, B, DB Boundary transition shifted to higher superficial liquid velocity and almost constant superficial vapour velocity.
Triplett et al. (1999)	Air-water	Circular and semi triangular/ horizontal/ Pyrex glass, acrylic and polycarbonate	1.097, 1.447 1.088, 1.493	B, S, C, S-A, A B, S, C, S-A, A
Zhao and Bi (2001)	Air-water	Triangular/ vertical/ Plexiglas	0.866, 1.433, 2.886	CaB, S, C, A DB, S, C, A
Hetsroni et al. (2003)	Air-water Steam-water	Triangular/ horizontal/ silicon	0.129, 0.103, 0.161	CaB, S, A
Qu et al. (2004)	Nitrogen-water	Rectangular/ horizontal/ acrylic	0.677	B, S, A

Table 2.4 Continued.

Sobierska et al. (2006)	Water	Rectangular/ vertical/ copper	1.2	B, S, A
Chen et al. (2006)	R134a	Circular/ vertical/ stainless steel	1.1, 2.01, 2.88, 4.26	DB, B, Con, S, C, A DB, B, S, C, A, A-M DB, B, S, C,A, A-M DB, B, S, C, A, M
Wang et al. (2007)	Water	Trapezoidal/ horizontal/ silicon	0.186	B, B-A/M, A/M, A/M-B
Yue et al. (2008)	Water-CO <sub>2</sub>	Square and rectangular/ horizontal/ acrylic	0.2, 0.4, 0.667	B, S, C, S-A, A
Sowinski and Dziubinski (2008)	Air-water	Rectangular/ vertical/ polycarbonate	1.13, 1.25	B, CaB, S, S-C, A
Sing et al. (2009)	Water	Trapezoidal/ horizontal/ silicon	0.109	B, S, A

Table 2.4 Continued.

Harrirchian and Garimella (2009)	FC-77	Rectangular/ horizontal/ silicon	0.159	S, C/A
			0.291	S, C/A
			0.379	B/S, C/A
			0.54	B/S, C/W, C/A
			0.634	B/S, C/W, C/A
			0.707	B, C/W, C/A
Venkatesan et al. (2010)	Air-water	Circular/ horizontal/ borosilicate glass	0.6	DB, B, S, S-A
			1.2, 1.7	DB, B, S, S-A, A
			2.6	DB, B, S, S-A, W, St
			3.4	DB, B, S, S-A, W
Wang et al. (2011)	Water	Rectangular/ vertical/ quartz glass	5.58	DB, CoB, C, A
DB: dispersed bubble; B: bubbly; CaB: cap bubble; CoB: coalesce bubble; EB: elongated bubble, S: slug, P: plug, C: churn, St: stratified; S-C: slug-churn; S-A: slug-annular; Con: confined bubble; M: mist; W: wavy annular; B/S: intermittent bubbly-slug; C/W: intermittent churn-wavy annular; C/A: intermittent churn-annular; B-A/M: intermittent bubbly to annular/mist; A/M: intermittent annular/mist; A/M-B: intermittent annular/mist to bubbly; A-M: annular-mist.				

### **2.4.3 Flow boiling heat transfer**

Flow boiling in microchannels and the associated heat transfer mechanisms have not been well understood due to their unique phenomena. Therefore, the objective of the present review of flow boiling heat transfer is to collate information of the effects of hydraulic diameter and several parameters, e.g. heat flux, mass flux and vapour quality and hydraulic diameter on heat transfer coefficient, on heat transfer coefficient and heat transfer mechanisms.

#### **2.4.3.1 Effect of hydraulic diameter**

As the definition of microchannels relates to the size of channels, it is very important to understand the effect of hydraulic diameter on heat transfer coefficient. However, the available literature reported results obtained at different experimental conditions, working fluid and size/geometries of test sections; thus, it is difficult to compare the published data directly.

Some studies cited here showed contradictory results. The decreased heat transfer coefficient with a decrease in hydraulic diameter was found by Peng et al. (1998), who investigated experimentally the geometrical effects of boiling heat transfer of water and methanol flowing through V-shaped stainless steel microchannels of 18 mm heated length with hydraulic diameters ranging from 0.2 to 0.6 mm. The authors' interpretation was that, the reduction in channel hydraulic diameter restricted the liquid flowing to the channel and the heat transfer process deteriorated. However, Lin et al. (2001), who examined flow boiling of R141b in four circular stainless steel tubes of diameters 1.1, 1.8, 2.8 and 3.6 mm and one square tube of  $2 \times 2 \text{ mm}^2$  cross section and a hydraulic diameter of 2 mm, reported that the confinement, which appeared with reducing channel diameter, strongly influenced the conditions at which dryout occurred. As the diameter was decreased, dryout was found to occur earlier at lower heat fluxes than with larger diameter channels. Although the factors that influenced the local heat transfer coefficient were complex, the authors found that the average heat transfer coefficient without considering dryout was independent of tube diameter. Similar to that of Lin et al. (2001), Yen et al. (2003) found an unclear effect

of hydraulic diameter on heat transfer coefficient. They investigated flow boiling of R123 and FC-72 in three stainless steel tubes of heated length 280 mm, and of diameters 0.19, 0.3 and 0.51 mm. They excluded the results of the 0.3 mm diameter tube because of instability problems in conducting measurements. The heat transfer coefficient in the two remaining tubes was found to decrease from its high value at  $x \sim 0$  until  $x \sim 0.4$  then remain constant up to a quality of 1.

In contrast, Ribatski et al. (2006) carried out an extensive review on microchannel flow boiling heat transfer and pressure drop and concluded that the flow boiling heat transfer coefficient increased with a decrease in channel diameters. However, Hetsroni et al. (2006) investigate periodic boiling in parallel microchannels at low vapour quality using water and ethanol as the working fluids. The hydraulic diameters used ranged from 100 to 220  $\mu\text{m}$ , the mass fluxes were between 32 and 200  $\text{kg/m}^2\text{s}$  and the heat fluxes were from 120 to 270  $\text{kW/m}^2$ . The vapour qualities employed were very low; 0.01 to 0.08. They plotted average heat transfer coefficient versus boiling number rather than vapour quality. There was a significant effect of hydraulic diameters. As the hydraulic diameter was decreased, the heat transfer coefficient decreased too. At the same boiling number, the smaller diameter resulted in the lower heat transfer coefficient. In the same way, Yun et al. (2006), who investigated flow boiling of R410A in two commercial heat exchangers produced for automobile and residential air conditioners with hydraulic diameters of 1.44 mm and 1.36 mm, revealed that the heat transfer coefficient obtained in the 1.36 channel was larger than that in 1.44 mm. In addition, Karayiannis et al. (2008), who presented experimental results for a wide range of tube diameters including 4.26, 2.88, 2.01, 1.1 and 0.52 mm, found that there was no significant effect of diameter on the magnitude of the heat transfer coefficient for a reduction in diameter from 4.26 to 2.88 mm. However, increases of 14 %, 17% and 73 % in the heat transfer coefficient were found when the diameter was decreased from 2.88 to 2.01 mm, 1.02 to 1.1 mm and 1.1 to 0.52 mm, respectively.

On the contrary, Harirchian and Garimella (2008), who investigated the effect of channel size on the local flow boiling heat transfer of FC-77 in rectangular channels having a

constant depth of 400  $\mu\text{m}$  and variable widths ranging from 100 to 5850  $\mu\text{m}$ , revealed that when the base heat flux was used, the heat transfer coefficient decreased with a decrease in the width of the channel, whilst when wall heat flux was used, the heat transfer coefficient was nearly independent of hydraulic diameter. The authors (Harirchian and garimella, 2009) then extended the work to include the effect of varying channel depth as well. They presented the variation in heat transfer coefficient graphically as a function of channel cross-sectional area at different heat fluxes. It was found that the heat transfer coefficient remained constant with decreasing cross-sectional area down to a value of 0.089  $\text{mm}^2$ , below which it rapidly increased due to the confinement and the contribution of thin liquid film evaporation. Since the heat transfer coefficient of the 100  $\times$  100  $\mu\text{m}$  channel was found to be higher than that of 400  $\times$  400  $\mu\text{m}$ , they emphasized that the cross-sectional area, rather than the aspect ratio of the channel, was the determining geometric factor affecting the boiling heat transfer coefficient.

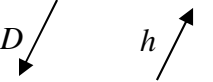
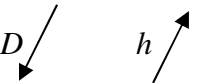
As mentioned in the previous sub section, Wang and Sefiane (2012) studied effect of hydraulic diameter on heat transfer coefficient using three channels with hydraulic diameters of 0.571 mm, 0.762 mm and 1.454 mm. They compared their results for the 0.571 mm and 0.762 mm channels. They stated that the heat transfer coefficient in the 0.571 mm was higher than that for the 0.762 mm channel at the same heat flux and mass flux.

Table 2.5 presents the summery of findings to see the effect of hydraulic diameter on heat transfer coefficient. From Table 2.5, in four papers authors claimed that the heat transfer coefficient increased as the hydraulic diameter decreased, in two papers authors stated that heat transfer coefficient decreased as the hydraulic diameter decreased, one paper exposed that the heat transfer coefficient was independent of hydraulic diameter and in the rest paper authors did not explained the dependence of the heat transfer coefficient on hydraulic diameter.

Table 2.5 Effect of decreasing hydraulic diameter on heat transfer coefficient.

Author	Fluid	Geometry/material	Range	Heat transfer coefficient ( $h$ )
Peng et al. (1998)	Water and Methanol	V shape/ stainless steel	$D = 0.2 - 0.6$ mm	$D \searrow$ $h \searrow$
Lin et al. (2001)	R141b	Circular and square tubes/ stainless steel	$D = 1.1, 1.8, 2.8, 3.6$ mm $W = 2$ mm $H = 2$ mm, $D_h = 2$ mm	$D \searrow$ $h \rightarrow$
Yen et al. (2003)	R123 and FC-72	Circular tube/ stainless steel	$D = 0.19, 0.3, 0.51$ mm	$D \searrow$ $h$ not stated
Ribatski et al. (2006)	R134a, R113, R12, R11, R123, R141b, R407C, R410A, R22, CO <sub>2</sub> , Water	Circular and rectangular/ Stainless steel, aluminum, brass, copper	$D_h = 0.2 - 3$ mm	$D \searrow$ $h \nearrow$

Table 2.5 Continued.

Hetsroni et al. (2006)	Water and ethanol	Rectangular/ silicon	$D_h = 0.1 - 0.22$ mm	
Yun et al. (2006)	R410A	Rectangular/	$D_h = 1.36, 1.44$ mm	
Karayiannis et al. (2008)	R134A	Circular/ stainless steel	$D_h = 0.52, 1.1, 2.01, 2.88, 4.26$ mm	
Harrirchian and Garimella (2008)	FC-77	Rectangular/ silicon	$D_h = 0.16, 0.571$ mm	
Wang and Sefiane (2012)	FC-72	Rectangular/ borosilicate glass	$D_h = 0.571, 0.762$ mm	

#### 2.4.3.2 Heat transfer mechanisms and effect of heat and mass flux

Heat transfer mechanisms for flow boiling in microchannels have been the subject of many studies; however, differences found by researchers in the mechanisms are still encountered in recent publications. In circular conduits, Lazarek and Black (1982), Tran et al. (1996), Bao et al. (2000), Wen et al. (2004) and Huo et al. (2007), all concluded that heat transfer mechanisms were dominated by nucleation and affected by the working system pressure. For rectangular conduits, Lee and Mudawar (2008) found the nucleate boiling heat transfer coefficient in four different hydraulic diameter microchannels. They used hydraulic diameters of 0.176, 0.2, 0.334 and 0.416 mm. In the heat transfer result section, they explained that decreasing hydraulic diameter did not yield a monotonic increase in two-phase heat transfer coefficient. They stated that the highest heat transfer coefficient was obtained using the test section #3 ( $D_h = 0.334$  mm), then followed by test section #2 ( $D_h = 0.2$  mm) and #1 ( $D_h = 0.176$  mm) whilst the lowest heat transfer coefficient was attained for the 0.416 mm. However, in the conclusion section, they reported that smaller hydraulic diameters enhanced two-phase cooling performance. Regarding an inconsistency result obtained in four test sections, they revealed that several parameters such as channel width, sidewall thickness and aspect ratio might affect the heat transfer performance of flow boiling in microchannels.

Lazarek and Black (1982) carried out measurements of local flow boiling heat transfer coefficient on a highly sub-cooled R113 ( $\Delta T_{sub} = 33\text{K}$ ) in a stainless steel tube of 3.1 mm diameter. In their experiments, the liquid Reynolds number at channel inlet varied from 791 to 4745, covering both laminar and turbulent regimes. They found that the saturated boiling heat transfer coefficient increased strongly with heat flux, but was not significantly dependent on the local vapour quality. They concluded that the heat transfer mechanism was nucleate boiling.

Similarly, the effect of heat flux on the local heat transfer coefficient was found by Bao et al. (2000), who measured the local heat transfer coefficient of R11 and R123 using a

smooth horizontal copper tube of 1.95 mm diameter and 270 mm heated section. The liquid inlet Reynolds number ranged from 333 to 11976 (or mass flux  $G$  from 50 to 1800 kg/m<sup>2</sup>s), heat flux from 5 to 200 kW/m<sup>2</sup> and exit quality from 0 to 0.9. The test section was surrounded by 10 pieces of copper block, which were separately heated by a band heater. The copper blocks were soldered to the tube surface to improve the thermal contact. The tube outer wall temperature was measured by inserting thermocouples through a narrow hole < 1 mm diameter drilled in the copper block and 2 mm away from the tube wall. The applied heat flux was not perfectly constant across the heating sections due to the difference in the heat input and to inter-block heat transfer. It was found that the heat transfer coefficient increased with increasing heat flux but not with mass flux or vapour quality. Finally, the authors concluded that the nucleate boiling controlled the heat transfer mechanism. In contrast, Lee & Lee (2001) investigated the heat transfer of flow boiling of R113 in rectangular horizontal channels with low aspect ratios. The gap between upper and lower plate ranged from 0.4 to 2 mm and the channel width was kept constant at 20 mm. They used heat fluxes up to 15 kW/m<sup>2</sup> with the qualities ranging from 0.15 to 0.75. The effect of heat flux was insignificant on the heat transfer coefficient, but it increased with higher values of both mass flux and vapour quality. The latter effect was attributed to evaporation of the liquid film. The authors concluded that the heat transfer mechanism was convective flow boiling. The heat transfer mechanisms, nucleate or convective boiling, may occur altogether. This was found by Lin et al. (2001) and Sumith et al. (2003). Lin et al. (2001) studied flow boiling heat transfer for R141b in vertical stainless steel circular and square tubes with diameters 1.1, 1.8, 2.8, 3.6 mm and a hydraulic diameter of 2 mm, with qualities ranging up to 1. They found that at low heat fluxes the heat transfer coefficient increased with quality, at medium heat fluxes, it was independent of quality and at high heat fluxes, it decreased with quality. The authors then concluded that the heat transfer mechanisms were nucleate and convective boiling and they found that the decreased heat transfer coefficient at high heat fluxes was due to the high pressure drop. Sumith et al. (2003) measured the local heat transfer coefficient of water in a vertical stainless steel tube having inner diameter of 1.45 mm. They used the flow pattern map of Triplett et al. (1999) developed for adiabatic air-water flow in a 1.45 mm tube to predict the transition

boundaries. The local heat transfer coefficient was presented as a function of the local superficial vapour velocity rather than local quality. Three flow patterns were identified: slug flow, slug-annular and annular flow, of which the latter two were dominant. The results indicated that in the slug and initial slug-annular flow regimes the nucleate boiling mechanism dominated. They attributed its occurrence to the existence of a thick liquid film in slug-annular flow and even to the film of wavy-annular flow. A threshold superficial vapour velocity value of 7 m/s ( $x = 0.05$ ) was found between nucleate and convective boiling. For velocities less than 0.05 m/s, the heat transfer coefficient increased with heat flux, whilst for velocities above 7 m/s, it was independent of heat flux. However, it also increased with mass flux and vapour quality. Like Lee & Lee (2001), the authors concluded that the heat transfer enhancement caused by the quality, was due to the evaporation of liquid film.

A convective flow boiling mechanism was also attained by Qu & Mudawar (2003b), who investigated flow boiling of de-ionized water in an array of 21 parallel microchannels of cross sectional area  $231 \times 713 \mu\text{m}^2$  (or  $348.95 \mu\text{m}$  in hydraulic diameter), and Qu et al. (2004), who conducted experiments on flow boiling heat transfer of water in microchannels with a hydraulic diameter of 0.349 mm. In addition, Qu & Mudawar (2003b) found the unique trends of heat transfer coefficient, which decreased with quality but increased with mass flux and was attributed to the appreciable droplet entrainment at the onset of annular flow regime development. Whilst the increased heat transfer coefficient with mass flux was caused by droplet deposition in the liquid film. Similarly, Qu et al. (2004) also found that the heat transfer coefficient decreased with quality, but the authors did not explain the causes.

Similar to Lazarek and Black (1982), Wen et al. (2004) also found the effect of heat flux on heat transfer coefficient. They investigated flow boiling of water in a vertical narrow channel with a hydraulic diameter of 1.33 mm, at mass fluxes 57-211  $\text{kg/m}^2\text{s}$ , heat fluxes 27-160  $\text{kW/m}^2$ , thermodynamic qualities 0-0.3 and inlet subcooling 1-12 K. The heat

transfer coefficient was found to be a function of heat flux,  $h = 162q^{0.44}$ . Therefore, this behaviour would be interpreted as nucleate boiling mechanisms. However, there was a significant effect of mass flux on heat transfer coefficient and a lower heat transfer coefficient at high heat fluxes was attributed to transient local dryout. The maximum heat transfer coefficient achieved in their experiment was 25 kW/m<sup>2</sup>K, at a mass flux of 122 kg/m<sup>2</sup>s, and a quality of 0.225. Hetsroni et al. (2006), who studied periodic flow boiling in parallel microchannels for water and ethanol at low vapour qualities, found the effect of heat flux in terms of Boiling number. The channels used were made of silicon with hydraulic diameters ranging from 100 to 220 μm. Tests were performed over the ranges of mass flux 32 - 200 kg/m<sup>2</sup>s, heat flux 120 - 270 kW/m<sup>2</sup>, and vapour quality 0.01 - 0.08. The period between successive events depended on the Boiling number ( $Bo = q / \rho h_g$ ) and decreased with an increase in that number. Further, the authors explained how the heat transfer coefficient depended on the Boiling number. As the Boiling number increased, the heat transfer coefficient decreased over the entire range of hydraulic diameters tested, and for a given Boiling number a smaller diameter resulted in a lower heat transfer coefficient. This latter trend, however, does not meet the purpose of using microchannels. Nevertheless, the authors did not give a statement for the dominant heat transfer mechanism. Using an infrared camera, Diaz et al. (2005) measured the heat transfer coefficient of water and hydrocarbons and hydrocarbon mixer in several test sections made of Inconel 600 (nickel alloy): (i) a circular channel of 1.5 mm diameter, (ii) rectangular channels with hydraulic diameters ranging from 0.583 – 1.31 mm. They found that the heat transfer coefficient increased with heat flux but decreased with quality. However, they stated that the heat transfer mechanism was convective boiling because of the decrease in heat transfer coefficient with the quality. They explained that the decrease in heat transfer coefficient was due to dryout.

A nucleate boiling mechanism was attained by Sobierska et al. (2006), who performed flow boiling experiments using water in minichannels with a hydraulic diameter of 1.2 mm, and Huh and Kim (2007), who investigated flow boiling heat transfer for de-ionized water in a

single microchannel 40 mm long and 100  $\mu\text{m}$  in hydraulic diameter made of Polydimethylsiloxane (PDMS). The heat transfer coefficient found by Sobierska et al. (2006) decreased with quality and mass flux but increased with heat flux. Therefore, the concluded that the heat transfer coefficient was nucleate boiling. In terms of relationship between heat transfer and flow patterns, an unusual heat transfer mechanism was observed by Huh and Kim (2007). They found that the dominant flow pattern was annular but the heat transfer mechanism was nucleate boiling because the heat transfer coefficient strongly depended on the heat flux. They authors then addressed the unusual heat transfer mechanism to fast bubbles growing.

As revealed by Sumith et al. (2003) that the nucleate and convective boiling could occur altogether, Lee & Garimella (2008), who studied saturated flow boiling of de-ionized water in an assembly of twenty five parallel microchannels, made of silicon, also found the two heat transfer mechanism. They employed channels a height of 400  $\mu\text{m}$  and widths ranging from 102 - 997  $\mu\text{m}$  ( $D_h = 162.55 \mu\text{m}$  to 571  $\mu\text{m}$ ). At low to medium heat fluxes, the local heat transfer coefficient increased almost linearly with heat flux, whilst at the higher heat fluxes, the saturated heat transfer coefficient became largely insensitive to heat flux. Furthermore, the maximum heat transfer coefficient found in their experiment was around 40  $\text{kW/m}^2\text{K}$ .

Wang et al. (2008) studied the effects of inlet and outlet configuration on flow boiling instability in parallel microchannels of hydraulic diameter 186  $\mu\text{m}$  made of silicon wafer. They used water as the working fluid with an inlet temperature of 35°C. The maximum heat transfer coefficient of 35  $\text{kW/m}^2\text{K}$  occurred at or near zero quality, decreasing as the quality increased. For qualities below 0.2, the heat transfer coefficient increased with the heat flux, whilst above that level the coefficient did not depend on the heat flux but decreased with an increase in quality. The decrease in heat transfer coefficient was due to dryout. Similar trend of heat transfer coefficients was found by Wang et al. (2010), who proposed a four-zone model for saturated flow boiling of water in a 0.137 mm hydraulic diameter rectangular microchannel. The model employed qualities up to 0.475. The

authors found that the heat transfer coefficient decreased with quality and the effect of heat flux was significant at near zero qualities. However, they did not perform their modeling for high qualities nor mention the heat transfer mechanism. Recently, Wang and Sefiane (2012) studied experimentally effects of heat flux, vapour quality and hydraulic diameter on heat transfer coefficient. They used microchannels made of borosilicate glass with hydraulic diameters of 0.571 mm, 0.762 mm and 1.454 mm. FC-72 was used as the working fluid. They found that the heat transfer coefficient increased with an increase in heat flux for the 0.571 mm channel. However, the effect of heat flux on the heat transfer coefficient was not clear for the 0.762 mm channel. Furthermore, the heat transfer coefficient decreased with an increase in vapour quality. They revealed that the decrease in heat transfer coefficient was due to dryout and the heat transfer mechanism was found to be convective boiling.

From the above review, it is not clear what mechanisms are dominant in microchannels; therefore, Table 2.5 is presented to attempt to see the heat transfer mechanism obtained from the literature review. From the Table, in 7 papers authors stated that the heat transfer mechanism was nucleate boiling, in 4 papers authors stated convective boiling and in 2 papers authors mentioned convective and nucleate boiling and the last in 2 papers authors did not explained the heat transfer mechanism. However, there is no indication of consistent heat transfer mechanism as the hydraulic diameter decreases.

Table 2.6 Summary of the findings of heat transfer mechanisms in the previous studies.

Author	Fluid	Geometry	Range of diameter	Heat transfer mechanism
Lazarek and Black (1982)	R113	Circular tube mad of stainless steel	$D = 3.1$ mm	Nucleate boiling
Bao et al. (2000)	R11, R123	Circular tube made of copper	$D = 1.95$ mm	Nucleate boiling
Lee and Lee (2001)	R113	Rectangular made of stainless steel plate	$W = 20$ mm $H = 0.4, 1, 2$ mm $D_h = 0.784, 1.9, 3.64$ mm	Convective boiling
Lin et al. (2001)	R141b	Circular and square tubes made of stainless steel	$D = 1.1, 1.8, 2.8, 3.6$ mm $W = 2$ mm $H = 2$ mm, $D_h = 2$ mm	Nucleate and convective boiling
Sumith et al. (2003)	Water	Circular tube made of stainless steel	$D = 1.45$ mm	Nucleate and convective boiling
Qu and Mudawar (2003)	Water	Rectangular made of copper	$W = 0.231$ mm $H = 0.713$ mm $D_h = 0.349$ mm	Convective boiling

Table 2.6 Continued.

Qu et al. (2004)	Water	Rectangular mad of copper	$D_h = 0.349$ mm	Convective boiling
Wen et al. (2004)	Water	Rectangular made of stainless steel	$D_h = 1.33$ mm	Nucleate boiling
Hetsroni et al. (2006)	Water and ethanol	Rectangular made of silicon	$D_h = 0.1 - 0.22$ mm	Not stated
Diaz et al. (2005)	Water and hydrocarbon	Circular and rectangular tubes made of inconel 600	$D = 1.5$ mm $D_h = 0.583 - 1.31$ mm	Convective boiling
Sobierska et al. (2006)	Water	Rectangular made of copper	$D_h = 1.2$ mm	Nucleate boiling
Huh and Kim (2007)	Water	Rectangular made of polydimethylsiloxane (PDMS)	$D_h = 0.1$ mm	Nucleate boiling
Lee and Garimella (2008)	Water	Rectangular made of silicon	$D_h = 0.16, 0.571$ mm	Nucleate boiling
Wang et al. (2008)	Water	Rectangular mad of silicon	$D_h = 0.186$ mm	Nucleate boiling
Wang et al. (2010)	Water	Rectangular made of pirex glass	$D_h = 0.137$ mm	Not stated
Wang and Sefiane (2012)	FC-72	Rectangular/ borosilicate glass	$D_h = 571, 762$ and $1454$ $\mu\text{m}$	Convective boiling

#### 2.4.4 Heat transfer correlations

Lazarek and Black (1982) investigated flow boiling heat transfer of R113 in a stainless steel tube with diameter of 3.1 mm and heated length of 126 mm. The measured heat transfer coefficient was independent of mass flux and vapour quality but increases with increasing heat flux. The correlation was created based on 728 data points using the least square method algorithm. The exponent of Reynolds number in the equation is very similar to that of Dittus-Boelter's equation for single-phase. The exponent of the boiling number ( $Bo$ ) reflects the strong heat flux effect; hence the correlation confirms the dominance of nucleate boiling. However, the mass flux effect is insignificant where the exponent of the mass flux is 0.143. Furthermore, the correlation had been tested with standard deviation (RMS) of 9% and predicted the data within 15%.

Shah (1982) proposed a correlation for nucleate and convective boiling. He revealed that the convective boiling term depended greatly on the convection number  $N_{Co}$  rather than the Martinelli parameter ( $X$ ). However, the convection number was similar to the turbulent-turbulent Martinelli's parameter. On the other hand, the nucleate boiling term was expressed only as a function of the boiling number  $Bo$ .

Gungor and Winterton (1986) proposed a general correlation for forced convection boiling based on a large databank consisting 4300 data points. This correlation was used to predict the heat transfer coefficient with various fluids such as water, refrigerant and dethyleneglycol. This was also intended to be applied for subcooled and saturated flow boiling in vertical and horizontal tubes and was considered as a simpler correlation. The correlation had been tested and could predict the experimental data of saturated flow boiling with mean deviations of 21.4% and 25% for subcooled flow boiling.

Kandlikar (1990) utilized the single-phase liquid heat transfer coefficient to predict the saturated nucleate boiling and convective boiling covering water and refrigerants such as R11, R22, R113,

R134a and R152a. The correlation was applicable for flow boiling in tubes with diameters ranging from 4 to 32 mm and system pressures varying from 0.4 to 64.2 bar.

Kew and Cornwell (1997) investigated flow boiling heat transfer of R141b in stainless steel tubes with diameters of 1.39 – 3.69 mm and heated length of 500 mm. As their experimental data showed the increase in heat transfer coefficient with quality, they modified the correlation of Lazarek and Black (1982) by multiplying their equation by  $(1 - x)^{-0.143}$ .

Yu et al. (2002) studied experimentally two-phase pressure drop, boiling heat transfer, and critical heat flux of water using a horizontal tube with an inner diameter of 2.98 mm and a 0.91 m heated length. Experiments were performed at a system pressure of 200 kPa, mass fluxes of 50–200 kg/m<sup>2</sup>s, and inlet temperatures from ambient to 80°C. The heat transfer coefficient was found to be dependent on heat flux but essentially mass-flux-independent. This trend was consistent with refrigerant boiling in small channels but significantly different from larger-channel boiling, where the mass flux effect might dominate. This result indicated to a dominance of the nucleation heat transfer mechanism over the convective mechanism in small channels, and it was persisted to high qualities above 0.5. A correlation for two-phase heat transfer coefficient for water flow boiling in a small horizontal channel was developed based on boiling results. The correlation had been tested to predict their experimental data with an error of 2%.

Sun and Mishima (2009) modified the correlation of Lazarek and Black due to similar trend of being weakly dependent on vapour quality. However, they explained that the heat transfer coefficient depended on the Weber number. Therefore, the correlation was developed based upon the Lazarek\_Black's correlation by taking the effect of Weber number using the regression method. The correlation had been tested to predict the experimental data with a MAE of 30.8%.

Lee and Mudawar (2005) investigated flow boiling heat transfer of R134a in a microchannel heat sink with a hydraulic diameter of 0.35 mm. Since the macro and microscale correlations failed to predict their experimental data, they proposed a new correlation for saturated flow boiling in

microchannels. The correlation was developed based on 318 data points of which 111 data points for R134a and the remaining was for water. They calculated the local quality at one location in the middle of the channel and the quality was varied from 0.001 to 0.25 using an expansion device. Additionally, the R134a experiments were conducted by varying the mass flux for a constant heat flux value whilst the water experiments were conducted in an opposite way. To correlate the data of water and R134a, they found that Boiling number, liquid Weber number and Martinelli parameter were the important dimensionless parameters to be included in the correlation. To achieve accurate predictions, they divided the quality domain into three ranges based on the dominant mechanism and proposed a correlation for each range. In the first range ( $x < 0.05$ ), the dominant mechanism was nucleate boiling whereas convective boiling dominated at intermediate quality range ( $x = 0.05 - 0.55$ ) and high quality range ( $x > 0.55$ ).

Warrier et al (2002) investigated flow boiling heat transfer of FC-84 in aluminum multichannels with a hydraulic diameter of 0.75 mm. They proposed a correlation for saturated flow boiling for a quality range of  $x = 0.01 - 0.55$ . The two-phase heat transfer coefficient was normalized by the fully developed single-phase laminar heat transfer coefficient based on four heated wall sides.

Li and Wu (2010) collected a large number of experimental data points from the open literature covering saturated flow boiling heat transfer in mini/micro-channels. The database consists of 3744 data points, a wide range of working fluids and covered hydraulic diameters ranging from 0.16 to 3.1 mm with Reynolds numbers less than 2000. They had correlated the data as a function of three dimensionless parameters namely boiling number, Bond number and Reynolds number. The boiling number was considered for the heat and mass flux effects and the Reynolds number referred to inertia and viscous effects, whilst the Bond number was intended for gravity and surface tension effects. The correlation had been tested and was able to predict the experimental data with a MAE of 26.13%.

#### **2.4.5 Flow boiling pressure drop**

Previous studies on flow boiling pressure drop depicted that when boiling commenced, the pressure drop increased rapidly and continued to increase as the heat flux was increased, e.g. Warriar et al. (2002), Lee and Mudawar (2005), Lee and Garimella (2008), Mahmoud et al. (2009). In the literature, not all authors presented their experimental pressure drops versus heat flux. Some of them presented the pressure drop versus quality or mass flux. Nevertheless, the trends of pressure drop were almost the same. As the quality increased, the pressure drop increased too, e.g. Tran et al. (2000), Yu et al. (2002), Agostini et al. (2008). Pressure drop versus mass flux was also found in the literature, e.g. Wu et al. (2006).

Tran et al. (2000) studied pressure drop of refrigerants R134a, R113 and R12 during flow boiling in small tubes with diameters of 2.46 mm and 2.92 mm. A lower saturation pressure working system resulted in higher pressure drop at the same exit quality. R134a and R12 pressure drops also increased with an increase in mass flux and exit quality; however, R12 pressure drop was lower than that of R134a at the same saturation pressure and exit quality. The author explained that this was due to the property differences. The maximum pressure drop in their experiments was 48 kPa at the mass flux of 500 kg/m<sup>2</sup>s, saturation pressure of 365 kPa and at the exit quality of 73%.

Cho and Cho (2006) investigated two-phase flow pressure distribution and pressure drop in microchannel tubes under non- heating and heating condition using R-22. The test section consisted of inlet and outlet headers with an inner diameter of 19.4 mm and 15 or 41 parallel microchannel tubes. All tubes were made of copper. Each microchannel tube had 8 rectangular ports with a hydraulic diameter of 1.3 mm. They found that the effects of orientation of the headers on two-phase flow pressure distribution and pressure drop was greater under non heating condition. The two-phase pressure drop through microchannel tubes with a horizontal header was higher than vertical header. They suggested this to the gravitational effects. Furthermore, under the heating condition, the cooling capacity of three prototype evaporators was changed as the mass flow rate and inlet quality were increased. This was due to the flow mal-distribution.

Sobierska et al. (2006) investigated heat transfer and pressure drop of water flowing in a vertical single channel. They reported the effect of mass flux on the two-phase pressure drop. As the mass flux increased, the two-phase pressure drop increased. However, at low mass flux the effect was not clear because the lines of pressure drop at 50 kg/m<sup>2</sup>s and 100 kg/m<sup>2</sup>s merged together.

#### **2.4.6 Pressure drop correlations**

The correlation is selected when it can be applied for general purposes or its applicability is close to the experimental condition in this project. The correlations used for a comparison are listed in appendix A and are proposed by Lockhart-Martinelli (1949), Mishima and Hibiki (1996), Yu et al. (2002), Warriar et al. (2002), Qu and Mudawar (2003b), Lee and Lee (2008), Lee and Garimella (2008), Zhang et al. (2010) and homogenous model (1994). The homogenous flow model was selected due to the fact that homogenous model was the fundamental pressure drop prediction and proposed for laminar and turbulent flows in horizontal channels using steam-water mixture and a wide range of system pressure. This model also has been used practically in steam generation, petroleum, and refrigeration industries for a considerable time. Basically, this model was proposed based on the following assumptions: (i) equal vapour and liquid velocities, (ii) the attainment of thermodynamic equilibrium between the phases and (iii) the use of defined single-phase friction factor for two-phase flow. The reason of choosing the Lockhart-Martinelli (1949)'s correlation was due to the wide range of fluids used including water for laminar and turbulent regimes and was intended to predict the pressure drop in minichannels. A correlation proposed by Mishima and Hibiki (1996) is selected for the comparison because it was invented for flow in vertical and horizontal channels, circular and rectangular channel geometries. In addition, this correlation was based on water as the working fluid. Yu et al. (2002)'s correlation was selected due to the use of water as the working fluid and for flow boiling in horizontal tubes. Warriar et al. (2002)'s correlations is chosen for a comparison with the experimental data because the correlation was subjected for saturated flow boiling in rectangular channel with hydraulic diameter of  $D_h = 0.75$  mm. A correlation proposed by Lee and Lee (2008) is also chosen, as this correlation was aimed for predicting flow boiling pressure drop in rectangular horizontal channels using water as the working fluid. Correlations proposed by Qu and Mudawar (2003b)

and Lee and Garimella (2008) were used to compare with the experimental data for a reason that those correlations were invented for flow boiling in horizontal rectangular microchannels using water as the working fluid. More specific, the correlations were applied for flow in horizontal rectangular microchannels. Zhang et al. (2010) conducted an extensive analysis using the artificial neural network to find the most important parameters that significantly influence the frictional pressure drop. They have found that mass flux, system pressure and vapour quality have minor effects whereas the hydraulic diameter and the dimensionless Laplace constant have the strongest effects. Based on that, they modified the correlation of Mishima and Hibiki (1996) and proposed a correlation for the laminar liquid and laminar vapour regimes. The correlation was valid for channels with diameters ranging from 0.014 to 6.25 mm, see Appendix A.

#### **2.4.7 Flow boiling instability**

Flow boiling instabilities in microchannels are often encountered and also have been reported in the previous studies. These matters actually are not expected to occur in microchannels because these can decrease the performance of microchannels themselves or even break down them. In general, two phase instabilities are categorized as static and dynamic, depending on whether or not steady state conservation laws can be applied to explain the instability. The two-phase static instabilities such as flow excursion (ledinegg instability) and flow pattern transition instability are governed by the steady state conservation laws. On the other hand, the dynamics instabilities such as acoustics oscillation, and parallel channel instability, involve transient inertia and dynamics feedback effects which cannot be described by steady state conservation laws. Qu and Mudawar, (2002, 2003a) revealed that two types of instabilities were observed. Pressure drop oscillation was commonly triggered by flow excursion and sustained by interaction between the vapour generation and the upstream compressible volume including the liquid reservoir and pump. Mild hydrodynamics instability was sustained by feedback effects between the channel intrinsic and the heat sink. In contrast, Wu and Cheng (2004), Wu et al. (2006) and Begojovic et al. (2009) found different types of instabilities. Wu and Cheng (2004), who conducted an observation on flow instability of flow boiling in a trapezoidal silicon with a hydraulic diameter of 186  $\mu\text{m}$  and Wu et al. (2006), who investigated instability of flow boiling in a silicon

microchannels with a hydraulic diameter of 72.7  $\mu\text{m}$ , found three types of instabilities, namely; (i) liquid two-phase alternating flow (LTAF) at low heat flux and high mass flux, (ii) continues two-phase flow (CTF) at medium heat flux - medium mass flux and (iii) liquid two-phase vapour alternating flow (LTVAF) at high heat flux -low mass flux. Among the instability modes, LTVAF was the largest in the oscillation amplitude with oscillations of pressure drop and mass flux nearly out of phase, whilst CTF was the smallest one. Whilst Begojovic et al. (2009) found two types of instabilities, HALF (high amplitude low frequency) with frequencies ranging from 0 – 3 Hz and LAHF (low amplitude high frequency) with frequencies between 23 and 25 Hz.

In terms of frequency, Balasubramanian and Kandlikar (2005) found that at the mass flux of 120  $\text{kg}/\text{m}^2\text{s}$ , the pressure drop observed was 8.5 kPa and the fluctuation of pressure drop had a frequency of 1 kHz. However, at the different surface temperature, the frequency of the pressure drop fluctuation was also different. The frequency observed in their experiment at surface temperatures ranging from 104 to 111°C was 0.6 to 1.7 Hz. Zhang et al. (2005) found that the transient pressure fluctuation of flow boiling in silicon microchannels with hydraulic diameters ranging from 27 to 171  $\mu\text{m}$  was between 69 and 138 kPa. This high amplitude was due to the bubble nucleation. In addition, the fluctuation of pressures was found to have frequencies ranging from 3-5 Hz and from 30-40 Hz. The high frequency, 30-40 Hz, was because of more bubble generation and the development of annular flow.

Several methods to overcome instability problems have been investigated; see Kandlikar et al. (2006), Lu and Pan (2008) and Xu et al. (2009). Kandlikar et al. (2006) used pressure drop element and nucleation site to stabilize water flow in boiling state in microchannels with a hydraulic diameter of 332  $\mu\text{m}$ . They explained that using a nucleation site in conjunction with a 4% area pressure drop elements completely eliminated the stability in associated with the reversed flow. Lu and Pan (2008) employed diverging cross section silicon parallel microchannels to stabilize flow boiling of water. They explained that the heat flux and mass flux significantly influenced the stability of flow boiling. Further, the parallel microchannels with the diverging cross section significantly stabilized the flow boiling. Xu et al. (2009) introduced seed

bubble for stabilizing the flow in parallel microchannel. They used silicon triangular parallel microchannels with a hydraulic diameter of 100  $\mu\text{m}$  and acetone as the working fluid. At low frequency up to 10 Hz, seed bubbles not only decrease the oscillation amplitudes of pressure drop, fluid inlet and outlet temperatures and heating surface temperature, but also shortened the oscillation cycle period. At high frequency up to 100 Hz or more, seed bubbles completely suppressed the flow instability and the heat transfer system displayed stable parameter of pressure drop, fluid inlet and outlet temperatures and heating surface temperature. Also the seed bubbles technique almost did not increase the pressure drop across the microchannel system.

Pressure systems may influence flow boiling instability. This was experimentally studied by Kuo and Peles (2009). Experiment were conducted using water in 223  $\mu\text{m}$  hydraulic diameter microchannels with mass fluxes ranging from 86 to 520  $\text{kg/m}^2\text{s}$  and system pressure ranging from 50 to 205 kPa. They elucidated that the effects of pressure system was relatively significant on the flow instability. For higher pressure system, it was observed that boiling instabilities were significantly delayed and CHF was extended to high mass qualities. Local temperature measurements showed lower magnitudes and higher frequencies of oscillation at high system pressure.

## **2.5 Summary of the findings**

A review on single phase-flow and two-phase flow has been presented above and some conclusions can be drawn as follows:

### **2.5.1 Single-phase flow**

It is possible to sum up the main results quoted in the open literature on the friction factor in microchannels highlighting the peculiarities, proposed by different authors, with respect to the conventional macrochannels:

1. Friction factor (Poiseuille number) was found to be:
  - a. Higher than conventional theory: Urbanek et al. (1993), Papautsky et al. (1999), Pfund et al. (2000), Qu et al. (2000), Jiang et al. (2001), Shen et al. (2006),

- b. The same as conventional theory: Harms et al. (1999), Gao et al. (2002), Yue et al. (2004), Akbary et al. (2009).
  - c. Lower than conventional theory: Jiang et al. (2008).
- 2. The friction factor depends on surface characteristics of the channel wall: Qu et al. (2000), Jiang et al. (2001), Kandlikar et al. (2003).
- 3. The friction factor depends on the polarity of the fluid: Ren et al. (2001).
- 4. Dependence of the Poiseuille number ( $Po = fRe$ ) on Reynolds number, especially in laminar flow regimes: Jiang et al. (1995), Mala and Li (1999), and Xu et al. (2000).
- 5. There is a contradictory on the effect of fluid temperature on friction factor: Urbanek et al. (1993), Toh et al. (2002).
- 6. The discrepancy of results is due to the scaling effects: Rosa et al. (2009).
- 7. The Nusselt number was found to be:
  - a. Higher than conventional theory: Tukerman and Pease (1981), Jung and Kwak (2008).
  - b. The same as conventional theory: Harms et al. (1999), Lelea et al. (2004), Lee et al. (2005), Mishan et al. (2007).
  - c. Lower than conventional theory: Wang and Peng (1994), Gao et al. (2002), Jiang et al. (2008), Silverio and Moreira (2008).

### **2.5.2 Two-phase flow**

A detailed review on two phase flow boiling studies in microchannels has been presented. The review covered several issues such as flow patterns and flow pattern maps, effects of heat flux, mass flux, quality and hydraulic diameter on flow pattern, heat transfer and pressure drop and flow boiling instability. The main conclusions which can be drawn from the above review are summarized as follows:

#### **2.5.2.1 Flow patterns:**

The different flow patterns observed as the channel size decreases are summarized here.

1. The surface tension is dominant over gravity and buoyancy forces.

2. Some conventional flow patterns diminished and some new flow patterns appeared as the channel size decreased.
3. There is a contradictory conclusion regarding the transition boundary line of flow pattern maps. As the hydraulic diameter decreased, researchers reported that the boundary transition line could shift to higher or lower superficial liquid and gas velocities.
4. There is inconsistency flow pattern observed in several hydraulic diameter channels both for mini to microchannels.
5. In the adiabatic two-phase flow experiments, the flow patterns may be affected by how the gas flowed into the test section; coaxially injected, injected through three holes distributed at 120 degree intervals on the circumference or the gas was mixed with the liquid in a chamber before the tube inlet.
6. There is no accurate flow pattern map and boundary transition correlation.
7. Different flow patterns observed could be due to the lack of a standard definition of flow patterns.

#### 2.5.2.2 Heat transfer:

The effect of hydraulic diameter, heat flux, mass flux and vapour quality on flow boiling heat transfer coefficient and mechanism:

1. It was reported that as the hydraulic diameter decreased the heat transfer coefficient increased, however, in general, the effect of hydraulic diameter needs further investigation.
2. The heat transfer coefficient increases as the heat flux increases, but does not depend on the vapour quality and the mass flux: nucleate boiling.
3. The heat transfer coefficient increases as the mass flux and vapour quality increase: convective boiling.
4. The heat transfer coefficient increases as the heat flux increases at lower quality, at higher quality the heat transfer coefficient increases as the quality increases: nucleate – convective boiling.

5. The heat transfer coefficient decreases as the quality increases but is independent of heat flux and mass flux.
6. The heat transfer coefficient decreases as the quality increases, but increases as the mass flux increases.
7. The heat transfer coefficient decreases as both the quality and mass flux increase.
8. Heat transfer mechanisms in microchannels need to be explored further.

### **2.5.3 Two-phase pressure drop**

Similar to that in the single-phase flow, as the mass flux increased the pressure drop was reported to increase. At the same heat flux, after boiling commences, bigger mass fluxes result in higher pressure drop. At the same mass flux, as the heat flux increases the pressure drop increases. As the size of channels decreases the pressure drop increases. Hence, the trend of two-phase pressure drop in microchannels and in macrochannels is not significantly different. The increased in pressure drop with heat flux was reported due to the increase in vapour quality or bubble generation.

### **2.5.4 Flow boiling instability**

Instabilities of flow boiling basically are classified into two groups: static instability and dynamic instability. Pressure drop and pressure fluctuations can be bigger when the flow boiling occurs at low system pressure and low mass flux. The instability which generates a flow reversal is due to the interaction between the bubble generation and the upstream conditions and pump performance. Several efforts have been done to overcome flow boiling instabilities such as pressure drop element, nucleation site, seed bubble injection, throttling valve, inlet restriction and orifice, divergent channel. There is no clear effect of decreasing hydraulic diameter on the magnitude of instability, but as the channel size decreases the dryout happens earlier and easily. The instability in flow boiling influences the performance of microchannels, e.g. decreasing the heat transfer coefficient and damaging the microchannels.

# Chapter 3

## Experimental Facility and Method

### 3.1 Introduction

This chapter gives detailed description of the experimental facility and procedures employed in this research project. An introduction to the experimental facility and an overview of the main equipment involved is provided in Section 3.1. A description of the water flow loop system and its main components is given in Section 3.2 and the microchannel test sections are described in Section 3.3. Section 3.4 and 3.5 deal, respectively, with the visualization system used to capture and record flow boiling images and the computer-based data acquisition system used for the measurement and logging of experimental data. The chiller system used to provide cooling for the test rig is described in Section 3.6. The experimental procedures are set out in Section 3.7 and preliminary tests carried out to estimate the test section heat loss is described in Section 3.8. The calibration of measurement sensors is discussed in Section 3.9. The experimental data reduction equations are presented in Section 3.10. A brief chapter summary is given in Section 3.11.

The test rig used in this experimental investigation consisted of a recirculating flow loop system incorporating the microchannel and was designed to deliver the desired inlet flow conditions to the test section. The main components of the flow loop are described in detail in section 3.2. The entire loop was constructed using stainless steel pipes and components, a part from the flexible tube connections at inlet to and outlet from the test section. The test rig was originally built by a postdoctoral researcher for microchannel studies in the year 2008/2009 and was modified and further developed during this work. The rig is located in Room TB113, Tower B building at Brunel University within the Centre for Energy and Built Environment Research (CEBER) research laboratories.

In addition to the flow loop, the test rig was equipped with a visualization system to capture images of flow boiling and the movement of bubble inside the test section. The visualization system included a Phantom V6.0 high speed camera and software for image acquisition, playback and analysis. The camera was installed on a movable camera support which was designed and built as a part of this study. A detailed explanation of the visualization system is given in section 3.4.

A computer data acquisition system was used to measure, process and record the signal from the various sensors connected to the test rig. The system handled signal conditioning, analog-to-digital conversion and transfer of measurement data to a desktop computer and comprised National Instrument data acquisition hardware and LabView programmable software (version 8). The data acquisition system is described in Section 3.5.

Additionally, to prevent damage to components of the test rig and to establish steady thermal operating conditions, a chiller unit was used to supply coolant for heat rejection from the test rig. This system served several essential purposes including subcooling the hot water flowing from the main reservoir to the pump, condensing the vapour exiting the test section under flow boiling conditions and reflux condensation of vapour in the main reservoir. A detailed explanation of the test rig cooling system is given in Section 3.6.

A schematic diagram of the experimental test rig is shown in Fig 3.1. A photograph of the test facility is shown in Fig. 3.2. Modifications were made to the rig in order to: (1) reduce the upstream compressibility, (2) minimize the flow losses, (3) provide new pre-heaters in order to ensure that the inlet temperature was as close as possible to the saturation temperature corresponding to the test section inlet pressure and (4) provide a camera support which could be moved horizontally along the length of the test section, (5) design and manufacture new test sections.

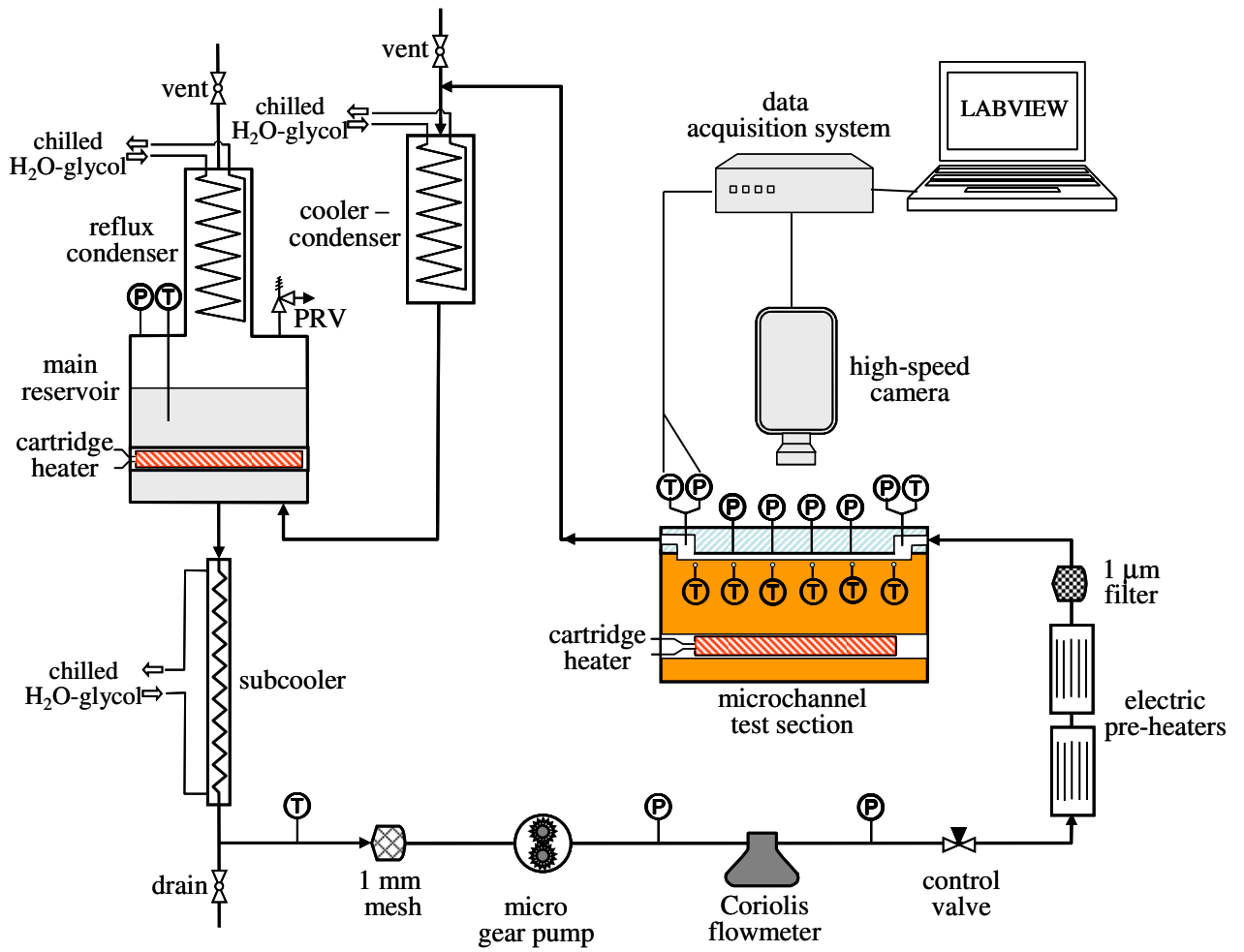


Figure 3.1. Schematic diagram of the test rig (Gedupudi et al. 2009).

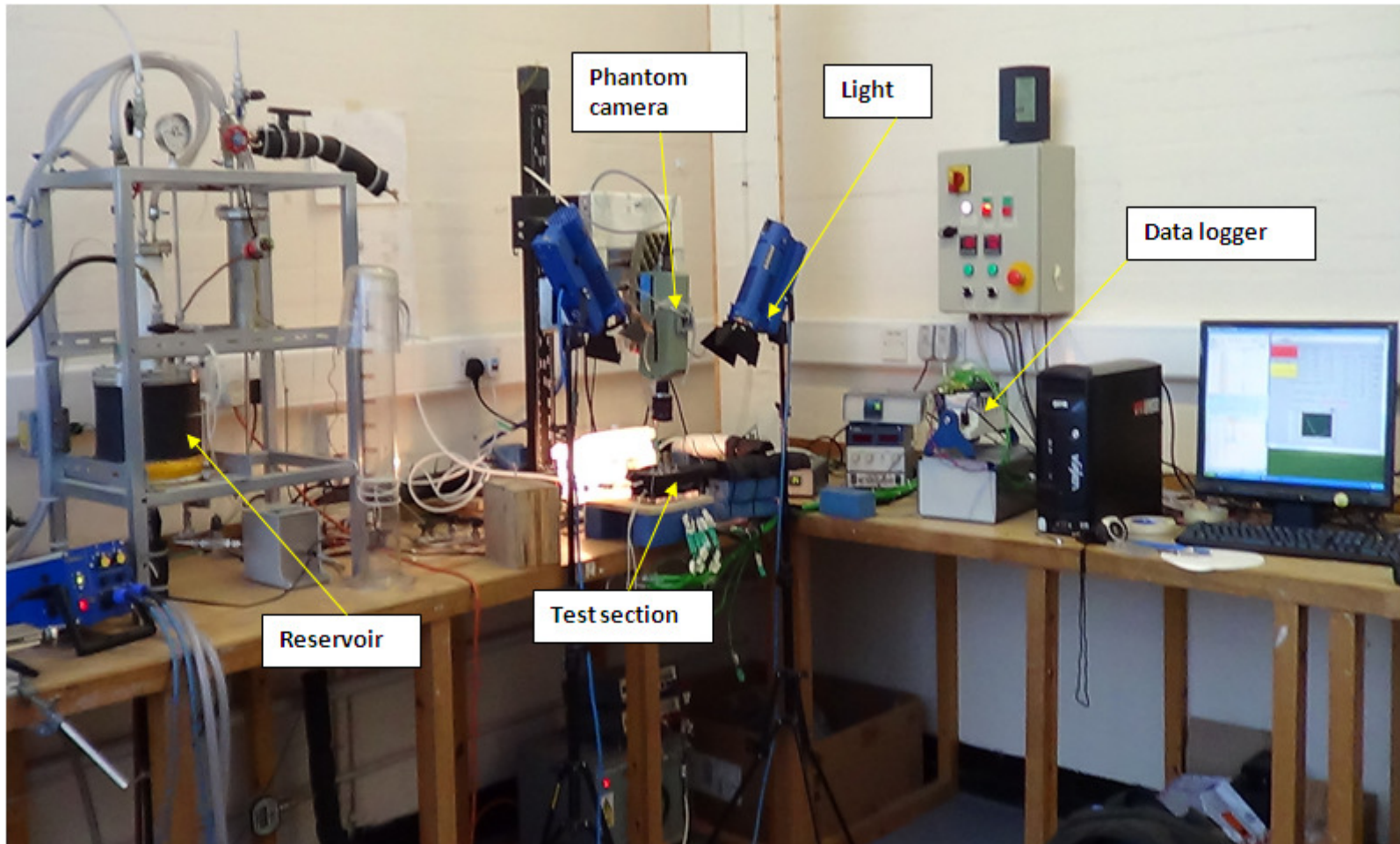


Figure 3.2 Photograph of experimental facility.

## **3.2 Water flow loop system**

In addition to the test section, the flow loop system comprised the main reservoir, two condensers, a subcooler, a gear pump, a rotameter, a Coriolis mass flowmeter and three electric pre-heaters. The reservoir was used to boil the working fluid, both prior to experiments to release trapped and dissolved gasses to be vented to atmosphere. The reflux condenser coil mounted on the reservoir condensed the vapour above the boiling liquid and returned the condensate to the reservoir. The gear pump circulated water around the closed flow loop and was preceded by a subcooler which cooled the water entering the pump to below approximately 50°C. The rotameter was used only to monitor the flow rate, which was measured accurately by the Coriolis mass flowmeter. Three pre-heaters with PID controllers were employed to raise the water temperature at the section inlet to the desired value. The microchannel test section was the central focus of the water loop system on which experiments were performed in this study. After exiting the test section, the working fluid including any vapour formed in the test section passed through a cooler-condenser before returning to the main reservoir. Other flow loop components included a 1 mm mesh and 1 µm filter which were fitted to remove any particles suspended in the fluid.

### **3.2.1 Main reservoir**

The main reservoir was basically a cylindrical vessel made of stainless steel SS316L with an inner diameter of 161.5 mm and a height of 150 mm. To supply heat to the reservoir, a 1500 W cartridge heater, 19 mm in diameter and 152 mm long, was inserted into a horizontal stainless steel tube welded diametrically across the reservoir. To ensure good thermal contact thermal paste was applied in the gap between the tube and the cartridge heater. The heater was controlled using a PID (West 6100) set, so that the saturation temperature of the boiling fluid inside the reservoir remained constant at 102°C.

To maintain the boiling equilibrium in the main reservoir, a reflux condenser was connected above it to condense vapour formed by the boiling process inside the reservoir. A degassing line was connected at the top of reflux condenser with a vent valve, which was open periodically to release trapped gasses to the atmosphere. This line was also used as a water feeder line to fill the reservoir. A sight glass for

monitoring the water level inside the reservoir was mounted in the reservoir wall. A pressure relief valve was fitted to the reservoir to prevent the internal pressure exceeding the maximum allowable value. A vacuum line with a ball valve was connected to the top of the reservoir and connected to a vacuum pump to evacuate air from the vessel before filling.

### **3.2.2 Subcooler**

The purpose of the subcooler was to cool the working fluid (deionized water) flowing from the main reservoir to the pump and flowmeters. It was fabricated from stainless steel SS316 as a concentric double pipe heat exchanger. The inner pipe had an internal diameter of 6 mm and a wall thickness of 1mm and the outer pipe was of 13 mm internal diameter and 1.5 mm wall thickness. The length of the subcooler was 600 mm. The working fluid flowed in the inner pipe whilst chilled water-glycol solution flowed in the annulus (shell side). The chilled water-glycol solution supplied by the chiller unit could be adjusted using a ball valve, and its temperature could be set at a desired value using the temperature regulator mounted on the chiller unit. The subcooler delivered water cooled from 102°C to under 50°C at a maximum flow rate of approximately 100 g/min.

### **3.2.3 Gear pump**

A magnetically coupled gear pump (Micropump model GA-T23PFBS) equipped by an Ismatec Reglo ZS digital drive speed regulator was used to circulate the working fluid around the flow loop. The pump construction is chemically resistant with wetted parts manufactured from stainless steel, PTFE, PPS and carbon fibre. The allowable working temperature range is -46 to 177°C, but in this work the liquid inlet temperature was kept lower than 50°C. It can deliver pulse-free flow rates ranging from 5 to 400 ml/minute with a maximum differential pressure of 5.2 bar and maximum working system pressure of 21 bar. The pump drive can be operated over a rotational speed range of 500 to 4000 rev/min. The performance of the T23 model pump is shown in Fig. 3.3.

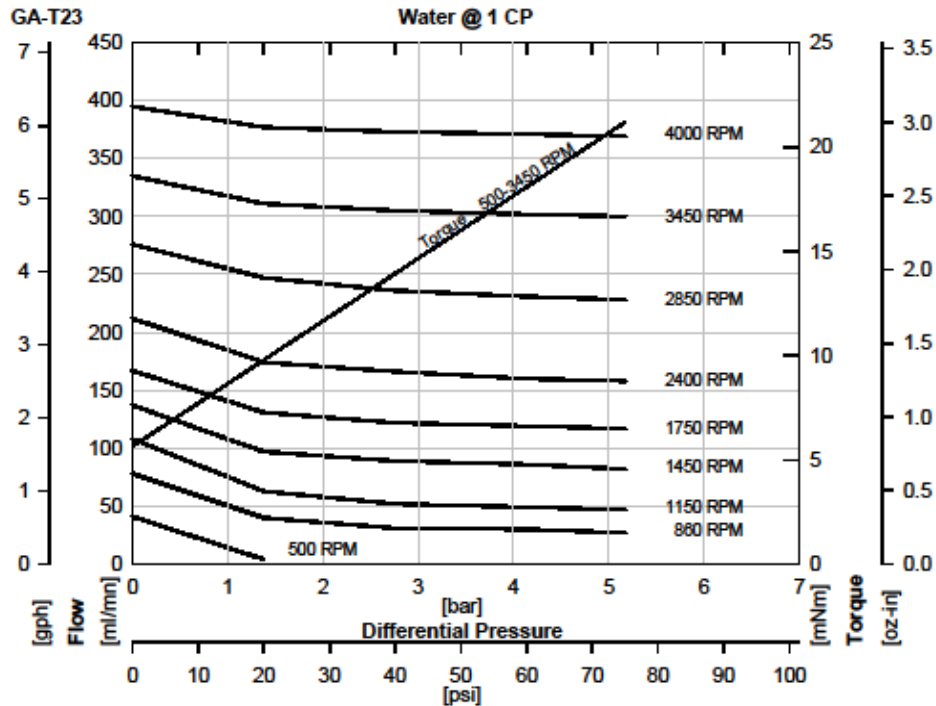


Figure 3.3 Micropump GA-T23 performance with water at 1 cP.

### 3.2.4 Purging system

The purging system comprising six separate capillary tubes and ball valves was devised for the local pressure transducers and pressure tapping connections to the test section to flush out any trapped gas/air. The pressure required flushing periodically and after a rebuild of the test section, so that accurate pressure measurements could be made. The purging tube ball valves can be open individually, allowing liquid bled from upstream of the control valve in the flow loop to pass directly through a 1 mm diameter tube inserted into the body of pressure transducer, thereby flushing out any air bubbles via the pressure tapping connections to the test section. The method of flushing the air from the pressure transducers is described in section 3.7.1.

### 3.2.5 Coriolis flowmeter

The mass flow rate of liquid delivered to the test section was measured using a Micro Motion Coriolis flowmeter comprising an Elite sensor (model CMF010M323NB) and a transmitter (model RFT9739E). The flowmeter was configured by the manufacturer for measurements up to 400 g/min. The output signal of the Coriolis flowmeter was 4 - 20

mA, which was converted to a voltage ranging from 2 - 10 V by a 500  $\Omega$  resistor connected across the output terminals. The flowmeter had a low flow cut off limit of 3 g/min, below which the voltage output remained at 2 V, equivalent to no flow. The accuracy characteristics of the flowmeter, as given by the company, are shown in Fig. 3.4. The accuracy falls as the mass flow rate decreases. The company also provided a calibration line for the flowmeter namely  $Y = 50X - 100$ , where  $Y$  is the mass flow rate (in g/min) and  $X$  is the output (in V).

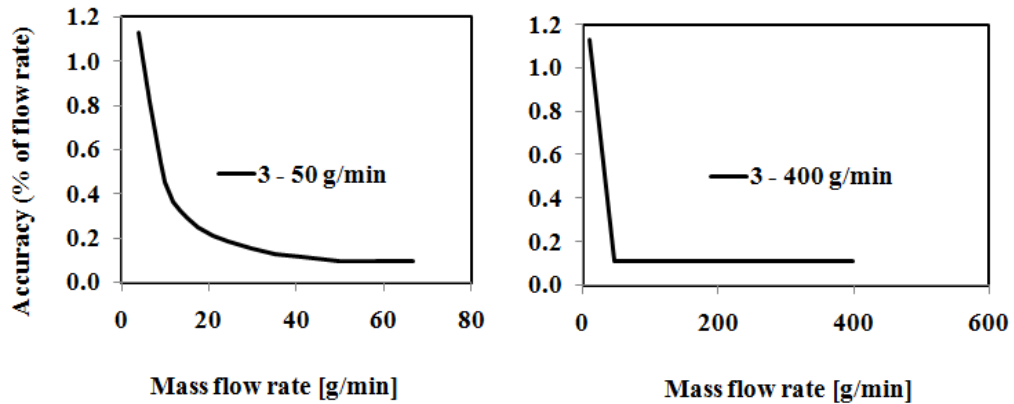


Figure 3.4 Accuracy levels of the Coriolis flowmeter given by the manufacturer.

### 3.2.6 Electric pre-heaters

The original pre-heaters mounted on the rig were replaced because they were not capable of raising the water temperature at inlet to the test section to a value close to the saturation temperature corresponding to the inlet pressure. Three new pre-heaters were manufactured and installed, which were able to increase the water temperature from 20 to 100°C at mass flow rates ranging from 10 to 150 g/min. One of the replacement pre-heaters was made from an aluminium block (50 mm x 50 mm x 200 mm) fitted with two 6.35 mm diameter, 63.5 mm long cartridge heaters (Omegalux, model CIR-1029/240V 250 W). Nine flow channels with a depth of 2 mm, connected by inlet and outlet manifold, were milled into the top surface of the block. A cover plate was fitted over the channels. The other two pre-heaters were made with copper block, each with dimensions of 25 mm x 12 mm x 72 mm. A cartridge heater (Omegalux, model CIR-1029/240V 250 W) was inserted into each copper block as the heat source. A single flow channel 1 mm wide, 0.6 mm deep and 62 mm long was machined in one of the

copper block pre-heaters and a cover plate fitted. In the other copper block pre-heater, the flow channel was made by cutting a slot 5 mm wide and 50 mm long through the 0.2 mm thick paper gasket between the copper block and cover plate. The electrical power input to the cartridge heaters were automatically adjusted by a PID controller to give a steady outlet temperature or wall temperature for each pre-heater. As a result, if the water flow rate changed, the temperature of the water entering the test section could be maintained at a constant value.

### **3.2.7 Cooler-condenser and reflux condenser**

The cooler-condenser cooled the working fluid returning from the test section outlet to the main reservoir, condensing the vapour generated in the test section during flow boiling experiments. The reflux condenser, installed on top of the main reservoir condensed the vapour formed above the boiling liquid inside the reservoir. Both condensers were of identical coiled tube design and were made of stainless steel SS316. The helical coils had a mean diameter of 30 mm with 13 coils on a pitch of 15 mm. The inner diameter and the length of the shell were 60.2 mm and 200 mm respectively. Both condensers were cooled using chilled water-glycol solution supplied from the chiller unit.

### **3.2.8 Water manometer**

A vertical column 1320 mm high was connected to the flow loop between the Coriolis flowmeter and pre-heaters. The manometer indicated the gauge pressure in the flow loop and was used in the calibration of the local pressure transducers connected to the test section (see Section 3.9.6.4). The manometer can be seen in Fig. 3.2.

## **3.3 Microchannel test sections**

The most important component of the flow loop was the microchannel test section on which the experiments were performed. Three test sections were manufactured and tested, each made from an Oxygen-free copper block with dimensions of 25 mm x 12 mm x 72 mm. A single rectangular microchannel was cut in the top surface of each block between the 2 mm diameter inlet and outlet plenums using a Kern HSPC 2216 high-precision micromilling machine with a speed rotation of 10000 RPM, feed rates of 100 mm/min and cut of depth of 0.24 mm (first cut) to 0.08 mm (finishing). The

microchannel length between the plenums was 62 mm. All three microchannels had the same length and depth but were different in width, as given in Table 3.1. The width of the microchannels was measured using a field effect scanning electron microscope (SEM) (Zeiss Supra 35 VP) at the Experimental Technique Centre of Brunel University, see Fig. 3.5. The SEM has a resolution down to 1 nm and an accuracy of  $\pm 1 \mu\text{m}$ . The channel depth was measured using a microscope (TSER Technology V-200) with an accuracy of  $\pm 1 \mu\text{m}$ . The length of the test section was measured using a digital vernier calliper with a resolution of  $10 \mu\text{m}$ .

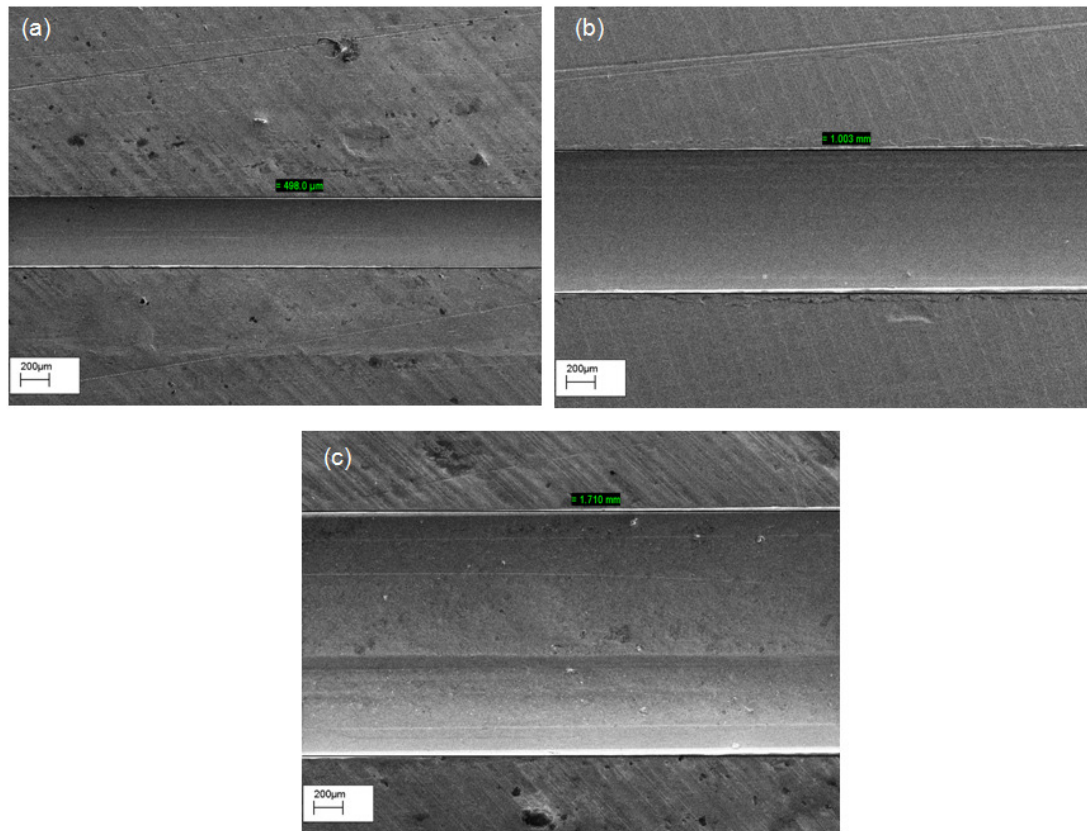


Figure 3.5 Width measurements using a Zeiss Supra 35 VP electron microscope: (a) Test section 1, (b) Test section 2, (c) Test section 3.

Table 3.1 Details of test section dimensions.

Test section	Width, $W$ (mm)	Height, $H$ (mm)	Hydraulic diameter, $D_h$ (mm)	Aspect ratio, $\beta$	Length, $L$ (mm)
Test section 1	0.50	0.39	0.438	0.78	62.0
Test section 2	1.00	0.39	0.561	0.39	62.0
Test section 3	1.71	0.39	0.635	0.23	62.0

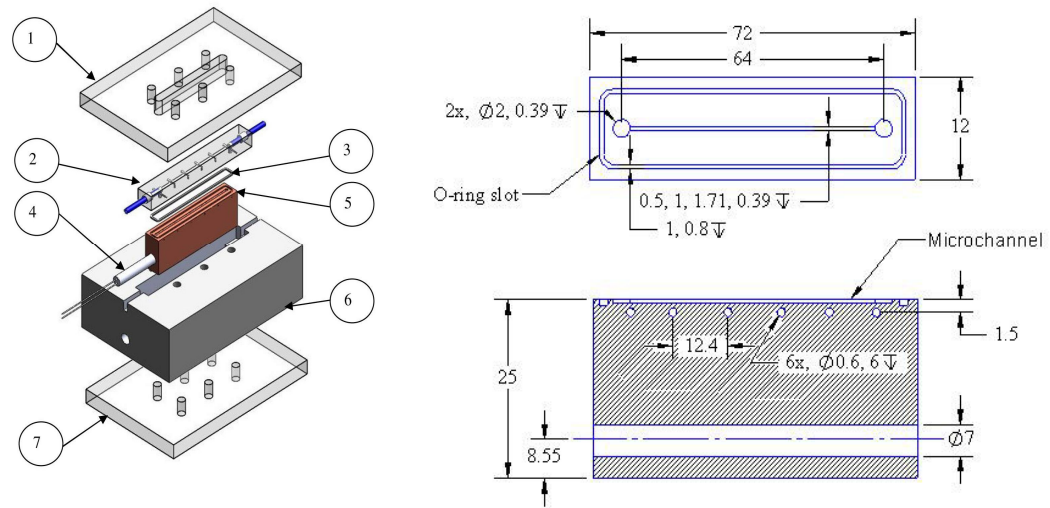
Preliminary design studies and engineering drawings of the test sections are included in Appendix C.

The construction of the microchannel test section assembly can be seen in exploded view in Fig. 3.6. Six holes, 0.6 mm diameter and 6 mm deep, were drilled in the side of each copper test section, 1.5 mm below the top surface, for inserting thermocouples to measure the wall temperature distribution along the channel. The thermocouple holes were located 1.11 mm below the microchannel base and equi-spaced 12.4 mm apart in the flow direction. A 7 mm diameter hole was drilled through the copper body, parallel to the microchannel, to accommodate the cartridge heater used as a heat source. A transparent polycarbonate cover was clamped to the top of the copper test section and sealed with an O-ring. The cover formed the upper surface of the microchannel and incorporated the flow connections and associated 2 mm diameter plenums leading to and from the microchannel. Static pressure tapping holes were drilled in the cover of six positions: inlet plenum, outlet plenum and four equi-spaced locations along the microchannel.

For this research, three new copper test sections were designed and manufactured to overcome the following problems encountered in a previous study using an earlier version of the test rig:

1. Leakages due to holes in the inlet and outlet plenums and the poor seal between the top surface of the copper block and the microchannel cover.
2. The resistance heater wire was easily broken because it was very thin and a high pressure was exerted on it because the rear surface of the channel was not flat.

3. Heat losses to the ambient were high due to the difficulty of insulating the test section.
4. The previous test section was difficult to dismantle and reassemble.



1. Cover plate (polycarbonate); 2. Channel cover (polycarbonate); 3. O-ring seal; 4. Cartridge heater; 5. Copper block; 6. Nitrile foam rubber insulation; 7. Bottom plate (polycarbonate).

Figure 3.6 Test section construction showing the main parts (all dimensions in mm).

The inlet and outlet plenums were properly sealed in the new test sections and a cartridge heater was used as the heat source which was more robust and powerful than the resistance wire heater used previously. Furthermore, the test section was insulated using nitrile foam rubber. The new test sections were easy to dismantle and reassemble for maintenance, such as changing a part or a thermocouple.

Photographs of the top views of the three new test sections are presented in Fig. 3.7. Around each microchannel there was a slot for an O-ring seal (Viton rubber cord) with a depth of 0.8 mm and a width of 1 mm to prevent leakage. This seal also provided an easy way to assemble the test section with the cover.

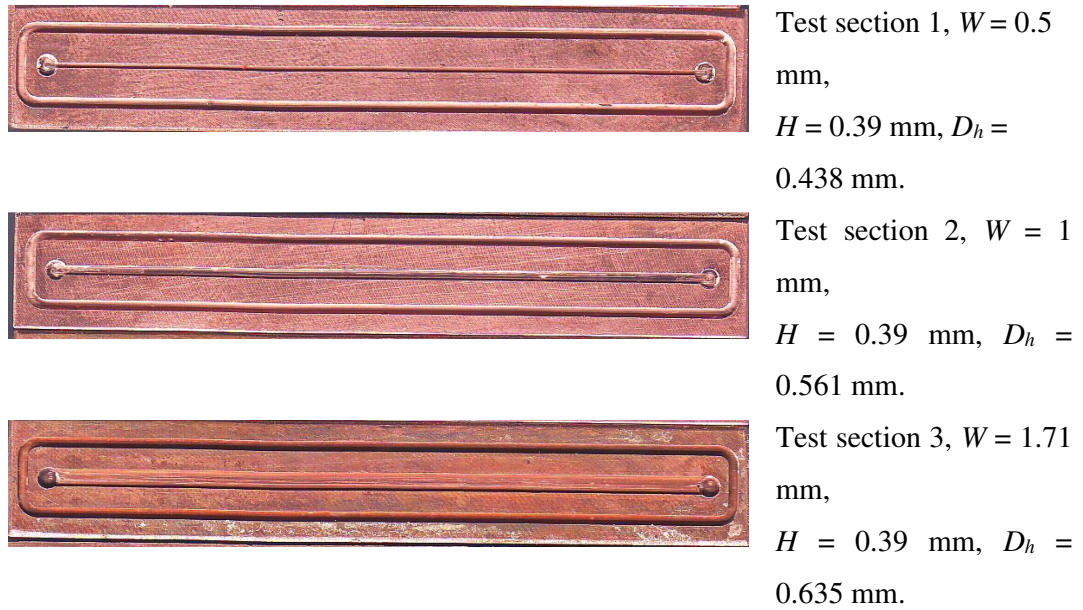


Figure 3.7 Photographs showing the top view of the three microchannel test sections.

Because the roughness of the wall surfaces may influence the flow behaviour for in small channels, a surface analysis was performed. This investigation involved scanning electron microscope (SEM) and surface roughness measurements on the base surfaces of the microchannel test sections. The SEM measurements were conducted at the Experimental Techniques Centre, Brunel University using a Zeiss Supra 35 VP electron microscope, using setting of 20 kV, 26 mm lens distance, 30  $\mu$ m aperture and 100X magnification. The surface roughness measurements were performed using a Zygo NewView 5000 surface profiler in the Advanced Manufacturing Technology laboratory, Brunel University. The SEM images obtained presented in Fig. 3.8 show that all test sections appear to have similar surface characteristics. The surface of Test section 1 looks dirty and there are many white black marks. Test section 2 has many scratches as a result of machining, but there is no debris. Test section 3 seems rougher than Test section 1 or Test section 2 and there are many scratches and possibly some debris or dust (circled in yellow).

Surface roughness measurements made on the channel base surface at mid-length along each microchannel are shown in Fig 3.9 for each test section. The roughness was measured at three different axial locations and an average absolute surface roughness was calculated. Local and average surface roughness values for each test section are given in Table 3.2. Relative surface roughness values for the three test sections were

estimated based on the data in Tables 3.1 and 3.2 to be 0.0023, 0.00226 and 0.00176 for test sections 1, 2 and 3 respectively. These values may be compared with those of Kandlikar et al. (2003), who employed microchannels with relative surface roughnesses ranging from 0.00178 to 0.00355. They concluded from their experiments that the relative roughness of 0.00355 only affected the friction factors and heat transfer coefficients for microchannels with a hydraulic diameter of 0.62 mm or less. Since the relative roughnesses of the channel tested in this work are smaller than those of Kandlikar et al. (2003), the acceptance of their conclusions means that surface roughness should not affect the measured values of friction factor and heat transfer coefficient in this study.

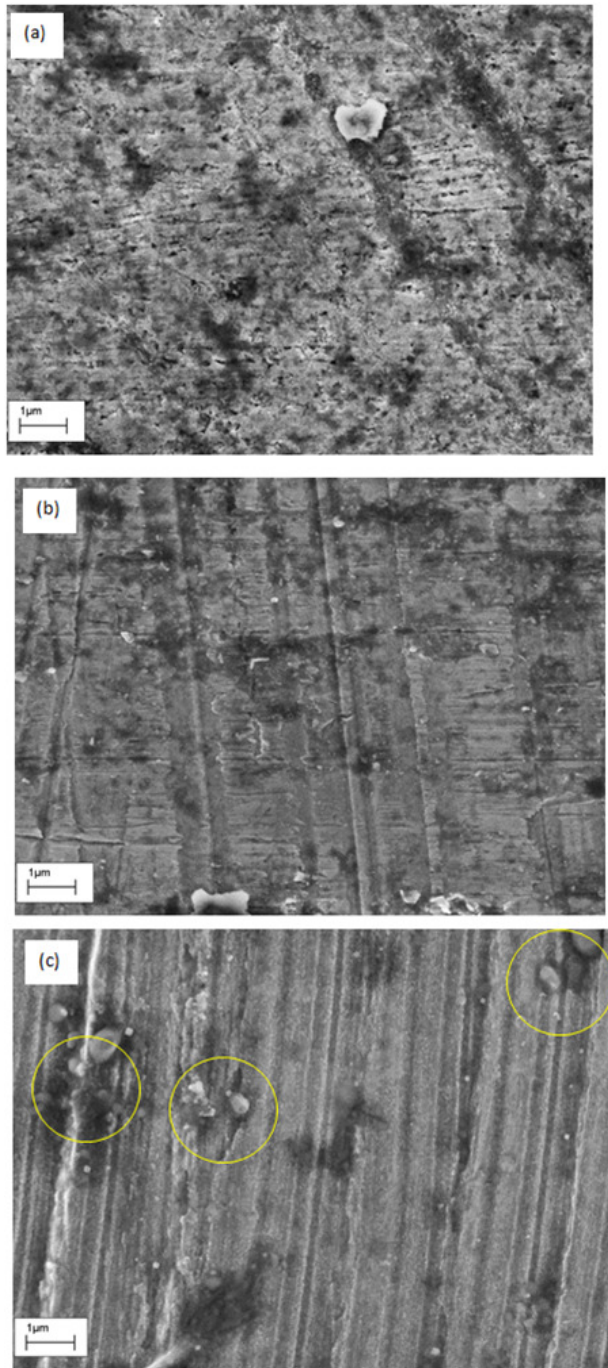


Figure 3.8 SEM images of microchannel base surfaces: (a) Test section 1, (b) Test section 2 and (c) Test section 3.

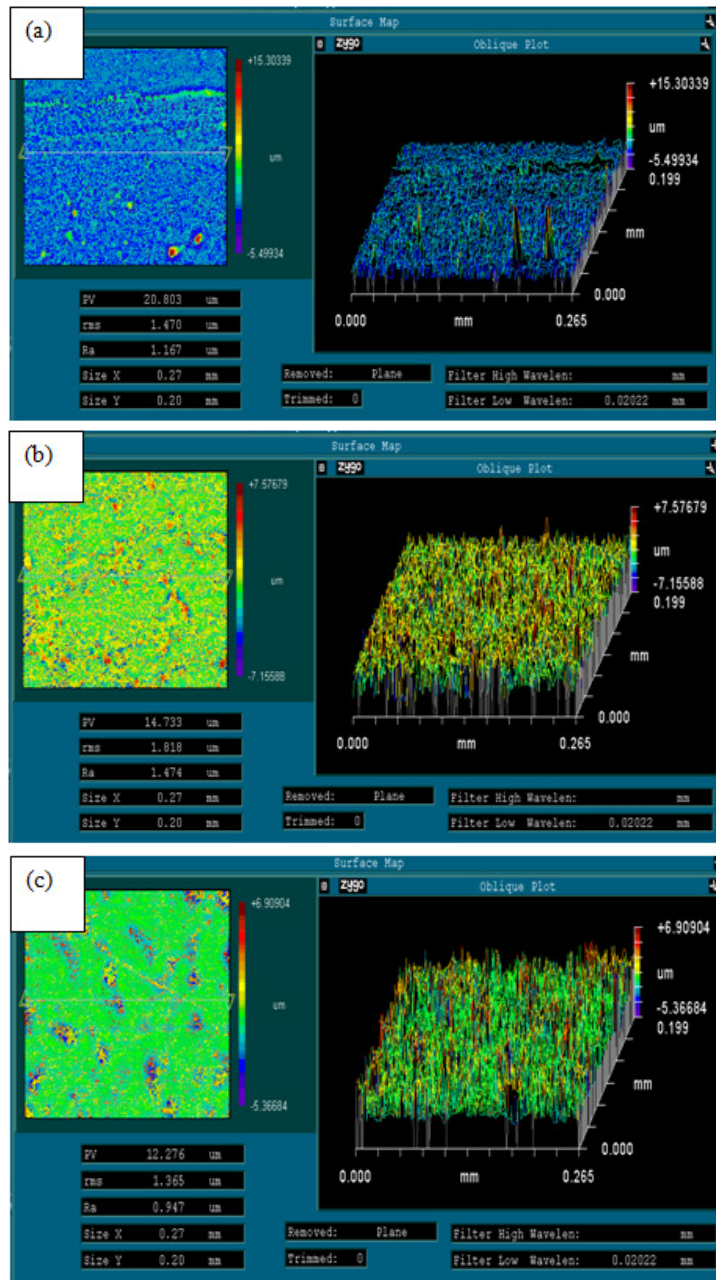


Figure 3.9 Surface roughness measurements; (a) Test section 1, (b) Test section 2 and (c) Test section 3. The measurements shown were taken at a location near the middle of each microchannel for a sample test area of  $0.265 \times 0.199 \text{ mm}^2$ .

Table 3.2 Local surface roughness (Ra) measurements and averaged values for each microchannel.

Test section	Near inlet ( $\mu\text{m}$ )	Near middle ( $\mu\text{m}$ )	Near outlet ( $\mu\text{m}$ )	Average ( $\mu\text{m}$ )
1	0.979	1.167	0.89	1.01
2	0.954	1.474	1.382	1.27
3	0.961	0.947	1.449	1.12

The local Ra values shown in Table 3.2 evaluated over sample areas ( $0.265 \times 0.199 \text{ mm}^2$ ) on the base of each microchannel test section near the inlet, middle and outlet. The average Ra value for each microchannel is the arithmetic mean of the local values.

### 3.4 Visualization system

To observe flow boiling patterns, a high-speed camera Phantom V6.0 camera was mounted on a movable camera support above the test section. The camera support could be easily traversed vertically and horizontally, so that the images of bubble movement and growth inside the test section could be captured at different locations along the entire microchannel length. The CMOS camera head sensor had an image resolution of  $512 \times 512$  pixels. For the experiments, the camera was set for a sample rate of 1000 pictures per second, allowing full sensor resolution and post-trigger recording set at 10000 pictures.

In preparation for each experiment, the camera position, focus, speed and resolution were adjusted. Image capture was started once an experiment was running steadily at the desired mass flow rate, inlet temperature and heat flux with flow boiling established. Readings of 1 second duration (1000 pictures) were saved to a computer, in CIN image file format by the Phantom software at each operating condition for subsequent flow patterns analysis. In the visualisation system, illumination should be provided. Phillips halogen lights, 24V, 250 W, were employed for illumination as shown in Fig. 3.10.

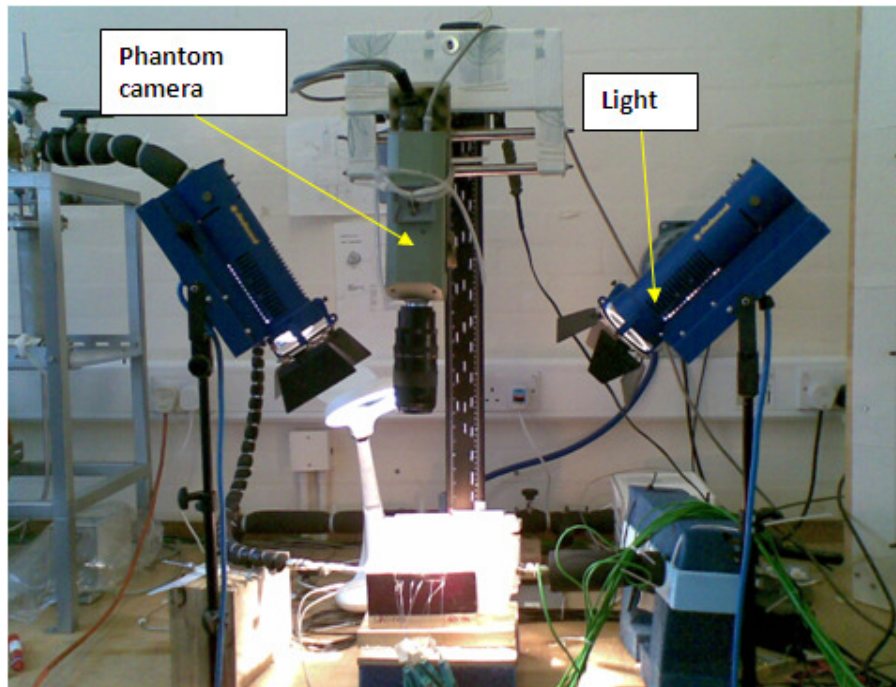


Figure 3.10 Visualisation system.

### 3.5 Data acquisition system

A National Instruments compact data acquisition (DAQ) system forms part of the experimental equipment. The system hardware consists of an 8-slot chassis with a number of plug-in modules (NI9401, NI9205, NI9211, NI9481 and NI9219) connected over USB to a desktop computer with LabView (version 8) programmable software. The NI9401 is a digital input/output module used for TTL pulse generation to trigger or start the high-speed camera scanning input data. The NI9205 analogue input module has 16 differential channels and was used to measure voltage signal from the Coriolis mass flowmeter and the pressure transducers.

Three 4-channel thermocouple input modules (NI9211) incorporating cold-junction compensation were used for measuring the fluid and wall temperatures in the test section and the ambient temperature. The NI9481 relay module operated when the LabView program ran and switched on the electrical power supply routed through test rig control box to the main reservoir heater and other components.

The NI9219 4-channel universal analogue module was used for monitoring temperature signal from other thermocouples installed around the test rig. A photograph of the data acquisition system chassis and modules is shown in Fig. 3.11.

In the experiments, the data acquisition system measured and recorded the mass flow rate, all temperatures and pressures every 0.1 s. When the experimental conditions were steady, readings were normally taken over duration of 3 minutes ( $\equiv$  1800 readings / channel) and averaged. The ambient pressure and the multimeter readings used to determine the power supplied to the test section were recorded manually.

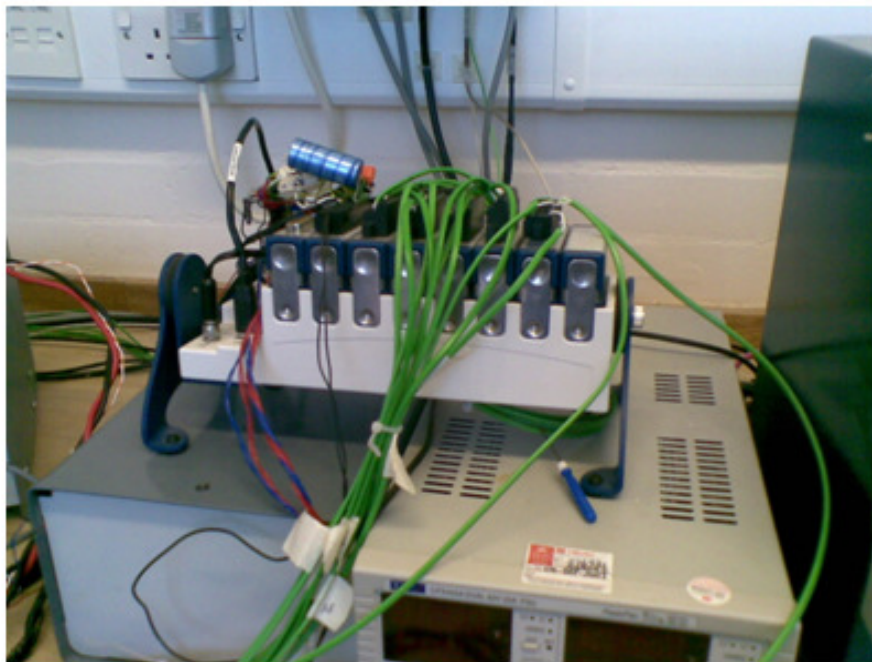


Figure 3.11 Data acquisition system.

### **3.6 Chiller system**

A chiller system was used to supply chilled water-glycol solution for cooling the cooler-condenser, reflux condensers and the subcooler in the test rig flow loop. This system consists of a vapour compression refrigeration cycle and a liquid chiller circuit. The refrigerant used in this equipment is R22. A schematic diagram of this system is shown in Fig. 3.12.

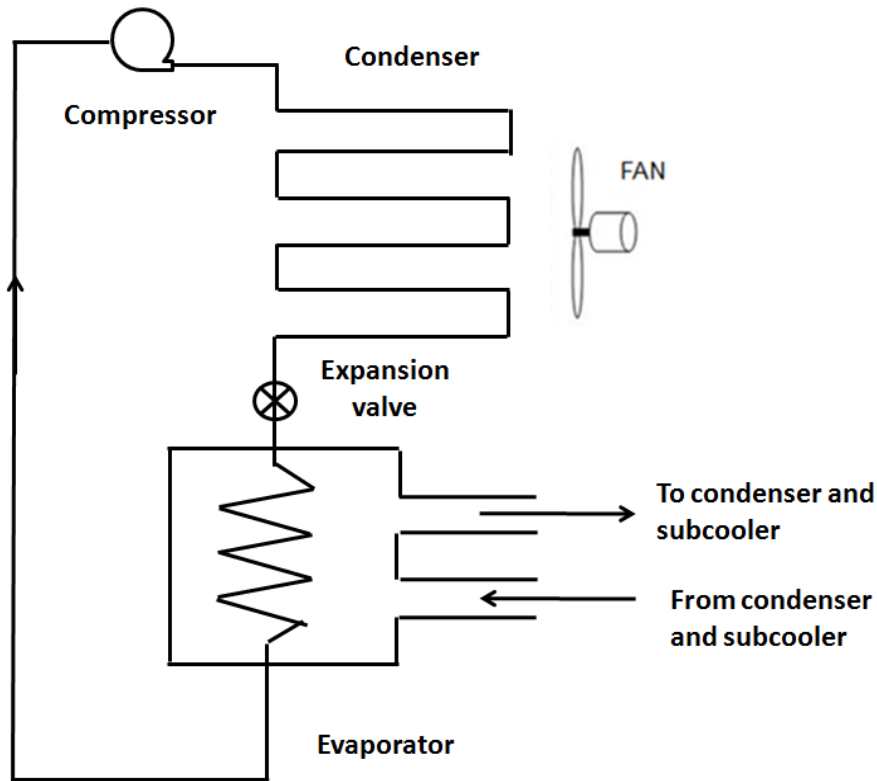


Figure 3.12 Schematic diagram of chiller system.

### 3.7 Running the test rig: experimental procedures

This section describes the procedures involved in running the test rig. Additionally, in order to prepare the rig before running an experiment a degassing procedure needs to be followed.

#### 3.7.1 Degassing procedure

Assuming that the microchannel test section is already installed in the test rig, a degassing procedure should be carefully followed to ensure that the flow loop system is free from gases. This procedure is given below as a sequence of instructions.

1. Switch on the computer and run the LabView program so that the main power supply in the test rig control box is turned on.
2. Close all valves on the rig and isolate the main reservoir from the flow loop by closing the valves connecting the reservoir and the flow loop.

3. Evacuate the reservoir by using the vacuum pump. When the gauge pressure inside the reservoir is reduced to approximately -30 inHg (-100 kPa), close the vacuum pump valve and switch off the vacuum pump.
4. Fill the main reservoir with deionized water through the degassing line until the water level inside the reservoir reaches the water level mark on the sight glass.
5. Boil the liquid in the reservoir over a period of time and periodically open the degassing line vent valve on the top of the reflux condenser to release any trapped air or gas to the atmosphere. This step should be repeated until the pressure inside the reservoir does not change at the corresponding saturation temperature, e.g. 102°C.
6. Switch on the chiller unit to supply chilled water-glycol coolant to the subcooler.
7. Open valves between reservoir and flow loop and switch on the gear pump. Note: that the temperatures of water at the inlet pump should be less than 50°C.
8. Open the valves on the local pressure transducer purging lines. Water will then flow through the pressure transducers so that gas or air trapped inside the transducers and the tubes connecting the transducers to the test section is flushed away.
9. Continue circulating water around the flow loop. The vent valve on the top of the reflux condenser should be opened periodically so that air or gas in the loop or reservoir can escape to the atmosphere. This step should be repeated until the pressure inside the reservoir does not change at the corresponding saturation temperature.
10. The rig is now ready to be used for conducting experiments.

### **3.7.2 Sequence of steps for running an experiment**

In this section, the experimental procedures are grouped separately for the single-phase and two-phase flow boiling tests.

#### **3.7.2.1 Single-phase experiments**

The objectives of the single-phase experiments are to obtain adiabatic and non-adiabatic measurement data to establish the pressure drop, friction factor and heat transfer

characteristics. The following procedures are adopted, again given in the form of instructions.

For adiabatic experiments:

1. Switch on the computer and run the LabView program.
2. Open the degassing vent valve on the main reservoir so that the pressure inside the reservoir is approximately equal to the ambient pressure. The water inside the main reservoir does not need to be boiled.
3. Run the pump to circulate the water through the flow loop.
4. Flush any air, trapped inside the local pressure transducers, or inside the tubes connecting the pressure transducers to the test section, by opening the purging valves one-by-one.
5. Stop the pump and open the valve connecting the water manometer to the flow loop. Turn on the lamp inside the pressure transducer enclosure to keep the temperature inside at approximately 50°C. Check the calibration of all local pressure transducer against the water manometer.
6. Close the water manometer valve.
7. Re-start the pump.
8. Adjust the pump speed to give the required mass flow rate. Switch on the pre-heaters one or more to raise the water temperature at the channel inlet to the required level.
9. After approximately 15 minutes, the flow and the heating process in the preheater will be steady; the steady condition is achieved when the mass flow rate, inlet temperature and pressures show constant values.
10. Record all data, including temperatures, pressures and mass flow rate using the LabView program.
11. Repeat procedures 8 and 9 for different inlet temperatures and mass flow rates, e.g. 20 g/min, 30 g/min, 40 g/min, and further as required.
12. After finishing the experiment, switch off the pre-heaters, decrease the mass flow rate and turn off the pump. Shut off the valves connecting the main reservoir and the flow loop and the degassing vent valve.

For non-adiabatic experiments:

In this group of experiments, the aim is to obtain single-phase heat transfer coefficients. Hence, power should be applied to the microchannel test section to heat the water flowing through it.

- 1 – 8. Follow the same steps as for the adiabatic experiments.
9. Switch on the electrical supply to the test section and use the Variac to adjust the power to the required value, e.g. 11 W. The power setting chosen should not cause boiling to occur inside the test section, even for the minimum mass flow rate selected. Run a mass flow rate, e.g. 20 g/min, and wait until conditions are steady. This condition is reached when there are no changes with time in the mass flow rate, pressure and temperature readings. After steadiness is reached, record all data using the LabView program. Increase the mass flow rate, e.g. 30, 40, 50 g/min and further as desired, and record all data for every mass flow rate used.
10. Repeat step 9 for different input power setting, e.g. 12, 15, 20, 24, 30 W.

### 3.7.2.2 Flow boiling experiments

The objectives of these experiments are to investigate the mechanisms of flow boiling in microchannel and to obtain heat transfer coefficient, two-phase pressure drop and instability data for a range of mass fluxes and heat fluxes. In addition, flow boiling patterns are visualized to inform the construction of flow pattern maps. To fulfil the above objectives, the experiment should be conducted as follows:

1. If the main reservoir is empty, fill with deionized up to the water level mark on the sight glass.
2. Open the degassing vent valve so that the pressure inside the reservoir is approximately equal to the ambient pressure. Switch on the lamp inside the pressure transducer enclosure.
3. Run the pump and operate the purging valves to flush out air/gas trapped inside the local pressure transducers and the tubes connecting the transducers to the test section.
4. Stop the pump and open the water manometer valve.

5. When the temperature inside the transducer enclosure reaches approximately 50°C, check the calibration of all the local pressure transducers against the water manometer.
6. Closed all valves on the flow loop and the degassing vent valve, but do not turn off the lamp inside the transducer enclosure.
7. Perform degassing procedures.
8. Adjust the speed of the pump so that the required water flow rate is delivered to give a mass flux of 200 kg/m<sup>2</sup>s.
9. Switch on the pre-heaters (one or more) and adjust the pre-heaters to raise the water temperature at the channel inlet rise to 98°C.
10. Switch on the Variac power supply and adjust the test section heating to the desired value. After steadiness is reached indicated by no changes in the mass flow rate and all temperatures, record all the required measurement data using the LabView program. Increase the power carefully by adjusting the Variac setting. Wait until the flow rate and temperature are steady and then again record all the measurement data. Increase the power further in steps until the fluid starts to boil. Stop increasing the power when either the test section wall temperatures reach values of approximately 120°C, or the pressure in the main reservoir cannot be decreased further. Record all data and the ambient pressure at each step as the test section heating power is increased. Under flow boiling conditions, increasing the heat flux causes the mass flux to decrease and the inlet pressure to increase. Consequently, both the mass flux and inlet pressure need to be adjusted to maintain constant values. The test section inlet pressure can be decreased by reducing the system pressure or the temperature in the main reservoir.
11. For flow boiling conditions, at each step of increasing power input, images of bubble movements should be captured and recorded at three different locations along the test section (i.e. near inlet, middle and near outlet) using the Phantom V6.0 high-speed camera.
12. Decrease the power input to the test section step-by-step until the Variac auto transformer is at the zero setting position. Record all data and the ambient pressure at each step. Switch off the Variac power supply and turn off the pre-heaters.

13. Repeat steps 8 to 12 for different mass fluxes, i.e. 300, 400, 500 kg/m<sup>2</sup>s, and further as required.
14. After finishing the experiments, turn off power to all heaters and after the test section wall temperatures fall below 90°C, switch off the pump and close all valves on the rig. Shut down the LabView program and the main power supply to the test rig. Finally, turn off the Coriolis flowmeter, the camera lamps and the camera.

### 3.8 Heat loss measurement procedures

Heat losses from the microchannel test section occur due to natural convection and radiation to the ambient air and surroundings, and conduction losses through the supporting structure, connections and cables. The rate of heat loss can be estimated by energy balances with and without fluid flowing inside the test section. To determine the heat loss from the test section when fluid is flowing through it, the enthalpy rise of the fluid is compared to the electrical power input to the test section. The rate of heat loss is then equal to  $q_{loss} = P - \dot{m}c_p(T_o - T_i)$ , where  $P$  is the input power,  $\dot{m}$  is the mass flow,  $c_p$  is the specific heat capacity of the fluid,  $T_i$  is the inlet temperature and  $T_o$  the outlet temperature. For the case of heat loss with no fluid flowing, the following test is performed before the test section is charged with liquid. A small constant power is applied to the test section cartridge heater, which causes the temperature of the test section to increase. This temperature rise is monitored by the thermocouples inserted at six locations in the body of the test section. When conditions become steady the wall temperatures on the test section together with that of the ambient, are recorded and correlated with the power input to the cartridge heater. This procedure is repeated for several levels of input power. In this work, a linear relation of the form  $q_{loss} = 0.0508\Delta T_{ma} - 0.636$  was obtained, where  $\Delta T_{ma}$  is the average wall-to-ambient temperature difference ( $\Delta T_{ma} = T_w - T_a$ ). This method was also used by Lee and Garimella (2008). The difference between the heat losses obtained by the two approaches was approximately 3.2%. Although the heat loss varies with test section wall temperature, it is almost constant percentage of the electrical power supplied. The average heat loss value was found to be approximately 6.8% of the input power.

### **3.9 Calibration procedures**

Calibration data was obtained, by performing tests or from manufacturers, for each of the sensors and instruments used to collect experimental measurements from the test rig. The calibration of the Coriolis flowmeter, the thermocouples and pressure transducers and the multimeters used to determine the electrical power input to the test section are discussed in Section 3.9.6. The calibration data thus obtained are presented in tabular or graphical form for the sake of simplicity and ease of understanding. Section 3.9.1 and 3.9.3 describe checks carried out on equipment used in the calibration of the thermocouples and the Coriolis flowmeter. Evaluation of the local value of the acceleration due to gravity and the determination of the local atmospheric pressure are described in Section 3.9.4 and 3.9.5 respectively.

#### **3.9.1 Precision thermometer and PRT**

All thermocouples were calibrated against an ASL F250 MK II precision thermometer connected to a platinum resistance thermometer (PRT) probe of 6 mm diameter and 250 mm long (Model T100-250). The accuracy of this instrument was  $\pm 0.025$  K according to the manufacturer. Spot checks were carried out in ice and boiling water.

For the ice point check, the PRT probe was partially immersed in Dewar flask containing melting ice made with means of tap water. When the temperature reading was steady, the temperature indicated on the precision thermometer alternated between  $-0.14^{\circ}\text{C}$  and  $-0.15^{\circ}\text{C}$ . This check was performed at an ambient temperature of  $21^{\circ}\text{C}$  and a pressure of 1015 mbar. On a different day, ice made of deionized water was used to conduct another ice point check. This second check was performed at an ambient temperature of  $20^{\circ}\text{C}$  and a pressure of 1015 mbar. The temperature shown on the precision thermometer was  $-0.11^{\circ}\text{C}$ .

For the boiling water check, the PRT probe was inserted into the main reservoir of the test rig with the end of the probe below the liquid level. The reservoir was not completely sealed, so that the inside pressure was close to atmospheric. The power input to the immersed cartridge heater in the reservoir was controlled by a PID set to  $100^{\circ}\text{C}$ , causing the water inside the reservoir to boil. After several minutes, the condition inside the reservoir was steady, the temperature reading shown on the

precision thermometer varied between 100.12°C and 100.13°C (at an ambient temperature of 21°C and a pressure of 1015 mbar). A further check was repeated and performed using tap water boiling in a kettle. The temperature shown on the precision thermometer oscillated between 99.64°C and 99.70°C (at an ambient temperature of 19.5°C and a pressure of 1008 mbar).

### 3.9.2 Digital electronic balance

A Sartorius digital electronic balance was used in calibrating the Coriolis flowmeter by a collection and weighing method. The balance has a resolution of 0.1 mg. The calibration of the balance was checked using standard weights ranging from 1 g to 200 g taken from a traditional mechanical balance. The results shown in Table 3.3 indicate that the balance is accurate within approximately  $\pm 0.1\%$  of the reading, for weights of 5 g and above. For the 1 g and 2 g weights the deviation is approximately  $\pm 0.2\%$  of the reading.

Table 3.3 Comparison of applied weights and balance readings.

Standard weight (g)	Weight indicated by balance (g)
1	1.0015
2	1.9967
5	4.99912
10	10.00177
20	20.007
50	49.9714
100	100.064
200	199.977

### 3.9.3 Digital electronic stop watch

A Lonsdale digital electronic stop watch was used for timing the water collections during calibration of the Coriolis flowmeter. The stop watch has a resolution of 0.01 s and was compared with a similar RS components stop watch. The RS stop watch also had a resolution of 0.01 s. A comparison of times displayed by the two stop watches was made by synchronising the starting and stopping of the watches as closely as possible. The results recorded for a number of time durations are shown in Table 3.4.

Differences between the times recorded using the two watches are within  $\pm 0.03$  s, and are most likely due to errors in synchronisation.

Table 3.4 Comparison of times indicated by Lonsdale and RS stop watches.

Time (Lonsdale stop watch), [s]	Time (RS stop watch), [s]
17.62	17.63
30.56	30.53
60.63	60.66
301.13	301.12
764.69	764.68

### 3.9.4 Gravitational acceleration

The value of gravitational acceleration varies with latitude and altitude. The university building where the laboratory is located is at latitude 51.53 degrees North and longitude 0.4740 degree West where the ground level is approximately 37.8 m above sea level. This information was taken from <http://www.daftlogic.com/sandbox-google-maps-find-altitude.htm>. According to the National Physical laboratory (see <http://www.npl.co.uk/reference/faqs/>), the local value of gravitational acceleration,  $g$ , can be estimated with an uncertainty of  $\pm 5$  parts in  $10^5$  using Eq. (3.1).

$$g = 9.78032 \left( 1 + A \sin^2(L_a) - B \sin^2(2L_a) \right) - 3.086 \times 10^{-6} H_s \quad (3.1)$$

where  $A$  and  $B$  are constants equal to 0.0053024 and 0.0000058,  $L_a$  is the latitude (in degrees) and  $H_s$  is the height of the location above sea level (in metres). Using the above values of  $L_a$  and  $H_s$ , the local acceleration due to gravity was calculated  $g = 9.812 \pm 0.0005$  m/s<sup>2</sup>. In the calibration procedures, the gravitational acceleration was used to calculate the hydrostatic pressure equivalent of a column of liquid mercury (see Section 3.9.5) or water (see Section 3.2.8). In addition,  $g$  is involved in calculating the hydrostatic pressure correction to be applied to atmospheric pressure measurements to account for altitude differences. Finally, it is noted that if the local gravitational acceleration is assumed to be 9.81 m/s<sup>2</sup> (rather than the value of 9.8120 m/s<sup>2</sup> found above), the difference of approximately 0.02% is negligibly small.

### 3.9.5 Digital barometer

A Cole Parmer digital barometer (Model EW-99760-00) was available in the first floor laboratory (Room TB 113) where the test rig is located. This instrument has a barometric pressure range of 795 to 1050 mbar and a resolution of 1 mbar. However, the accuracy of barometric readings for this device quoted by the manufacturer of  $\pm 5$  mbar is rather poor. Readings taken using the Cole Parmer digital barometer are compared in Table 3.5 with the readings indicated at corresponding times by the following instruments:

- (i) A Fortin pattern mercury barometer located in the combustion engines laboratory on the ground floor of the same building, and
- (ii) The on-line barograph maintained at <http://resource.npl.co.uk/pressure/pressure.html>, by the National Physical Laboratory (NPL) at Teddington, Middlesex, which is approximately 10 m above sea level and has an uncertainty of  $\pm 0.3$  mbar. NPL is approximately 13 km from Brunel University.

Table 3.5 Comparison of atmospheric pressure readings from the three instruments at corresponding times.

Cole Parmer barometer	Fortin mercury barometer	Corrected value of Fortin mercury barometer	NPL on-line barograph
[mbar]	[mmHg]	[kPa]	[mbar]
1008	756.80	100.82	1009.6
1010	757.90	100.97	1011.0
1011	758.35	101.03	1011.7
1015	761.75	101.48	1016.2
1016	762.85	101.63	1017.6
1017	763.90	101.77	1019.2
1018	763.85	101.76	1019.0
1023	768.35	102.36	1024.9
1025	769.85	102.56	1027.0
1028	772.25	102.88	1030.3

From Table 3.5, a linear equation is obtained,  $Y = 0.1055X - 5.58$ , with a standard deviation of 0.08 kPa, where  $Y$  is the atmospheric pressure (in kPa) and  $X$  is the Cole Parmer barometer readings (in mbar). A graph showing curve fitting of line  $Y = 0.1055X - 5.58$  is presented in Appendix B. The ambient pressure is used for converting the gauge pressures indicated by all pressure transducers mounted on the test section to absolute pressures.

### **3.9.6 Sensor calibrations**

This section describes the procedures used in calibrating all sensors installed on the test rig including the microchannel test section and the calibration results obtained. The sensors calibrated include all thermocouples, the Coriolis mass flowmeter, a reference pressure transducer used to measure the fluid pressure at six locations along the microchannel test section. All sensors were calibrated with their outputs connected to a National Instruments data acquisition system interfaced to a desktop computer running LabView software for measurement, data logging and storage. By calibrating each sensor together with the data acquisition system as used in the experiments, systematic error associated with the sensor and the data acquisition system are accounted for in the resulting calibration. Any error introduced by a standard used in the calibration process, however, will still be present. Calibration equations were implemented in the LabView data acquisition programs developed for this work.

#### **3.9.6.1. Thermocouple calibration**

Mineral insulated, stainless steel sheathed, type K thermocouples are used to measure the fluid temperatures at the microchannel inlet and outlet, the wall temperatures at six equi-spaced locations along the microchannel, the ambient temperature and the temperature of the enclosure housing local pressure transducers. The length and diameter of all the thermocouple probes were 150 mm and 0.5 mm respectively. Cold junction compensation is provided by built-in thermistors in the data acquisition (DAQ) system.

The thermocouples were calibrated against an ASL F250 MKII Precision Thermometer coupled with a platinum resistance thermometer (Model T100-250). The specified accuracy of this instrument was  $\pm 0.025$  K over the range from  $-50^{\circ}\text{C}$  to  $250^{\circ}\text{C}$ . The

thermocouples were fastened tightly to the PRT and immersed in an Omega constant-temperature circulating liquid bath. The bath was fitted with a thermoregulator (Model HCTB-3030) consisting of an immersion heater, a circulation pump and a temperature controller. The bath provides a temperature stability of  $\pm 0.005^\circ\text{C}$  and has a set point accuracy of  $\pm 1^\circ\text{C}$ . The liquid used in the bath was Diphyl PHT (Partially Hydrogenated Terphenyl) which has an initial boiling point of  $352^\circ\text{C}$ . Thermocouple calibrations were performed, for both increasing and decreasing temperature, at seven different points over the temperature range from  $24 - 120^\circ\text{C}$ . The ambient pressure and temperature during the calibrations were 1017 to 1018 mbar and  $21-23^\circ\text{C}$  respectively. Readings were taken after the liquid bath temperature became steady, as indicated by no change of the PRT reading. The temperatures measured using the thermocouples were recorded simultaneously by the LabView software. The temperature measured by the PRT, as indicated on the precision thermometer, was noted manually.

The thermocouple calibration results are presented in Appendix B, Fig. B9 in graphical form together with the linear calibration equation fitted to the data for each thermocouple. The standard deviations of the data for each calibration are listed in Table 3.6.

Table 3.6 Standard deviations of thermocouple calibration.

Sensor	$S(\text{K})$	$2S(\text{K})$	Sensor	$S(\text{K})$	$2S(\text{K})$
$T_i$	0.07	0.14	$T_5$	0.10	0.20
$T_1$	0.11	0.22	$T_6$	0.10	0.20
$T_2$	0.10	0.20	$T_o$	0.10	0.20
$T_3$	0.11	0.22	$T_{box}$	0.10	0.20
$T_4$	0.10	0.20	$T_a$	0.11	0.22

In Table 3.6,  $T_i$  refers to the fluid inlet temperature thermocouple,  $T_1$  to  $T_6$  the microchannel wall temperature thermocouples,  $T_o$  the fluid outlet temperature sensor,  $T_{box}$  the temperature thermocouple in the pressure transducer enclosure and  $T_a$  the ambient temperature thermocouple. In addition to the standard deviation ( $S$ ) values, Table 3.6 lists values of  $2S$ , the estimated random uncertainties associated with temperatures determined using the thermocouple sensors calibration lines for a 95%

level of confidence. This can be considered a reasonable achievement, since the specified tolerance (Class 1) for Type K thermocouples over the temperature range - 40°C to 375°C is  $\pm 1.5$  K. An uncertainty of 0.2 K is thus used for all thermocouple temperature measurements in this work.

### 3.9.6.2 Coriolis mass flowmeter calibration

The mass flow rate in the test loop is measured using a Micro Motion Coriolis mass flowmeter, comprising an Elite sensor (Model CMF010M323NB) and a transmitter (Model RFT9739E). The mass flow rate range of the flowmeter is 0 - 400 g/min. The output signal from the Coriolis meter utilizes a 4-20 mA current loop incorporating a 500  $\Omega$  resistor, thus giving a voltage output of 2-10V. The flowmeter has a low flow cut off of 3 g/min, below which the output defaults to the zero flow level of 2V. The calibration supplied by the manufacturer is a linear equation expressed as:  $Y = 50X - 100$ , where  $Y$  is in g/min and  $X$  in volts. The accuracy of the mass flow rate quoted by the manufacturer is 0.1% for mass flow rates above 40 g/min, but gradually rises to about 1.1% at 3 g/min.

Calibration of the flowmeter was performed using a collection and weighing method. A Sartorius electronic balance with a resolution of 0.1 mg was used to determine the mass of fluid collected. Calibrations were carried out for both increasing and decreasing flow rates. The time duration for each collection was measured using a Lonsdale stop watch with a resolution of 0.01 s. The calibration was performed using deionized water at a temperature of approximately 20°C. The results of the calibration are presented in the appendices. The flowmeter calibration line given by the manufacturer is also plotted for comparison. The best straight line fits obtained for increasing flow rates and decreasing flow rates fall slightly below the manufacturer's calibration line, see Appendix B, Fig. B7. The line derived using the combined data results in a standard deviation of 0.6 g/min in the terms of a 95% confidence level. The slope value of 49.92 g/min per volt is 0.16% less than the 50 g/min per volt value for the manufacturer's calibration line. The intercept value of -102.1 g/min obtained represents a difference of 2.1% from the manufacturer's value of -100 g/min.

### 3.9.6.3 Druck pressure transducer calibration

A silicon diaphragm differential pressure transducer (Druck, Model PDCR4170-3400) was connected to the test loop to measure the liquid pressure against atmospheric pressure. This transducer was also used as a secondary standard in the calibration of the local differential pressure transducers fitted to the test section. The transducer measurement range is 0 - 5 bar and its specified accuracy is 0.08% of full scale. The transducer required an energisation voltage of 10 V and produces an output voltage ranging from 0 - 100 mV, corresponding to the 0 - 5 bar range, or 20 mV/bar.

Calibration of the transducer was performed at an ambient pressure and temperature of 1010 mbar and 19.5°C respectively. It was calibrated against a deadweight tester with a resolution of 1 lbf/in<sup>2</sup> (6.895 kPa) over the range of 10 – 70 lbf/in<sup>2</sup> (68.95 – 483 kPa). Readings were recorded for both increasing and decreasing applied pressures. A linear calibration was obtained with small scatter of data around the best straight line. The standard deviation of the data was found to be  $\pm 0.85$  kPa for increasing pressures and  $\pm 0.89$  kPa for decreasing pressures. The calibration line obtained by combining the increasing and decreasing pressure data gave a standard deviation of  $\pm 0.86$  kPa. The slope of this calibration line was equivalent to 19.84 mV/bar, a difference of 0.8% from the slope of 20 mV/bar given in the manufacturer's specification. The calibration data for the pressure transducer are presented in Appendix B, Fig. B2.

### 3.9.6.4 Local pressure transducer calibration

Local pressure transducers were fitted to measure the difference between local liquid pressure and atmospheric pressure at six positions along the length of the test microchannels and in the channel entry and outlet plenums. Low-cost differential pressure transducers (Honeywell PCC26) were used with a measurement range of 0 – 1 bar. The sensors used an excitation voltage of 12 V and gave an output voltage ranging from 0 – 10 V. According to the manufacturer, the transducers are temperature compensated but it was found that a consistent calibration could not be obtained if the operating temperature varied. To ensure the transducers were kept at a constant environment temperature, they were mounted in a plastic enclosure held at a steady temperature of approximately 50°C by an internal 60 W light bulb controlled by a dimmer circuit.

The local pressure transducers were calibrated in situ on the test rig against the Druck differential pressure transducer (see Section 3.9.6.3) at high pressures and a water column manometer connected to the test loop for low pressures up to approximately 1200 mm H<sub>2</sub>O. The height difference between the Druck pressure transducer and local pressure transducers was approximately 100 mm. To compensate for this elevation difference a hydrostatic pressure correction of 0.98 kPa was subtracted from the pressures indicated by the Druck pressure transducer to refer these readings to the height of the local pressure transducers. Prior to calibration of the local pressure transducers, liquid (deionized water) was pumped through the test loop at high mass flow rate in order to flush any air from the system. Flushing of the local pressure transducer connections was achieved, one by one, by operating valves on purging pipes. After flushing, the pump was stopped to perform calibration of the transducers under zero flow conditions. Calibrations were conducted for both increasing and decreasing system pressures. The system pressure level was set by adjusting the saturation temperature at which water boils inside the mean reservoir. This was achieved by controlling the power input to the cartridge heater in the reservoir, using a West 6100 PID with a type K thermocouple immersed below the liquid surface in the reservoir as the feedback temperature sensor.

The results of the calibrations for the six local pressure transducers are given in Appendix B, Fig. B4. The standard deviations of the calibration data with respect to the calibration lines are presented in Table 3.7.

Table 3.7 Standard deviations of calibration data for the local pressure transducers.

Sensor	Increasing pressure		Decreasing pressure	
	$S(\text{kPa})$	$2S(\text{kPa})$	$S(\text{kPa})$	$2S(\text{kPa})$
$p_i$	0.09	0.18	0.09	0.18
$p_o$	0.10	0.20	0.09	0.18
$p_1$	0.08	0.16	0.09	0.18
$p_2$	0.09	0.18	0.09	0.18
$p_3$	0.08	0.16	0.09	0.18
$p_4$	0.09	0.18	0.09	0.18

Based on the standard deviations of the calibration data shown in Table 3.7, the uncertainty for the local pressure measurements is taken to be approximately  $\pm 0.2$  kPa. This value is used in the analysis propagated uncertainties in the results derived from the experimental measurements.

#### 3.9.6.5 Digital multimeter calibration

Digital multimeters (Black Star, model 3225 MP) were used to measure the alternating current and voltage of the supply to the cartridge heater inserted in the microchannel test section. These meters have five AC voltage and six AC current measuring ranges of 200 mV to 750 V and 200  $\mu$ A to 10 A respectively. In the manufacturer's specification the stated accuracy of this meter is given as 0.25% of the reading.

One of the multimeters was calibrated against a Fluke 5500A multi-function calibrator by Optical Test and Calibration Ltd and issued with a calibration certificate. The calibration was performed at an ambient temperature of 21°C and a relative humidity of 44%. The results of calibration checks covering all AC current and AC voltage measurement range of the instrument at 60 Hz are shown in Appendix B, Fig. B8. The standard deviation values obtained from the calibrations are  $\pm 0.01$  A for AC current and  $\pm 0.3$  V for AC voltage. The second multimeter had also been checked and found to be accurate.

### 3.10 Data reduction

Section 3.10.1 and 3.10.2 below present equations used for the experimental data for the single-phase and flow boiling tests respectively. The uncertainty analysis is based on the equations derived in Section 3.10.3. The method used for analysing the propagation of experimental uncertainties into the results is taken from Coleman and Steele (2009).

#### 3.10.1 Single-phase data reduction

For the single-phase flow and heat transfer tests, the variables to be determined are: (1) Pressure drop, friction factor and Poiseuille number, (2) Heat transfer coefficient and Nusselt number.

The experimental pressure drop in the test section is determined directly using the pressure sensor measurements for the inlet and outlet plenums,  $p_i$  and  $p_o$  respectively. Thus, the overall measured pressure drop in the test section between the inlet and outlet plenums,  $\Delta p_{meas}$ , is calculated using Eq. (3.2).

$$\Delta p_{meas} = p_i - p_o \quad (3.2)$$

As the test section is very short and there is no upstream calming section, the pressure losses that occur between the inlet plenum and inlet of the test channel must be taken into account when the channel pressure drops is determined. These losses result from 90 degree turn of the flow and the sudden contraction at the channel inlet. Similar flow feature losses occur at the outlet of the channel due to a 90 degree turn and a sudden enlargement. Therefore, the channel pressure drop due to wall friction and flow profile development in the channel,  $\Delta p_{ch}$ , is given by :

$$\Delta p_{ch} = \Delta p_{meas} - \Delta p_{loss} \quad (3.3)$$

Where  $\Delta p_{loss}$  is given by:

$$\Delta p_{loss} = \frac{1}{2} \rho \bar{V}_p^2 2K_{90} + \frac{1}{2} \rho \bar{V}_{ch}^2 (K_c + K_e) \quad (3.4)$$

It is assumed that the reversible pressure changes due to acceleration of the fluid at the channel inlet and deceleration of the fluid at the channel exit cancel each other. In Eq. (3.4)  $K_{90}$  is the loss coefficient associated with each of the 90 degree turns at the channel inlet and outlet and is approximated as 1.2, as recommended by Phillips (1987).  $\bar{V}_p$  and  $\bar{V}_{ch}$  are the mean velocities in the plenum and in the channel respectively.  $K_c$  and  $K_e$  are the inlet and exit loss coefficients for the sudden contraction at the channel inlet and the sudden enlargement at the channel exit. Their values are dependent on the ratio of channel cross sectional area to plenum cross sectional area,  $A_{ch}/A_p$ . They also depend on the channel cross section shape and the flow regime. The

values of  $K_c$  and  $K_e$  were estimated from the graphical information given for a square channel by Kays and London (1984).

The experimental Fanning friction factor,  $f_{ch}$ , was calculated using Eq. (3.5) and the experimental Poiseuille number, Po, using Eq. (3.6).

$$f_{ch} = \frac{\Delta p_{ch} D_h}{2L\rho\bar{V}_{ch}^2} \quad (3.5)$$

$$Po = f_{ch} Re \quad (3.6)$$

where  $L$  is the channel length,  $Re$  is the Reynolds number,  $Re = \rho\bar{V}_{ch}D_h / \mu$ , and  $\mu$  and  $\rho$  are the dynamic viscosity and density of the fluid respectively. The channel hydraulic diameter,  $D_h$ , is calculated as  $D_h = 2HW/(W+H)$ , where  $H$  and  $W$  represent the height and width of the rectangular cross-section channel respectively.

## 2. Heat transfer coefficient and Nusselt number

Calculation of the heat transfer coefficient requires the rate of heat removal by the fluid,  $q_{rem}$ , to be determined. This can be estimated as follows:

$$q_{rem} = P - q_{loss} = \dot{m}c_p(T_o - T_i) \quad (3.7)$$

where  $P$  represents the electrical heating power applied to the test section, given by the product of the voltage ( $V$ ) and the current ( $I$ ) supplied to the cartridge heater and  $q_{loss}$  is the rate of heat loss from the test section found as described in Section 3.8. The effective average to the fluid flowing through the channel is then calculated by applying Eq. (3.8) below:

$$q'' = \frac{q_{rem}}{A_{ht}} \quad (3.8)$$

where  $A_{ht} = (2H + W)L$  is taken as the heat transfer area of the channel. It is assumed that heat is transferred to the fluid through three of the channel walls only and the fourth wall is adiabatic. This assumption has also been used by other researchers, for instance Harms et al. (1999).

In the single-phase heat transfer tests, it was found that the measured wall temperature remained almost uniform along the channel; see Fig. 4.9 in Chapter 4. Assuming a constant wall temperature,  $T_w$ , the average heat transfer coefficient over the length of the channel,  $\bar{h}$ , see Incropera et al. (2006), is given by:

$$\bar{h} = \frac{q_{rem}}{A_{ht} \Delta T_{lm}} = \frac{q''}{\Delta T_{lm}} \quad (3.9)$$

where the logarithmic mean temperature difference,  $\Delta T_{lm}$ , is defined as

$$\Delta T_{lm} = \frac{T_o - T_i}{\ln\left(\frac{T_w - T_i}{T_w - T_o}\right)} \quad (3.10)$$

The corresponding average Nusselt number,  $\bar{Nu}$ , is then calculated as:

$$\bar{Nu} = \frac{\bar{h} D_h}{k_f} \quad (3.11)$$

Based on the assumptions of uniform wall temperature, the variation of the local bulk temperature of the water along the channel,  $T_f(z)$ , can be estimated from Eq. (3.12), Incropera et al. (2006):

$$T_f(z) = T_w - (T_w - T_i) \exp\left(\frac{-(2H + W)z \bar{h}}{\dot{m} c_p}\right) \quad (3.12)$$

where  $c_p$  is the specific heat,  $\dot{m}$  is the mass flow rate, and  $T_i$  and  $T_o$  are the inlet and outlet bulk temperatures of the fluid respectively.

For the single-phase experiments, the Thermophysical properties of water were evaluated at either the inlet temperature in the case of adiabatic test, or the arithmetic mean of the inlet and exit bulk temperatures, for the heat transfer tests.

### 3.10.2 Flow boiling data reduction

The parameters determined from the experimental data for the flow boiling experiments are the two-phase pressure drop, the local and average two-phase heat transfer coefficients, local values of the specific enthalpy and the thermodynamic vapour quality.

#### 1. Two-phase pressure drop

The flow entering the test section is maintained at a constant inlet temperature of 98°C, subcooled by approximately 7 K below the saturation temperature at the inlet pressure. Following Qu and Mudawar (2003), the heated channel is considered in two regions: (i) a subcooled region of length  $L_{sub}$  from the inlet up to the location where saturation is first achieved at zero thermodynamic quality, and (ii) a saturated region for the remainder of the channel length from  $L_{sub}$  to  $L$ . Bubble generation can start at low negative values of the thermodynamic quality in the subcooled region. Nevertheless, it is assumed that the pressure drop and heat transfer coefficient in the subcooled region can be determined using equations for single-phase flow; consequently, the local heat transfer coefficient in the subcooled region is calculated as

$$h(z) = \frac{q''}{T_w(z) - T_f(z)} \quad (3.13)$$

where  $T_w(z)$  is the local channel wall temperature, calculated using  $T_w(z) = T_{tc}(z) - q''t/k_{cu}$ ,  $T_{tc}(z)$  is the temperature measured by a thermocouple located a distance  $t$  below the channel and  $T_f(z)$  is the local liquid bulk temperature. It should be noted that for the flow boiling experiments the wall heat flux,  $q''$ , is assumed to be uniform along the channel, so that the increase in  $T_f$  is essentially linear with increasing  $z$  in the subcooled region.

However, prior to calculating the heat transfer coefficient in the subcooled region, the length of the subcooled region ( $L_{sub}$ ) should be known. The length of this region,  $L_{sub}$ , is determined using the energy balance, expressed by Eq. (3.14) and the pressure drop given by Eq. (3.15).

$$L_{sub} = \frac{\dot{m}c_p(T_{sat}(z_{sub}) - T_i)}{q''(2H + W)} \quad (3.14)$$

$$p_{sat}(z_{sub}) = p_i - \frac{2f_{app}G^2}{\rho_l D_h} L_{sub} \quad (3.15)$$

where  $p_i$  is the channel inlet pressure converted for the inlet pressure losses. To determine  $L_{sub}$ , an iteration procedure using Eq. (3.14) through (3.15) is necessary, as described in the following instruction sequence. First, insert a value of  $T_{sat}(z_{sub})$  in Eq. (3.14) to obtain  $L_{sub}$ . Then substitute  $L_{sub}$  into Eq. (3.15) to give  $p_{sat}(z_{sub})$ . Find  $T_{sat}$ , the saturation temperature corresponding to  $p_{sat}(z_{sub})$ , from the saturated water property tables or EES (Engineering Equation Solver) software. Continue this iteration procedure until the values of  $T_{sat}(z_{sub})$  and  $T_{sat}$  are within a predetermined closeness thereby providing converged values of  $L_{sub}$  and  $p_{sat}(z_{sub})$ . The apparent friction factor,  $f_{app}$ , used in Eq. (3.15) is calculated using Eq. (3.16), as proposed by Shah (1978) for hydrodynamically developing laminar flow:

$$f_{app} = \frac{3.44}{\text{Re}\sqrt{L_{sub}^*}} + \frac{(f_{FD} \text{Re}) + \frac{K(\infty)}{4L_{sub}^*} - 3.44/\sqrt{L_{sub}^*}}{\text{Re}(1 + C(L_{sub}^*)^{-2})} \quad (3.16)$$

where  $L_{sub}^* = L_{sub}/(\text{Re}D_h)$  and the fully developed Poiseuille number,  $f_{FD} \text{Re}$ , is a function of the channel aspect ratio,  $\beta$ , given by Shah and London (1978) as

$$(f_{FD} \text{Re}) = 24(1 - 1.3553\beta + 1.9467\beta^2 - 1.7012\beta^3 + 0.9564\beta^4 - 0.2537\beta^5) \quad (3.17)$$

For the three microchannel test sections used in this work, values of  $(f_{FD} Re)$ ,  $C$  and  $K(\infty)$  used in Eq. 3.16, are presented in Table 3.8.

Table 3.8 Values of Poiseuille number, constant  $C$  and the incremental pressure drop.

Test section	$(f_{FD} Re)$	$C$	$K(\infty)$
1	14.42	0.00029	1.41
2	16.48	0.00029	0.97
3	18.59	0.00008	0.97

Source: Shah and London (1978).

Once the length of the subcooled region,  $L_{sub}$ , has been found, the length of the saturated flow boiling region is given by Eq. (3.18).

$$L_{tp} = L - L_{sub} \quad (3.18)$$

The pressure in the saturated region is assumed to decrease linearly with distance  $z$ , as described by Eq. (3.19):

$$p_{sat}(z) = p_o + \frac{L - z}{L - L_{sub}} (p_{sat}(z_{sub}) - p_o) \quad (3.19)$$

The channel two-phase pressure drop in the saturated flow boiling region of the channel is:

$$\Delta p_{tp} = p_{sat}(z_{sub}) - p_o \quad (3.20)$$

## 2. Two-phase heat transfer

The local two-phase heat transfer coefficient in the saturated flow boiling,  $h_p(z)$ , is determined using Eq. (3.21) corresponding to the local pressure given by Eq. (3.19), which is used to represent the local temperature of the two-phase mixture. The average two-phase heat transfer coefficient in the saturation region,  $\bar{h}_p$ , is obtained by evaluating Eq. (3.22) using trapezoidal integration.

$$h_{tp}(z) = \frac{q''}{T_w(z) - T_{sat}(z)} \quad (3.21)$$

$$\bar{h}_{tp} = \frac{1}{L_{sat}} \int_{L_{sub}}^L h_{tp}(z) dz \quad (3.22)$$

The thermodynamic quality or vapour mass quality,  $x$ , is computed using Eq. (3.24) where the local specific enthalpy of the two-phase mixture is obtained from Eq. (3.23).

$$i(z) = i_i + \frac{q''(2H + W)z}{\dot{m}} \quad (3.23)$$

$$x(z) = \frac{i(z) - i_l(z)}{i_{lg}(z)} \quad (3.24)$$

where  $i_{lg}(z)$  is the local specific enthalpy for evaporation and  $i_i$  is the inlet liquid enthalpy.

### 3. Flow pattern map

For use in the construction of a flow pattern map, the superficial velocities of the liquid,  $J_l$ , and the gas,  $J_g$ , are determined using Eqs. (3.25) and (3.26).

$$J_g(z) = \frac{G x(z)}{\rho_g(z)} \quad (3.25)$$

$$J_l(z) = \frac{G(1-x(z))}{\rho_l(z)} \quad (3.26)$$

where  $\rho_g$  and  $\rho_l$  are the fluid densities for vapour and liquid, and  $G$  and  $x$  are the mass flux and thermodynamic quality respectively.

Experimental conditions and uncertainty analysis used in this project are provided in Appendix D.

### **3.11 Summary**

The pre-existing test facility was created and provided by Dr. Satees Gedupudi (research fellow) in 2008/2009. However, it was necessary to undertake certain modifications, e.g. pre-heaters, and test loop, to perform the research reported here. Three new test sections were made to overcome the problems encountered in using the previous test sections and have been tested for single-phase and two-phase flow boiling experiments. The test sections were made in 62 mm long copper blocks with hydraulic diameters of 0.438 mm, 0.561 mm and 0.635 mm. In addition all measurement sensors have been calibrated, and are considered to be of the required accuracy for measurement of all the variables involved, e.g. temperature, pressure, flow rate and heat flux. The experimental test rig can provide mass fluxes ranging from 278 to 51637 kg/m<sup>2</sup>s in single-phase flow experiments and 200 to 1100 kg/m<sup>2</sup>s in flow boiling experiments, the pre-heaters can provide fluid entry temperatures up to 100°C, and the test section heater, operated using AC variac 0 – 280 V, 0 - 5A, enables the planned flow boiling experiments to be performed. In general, the test rig is well able and ready to conduct the series of experiments necessary to achieve the objectives of the study.

## Chapter 4

### Single-phase flow: Experimental Results and Discussions

#### 4.1 Introduction

The aim in this chapter is mainly to present the experimental results for pressure drop (friction factor), Poiseuille number and heat transfer characteristics. The results are given in the form of graphs and tables so as to be easy to analyse them. It should be noted that the results presented here were obtained from experiments at an inlet temperature of 30°C and atmospheric pressure. The experiments were performed using three different hydraulic diameter channels. The test sections have been described thoroughly in chapter 3, they consisted of 0.438 mm, 0.561 mm and 0.635 mm hydraulic diameter channels. Comparisons of the experimental results with conventional theory and existing correlations for fully developed and developing friction factor such as correlations proposed by Shah and London (1978), Blasius, Dittus-Boelter, Gnielinski, Seider-Tate, Choi et al. (1991), and Bejan (2004) were conducted to see whether there is discrepancy with the theory.

The chapter is organized as follows: section 4.1 Introduction; section 4.2 Pressure drops; section 4.3 Single-phase heat transfer; section 4.4 Comparison with existing Nusselt number correlations; section 4.5 Repeatability of measurements; 4.6 Summary.

#### 4.2 Pressure drop

To ensure that the pressure transducers used for measuring the pressure drop functioned properly and accurately, the two pressure sensors (inlet and outlet) had previously been checked to measure the pressure drop of water flowing inside a stainless steel pipe with an inner diameter of 1.14 mm and outer diameter of 1.5 mm. The inner diameter was measured using a microscope TSER V-200 with an accuracy of  $\pm 1 \mu\text{m}$ . The length of the pipe was 200 mm (measured between the two locations of pressure transducers in the inlet and outlet). To provide a fully developed flow, the test section was extended 200 mm long before the inlet and after the outlet. Therefore, the test section could be used to perform experiments in two positions, namely inlet-outlet and by reversing the tube outlet-inlet. The positions of the pressure transducers could also be changed. The

results confirmed the accuracy and reliability of the pressure sensors because the experimentally derived laminar flow friction factors agreed with the classic theoretical relation  $f = 16\text{Re}^{-1}$ , as shown in Fig. 4.1. In turbulent flow, the experimental friction factors were slightly lower than predicted by the Blasius (2003)'s correlation for developing flow. However, taking the measurement uncertainty into account, it could be concluded that they were in reasonable agreement with the correlation.

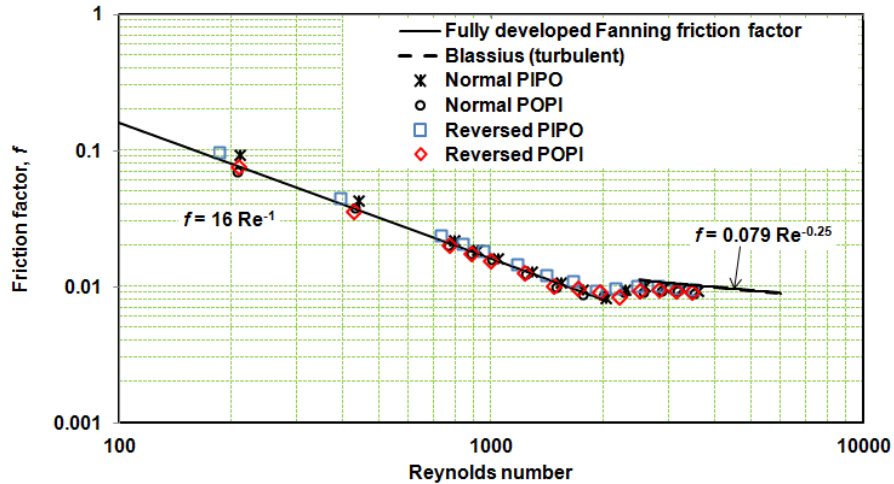


Figure 4.1 Experimental friction factors for fully developed flows in a stainless steel tube.

It has been mentioned that the position of the test section can be reversed. In Fig. 4.1, Normal PIPO refers to the usual test section position with the pressure transducers at their original positions. Normal POPI indicates that the test section is still at the usual position, but that the pressure transducer locations are changed. Reversed PIPO and POPI indicate that the test section has been turned round, with the inlet position becoming outlet and vice versa.

The pressure drop experiments to obtain friction factors and Poiseuille numbers have been performed with the experimental conditions and uncertainties as shown in Table 3.10 of Chapter 3. Also in Chapter 3 the dimensional uncertainties of the test sections have been described comprehensively. Pressure drops plotted in graphical form are for the channel only, which is excluding the inlet and outlet pressure losses, see Fig. 4.2. In order to obtain channel pressure drops, the following steps should be performed:

1. Calculate the pressure losses for 90 degree turns near the inlet and outlet locations.
2. Calculate the pressure losses for the sudden contraction and enlargement at the inlet and outlet locations.
3. Determine the channel pressure drop by subtracting the pressure losses in steps 1 and 2 from the total measured pressure drops, as in Eq. (3.2) and (3.3).

For steps 1 and 2 the loss coefficients  $K_c$  and  $K_e$  are dependent on the area ratio,  $A_r = A_{ch}/A_p$ , (channel cross sectional area ( $WH$ ) /plenum cross sectional area ( $\pi/4D^2$ )). They can be obtained from Kays and London (1984) by interpolating the data based on the aspect ratio. The values of  $K_c$  and  $K_e$  are given in Table 4.1 for all test sections.

Table 4.1  $K_c$  and  $K_e$  values for the three test sections.

Test section	$K_c$		$K_e$	
	Laminar	Turbulent	Laminar	Turbulent
1	1.10	0.75	0.96	0.98
2	0.95	0.61	0.79	0.83
3	0.88	0.54	0.59	0.66

The effect of mass flux on the pressure drop is very clear from Fig. 4.2 (a), where the pressure drop consistently increases with the Reynolds number. This is because the pressure drop varies with velocity which is equal to the mass flow rate divided by the cross sectional area and fluid density.

The effect of hydraulic diameter on the pressure drop is one of the objectives in this study; therefore, Fig. 4.2(b) presents a comparison of pressure drops for all three test sections at the same inlet temperature of 30°C. From the figure it is clear that as the hydraulic diameter decreases, the pressure drop increases. This is due to the fact that the pressure drop varies inversely with the channel diameter, see Eq. (4.1). At the same Reynolds number, for test section one ( $D_h = 0.438$  mm) the pressure drop is at the highest value and reduces for test section two ( $D_h = 0.561$  mm) and further for three ( $D_h = 0.635$  mm).

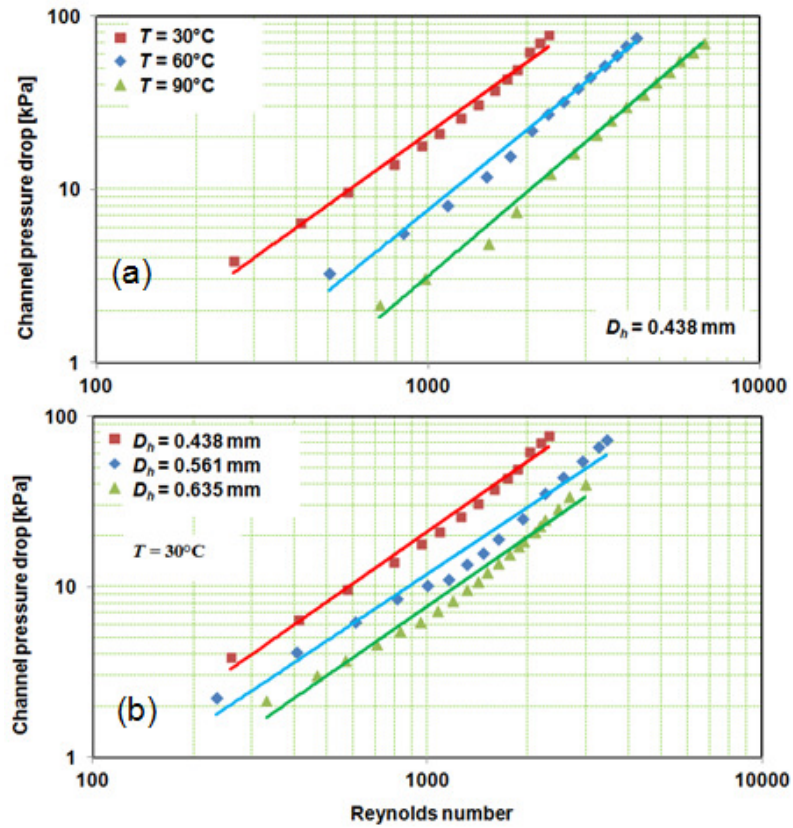


Figure 4.2 Channel pressure drops: (a) effect of inlet temperature and (b) effect of hydraulic diameter.

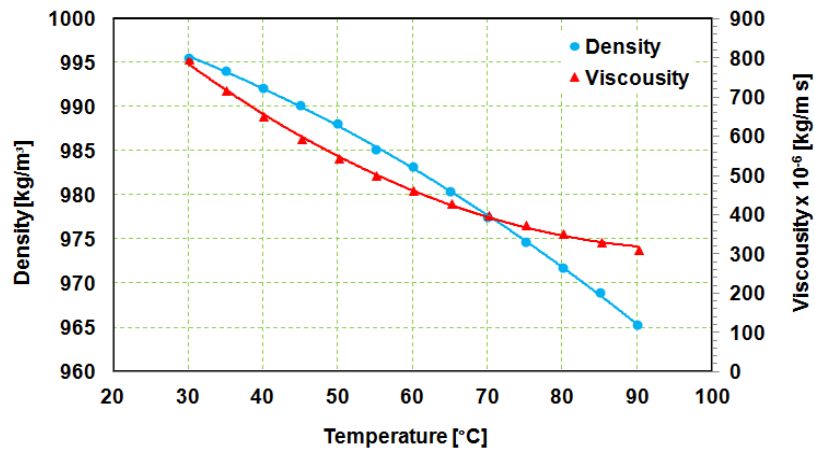


Figure 4.3 Effect of temperature on water property, density and viscosity obtained using EES software at saturation conditions.

$$\Delta p_{ch} = \frac{2f_{ch}L\rho\bar{V}_{ch}^2}{D_h} \quad (4.1)$$

In addition, as shown in Fig. 4.2 (a), the temperature clearly affects the pressure drop, which decreases with an increase in inlet temperature. For a given Reynolds number, the pressure drop for flow at an inlet temperature of 30°C is higher than those at 60°C and 90°C. This behaviour is common to all test sections and this was due to the change in fluid properties with temperature, e.g. density and viscosity. The liquid density and viscosity were obtained using EES. The decrease in density and viscosity with an increase in temperature from 30°C to 60°C was 1.28% and 42% respectively. For a further increase to 90°C, the density and viscosity decreased by 1.83% and 33%. Fig. 4.3 shows that as the temperature increases, the density and viscosity decrease, hence the pressure drop decreases too. For an increase in temperature from 30°C to 60°C, the pressure drop is reduced by 55% (for  $D_h = 0.438$  mm), 61% (for  $D_h = 0.561$  mm) and 66% (for  $D_h = 0.635$  mm). A further increase from 60°C to 90°C decreases the pressure drop by 65% (for  $D_h = 0.438$  mm), 67% (for  $D_h = 0.561$  mm) and 61% (for  $D_h = 0.635$  mm).

The effects of inlet temperature and hydraulic diameter on pressure drop are combined in tabular form in Table 4.2. First column is the inlet temperature values of 30°C, 60°C and 90°C. For each of these, second and third columns give the percentage changes in hydraulic diameter using Eq. (4.2) and (4.3) respectively.

$$\frac{D_{h,3} - D_{h,2}}{D_{h,3}} \times 100 \% \quad (4.2)$$

$$\frac{D_{h,2} - D_{h,1}}{D_{h,2}} \times 100 \% \quad (4.3)$$

The corresponding pressure drop data in columns 4 and 5 were calculated using

$$\frac{\Delta p_{\text{test section 2}} - \Delta p_{\text{test section 3}}}{\Delta p_{\text{test section 3}}} \times 100 \% \quad (4.4)$$

$$\frac{\Delta p_{\text{test section 1}} - \Delta p_{\text{test section 2}}}{\Delta p_{\text{test section 2}}} \times 100\% \quad (4.5)$$

Table 4.2 Effect of hydraulic diameter on pressure drop.

Inlet temperature [°C]	Decrease in hydraulic diameter [%] From 0.635 mm to 0.561 mm and from 0.561 mm to 0.438 mm		Increase in pressure drops [%]	
	30	12	22	35
60	12	22	52	113
90	12	22	18	140

In contrast to the pressure drop, the friction factor seems not to be affected by the inlet temperature. This contradicts the findings of Urbanek et al. (1993) and Toh et al. (2002), who used water as the working fluid. In the experimental investigation of Urbanek et al. (1993) the water temperature in the chamber was varied from 0 to 85°C. For their 12 μm channel, they found that the Poiseuille number increased with fluid temperature by as much as 25% of the theoretical value. Toh et al. (2002) made a numerical study of the effect of fluid temperature on the Nusselt number and friction factor. With a fixed inlet temperature of 20°C, variation in fluid temperatures was achieved by heating the test section. They found that as the temperature increased, especially at low mass flow rates, the Poiseuille number decreased. Shen et al. (2006) investigated temperature effects on pressure drop by varying the inlet temperatures of 30, 50 and 70°C with heating of the test section. In the current study, particularly for adiabatic pressure drop experiments, the fluid temperature variation was achieved by using inlet temperatures of 30, 60 and 90°C. Results presented here confirm those obtained by Shen et al. (2006), in that with higher fluid temperatures the pressure drop decreases. However, they did not report the effect of fluid temperature on friction factor, but they found higher friction factor values than predicted by theory. These were attributed to the higher relative surface roughness of 4 – 6%, compared with this study, in which the test section relative surface roughness was only 0.15 – 0.23%.

To obtain experimental friction factors and Poiseuille numbers it is necessary to apply Eq. (3.5) and (3.6) where the channel pressure drop,  $\Delta p_{ch}$ , can be determined firstly and the mean velocity of flow,  $\bar{v}_{ch}$ , can be replaced by  $\dot{m} / \rho A_c$ . As shown in Fig. 4.4, for any given test section the friction factors are nearly the same for all three inlet temperatures. However, the aspect ratio does appear to affect the friction factor, in terms of a noticeable decrease. For test sections one, two and three respectively, the aspect ratios were 0.78, 0.39 and 0.23 and the friction factor data were close to the lines  $f = 1442\text{Re}^{-1}$ ,  $f = 1648\text{Re}^{-1}$ , and  $f = 1859\text{Re}^{-1}$  respectively. Those lines are calculated using Eq. (3.18) in Chapter three for developing laminar flow. However, these results infer a distinguishable effect; it should be investigated further because when the aspect ratios were changed, the hydraulic diameters also changed. Hence, it is difficult to identify the effect of aspect ratio. In turbulent flow, the experimental friction factor is compared with the developing turbulent flow theory due to Phillips (1987), see Eq. (4.6) and Blasius correlation, see Hager (2003), Eq. (4.8).

$$f_{app} = \left( 0.0929 + \frac{1.01612}{L/D_h} \right) \text{Re}^{* \left( -0.268 \frac{0.3293}{L/D_h} \right)} \quad (4.6)$$

$$\text{Re}^* = \text{Re} \left( 2/3 + \frac{11}{24} \beta (2 - \beta) \right) \quad (4.7)$$

$$f = 0.079 \text{Re}^{-0.25} \quad (4.8)$$

where  $\text{Re}^*$  is the equivalent Reynolds number,  $\beta$  aspect ratio and  $f_{app}$  apparent friction factor.

Conversely, as shown in Fig. 4.5, for any given inlet temperature the friction factors for the three hydraulic diameters are almost the same. From this, it may be concluded that the effect of hydraulic diameter and the aspect ratio on the friction factor are not significant. Furthermore, the experimental friction factors reported here are in reasonable agreement with developing flow theory as proposed by Shah (1978), and given by Eq. (3.18). This means that conventional theory is still applicable for single-

phase flow in these particular microchannels and at these experimental boundary conditions.

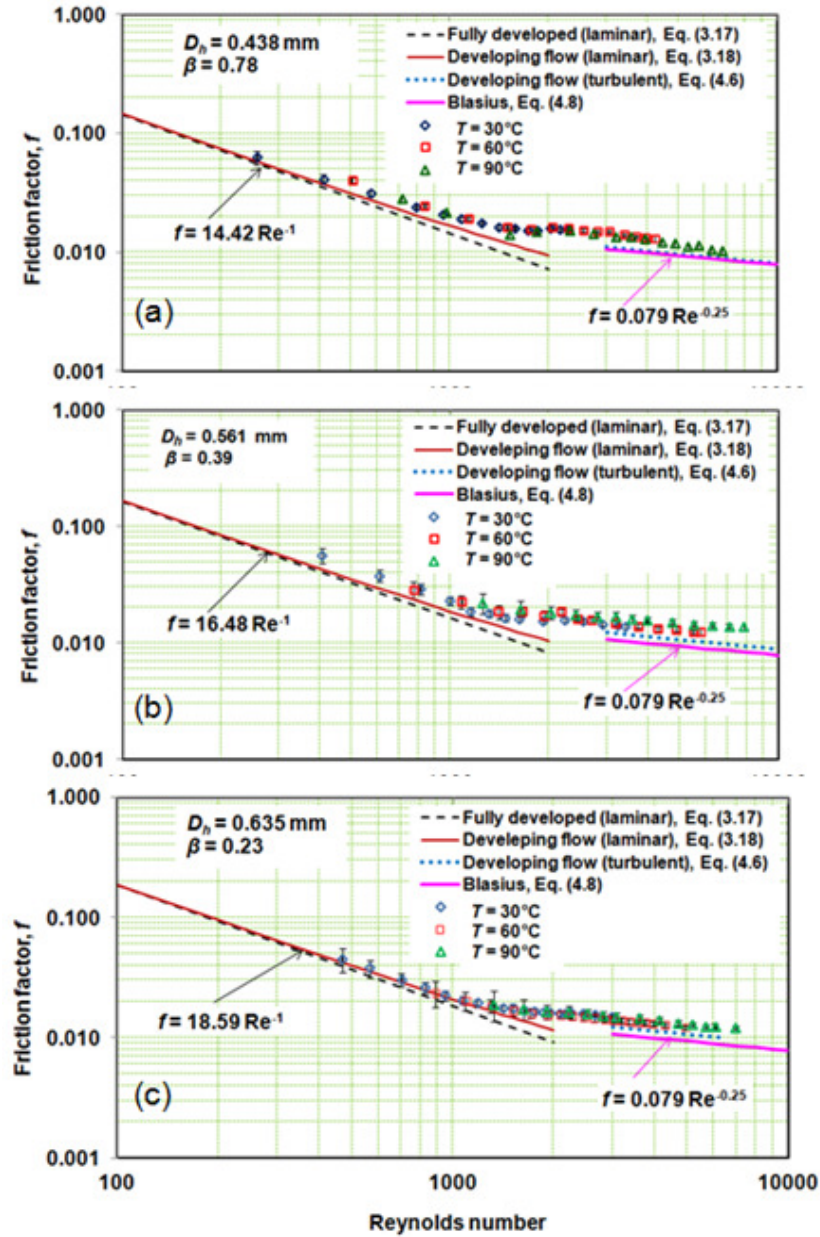


Figure 4.4 Effect of inlet temperature on friction factor: (a) test section one, (b) test section two, (c) test section three.

From Fig. 4.5, all experimental friction factors, irrespective of test section and inlet temperature, can be predicted from a trial-and-error simple correlation given by:

$$f = 1255\text{Re}^{-0.92} \quad (4.9)$$

Equation (4.9) is only applicable to microchannels with hydraulic diameters ranging from 0.438 mm to 0.635 mm, aspect ratios ranging from 0.23 to 0.78 and 62 mm long, and is only for laminar developing flows with water as the working fluid. Using mean absolute error (MAE) as defined by Eq. (4.10), Eq. (4.9) can predict the experimental friction factor data in laminar regimes with a MAE of 9.4 – 13.5%.

$$\text{MAE} = \frac{1}{N} \sum_{j=1}^N \frac{|f_{pred,j} - f_{exp,j}|}{f_{exp,j}} \times 100\% \quad (4.10)$$

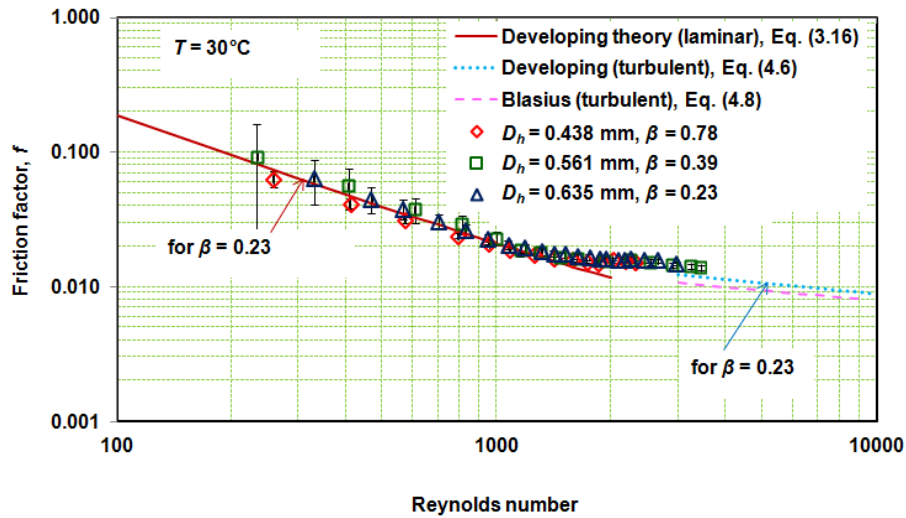


Figure 4.5 Effect of hydraulic diameter on the friction factor at the same inlet temperature of  $30^\circ\text{C}$ .

From Fig. 4.4 and 4.5, there is an indication that the flow departs from the laminar regime at a Reynolds number between 1000 and 2000, which is earlier than the theory. This is probably due to the effect of entrance length (developing region) and the sharp entrance. The sharp entrance produces flow disturbance facilitating the onset of turbulence. Similarly, at the macroscale, a sharp entrance causes turbulent flow to be achieved earlier. Another aspect of the turbulence inducing entrance effect is that the developing flow velocity profile is closely similar to that for turbulent flow. Evidence

for the flow being affected by the hydrodynamically developing flow region is presented in Table 4.3. This presents calculated entrance lengths at an inlet temperature of 30°C for the three test sections using the following equation proposed by Shah and London (1978),

$$L_{ehd} = L_e^* \text{Re} D_h \quad (4.11)$$

where  $L_{edh}$  is the hydrodynamic entrance length and  $L_e^*$  the dimensionless entrance length which depends on the aspect ratio. The information can be found in Table 50, page 217, Chapter VII of Shah and London (1978). The dimensionless entrance lengths relevant to test sections one, two and three respectively have the following values based on their respective hydraulic diameters: 0.044 for  $D_h$  of 0.438 mm ( $\beta = 0.78$ ), 0.051 for  $D_h$  of 0.561 mm ( $\beta = 0.39$ ), and 0.05 for  $D_h$  of 0.635 mm ( $\beta = 0.23$ ), that is, for test sections one, two and three respectively.

Table 4.3 also shows an entrance length effect at all Reynolds numbers. The effect is clear even at lower Reynolds numbers. For example, for a  $D_h$  value of 0.438 mm, at Reynolds numbers of 258, 1079 and 2016, the entrance lengths are respectively 4.97 mm (8% of channel length), 20.8 mm (33.5% of channel length) and 38.9 mm (62.4% of channel length).

Tabel 4.3 Calculated hydrodynamically entrance length for laminar flow.

$D_h = 0.438 \text{ mm}$		$D_h = 0.561 \text{ mm}$		$D_h = 0.635 \text{ mm}$	
Re	$L_{edh}$	Re	$L_{edh}$	Re	$L_{edh}$
258	4.97	233	6.68	330	10.49
411	7.92	406	11.63	467	14.84
573	11.04	608	17.40	566	17.97
789	15.21	809	23.16	702	22.29
951	18.34	999	28.59	826	26.22
1079	20.80	1153	33.01	949	30.15
1252	24.15	1308	37.43	1071	34.00
1408	27.15	1467	41.99	1185	37.62
1578	30.44	1625	46.50	1312	41.68

1721	33.18	1924	55.06	1411	44.81
1846	35.58			1509	47.92
2016	38.87			1631	51.79
				1751	55.60
				1865	59.21
				1941	61.64

A set of experimental Poiseuille number results obtained using test section three ( $D_h = 0.635$  mm) is presented in Fig. 4.6. For turbulent flow the values are slightly higher than the Blasius correlation, but in the laminar regime, they are in reasonable agreement with macroscale theory, Eq. (3.18). The small shifts from the lines of conventional theory of results for Poiseuille numbers here, and for friction factors as previously shown, might be due to the pressure tapping holes. The pressure tapping holes may give an additional restriction to the fluid as the holes can create a local turbulence. Therefore, the friction factor becomes slightly higher than the prediction.

Pressure distribution along the 0.438 mm test section at several Reynolds numbers are presented in Fig. 4.7 for an inlet temperature of 30°C. The marked decrease in pressure between the inlet plenum and  $z/L = 0.2$  includes contributions due to flow area change and the losses associated with the 90° turn and sudden contraction at channel inlet, besides the pressure drop due to wall shear stress and flow development. Similarly, the pressure change between  $z/L = 0.8$  and the outlet plenum includes the additional losses due to flow area change and at channel exit.

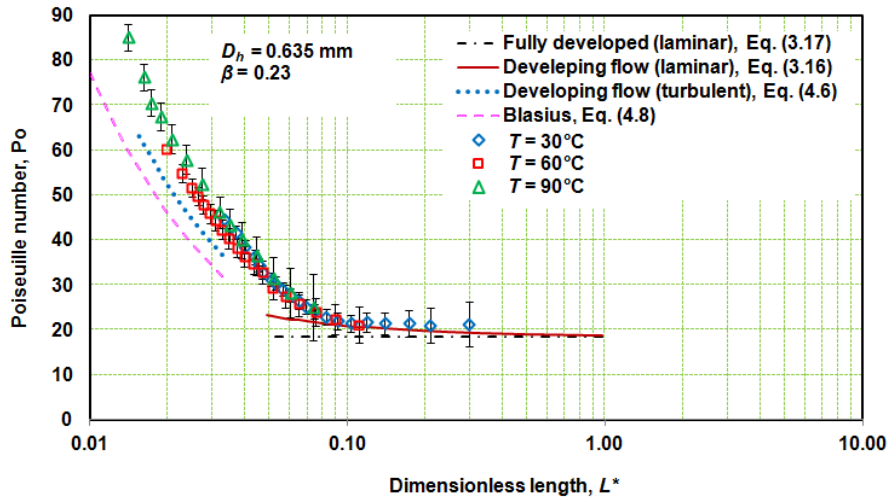


Figure 4.6 Effect of inlet temperature on the Poiseuille number for the 0.635 mm channel.

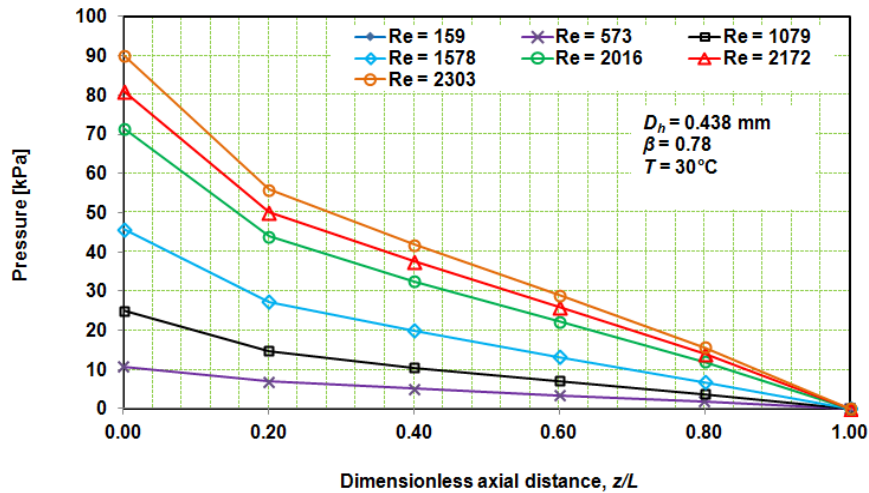


Figure 4.7 Pressure distributions along the channel at inlet temperature of 30°C for the 0.438 mm channel.

It should be noted that in Fig. 4.7, the pressure at position  $z/L = 0$  is the measured inlet pressure where the measurement was taken in the inlet header, whilst pressure at position  $z/L = 0.2$  was the pressure indicated by pressure sensor one at the distance of approximately 12.4 mm from the inlet. Therefore, the line decreases sharply from position zero to 0.2. From the figure, it can be seen that as the mass flux was increased the line of pressure distribution decreased sharper from inlet toward the outlet. It indicates that the pressure drop is proportional to  $G^2$ , the same behaviour as that of macroscale.

### 4.3 Single-phase heat transfer

This subsection presents the experimental data for single-phase heat transfer characteristics, the Nusselt number and comparisons of the data with existing conventional correlations. All heat transfer results are presented in classical graphical form, namely, ‘heat transfer coefficient versus Reynolds number’ and ‘Nusselt number versus Reynolds number’. Also, data obtained by Hamrs et al. (1999) are compared with these current results.

#### 4.3.1 Heat removal and heat loss

Before presenting the experimental results, it is worth discussing the heat removal and the heat losses. The heat removed by the fluid equals the heat input to the channel minus the heat lost to ambient. This is given as Eq. (3.7) in Chapter 3 with an example of heat removal and heat loss calculated from the experimental data being presented in Fig. 4.8 for the 0.635 mm channel.

The average difference between input power and heat removal does not exceed 10% of the former. In addition, heat removal for a range of input power is more or less independent of the Reynolds number, since the heat removal remains almost constant as the Reynolds number increases, see Fig. 4.8. This finding is important in estimating the average heat loss in order to calculate accurately the heat flux.

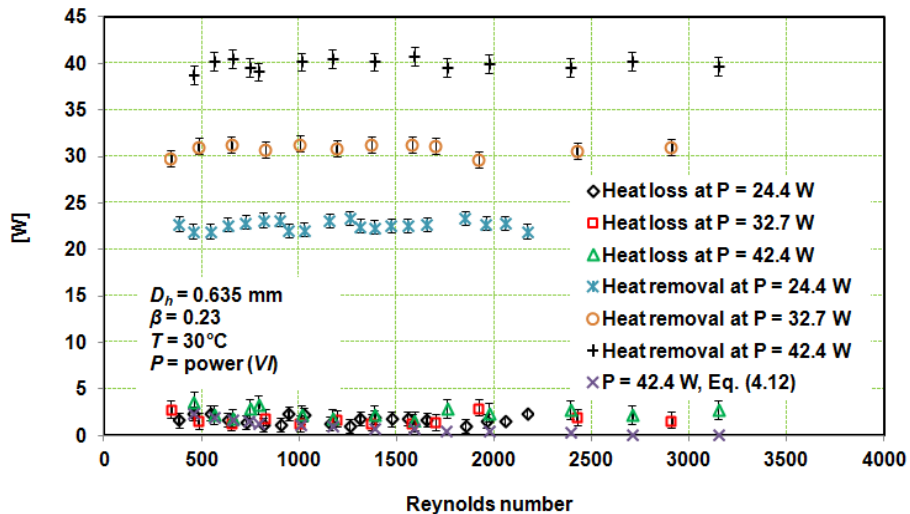


Figure 4.8 Heat removal and heat loss versus Reynolds number at several values of power for the 0.635 mm channel test section.

As discussed in section 3.8, the average heat loss is approximately 6.8%, see also Fig. 4.8. However, heat losses determined directly from single-phase experiments have more scatter than from using an equation based on wall and ambient temperatures ( $T_{ma}$ ), see Eq. (4.12). This is due to the propagated error having contributory errors from three variables (heat input, temperature and mass flow rate). Nevertheless, the above estimation of heat loss of 6.8% of input power will be used for all experiments whether for single-phase flow or for flow boiling.

$$q_{loss} = 0.0508 \dot{Q}_{ma} - 0.6364 \quad (4.12)$$

How to obtain Equation (4.12) was described thoroughly in Chapter three in subsection 3.8.

#### 4.3.2 Wall and fluid temperature distribution

The wall temperature distribution is important because it is used to identify the method of estimating the heat transfer coefficient and then the Nusselt number. If the wall temperature is uniform along the test section, the UWT (Uniform Wall Temperature) method is used; otherwise the UWH (Uniform Wall Heat flux) method is used. Measurements of wall temperature distribution and calculated fluid temperatures are presented in Fig. 4.9 for the three test sections for a range of Reynolds numbers. When the mass flow rate is low, the wall temperature distribution shows a slightly linear increment along the channel; whilst at high mass flow rates the wall temperature is constant. This is probably due to the high thermal conductivity, and large thermal mass of channel copper block and inlet-outlet headers machined into the same copper block as the channel slot. This finding is similar to that of Qu and Mudawar (2002), whose wall temperature gradient at a low Reynolds number was larger than at a high Reynolds number.

However, the gradient of wall temperature was higher than in this work, because the inlet-outlet headers were in different material to the channel. In contrast, Tiselj et al. (2004) found that the wall and water temperature distributions increased sharply, then peaked just after the middle of the test section, and decreased thereafter toward the outlet. Their parabolic curves of wall and water temperature distributions could be due

to the combination of the test section having a low thermal conductivity (of 149 W/m K being made of silicon wafer) and small thermal mass as well as heat losses.

For purposes of determining the data as presented in Fig. 4.9, the heat transfer coefficient for single-phase flow is calculated using the UWT method rather than UWH and the local fluid temperature can be obtained using Eq. (3.12) in Chapter 3.

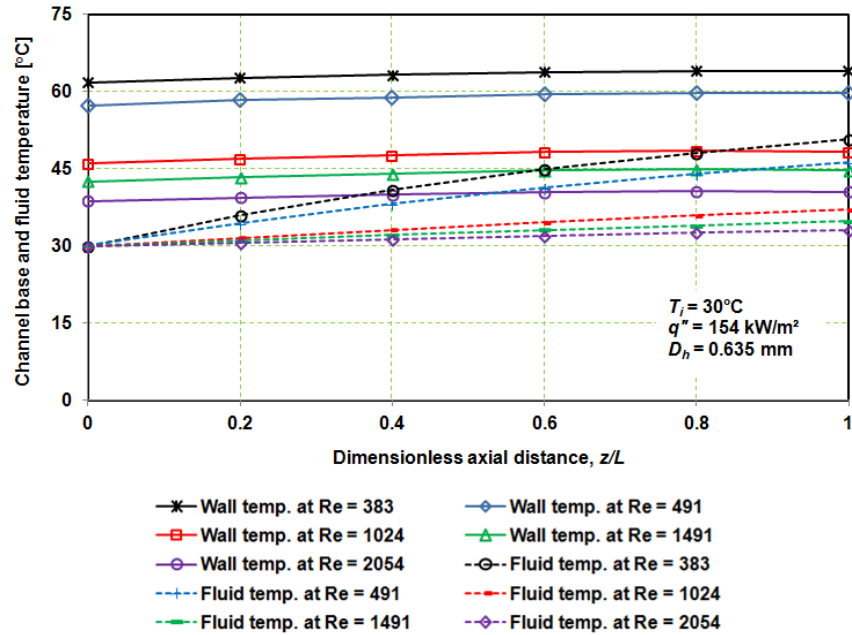


Figure 4.9 Variation of channel wall and fluid temperatures with distance from the entry in single-phase flow for the 0.635 mm channel at a heat flux of 154 kW/m<sup>2</sup>. Note: wall temperatures are at the thermocouple locations.

### 4.3.3 Heat transfer coefficient and the Nusselt number

As mentioned in the above subsection, the method used for predicting the heat transfer coefficient is UWT, therefore the average heat transfer coefficient can be directly determined using Eq. (3.9). The distance between the thermocouple locations and the base of the channel is  $t$  (1.11 mm), therefore, the local wall temperature should be corrected using Eq. (4.13)

$$T_w(z) = T_c(z) - q''t/k_{cu} \quad (4.13)$$

where  $T_c(z)$  is the local temperature at a thermocouple location,  $k_{cu}$  the thermal conductivity of the channel material (copper) and  $z$  the measured distance of the thermocouple from channel inlet. Note that  $T_w$  in Eq. (3.10) and (3.12) is an average of  $T_w(z)$ .

Fig. 4.10 shows how the estimated average heat transfer coefficient varies with Reynolds numbers over a range of heat fluxes for the 0.635 mm channel. In the laminar regime, the heat transfer coefficient is not constant but increases with Reynolds numbers. However, it may not mean that the heat transfer trend in microchannels differs from that in macrochannels, because in the current research, the test sections were not equipped with a calming section. Hence, the heat transfer process here is categorised as thermally developing heat transfer. This is evidenced by the fluid flow field being completely or partially within the developing region, as shown in Table 4.4 for all test sections. The thermally developing entrance length is calculated using the equation proposed by Shah and London (1978) and given by

$$L_{eth} = L_e * Re D_h Pr \quad (4.14)$$

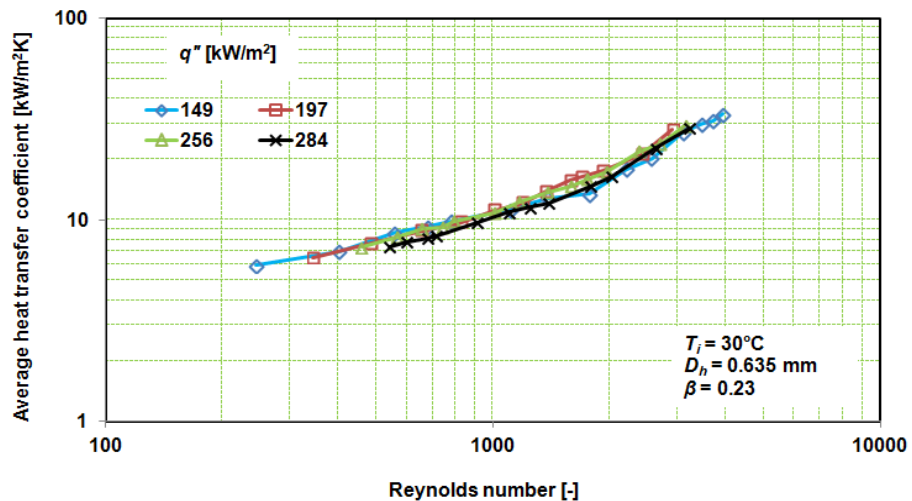


Figure 4.10 Variation of heat transfer coefficient with Reynolds number for the 0.635 mm channel, and for a range of heat fluxes.

It should be noted that the  $L_e^*$  in Eq. (4.14) is the dimensionless entrance length which has also been used in Eq. (4.11). Furthermore, Shah and London (1978) solved the thermally developing heat transfer problem analytically and their trend of Nusselt number was similar to that in this work. Also, this phenomenon has been analysed and described thoroughly by Incropera et al. (2006), Fig. 8.10 on page 512, Chapter 8, but for the macroscale. They found that the Nusselt number followed a trend with a length-dependent variable, namely the square root of dimensionless length, firstly decreasing as the variable increased in the developing region and then becoming constant after the flow reached full development. Thus, the heat transfer behaviour at the microscale of this study is consistent with the heat transfer trend for thermally developing flow described by Incropera et al. (2006) at the macroscale.

From Table 4.4, it should be noted that the entrance length covers completely or partially the channel length at every Reynolds number. Hence, it may be concluded that the entrance length effect creates the dependence of Nusselt number on Reynolds number in the laminar regime.

Table 4.4 Calculated thermal entrance length for all test sections, for a range of Reynolds numbers and at almost the same heat flux (197 kW/m<sup>2</sup> to 206 kW/m<sup>2</sup>).

$D_h = 0.438$ [mm] $q'' = 206$ [kW/m <sup>2</sup> ]			$D_h = 0.561$ [mm] $q'' = 197$ [kW/m <sup>2</sup> ]			$D_h = 0.635$ [mm] $q'' = 197$ [kW/m <sup>2</sup> ]		
Re	Pr	$L_{eth}$ [mm]	Re	Pr	$L_{eth}$ [mm]	Re	Pr	$L_{eth}$ [mm]
722	4.2	58.35	468	3.9	52.23	358	3.7	42.30
1110	4.6	98.91	761	4.4	96.53	535	4.2	71.13
1478	4.8	135.73	1099	4.7	149.19	701	4.5	100.00
1668	4.8	154.72	1399	4.9	196.32	901	4.7	133.04
1859	4.8	173.21	1531	5.0	217.31	996	4.7	149.50
2232	5.0	216.65	1725	5.0	244.42	1198	4.8	182.73
						1395	4.9	215.72
						1559	4.9	242.80
						1755	4.9	275.55
						1881	5.0	298.96

Other effects on the heat transfer coefficient are those of heat flux and hydraulic diameter. The influence of heat flux is not clear, some data being lower, but the rest of the data higher, for lower heat fluxes. However, the effect of hydraulic diameter is significant, an additional feature evident in Fig. 4.11 which shows the variation of heat transfer coefficient with Reynolds number. In particular, at almost the same heat flux, the heat transfer coefficients for the 0.438 mm channel are higher than those for the two other channels.

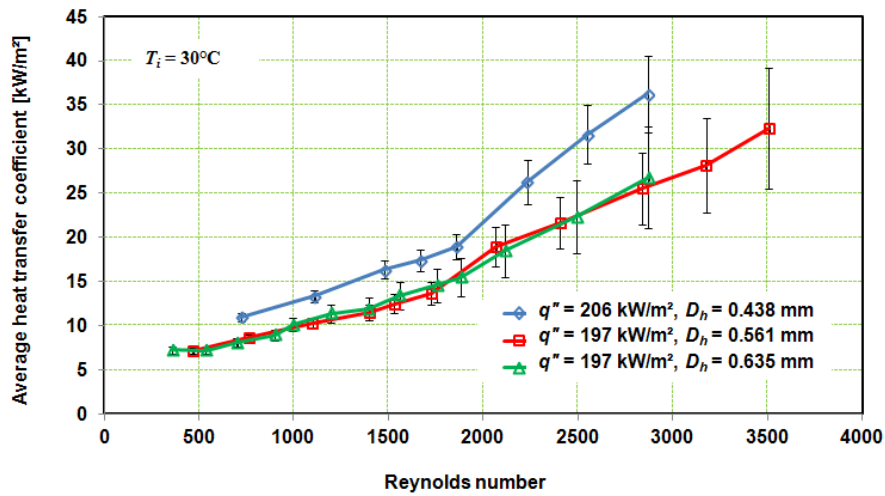


Figure 4.11 Variation of heat transfer coefficient with Reynolds number for almost constant heat flux and 30°C inlet temperature.

The effect of hydraulic diameter on the heat transfer coefficient is clear; however, it becomes insignificant or collapses when the heat transfer is converted into the dimensionless Nusselt number given in Fig.4.12 for the same measurement data. This may need further investigation by using, for instance, large differences in hydraulic diameter. Fig. 4.12 shows that the experimental data are slightly lower than those obtained by Harms et al. (1999). This is probably due to the heated side walls. Harms et al. (1999) used a very deep channel, meaning that the heated area compared to the perimeter area was larger than in this work.

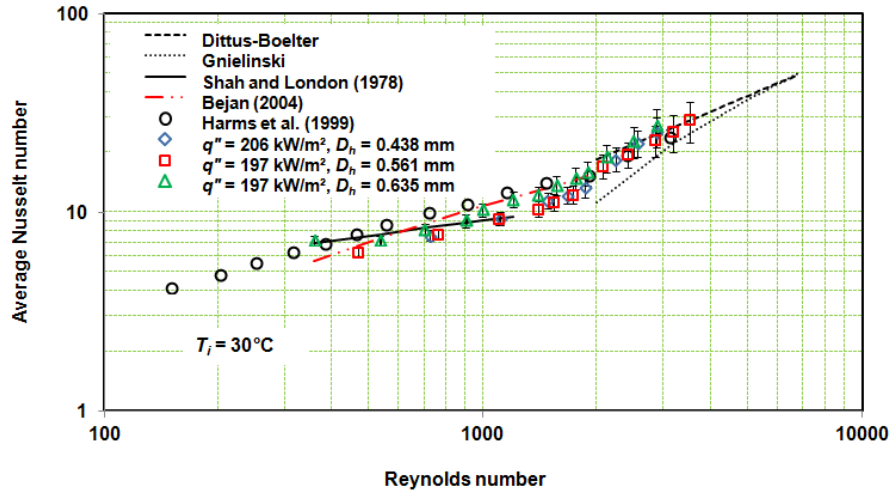


Figure 4.12 Variation of Nusselt number with Reynolds numbers at almost constant heat flux and inlet temperature of 30°C and comparisons with conventional correlations and results obtained by Harms et al. (1999).

From the primary presentation of data in Figs 4.11 and 4.12 both the heat transfer coefficient and the Nusselt number increase with Reynolds number. The same trend was also found by Bejan (2004) who proposed a correlation for flow in the entrance region for non-circular conduits as

$$\text{Nu} = C' \left( \frac{L}{\text{Re} D_h \text{Pr}} \right)^{-0.5} \quad (4.15)$$

From the figure, it can be seen that macroscale correlations such as Dittus-Boelter, Gnielinski, Shah and London (1978) and Bejan (2004) are able to predict the experimental Nusselt number reasonably well. However, the comparison of the data with the correlations will be explained in detail in the next subsection.

#### 4.4 Comparison with existing Nusselt number correlations

As there are still many contradictory published results, it is worth presenting comparisons of the experimental data with published Nusselt number correlations. Six macroscale correlations have been selected; however, the majority correlations are for circular conduits. Whilst the prediction of Shah and London (1978) was proposed for

rectangular channels and the correlation of Bejan (2004) was applicable for the developing regions of non-circular ducts.

The experimental data consist of 579 data points obtained from the three test sections. The Dittus – Boelter correlation can predict the experimental Nusselt numbers with a MAE of 7.4% but the correlation is for turbulent flow only. Hence, only 105 data points (18.13% of the total data points) are predicted, namely those for Reynolds numbers of 2500 and above. The Gnielinski correlation is for both turbulent and transitional flow regimes, and is therefore used to predict the experimental data for Reynolds numbers of 1500 and above. A Reynolds number of 1500 is attributed to the transitional regime because in this work, flow seems to depart from the laminar regime at Reynolds numbers between 1000 and 2000. Therefore, the Gnielinski correlation was able to predict 293 points (51% of the total data points) with an underestimated MAE of 31%. By contrast the Sieder – Tate correlation is for developing flow and all regimes, so was used to predict the whole set of experimental data. The overestimated MAE was 103%. The correlations proposed by Choi et al. (1991) also covered all flows, with the laminar correlation given in Eq. (4.16) and the turbulent correlation shown in Eq. (4.17).

$$\text{Nu} = 0.00097 \text{ Re}^{1.17} \text{ Pr}^{1/3} \quad (4.16)$$

$$\text{Nu} = 3.82 \times 10^{-6} \text{ Re}^{1.96} \text{ Pr}^{1/3} \quad (4.17)$$

All data were therefore predicted with a MAE of 48%. In laminar flow the correlation underestimates the experimental data whilst in turbulent flow; it is quite close to the data. Shah and London (1978), in Table 52 page 220 Chapter VII, tabulated their data in the form of Nusselt numbers for rectangular ducts in the laminar developing region and for uniform wall temperature. Since their data were given as a function of the inverse dimensionless length, they could be re-expressed and correlated as a function of dimensionless length.

However, the data in Table 52 were for the Prandtl number of 0.72 and also depended on the aspect ratio. The data for an aspect ratio of 0.78 could be achieved by interpolating the aspect ratio data and expressed as

$$\text{Nu}=1.335(L^*)^{-0.36} \text{ for } L^* < 0.02 \quad (4.18)$$

$$\text{Nu}=4.017(L^*)^{-0.21} \text{ for } L^* \geq 0.02 \quad (4.19)$$

with a standard deviation of  $\pm 0.13$  (95% confidence level). Corresponding equations for the other aspect ratios of 0.39 and 0.23 were formulated with a standard deviation of  $\pm 0.15$  (for both). All the correlations of Shah and London were able to predict 83% of the total data points with a MAE of 29%. The last correlation was that of Bejan (2004) for non-circular ducts and laminar developing regions. The correlation is given in Eq. (4.15), where  $C'$  is a constant, e.g. 1.375. The correlation could make predictions for 83% of the total experimental data points with a MAE of 17%.

Taking Fig.4.13 as a whole, from the above comparisons, it can be concluded that conventional correlations such as Dittus-Boelter's correlation, Shah and London (1978)'s correlation and Gnielinski's correlation are still applicable for microchannels for the ranges of experimental conditions tested in the current research. As part of this study new correlations based on experimental data have been formulated for (a) developing laminar flow and (b) developing turbulent flow. The first correlation covers laminar flow Reynolds numbers ranging from 244 to 1998 and Prandtl numbers from 3 to 5. The test section diameters used for creating this statistical correlation were 0.438 mm, 0.561 mm and 0.635 mm. The new equation can predict the laminar flow data with a MAE of 7.8% and within 30% error bars, as shown in Fig. 4.14 (a) and is given by

$$\text{Nu}=\text{Re}^{0.283}\text{Pr}^{-0.513}L^{*-0.309} \quad (4.20)$$

Equation (4.20) indicates that in laminar flow the Nusselt number depends on the Reynolds number as explained in the previous sub section.

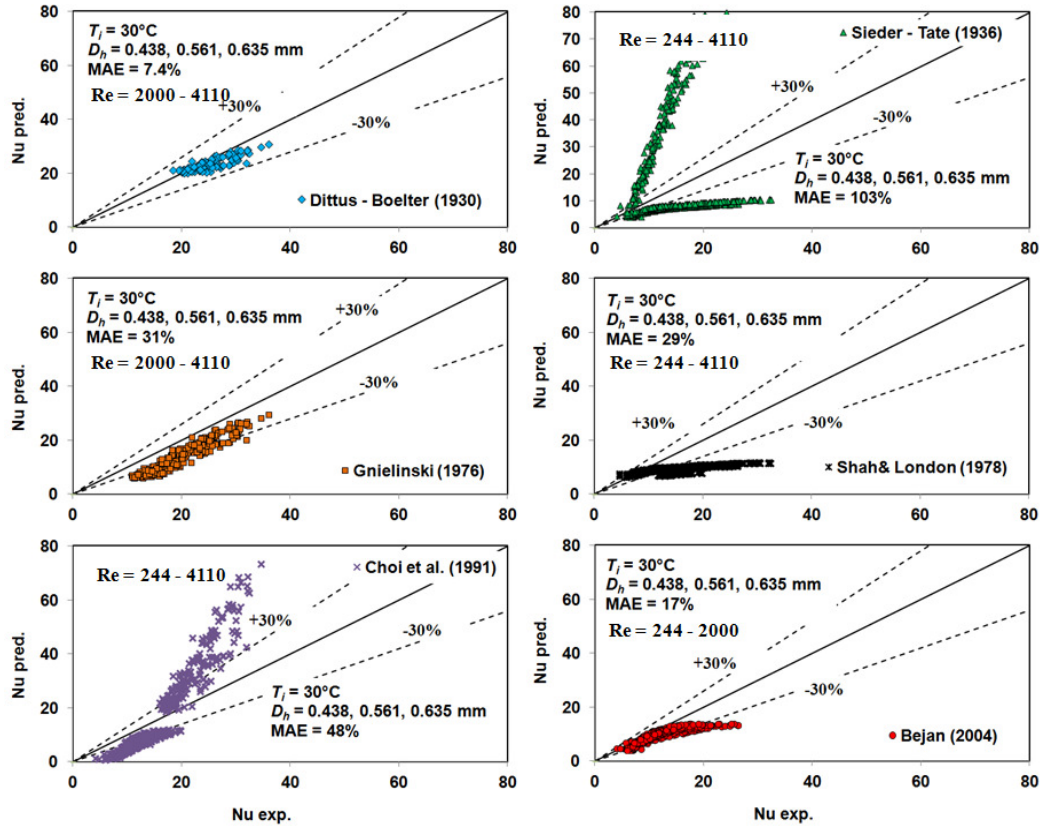


Figure 4.13 Comparison of experimental Nusselt numbers with published macroscale correlations at Reynolds numbers ranging from 244 to 4110.

Based on the same method a similar new correlation was formulated to predict Nusselt numbers for developing turbulent flow and shown in Fig. 4.14(b). The equation, covering Reynolds numbers varying from 2000 to 4100 and Prandtl numbers from 4 to 5, is given by

$$\text{Nu} = 0.032 \text{Re}^{0.841} \text{Pr}^{-0.51} L_*^{-0.153} \quad (4.21)$$

Equation (4.21) can predict the experimental data within 30% error bars and with a MAE of 5.8%. Equations (4.20) and (4.21) were obtained using multi linear regression for multiple variables; therefore, they are valid only within the experimental conditions, for rectangular channels with three heated wall sides and for developing flow.

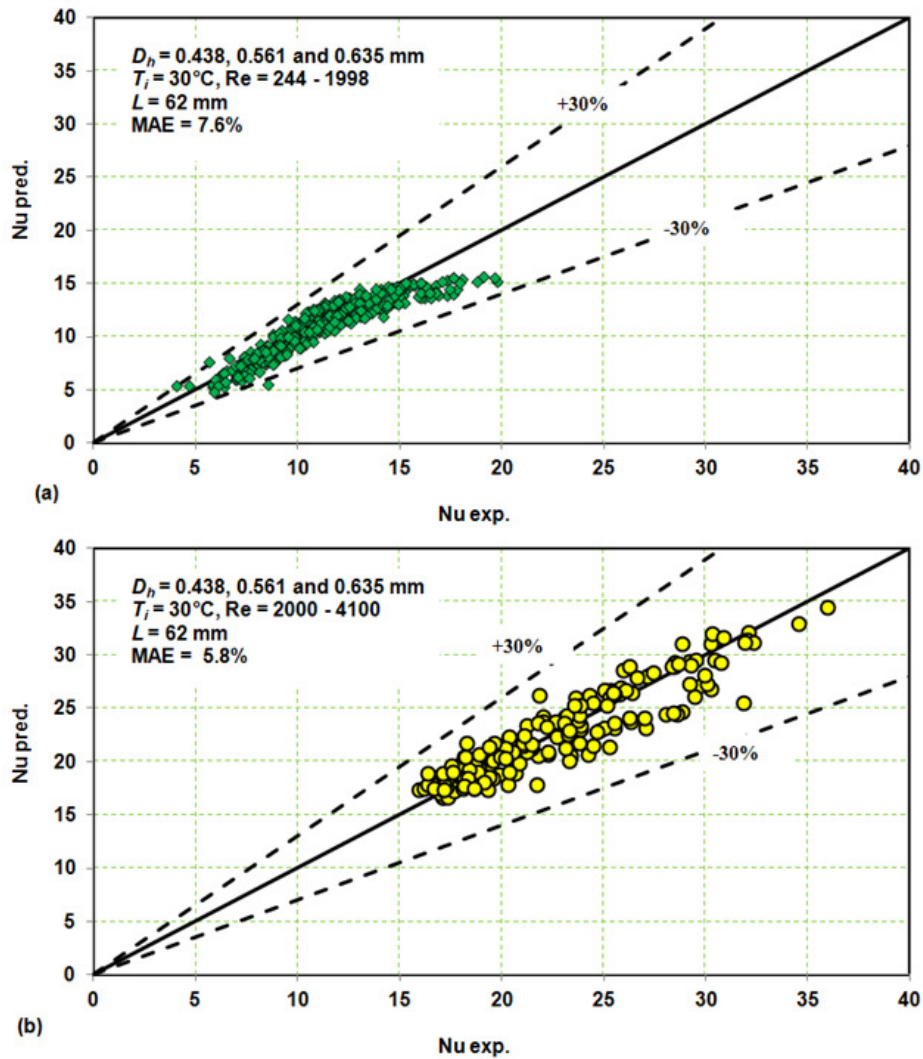


Figure 4.14 Comparison of experimental Nusselt number data with the new correlations for the 0.438 mm, 0.561 mm, and 0.635 mm channels: (a) developing laminar flow, (b) developing turbulent flow.

#### 4.5 Repeatability of measurements

The experiments were repeated after one to two months from the first experiments. The repeatability of the experimental results is reasonably good because the deviations are less than 10%. Figs 4.15 and 4.16 summarise the repeatability measurements of friction factor and Nusselt number respectively, with separate graphs (a), (b) and (c) for the 0.438mm, 0.561mm and 0.635mm channels respectively.

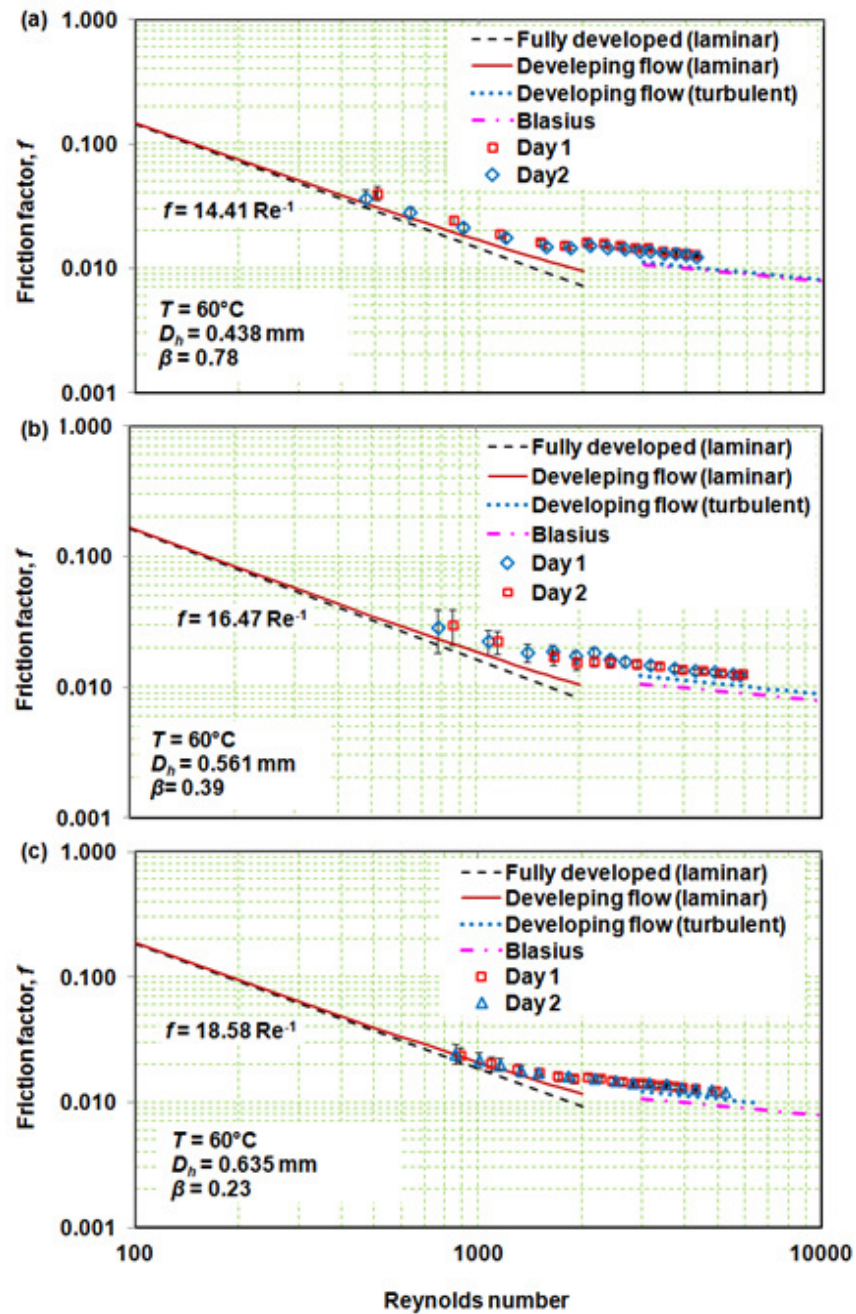


Figure 4.15 Repeatability of friction factor measurements at temperature of  $60^\circ\text{C}$ : (a)  $D_h = 0.438 \text{ mm}$ , (b)  $D_h = 0.561 \text{ mm}$ , (c)  $D_h = 0.635 \text{ mm}$ .

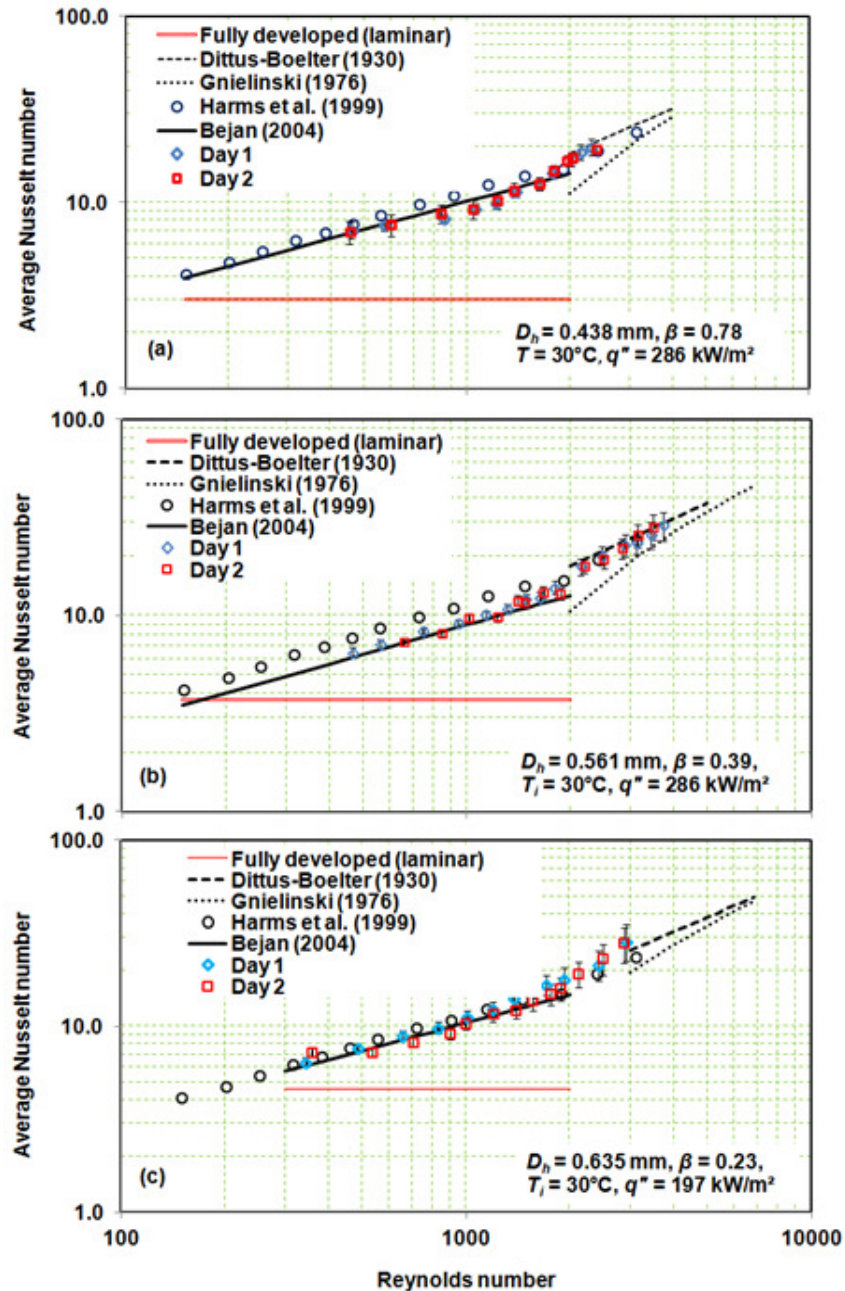


Figure 4.16 Repeatability of Nusselt number measurements at inlet temperature of  $30^\circ\text{C}$ : (a)  $D_h = 0.438 \text{ mm}$ , (b)  $D_h = 0.561 \text{ mm}$ , (c)  $D_h = 0.635 \text{ mm}$ .

## 4.6 Summary

Single-phase pressure drop and heat transfer experiments have been performed using three test sections (0.438 mm, 0.561 mm and 0.635 mm). Some of the findings are summarised in this subsection.

The effect of inlet fluid temperature is significant on the pressure drop but not significant on the friction factor. The experimental friction factors seem higher than predicted by theory especially in the turbulent regime. In the laminar regime, the experimental friction factors are in reasonable agreement with developing flow friction factor theory. The slightly higher experimental values could be due to the presence of four pressure tappings inside the test section for measuring the local pressures.

The smallest diameter test section (0.438 mm) exhibited different characteristics of heat transfer coefficient, in having the highest values compared to those obtained in the other larger test sections. However, when the heat transfer coefficients were expressed in the dimensionless form of Nusselt number, see Eq. (3.11) where the heat transfer coefficients were multiplied by the hydraulic diameter, the results were not significantly different.

For laminar flow, the experimental Nusselt numbers are higher than those predicted using fully developed flow theory but they are consistent with the correlations proposed by Bejan (2004) and Shah and London (1978). In turbulent flow, however, experimental Nusselt numbers agreed with correlations proposed by Dittus-Boelter and Choi et al. (1991) and were only slightly higher than those calculated using Gnielinski's correlation. So, in brief, it can be concluded that macroscale friction factor and Nusselt number correlations are still applicable at the microscale, at least for the three test sections and the ranges of experimental conditions tested.

Finally, the developing flow friction factor and Nusselt number correlations have been formulated for laminar and turbulent flow, based on the respective experimental data. The proposed friction factor for developing laminar flow can estimate the data within 30% error bar with a MAE of 9.4 – 13.5%, whilst the two proposed correlations for predicting the Nusselt number can predict the data within 30% error bar with MAEs of 7.8% and 5.8% respectively.

# **Chapter 5**

## **Flow Patterns and Heat Transfer: Results and Discussions**

### **5.1 Introduction**

This chapter presents and discusses the experimental results for flow boiling patterns, flow pattern maps and heat transfer characteristics. All results presented and discussed here were obtained from flow boiling experiments using three test sections with hydraulic diameters of 0.438 mm, 0.561 mm and 0.635 mm. In addition, the flow boiling heat transfer coefficients are compared with several selected correlations.

The aim here is mainly to investigate heat transfer characteristics whereas the flow patterns are recorded to assist in understanding the heat transfer and pressure drop results. The heat transfer results are presented in the form of:

- a. Local heat transfer coefficient versus local vapour quality.
- b. Local heat transfer coefficient versus axial distance.
- c. Local and average heat transfer coefficient versus heat flux.
- d. Classical boiling curves (heat flux versus wall superheat).

The chapter is organised as follows: an introduction of the Chapter is given in Section 5.1, experimental flow patterns and comparison with existing flow pattern maps are presented in Section 5.2, heat transfer results and discussion are given in Section 5.3, Section 5.4 describes heat transfer fluctuation and repeatability of measurements is presented in Section 5.5, Comparison with flow boiling correlations is described and discussed in Section 5.6 and the rest, Section 5.7 provides summary of the Chapter.

### **5.2 Flow pattern results**

It is helpful to start by discussing the flow patterns. The flow patterns here are classified using a definition which was also used by Chen et al. (2006) with some justifications. In the current experimental study, the patterns were observed at three locations; near the inlet, in the middle and near the outlet. All patterns were recorded

using a high speed video camera Phantom V6 at a speed of 1000 pictures per second, resolution of  $512 \times 512$  pixels and 10000 posts triggered. Experimental conditions include mass fluxes ranging from 200 to 1100 kg/m<sup>2</sup>s (Re = 442 to 1709), inlet pressure of 125 kPa (abs), inlet temperature of 98°C and heat fluxes ranging from 69 to 793 kW/m<sup>2</sup>.

### **5.2.1 Effect of hydraulic diameter on flow patterns**

#### **5.2.1.1 Flow patterns in the 0.561 mm channel**

As demonstrated by Zhao and Bi (2001), flow patterns observed in the channels with diameters less than 1 mm were different from those for the channels with diameters above 1 mm. For example, dispersed bubbles were observed in the larger channels, whilst cap-bubbles were observed in the smaller one. In contrast to this, slug, churn and annular flows have been observed in both large and small channels. Harirchian and Garimella (2009) found that slug patterns were formed immediately after boiling incipience in channels with hydraulic diameters smaller than 0.4 mm and bubbly flow regimes were not observed. In this work, by way of comparison, bubbly flow was still observed in the three test sections, but it occurred occasionally and sometimes intermittently with liquid or slug flow, however, it was not observed near the outlet. The flow patterns observed in this study were bubbly, slug, churn and annular, as shown in Fig. 5.1. From the figure, bubbly flow was observed in the middle of the test section at low heat flux. An example of this pattern presented in Fig. 5.1 only consisted of two bubbles. Dispersed bubbles were not observed probably due to the narrow channel which did not provide a lot of nucleation sites. Similarly, within the length of observation, the slug flow observed sometimes contained one bubble or two bubbles only. This was different with that found by Chen et al. (2003) in terms of the number of bubble of slug flow. They found more than two slug bubbles within the observation length as shown in Fig. 2.8 in Chapter 2, for the 1.1 mm tube diameter.

Due to the high inlet subcooling 7 K, boiling occurred around the middle of the test section. However, as the heat flux was increased, boiling nucleation extended towards the inlet. This caused the flow patterns to change from inlet to outlet. In this case, at the same heat flux several flow patterns can be identified depending on the observation location. As an example, at a mass flux of 601 kg/m<sup>2</sup>s and heat flux of 332 kW/m<sup>2</sup>, the

flow patterns observed were slug near the inlet, churn in the middle and annular near the outlet. It is interesting to note that, if the observation had only been taken at the outlet or after the channel, for these conditions only an annular flow pattern would have been found. In consequence it could be inferred that the observation location itself has contributed to the discrepancies in observed flow patterns in microchannels.

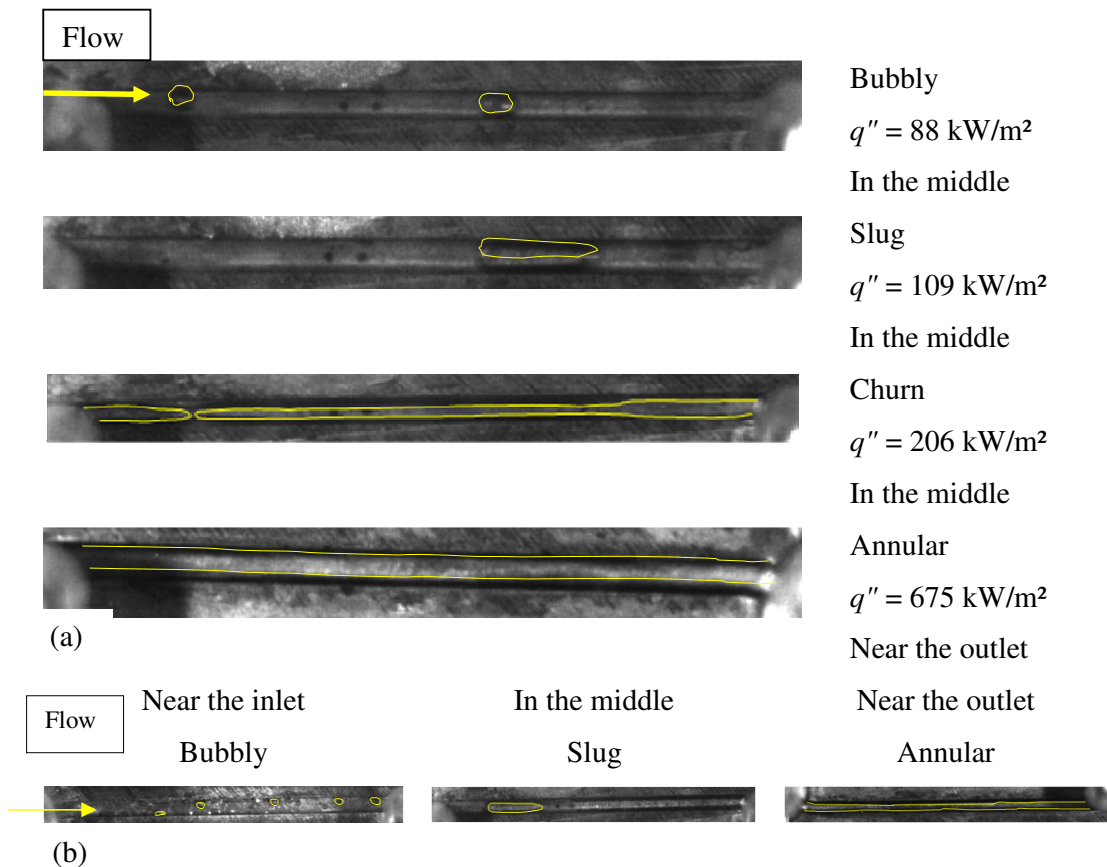


Figure 5.1 Flow patterns observed in the 0.438 mm channel at mass flux of 601 kg/m<sup>2</sup>s, inlet pressure and temperature of 125 kPa (abs) and 98°C: (a) at several heat fluxes, (b) at 175 kW/m<sup>2</sup>.

As shown in Fig. 5.1, when the channel size is relatively small, the bubble size can easily reach the channel diameter and eventually earlier onset to slug flow can occur. Therefore, as reported by Harrirchian and Garimella (2008), it is possible that in a very small channel bubbly flow is not observed. In consistency with this, in the current study

bubbly flow is still observed because the size of the channel is larger than that of Harrirchian and Garimella (2008).

#### 5.2.1.2 Flow patterns in the 0.561 mm channel

Figure 5.2 presents flow patterns observed in the 0.561 mm channel at a mass flux of 600 kg/m<sup>2</sup>s, inlet pressure of 125 kPa (abs) and inlet temperature of 98°C. In general, the patterns were the same as those in the 0.438 mm channel: bubbly, slug, churn and annular. The shape of the slug bubble is also similar to that found at 0.438 mm diameter, but the size is obviously different or larger as the bubble size depends on the channel diameter. For a large channel, the bubbly flow could be large and vice versa.

Bubbly flow patterns were characterized in the 0.561 mm channel at a heat flux of 79 kW/m<sup>2</sup> and mass flux of 401 kg/m<sup>2</sup>s near the outlet. However, this bubbly flow alternated with liquid flow and slug flow, and near the end of the observation length, the bubbly flow changed to slug flow. A continuous bubbly flow pattern appearing near the outlet was observed at a mass flux of 701 kg/m<sup>2</sup>s, heat flux of 148 kW/m<sup>2</sup>. The bubbles came from a single nucleation site close to pressure tapping 4 which was approximately 12.4 mm from the outlet. The bubbles appeared and left from this site and flowed in a sequence. This was almost the same as that found by Mishima and Hibiki (1996) and Zhao and Bi (2001). However, in this study the bubbles were growing and flowing within the length of observation whilst those observed by Mishima and Hibiki (1996) and Zhao and Bi (2001) were not obviously because their experiments were adiabatic flow using air-water.

As seen in Fig. 5.2, bubbly flow patterns were also observed at a mass flux of 600 kg/m<sup>2</sup>s and heat flux of 126 kW/m<sup>2</sup>s in the middle of the test section. The size of the bubbles was approximately 0.5 mm, and they did not collapse until they left the observation region. In the middle of the test section, at a higher heat flux, 224 kW/m<sup>2</sup>, slug flow patterns were found and sometimes accompanied by a bubble smaller than the width of the channel. At the same mass flux, but at different heat flux, 300 kW/m<sup>2</sup>, the flow pattern observed in the middle was churn flow. At heat flux of 485 kW/m<sup>2</sup>, the flow pattern found near the outlet was annular.

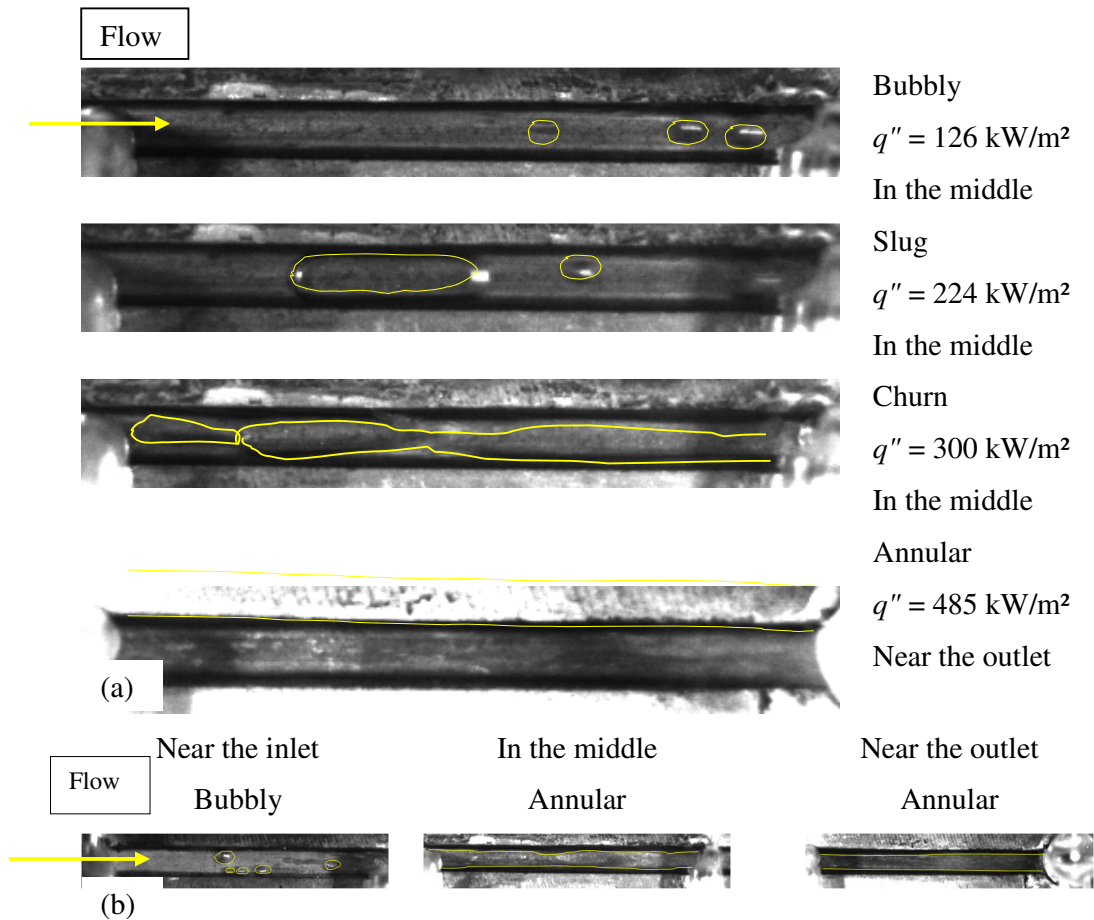


Figure 5.2 Flow patterns observed in the 0.561 mm channel at mass flux of 600 kg/m<sup>2</sup>s, inlet pressure and temperature of 125 kPa (abs) and 98°C: (a) at several heat fluxes, (b) at 445 kW/m<sup>2</sup>.

### 5.2.1.3 Flow patterns in the 0.635 mm channel

Figure 5.3 presents examples of flow patterns observed in the 0.635 mm channel at a mass flux of 602 kg/m<sup>2</sup>s, inlet pressure of 125 kPa (abs) and inlet temperature of 98°C. The quality of the flow pattern images was better than those in the two smaller test sections. Bubbly flow, slug flow, churn and annular flows could be seen clearly and it was easy to distinguish them.

However, the sequence of the flow pattern occurrence was the same as that in the two smaller channels. At low heat fluxes, bubbly flow was observed, but as the heat flux was increased, slug flow took its place and further increases in heat flux created churn

flow and eventually annular flow. The appearance or shape of the bubbles, being the same for all three test sections, but the size of the bubble was different with that in smaller test sections.

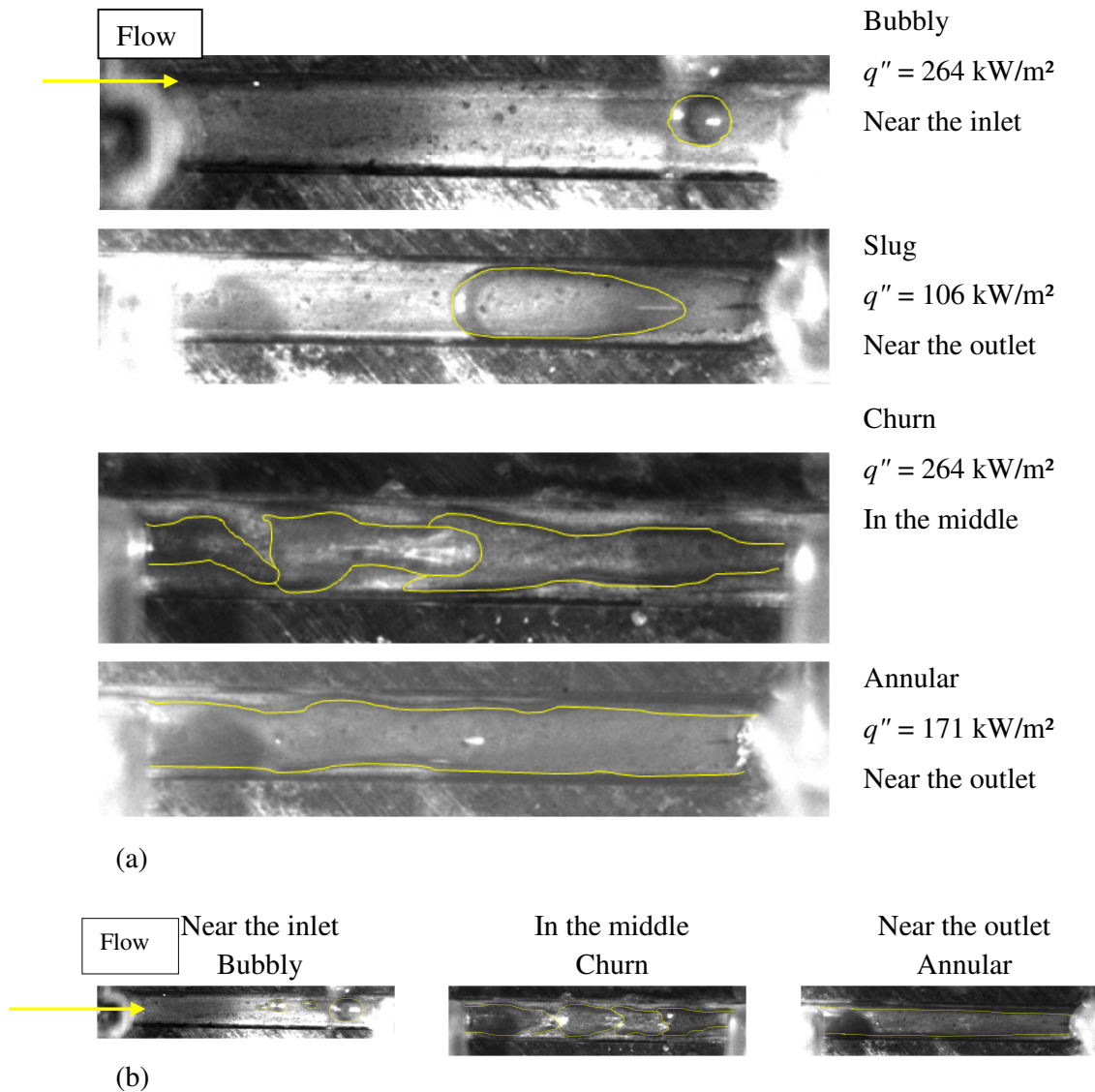


Figure 5.3 Flow patterns observed in the 0.635 mm channel at mass flux of 602 kg/m<sup>2</sup>s, inlet pressure and temperature of 125 kPa (abs) and 98°C: (a) at several heat fluxes, (b) at 290 kW/m<sup>2</sup>.

### 5.2.2 Effect of heat flux on flow patterns

As the shape of the flow patterns observed in the three test sections was the same, it was difficult to discern any disparity in the flow patterns; therefore, it is worth considering the effect of heat flux. Basically, an increase in heat flux caused a change in flow patterns, for example from bubbly to slug, slug to churn and churn to annular. However, the flow patterns did not change for every step of an increase in heat flux. Full information on this, is given in Table 5.1 for all three test sections.

Even with the information provided in Table 5.1, it is still difficult to identify any range of heat flux which changes the flow pattern. For example, for the 0.438 mm channel, at heat fluxes ranging from 88 to 121 kW/m<sup>2</sup>, the flow patterns remained the same near the inlet as liquid flow, but changed in the middle from bubbly to slug, and near the outlet from slug to churn flow. In the 0.561 mm and 0.635 mm channels inconsistent changes in the flow pattern also occurred. For the 0.561 mm channel, at heat fluxes ranging from 106 to 334 kW/m<sup>2</sup>, near the inlet the flow remained as liquid flow, in the middle it changed from liquid to churn and near the outlet altered from slug to annular flow. In the 0.635 mm channel, with heat fluxes varying from 106 to 203 kW/m<sup>2</sup>, near the inlet the flow was always liquid, in the middle it changed from liquid to slug and near the outlet from slug to annular flow.

When the considered observation location was near the outlet only, the effect of heat flux was clearer. For the 0.438 mm channel, at a heat flux of 88 kW/m<sup>2</sup>, the flow pattern observed was slug flow, then at heat fluxes between 109 and 121 kW/m<sup>2</sup> churn flow and between 161 and 675 kW/m<sup>2</sup> annular flow. For the 0.561 mm channel, at a heat flux of 106 kW/m<sup>2</sup>, the flow pattern was slug, at heat fluxes between 126 and 148 kW/m<sup>2</sup> churn and between 172 and 594 kW/m<sup>2</sup> annular. In the 0.635 mm channel, at heat fluxes between 106 and 141 kW/m<sup>2</sup>, the flow pattern observed was slug, at heat fluxes ranging from 171 to 685 kW/m<sup>2</sup> annular.

Table 5.1 Effect of heat flux on the flow pattern in different channels at a nominal mass flux of 600 kg/m<sup>2</sup>s, inlet temperature of 98°C (inlet subcooled 7 K) and inlet pressure of 125 kPa (abs).

Heat flux	Flow pattern observed		
$q''$ [kW/m <sup>2</sup> ]	Near the inlet	In the middle	Near the outlet
$D_h = 0.438$ mm.			
88	Liquid	Bubbly	Slug
109	Liquid	Slug	Churn
121	Liquid	Slug	Churn
161	Bubbly	Slug	Annular
175	Bubbly	Slug	Annular
206	Slug	Churn	Annular
222	Churn	Churn	Annular
274	Churn	Churn	Annular
293	Churn	Churn	Annular
332	Churn	Churn	Annular
374	Churn	Churn	Annular
418	Churn	Annular	Annular
441	Churn	Annular	Annular
488	Churn	Annular	Annular
538	Churn	Annular	Annular
564	Churn	Annular	Annular
591	Churn	Annular	Annular

618	Churn	Annular	Annular
646	Churn	Annular	Annular
675	Churn	Annular	Annular
$D_h = 0.561$ mm.			
106	Liquid	Liquid	Slug
126	Liquid	Bubbly	Churn
148	Liquid	Bubbly	Churn
172	Liquid	Bubbly	Annular
197	Liquid	Bubbly	Annular
224	Liquid	Slug	Annular
269	Liquid	Slug	Annular
300	Liquid	Churn	Annular
334	Liquid	Churn	Annular
369	Liquid	Churn	Annular
406	Liquid	Churn	Annular
445	Bubbly	Annular	Annular
485	Slug	Annular	Annular
527	Churn	Annular	Annular
594	Churn	Annular	Annular
$D_h = 0.635$ mm.			
106	Liquid	Liquid	Slug
123	Liquid	Slug	Slug

141	Liquid	Slug	Slug
171	Liquid	Slug	Annular
203	Liquid	Slug	Annular
226	Bubbly	Slug	Annular
264	Bubbly	Slug	Annular
290	Bubbly	Churn	Annular
332	Slug	Churn	Annular
362	Slug	Churn	Annular
408	Slug	Annular	Annular
441	Churn	Annular	Annular
475	Churn	Annular	Annular
529	Churn	Annular	Annular
585	Churn	Annular	Annular
644	Churn	Annular	Annular
685	Churn	Annular	Annular

### 5.2.3 Effect of mass flux on flow patterns

Observed flow patterns can differ for the same heat flux, but different mass fluxes. Table 5.2 gives patterns for the 0.635 mm channel for ranges of mass fluxes at the two fixed heat fluxes of 226 kW/m<sup>2</sup> and 685 kW/m<sup>2</sup>. The effect of mass flux is clear at low heat fluxes. As the mass flux was increased, the flow pattern changes to lower level, e.g. from churn to slug, from slug to bubbly. Nevertheless, at high heat fluxes, the effect of mass flux remains unclear. For example, at the heat flux of 226 kW/m<sup>2</sup>, the flow patterns for several mass fluxes do not show the same types of flow pattern near the inlet, in the middle and near the outlet. At the heat flux of 685 kW/m<sup>2</sup> and mass fluxes

ranging from 202 to 802 kg/m<sup>2</sup>s, flow patterns are the same, near the inlet the flow pattern observed was churn, in the middle and near the outlet was annular.

Table 5.2 Effect of mass flux on flow pattern at two fixed heat fluxes, inlet temperature and pressure of 98°C and 125 kPa (abs) respectively for the 0.635 mm channel.

Heat flux $q''$ [kW/m <sup>2</sup> ]	Mass flux $G$ [kg/m <sup>2</sup> s]	Flow pattern observed		
		Near the inlet	In the middle	Near the outlet
226	202	Liquid	Slug	Annular
	303	Liquid	Slug	Annular
	401	Liquid	Churn	Annular
	501	Liquid	Churn	Annular
	602	Bubbly	Slug	Annular
	703	Liquid	Churn	Churn
	802	Liquid	Churn	Churn
685	202	Churn	Annular	Annular
	303	Churn	Annular	Annular
	401	Churn	Annular	Annular
	501	Churn	Annular	Annular
	602	Churn	Annular	Annular
	703	Churn	Annular	Annular
	802	Churn	Annular	Annular

#### 5.2.4 Comparison with flow pattern maps

Many flow pattern maps, developed for small diameter tubes and microchannels are available in the open literature. However, only three pattern maps have been chosen to make a comparison with the experimental flow pattern data. Firstly, an adiabatic flow pattern map (air-water) for a horizontal semi-triangular conduit proposed by Triplett et al. (1999), secondly a universal map for horizontal conduits with hydraulic diameters less than 1 mm proposed by Hassan et al. (2005), and lastly the flow boiling pattern map for narrow channels proposed by Wang et al. (2011). The first flow pattern map was taken to compare with the experimental data because the map was intended to predict the flow patterns of two-phase flow in a horizontal non circular duct. The map was for an adiabatic two-phase flow (air-water), however, this was only to see if the map was applicable to predict the flow boiling patterns. The second flow pattern map was used for comparing with the data because it was a universal map for two-phase flow in horizontal channels having hydraulic diameters of less than 1 mm. The latter was chosen because it was based on a rectangular test section. In addition, the experimental data are also compared with a map proposed by Sobierska et al. (2006) for flow boiling in a vertical microchannel with a hydraulic diameter of 1.2 mm, in the form of mass flux versus quality and a map proposed by the group Chen et al. (2006) for a 1.1 mm diameter tube, in the form of Weber number planes.

Figure 5.4(a) compares experimental results for the 0.438 mm channel with the flow pattern maps proposed by Triplett et al. (1999), Hassan et al (2005) and Wang et al (2011). The maps proposed by Triplett et al. (1999) and Hassan et al. (2005) can predict the data successfully only for churn flow patterns, but they fail for other flow pattern data. Several bubbly flow data fall in the predicted slug or intermittent area, whilst most of slug pattern data are located in the predicted churn area. Current annular flow pattern data fall at the predicted churn area and only a few data points locate in the predicted area. Meanwhile, bubbly and slug patterns subsist at higher superficial vapour velocities. Finally, the flow pattern map proposed by Wang et al. (2011) for narrow rectangular channels, cannot predict the experimental data. Fig 5.4(b) gives comparisons for the 0.561 mm channel. Similar to that for the 0.438 mm channel, the experimental data cannot be predicted successfully using the existing flow pattern maps. Only some of the data points for annular and churn flow fall within the prediction areas of Triplett et al. (1999) and Hassan et al. (2005) maps. Several data points for slug flow

locate within the prediction area of Hassan et al. (2005) and almost all of them fall in the predicted slug-annular area of Triplett et al. (1999). Fig. 5.4(c) gives comparisons for the 0.635 mm channel. Again, similar to those for the other channels, some slug, churn and annular pattern data can be predicted using flow pattern maps proposed by Triplett et al. (1999) and Hassan et al. (2005), whilst bubbly flow data cannot be predicted at all. Also, as those for the smaller test sections, the bubbly flow and slug flow locate at higher superficial vapour velocities than the maps. This may be due to the thermodynamic quality. As the size of channel is reduced, the vapour quality becomes higher at the same mass flux and heat flux. The higher vapour quality results in the higher vapour superficial velocity. However, this indicates a different phenomenon with that found by Xu et al. (1999) who stated that the transitional boundary shifted to lower superficial gas velocity and Coleman and Garimella (1999) who explained that the transitional line shifted to higher liquid superficial velocity with the superficial vapour quality of being almost constant.

The possible reasons to explain the flow pattern maps used for comparison in Fig. 5.4 of being inaccurate are they obtained from different experimental conditions, channel materials and surface characteristics. The map proposed by Triplett et al. (1999) was created from adiabatic experiments, in which, the gas and the fluid mass flow rates can be adjusted, whilst in this project cannot. The material used in Triplett et al. (1999) was stainless steel tube, whilst in this experiment is copper. Furthermore, the map proposed by Hassan et al. (2005) was intended for universal purposes and horizontal channels with diameters less than 1 mm, but it also cannot predict the data. This may be due to the map being constructed from adiabatic experiment data. Therefore, the transition lines of the map are similar to that of Triplett et al. (1999). The flow pattern map proposed by Wang et al. (2011) clearly cannot predict the data. The reason can be due to the map being made from flow boiling data in a vertical channel with a big hydraulic diameter, 5.58 mm. In a big diameter vertical channel, the flow is strongly affected by the gravity. This causes the transition lines separating flow pattern regimes being at the gas and liquid superficial velocities. One thing that should be noted from the figure is that as the mass flux was decreased, the flow pattern data went to the lower area. For example, at a mass flux of 1000 kg/m<sup>2</sup>, the churn flow data points located exactly on the predicted area, whilst at a mass flux of about 600 kg/m<sup>2</sup>s, churn flow located nearly in the transition boundary line. Therefore, data obtained from flow boiling experiments in

the three different hydraulic diameters seem to contradict each other. This was due to different mass flux ranges used. For the smallest test section, the mass fluxes run ranged from 600 to 1100 kg/m<sup>2</sup>s, for the 0.561 mm channel from 400 to 1000 kg/m<sup>2</sup>s and for the biggest test section from 200 to 800 kg/m<sup>2</sup>s. However, this phenomenon indicates that the flow pattern maps should be corrected with the mass flux.

A comparison with the map proposed by Sobierska et al. (2006), as shown in Fig. 5.5, seems to be more accurate and successful in predicting the flow pattern data. However, most experimental bubbly flow data fall in the predicted slug region, with a part of them located in the subcooled region. As the hydraulic diameter becomes smaller, the observation is getting more difficult due to the limitation of camera.

Figure 5.6 shows an additional comparison with the flow pattern map proposed by Chen et al. (2006) based on the data obtained for the 1.1 mm diameter tube in the form of Weber number plane. The purpose of this flow pattern map was originally to identify the influence of surface tension on flow pattern. However, the map cannot predict the data. Again, the reason could be due to the different fluid or the Weber number is not suitable for classifying flow patterns. The working fluid used for constructing the map was refrigerant R134a which is different with the fluid used in this current study. As revealed by Chen et al. (2002) and Akhbar (2003), in microchannels, effect of surface tension becomes dominant, however, in the open literature, see Table 2.4 in Chapter 2, flow patterns observed in small to micro channels are scattered. Although, surface tension may affect the flow pattern, but may not accurate to cluster the flow pattern.

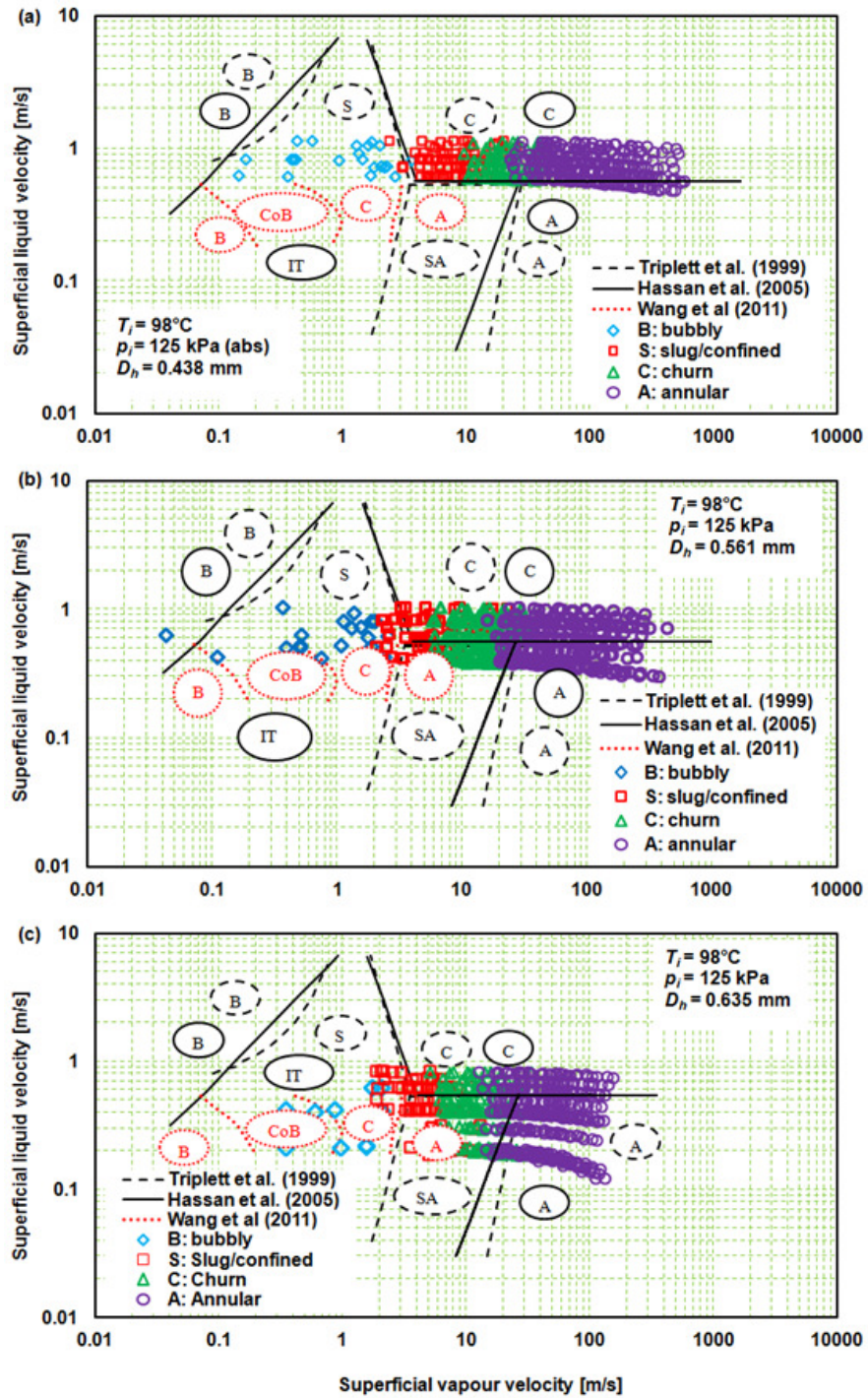


Figure 5.4 Comparison with three published flow pattern maps: (a)  $D_h = 0.438$  mm, (b)  $D_h = 0.561$  mm and (c)  $D_h = 0.635$  mm channels. IT: intermittent (slug and slug-annular).

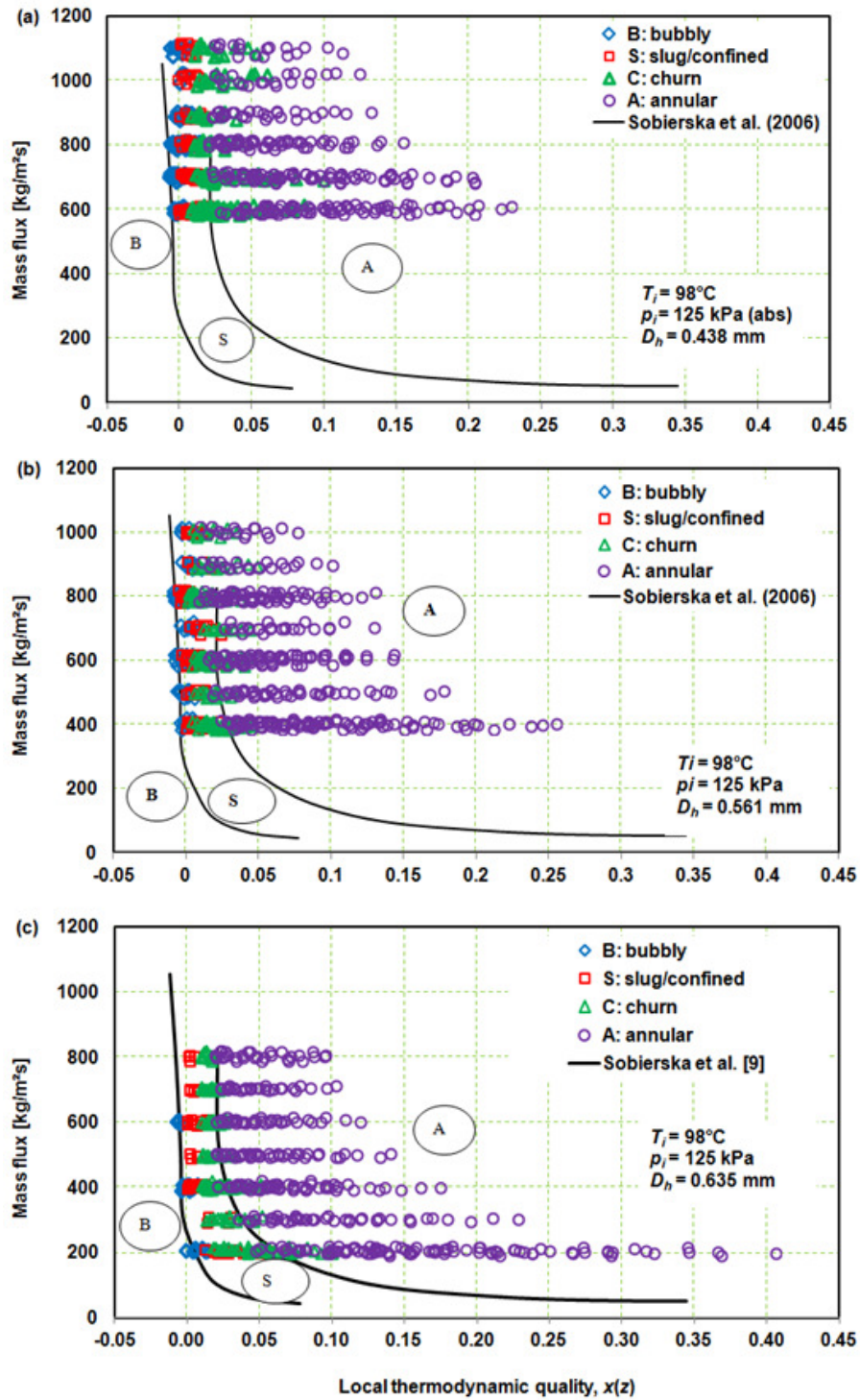


Figure 5.5 Comparison with the flow pattern map proposed by Sobierska et al. (2006):  
 (a)  $D_h = 0.438$  mm, (b)  $D_h = 0.561$  mm, (c)  $D_h = 0.635$  mm channels.

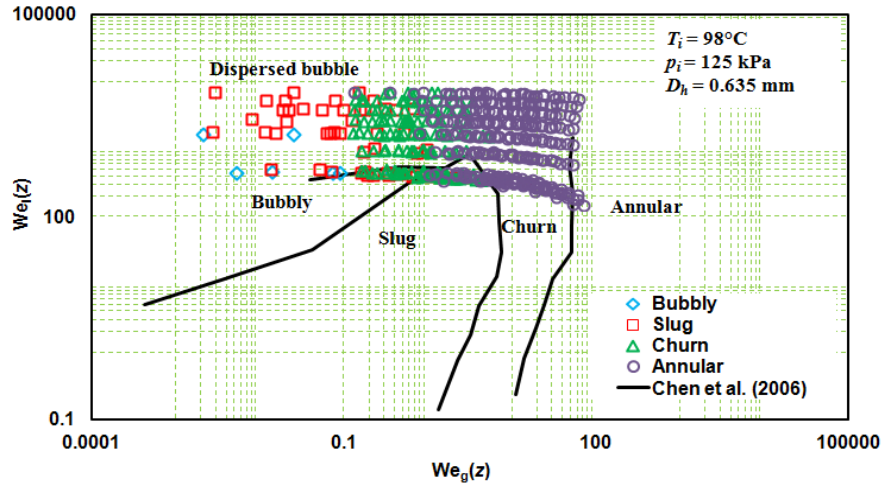


Figure 5.6 Comparison with the flow pattern map proposed by Chen et al. (2006) based on the data for the 1.1 mm diameter tube in the form of Webber number plane.

### 5.3 Flow boiling heat transfer results

This section presents the effects of heat flux, mass flux and hydraulic diameter on the local time averaged heat transfer coefficient. All measurements were recorded after the system reached a steady state condition, indicated by constant readings for average mass flow rate, pressure and temperature, see Fig. 5.7. After the mass flux and inlet pressure were adjusted to the required values, the heat flux was applied and varied step by step. It should be noted that at every increased heat flux, the mass flux and inlet pressure should be adjusted because they changed with an increase in heat flux. The mass flux decreased and the inlet pressure increased with an increase in heat flux. Figures 5.7 shows the oscillations in different parameters over a 20 s period at the heat flux of 222 kW/m<sup>2</sup>. The figure represents only one example for the 0.438 mm channel at an inlet pressure of 125.5 kPa (abs) and a mass flux of 601 kg/m<sup>2</sup>s. Similar plots can be produced for the other experimental conditions and test sections. In the figures the parameters indicate that the system has reached a steady state condition and all parameters are ready to be recorded.

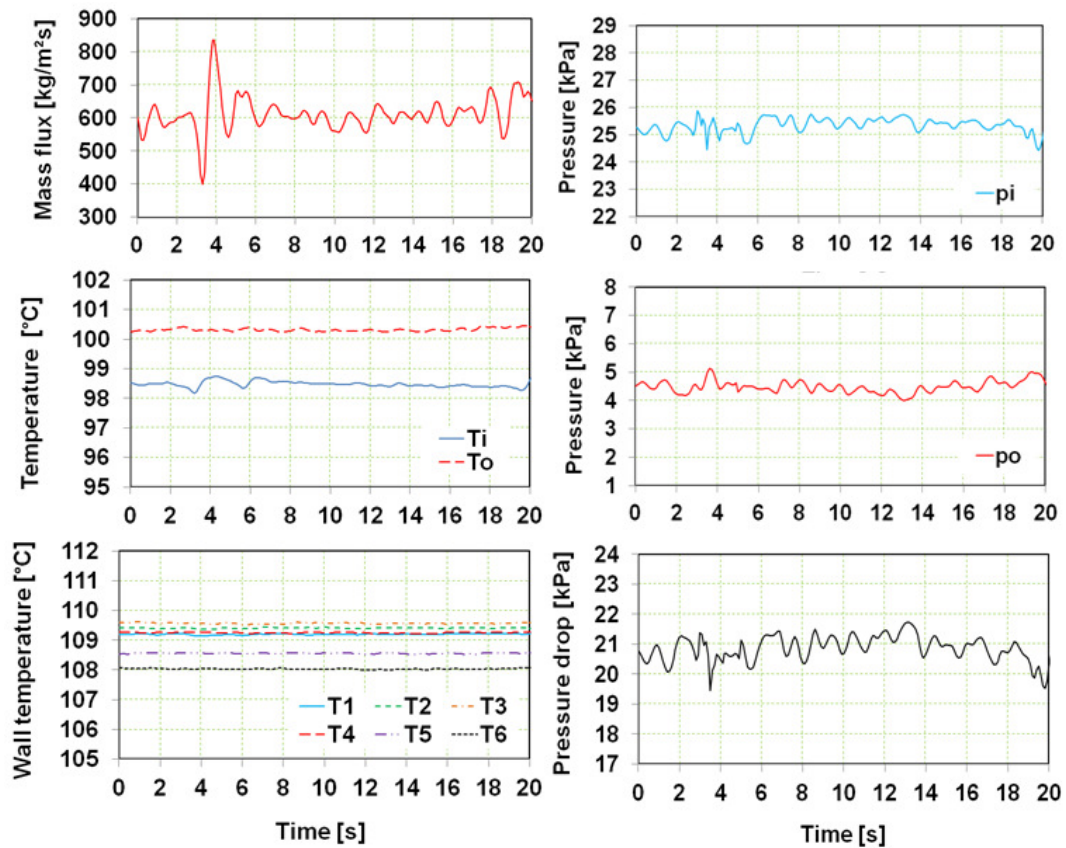


Figure 5.7 Oscillations of variables as a function of time at heat flux of  $222 \text{ kW/m}^2$ , mass flux of  $601 \text{ kg/m}^2\text{s}$ , inlet temperature and pressure of  $98^\circ\text{C}$  and  $125 \text{ kPa}$  (abs) for the  $0.438 \text{ mm}$  channel.

Figure 5.7 shows that the system is in a steady condition, because although there is fluctuation in mass flux, temperature and pressure but their average values are constant over recording period. For example, at the heat flux of  $222 \text{ kW/m}^2$ , fluctuations in all parameters occur. The mass flux fluctuation reaches a maximum amplitude of  $5.1 \text{ g/min}$  ( $437 \text{ kg/m}^2\text{s}$ ) which is larger than the uncertainty. This is obviously due to the occurrence of boiling in the test section. An amplitude of  $0.7 \text{ K}$  peak to peak indicated by inlet temperature was noted. This could be due to the interaction between the temperature fluctuation in the pre-heater and the test section. Nevertheless, the outlet temperature amplitude is smaller, at  $0.2 \text{ K}$  peak to peak. Inlet and outlet pressures also fluctuated with amplitudes of  $1.5 \text{ kPa}$  and  $1.9 \text{ kPa}$ , both of which are larger than their uncertainties. These high fluctuations were obviously due to the occurrence of boiling inside the test section. A fluctuation of the average wall temperature was found to be negligibly small,  $0.05$  to  $0.1 \text{ K}$  (peak to peak) whilst the fluctuation of pressure drop

was high at 2.4 kPa peak to peak. This fluctuation was mainly due to the interaction between inlet pressure fluctuation, bubble generation and outlet pressure fluctuation.

Data indicating the steady state conditions are listed in Table 5.3 with their standard and percentage deviations. These are for the test section of hydraulic diameter 0.438 mm at a mass flux of 601 kg/m<sup>2</sup>s. It should be noted that the steady condition is not indicated by a small or large fluctuation but with no change in the average values of parameters in the recording period. Although a fluctuation may be small, if the average values do not remain constant but decrease or increase with time, the condition is not steady.

Table 5.3 Standard and percentage deviations of parameter for 1800 data point samples.

$q''$ [kW/m <sup>2</sup> ]	Parameter	Mean value	Standard deviation	%
0	Mass flow rate, [g/min]	7.0	0.145	2
	Mass flux, [kg/m <sup>2</sup> s]	598.5	12.4	2
	Inlet temperature, [°C]	98.0	0.04	0.04
	Outlet temperature, [°C]	91.8	0.03	0.03
	Inlet pressure, [kPa](abs)	125.6	0.03	0.02
	Outlet pressure, [kPa](abs)	122.7	0.04	0.03
	Pressure drop, [kPa]	2.83	0.04	1.5
	Wall temperature, [°C]	90.9	0.004	0.004
675	Mass flow rate, [g/min]	7.11	0.29	4.1
	Mass flux, [kg/m <sup>2</sup> s]	608	24.7	4.1
	Inlet temperature, [°C]	98.3	0.04	0.04
	Outlet temperature, [°C]	79.1	0.09	0.11
	Inlet pressure, [kPa](abs)	125.3	0.21	0.17
	Outlet pressure, [kPa](abs)	45.8	0.18	0.4
	Pressure drop, [kPa]	79.5	0.32	0.4
	Wall temperature, [°C]	113.5	0.01	0.009

### 5.3.1 Effect of hydraulic diameter

In order to understand the effect of hydraulic diameter on the local heat transfer coefficient, Fig. 5.8 was constructed. The figure presents the variation in local heat transfer coefficient caused by both hydraulic diameter (results for the three test sections) and local thermodynamic quality. These are for a nominal mass flux of 600 kg/m<sup>2</sup>s, inlet temperature of 98°C and inlet pressure of 125 kPa (abs).

The effect of hydraulic diameter is clear at near zero qualities: a smaller diameter results in higher local heat transfer coefficients. The effect is unclear at higher qualities, greater than 0.08, the local heat transfer coefficients for the smaller test sections seem to be lower than those for the 0.635 mm channel. Overall, then, from Fig. 5.8, a conclusion regarding the effect of hydraulic diameter on the local heat transfer coefficient cannot be reached and this needs further investigation.

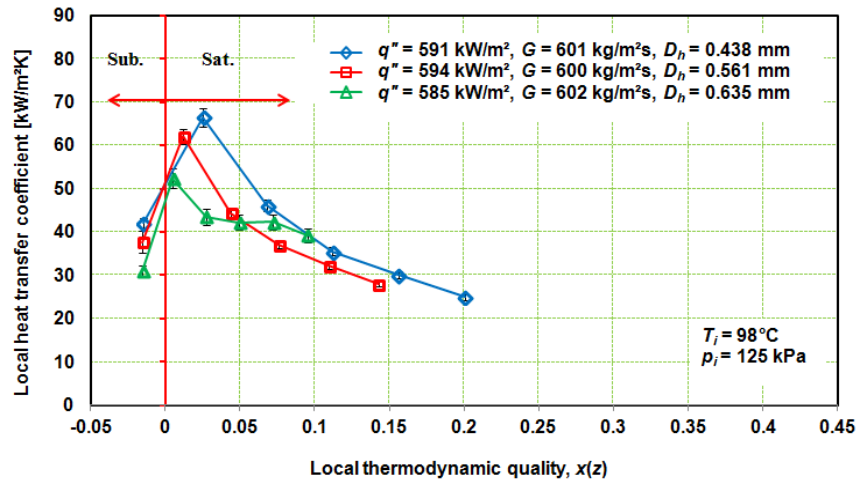


Figure 5.8 Effect of hydraulic diameter and local thermodynamic quality on the local heat transfer coefficient for the three test sections at a nominal mass flux of 600 kg/m<sup>2</sup>s, inlet temperature of 98°C and inlet pressure of 125 kPa (abs).

Fig. 5.9 also presents the effect of hydraulic diameter, but on average heat transfer coefficient, and is combined with heat flux as a primary parameter. The experimental conditions are the same as for Fig. 5.8. Clearly, as the hydraulic diameter decreases the heat transfer coefficient increases. However, at higher heat fluxes, the heat transfer coefficients for the three test sections seem to merge together. Therefore, it is

recommended that it would be better to use smaller channels in the bubbly and slug flow regimes.

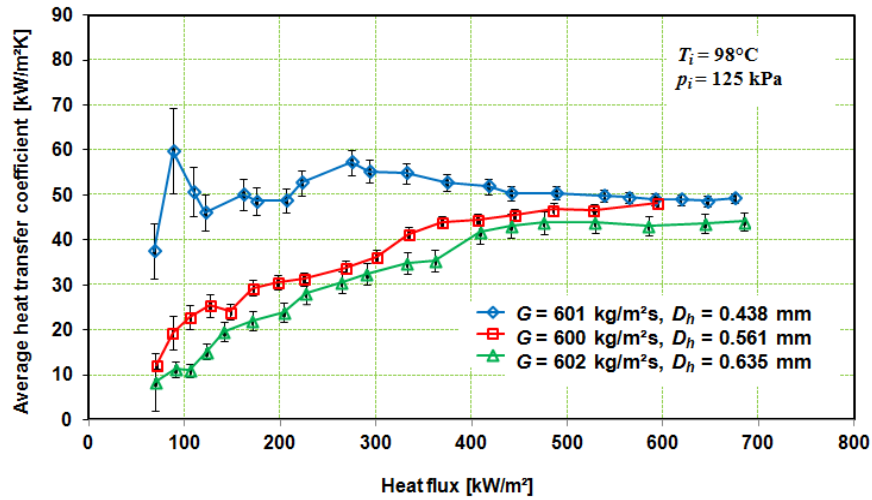


Figure 5.9 Effect of hydraulic diameter and heat flux on the average heat transfer coefficient for the three test sections at a nominal mass flux of 600 kg/m<sup>2</sup>s, inlet temperature of 98°C, and inlet pressure of 125 kPa (abs).

### 5.3.2 Effect of heat flux

The heat flux effect needs to be investigated because this parameter can be used to determine the mechanisms of flow boiling heat transfer. This will be examined using graphs with local heat transfer coefficient versus quality and local heat transfer coefficient versus the length of the channel.

#### Results for 0.438 mm channel

Figure 5.10 shows the effect of heat flux on local heat transfer coefficient at a mass flux of 601 kg/m<sup>2</sup>s and inlet pressure of 125 kPa (abs) for the 0.438 mm channel. The heat transfer coefficient is plotted as a function of local thermodynamic quality and axial distance. The water entered the channel in a subcooled condition, and progressively was heated up along the test section. Therefore, following Qu and Mudawar (2003), the flow boiling is divided into two regions: subcooled and saturated. At most applied heat fluxes, the heat transfer coefficient increases sharply from the subcooled region to the zero quality condition and thereafter decreases. This trend is consistent with that found by Wang et al. (2008), see Fig. 2.23 in Chapter 2. In Fig. 5.10, at qualities of between

approximately 0 and 0.02, the effect of heat flux is unclear. Above that, there is a significant effect of heat flux on local heat transfer coefficient. For instance, at a heat flux of 675 kW/m<sup>2</sup>, the heat transfer coefficient is approximately 10 kW/m<sup>2</sup>K higher (23% at the quality of 0.05) than at a heat flux of 441 kW/m<sup>2</sup>. The heat transfer coefficients had maximum values for the quality range 0 to 0.02, in which the flow patterns observed were bubbly or slug.

Within the saturated region, the thermodynamic quality increases along the test section, resulting in a change of flow pattern from slug to churn and from churn to annular. As shown in Fig. 5.10 the heat transfer coefficient decreases with quality. Leaving aside the effect of heat flux, this finding is consistent with those of Qu and Mudawar (2003), Sobierska et al. (2006), Berst et al. (2008), Wang et al. (2010) and Wang and Sefiane (2012). They all found that the heat transfer coefficient decreased with quality, explaining that the decrease in heat transfer coefficient was due to the dryout or the high pressure drop. The corresponding flow patterns observed in Fig. 5.10 at the heat flux of 675 kW/m<sup>2</sup> were churn near the inlet, annular in the middle and near the outlet.

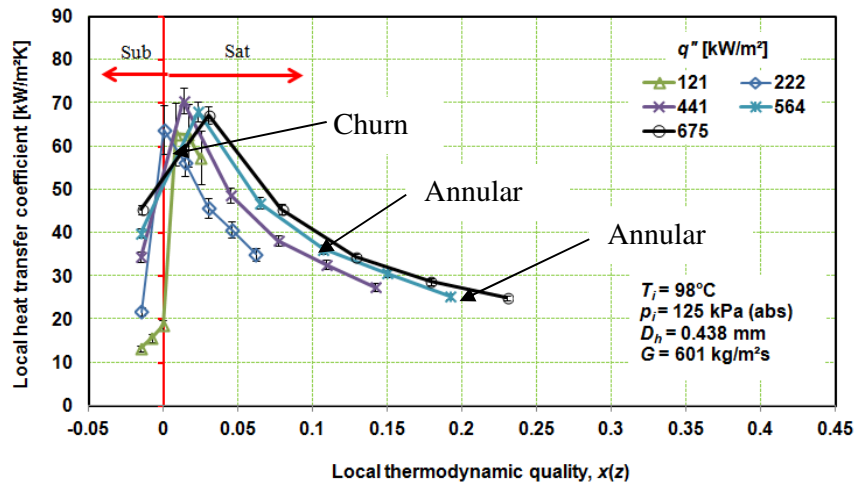


Figure 5.10 Effect of heat flux and local thermodynamic quality on the local heat transfer coefficient for 0.438 mm channel at 601 kg/m<sup>2</sup>s and inlet pressure of 125 kPa (abs).

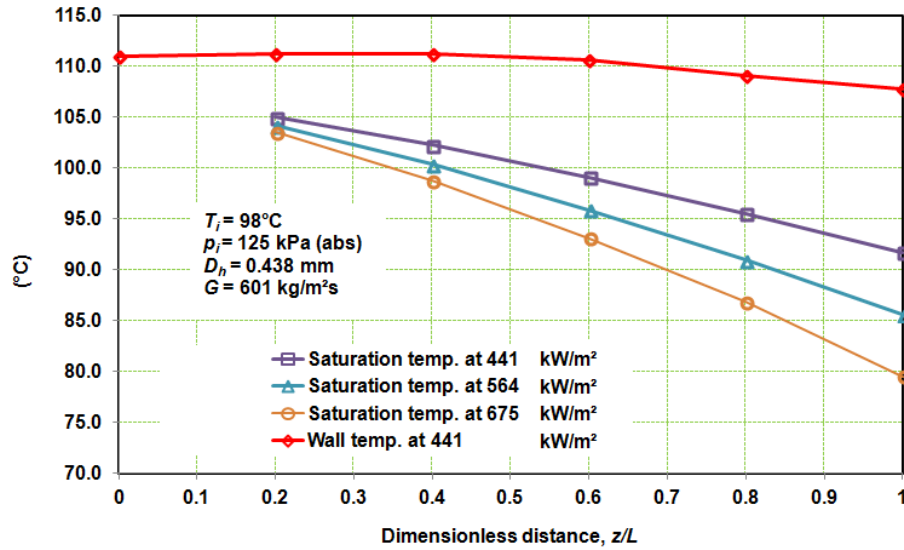


Figure 5.11 Saturation temperature distributions along the test section for the 0.438 mm channel, for a range of heat fluxes and at the mass flux of 601 kg/m<sup>2</sup>s.

Fig. 5.11 shows the variation in saturation temperature with dimensionless distance from entry, for a range of tested heat fluxes and for the 0.438 mm channel. Following Qu and Mudawar (2003), Mahmoud et al. (2009, 2011), the pressure gradient was assumed to fall linearly along the test section, so the results show that saturation temperatures decrease with the distance from the entry. Consequently,  $T_w(z) - T_{sat}(z)$  increases toward the outlet for a given value of heat flux and mass flux. Therefore, the heat transfer coefficient decreases along the test section. The wall temperature does not change much along the test section, but the saturation temperature does. This means that for this study, the decrease in heat transfer coefficient with quality was not due to dryout, but the high pressure gradient. Of course, a partial dryout was observed in the 0.635 mm channel, noticed by an occasionally appearing vapour blanket captured by the camera, but it was difficult to relate the dryout to the equation determining the heat transfer coefficient, Eq. (3.13) in Chapter three, because there was no appreciable increase in the wall temperature.

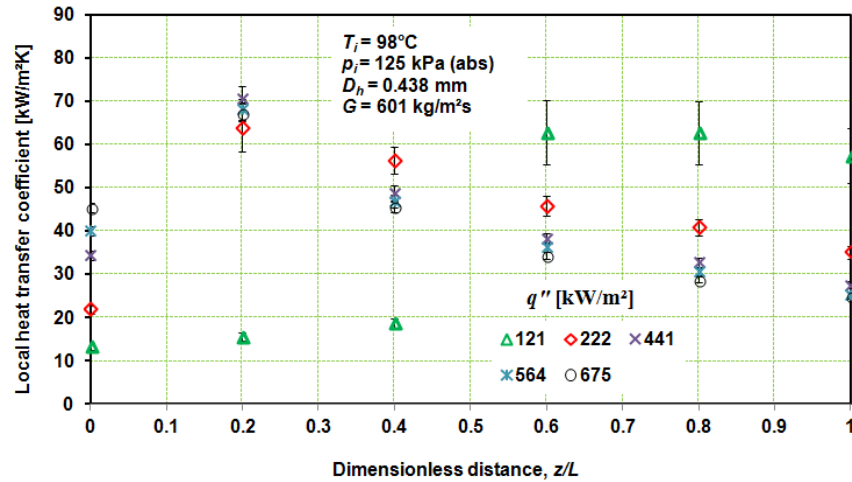


Figure 5.12 Effect of heat flux and dimensionless distance from entry on the local heat transfer coefficient, for 0.438 mm channel at a mass flux of 601 kg/m<sup>2</sup>s.

By contrast, Fig. 5.12 shows how the heat transfer coefficient varies with dimensionless distance as a primary parameter, in addition to heat flux. For the distance between 0 and 0.2, the effect of heat flux is significant, but not clear at greater distances, even deflating for distances beyond quality of 0.4. The trends of heat transfer remain the same as those shown in Fig. 5.8, at all heat fluxes. The heat transfer coefficient decreases toward the outlet, except at the heat flux of 121 kW/m<sup>2</sup>, which is due to the small quality.

### Results for 0.561 mm channel

Figure 5.13 shows the effects of heat flux and local thermodynamic quality on the local heat transfer coefficient, for the 0.561 mm channel at a mass flux of 600 kg/m<sup>2</sup>s. The effect of heat flux is clear: increasing the heat flux causes the heat transfer coefficient to increase. The trend of the local heat transfer coefficient with quality is similar to that for the 0.438 mm channel: as the quality increases, the heat transfer coefficient decreases at all heat fluxes used. The highest heat transfer coefficient can be achieved at near zero quality or in bubbly and slug/confined flow patterns. The corresponding flow patterns observed in Fig. 5.13, at the heat flux of 594 kW/m<sup>2</sup>, were churn near the inlet, annular in the middle and near the outlet.

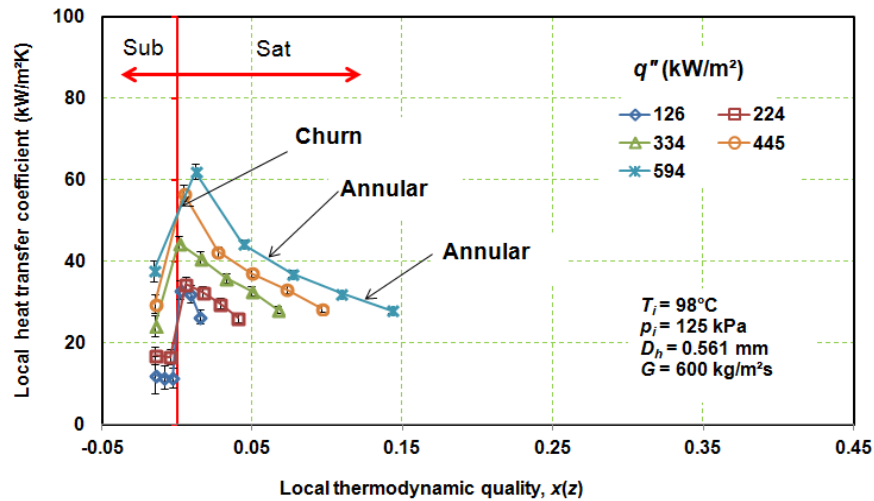


Figure 5.13 Effect of heat flux and local thermodynamic quality on the local heat transfer coefficient for 0.561 mm channel at 600 kg/m<sup>2</sup>s, inlet temperature of 98°C and inlet pressure of 125 kPa (abs).

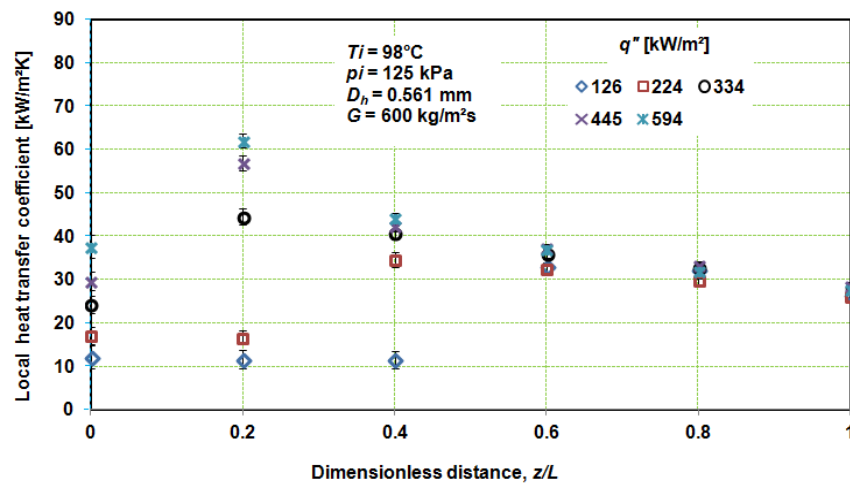


Figure 5.14 Effect of heat flux and dimensionless distance from entry on the local heat transfer coefficient for 0.561 mm channel at 600 kg/m<sup>2</sup>s, inlet temperature of 98°C and inlet pressure of 125 kPa (abs).

Again, the variation of heat transfer coefficient with dimensionless distance, given in Fig. 5.14, does not help in search of an understanding of the effect of heat flux on the local heat transfer coefficient. The trend of the heat transfer coefficient in Fig. 5.14 is

almost the same as that in Fig. 5.12 for the 0.438 mm channel; it generally decreases along the test section in the saturation region.

### **Results for 0.635 mm channel**

Figure 5.15 shows the effects of heat flux and local thermodynamic quality on the local heat transfer coefficient, for the 0.635 mm channel at two mass fluxes. Similar to that of the smaller test sections, the heat transfer coefficient increases with quality in the subcooled region, and reaches a maximum value near the zero quality. However, in the saturation region, the heat transfer coefficient slightly decreases and eventually becomes nearly constant, especially at a mass flux of 202 kg/m<sup>2</sup>s. The effect of heat flux is clear, the heat transfer coefficient increases with the heat flux.

The trend of heat transfer coefficient in Fig. 5.15(a) is consistent with those found by a number of researchers, e.g. Consolini and Thome (2009) and Mahmoud et al. (2011). Also from Fig. 5.15(a) a clear effect of heat flux is evident. However, at the mass flux of 602 kg/m<sup>2</sup>s, the trend of heat transfer coefficient is slightly different, see Fig. 5.15(b). In the saturation region, the heat transfer coefficient decreases with quality, nearly the same as that in the smaller test sections. The possible reason is that at a high mass flux, the pressure drop is high, causing a decrease in fluid saturation temperature along the test section. As a result, the heat transfer coefficient decreases. Furthermore, the effect of heat flux at the mass flux of 602 kg/m<sup>2</sup>s is clear at lower heat fluxes, whilst at higher heat fluxes it is not clear. This is probably due to the dominant flow patterns. Flow patterns observed in Fig. 5.15(b) at heat fluxes 441 kW/m<sup>2</sup> and above were churn near the inlet, annular in the middle and near the outlet. Usually, when the dominant flow pattern is annular, the heat transfer mechanism is convective boiling. However, as explained above, due to the high pressure drop, the heat transfer coefficient decreases with the quality.

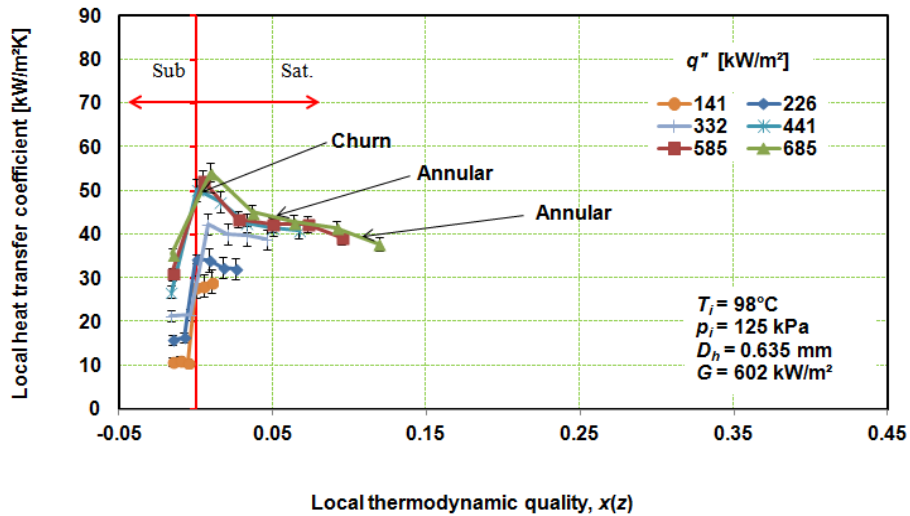
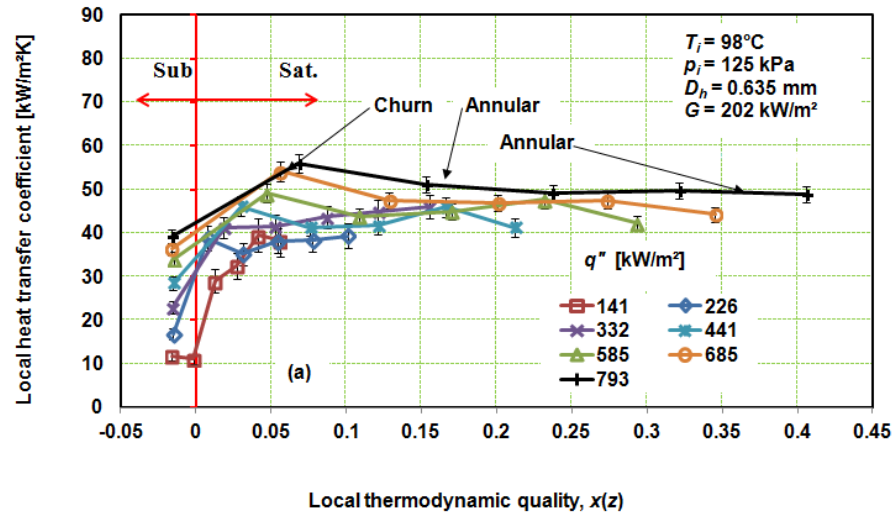


Figure 5.15 Effect of heat flux and local thermodynamic quality on the local heat transfer coefficient for 0.635 mm channel at inlet temperature of 98°C and inlet pressure of 125 kPa (abs): (a)  $G = 202 \text{ kg/m}^2\text{s}$ , (b)  $G = 602 \text{ kg/m}^2\text{s}$ .

Fig. 5.16 combines the effects of heat flux and dimensionless distance on heat transfer coefficient. Again, there is a significant effect of heat flux at lower heat fluxes but insignificant at high heat fluxes. Furthermore, consistent with that in Fig. 5.15(b), along the test section the quality increases and the heat transfer coefficient decreases.

In order to clarify further the heat flux effect, Fig. 5.17 shows the variation in local heat transfer coefficient as a direct function of heat flux, for two positions ( $z/L = 0.6$  and 1) in the 0.635 mm channel at a mass flux of 602 kg/m<sup>2</sup>s. The figure indicates that as the heat flux is increased, the local heat transfer coefficient increases. However, for heat

fluxes of greater than 400 kW/m<sup>2</sup>, the effect of heat flux seems to be unclear as the heat transfer coefficient shows a constant trend. This constancy is usually found in the convective boiling mechanism and is due to the coincidentally proportional relationship between the increment of heat flux and the wall superheat.

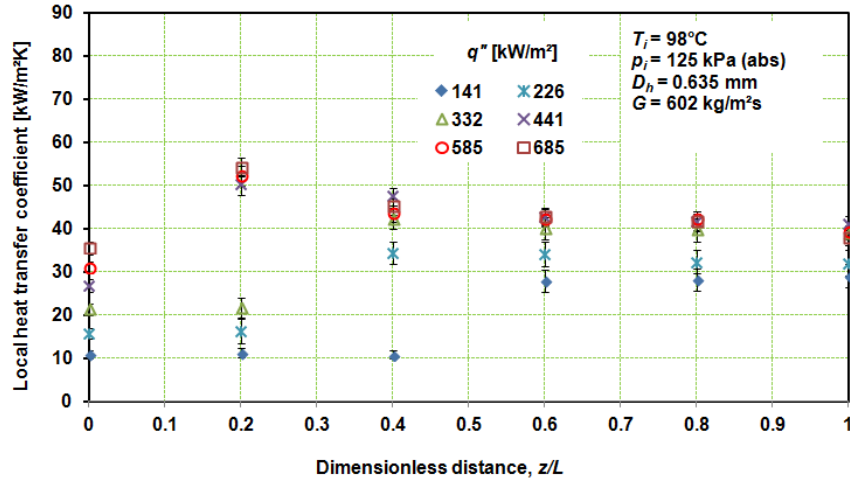


Figure 5.16 Effect of heat flux and dimensionless distance from entry on the local heat transfer coefficient for 0.635 mm channel at 602 kg/m<sup>2</sup>s, inlet pressure of 125 kPa (abs) and inlet temperature of 98°C.

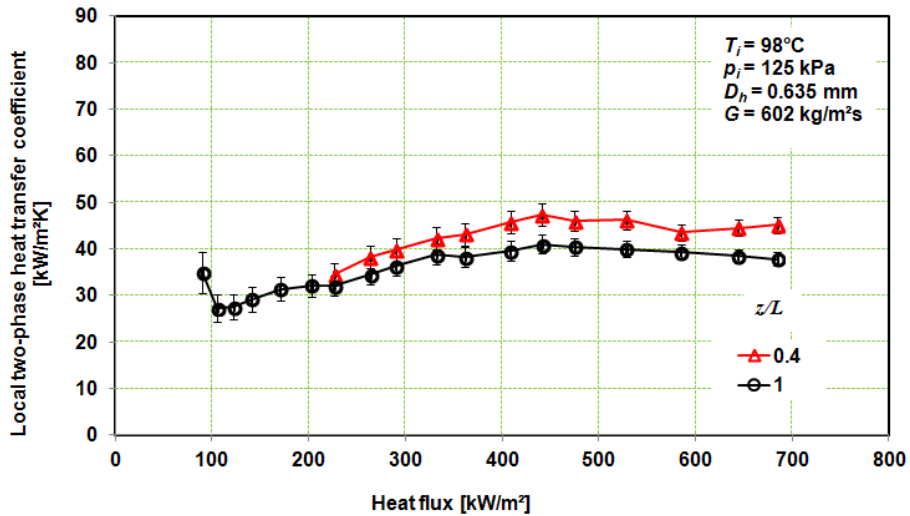


Figure 5.17 Effect of heat flux on the local heat transfer coefficient for 0.635 mm channel at 602 kg/m<sup>2</sup>s, inlet temperature of 98°C and inlet pressure of 125 kPa (abs) at two different locations.

### 5.3.3 Effect of mass flux

The effect of mass flux on heat transfer coefficient in previous publications is still not clear. In nucleate flow boiling, the expectation is that the mass flux and vapour quality do not affect the heat transfer coefficient; however, in convective flow boiling, as the mass flux and vapour quality increase the heat transfer coefficient is expected to increase. As explained in the literature review, Qu and Mudawar (2003) and Qu et al. (2004) found that the heat transfer coefficient decreased with an increase in quality but increased with an increase in mass flux. They concluded that the heat transfer mechanism was convective flow boiling. Wang et al. (2008) found that the heat transfer coefficient decreased with vapour quality and they explained the decrease in heat transfer coefficient was due to dryout. However, they did not report the effect of mass flux on the heat transfer coefficient. On the other hand, Kew and Cornwell (1997), who used high mass fluxes in a 1.39 mm diameter tube, and Sobierska et al. (2006), found that the heat transfer coefficient decreased with an increase in mass flux and in vapour quality. This phenomenon is in contradiction with the definitions of nucleate and convective boiling. Figs. 5.18 to 5.20 show the effects of mass flux and local thermodynamic quality on the heat transfer coefficient at almost constant heat flux for the 0.438 mm, 0.561 mm and 0.635 mm channels respectively. Almost all heat transfer coefficients obtained in the two smaller test sections decreased with an increase in mass flux and quality. This dependence is clear at low mass fluxes but unclear at high mass fluxes. The decrease in heat transfer coefficient in the 0.438 mm channel (Fig. 5.18) is sharper than that for the 0.561 mm channel (Fig. 5.19), indicating an effect of hydraulic diameter. Contrary behaviour occurs in the 0.635 mm channel (Fig. 5.20). The local heat transfer coefficient is almost independent of mass flux and quality, although at high mass fluxes the effect of mass flux is still detectable.

Previous studies have mentioned several reasons for the trend of local heat transfer coefficients. When the local heat transfer coefficient was found to decrease with an increase in quality, the authors commonly pointed to dryout, see Sumith et al. (2003), Yun et al. (2005), Wang et al. (2008) and Sclider et al. (2010). On the other hand, when the heat transfer coefficient increased with quality, they attributed it to an evaporation in the liquid film and an increased vapour velocity, see Lee and Lee (2001) and Sumith et al. (2003). The decrease in local heat transfer coefficient with quality was explained by Qu and Mudawar (2003) as due to the appreciable droplet entrainment and re-deposition

in annular flow whilst Huh and Kim (2007) stated that it was due to the elongated bubbles which travelled quickly. However, these authors did not present any evidence for their reasons. Dryout can be seen if there is a sudden increase in wall temperature. An appreciable level of which decreases the heat transfer coefficient: this is consistent with Eq. (3.21). The evaporation of the liquid film was suspected here to be one of the causes of an increase in local heat transfer coefficient with quality. However, this is difficult to prove.

In this work, the dependence of local heat transfer coefficient on the mass flux has been found to be due to the high pressure drop, as explained in the previous sub section. For a given test section, a higher mass flux results in a higher pressure drop, consequently the local heat transfer coefficient at higher mass fluxes is lower. This finding confirms the results obtained by Sobierska et al. (2006). They found for a mass flux of 673 kg/m<sup>2</sup>s at a heat flux of 66 kW/m<sup>2</sup>, the heat transfer coefficient was much lower than that for 53 kg/m<sup>2</sup>s at almost the same heat flux of 67 kW/m<sup>2</sup>. The heat transfer mechanism obtained by Sobierska et al. (2006) was nucleate boiling because the effect of heat flux was detected. Similarly, in this research, the effect of heat flux was significant, even for all the test sections, so the heat transfer mechanism was nucleate boiling.

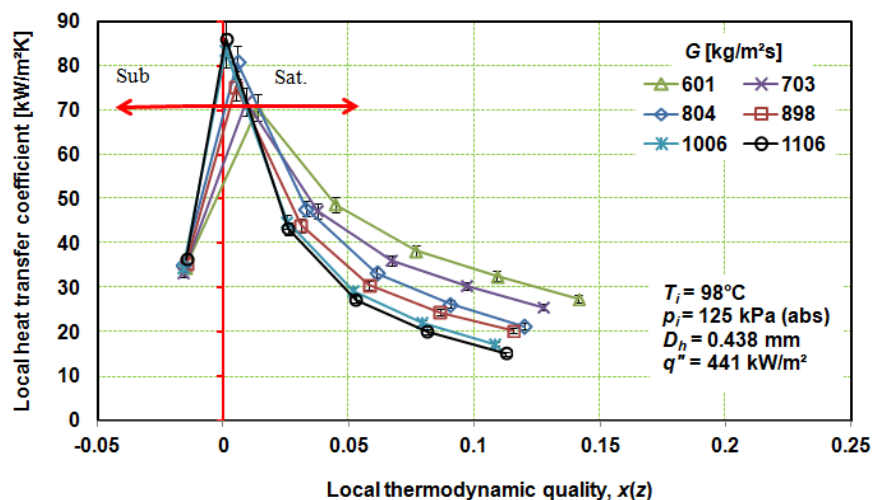


Figure 5.18 Effect of mass flux and local thermodynamic quality on the local heat transfer coefficient at the heat flux of 441 kW/m<sup>2</sup>, inlet temperature of 98°C and inlet pressure of 125 kPa (abs) for the 0.438 mm channel.

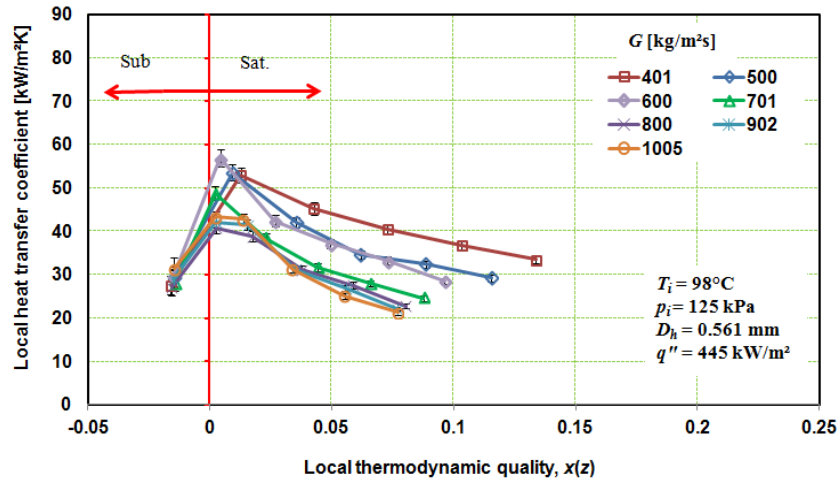


Figure 5.19 Effect of mass flux and local thermodynamic quality on the local heat transfer coefficient at the heat flux of 445 kW/m<sup>2</sup>, inlet temperature of 98°C and inlet pressure of 125 kPa (abs) for the 0.561 mm channel.

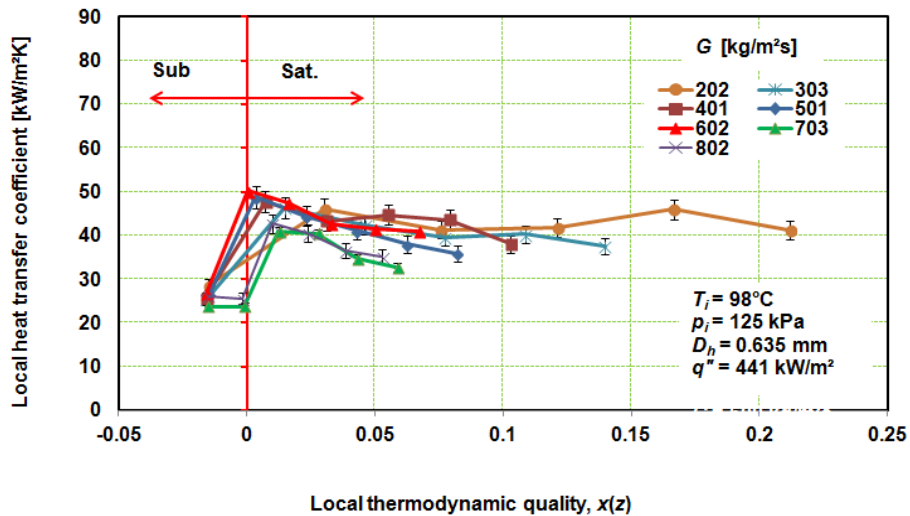


Figure 5.20 Effect of mass flux and local thermodynamic quality on the local heat transfer coefficient at the heat flux of 441 kW/m<sup>2</sup>, inlet temperature of 98°C and inlet pressure of 125 kPa (abs) for the 0.635 mm channel.

### 5.3.4 Flow boiling curve

Although in this study the topics is flow boiling, but it is worth presenting a brief explanation regarding pool boiling in order to know the difference between them. At least there are four modes in pool boiling, i.e. free convection boiling, nucleate boiling,

transition boiling and film boiling, see Incropera et al. (2006). When wall superheat is between 1 and 5°C or below ONB (onset of nucleate boiling), boiling is termed free convection boiling. It is usually indicated by fluid motion determined principally by free convection effects. At higher wall superheat, namely between 5 and 30°C, it is called nucleate boiling. It is noted by existing isolated bubbles at wall superheat between 5 and 10°C and coalesce bubbles and more nucleation at wall superheat above 10°C. In the transition mode, bubble formation is very rapid and a vapour film or blanket begins to form on the surface. The transition mode occurs for wall superheat between 30 and 120°C. Finally, film boiling results for wall superheat above 120°C and until burnout is reached.

Figures 5.21(a) to (c) show the effects of mass flux and wall superheat on the boiling curve for the 0.438 mm, 0.561 mm and 0.635 mm channels respectively, plotted at  $z/L = 0.4$  and developed by gradually increasing the heat flux. Compared to the pool boiling curve, the boiling curve here has no different trend. In Fig. 5.21(a), however, for the smallest test section, the boiling line is higher than for the two larger test sections. It probably indicates that in the smallest test section boiling is followed by lower fluid saturation temperatures due to the higher pressure drop, thus increasing the wall superheat. In the whole of Fig. 5.21, in the range of mass flux studied, there is no detectable effect of mass flux on the boiling curve. This lack of effect on the boiling curve was also found by Mahmoud et al. (2011) for both the channels that they tested (seamless and welded tubes,  $D = 1.1$  mm). Further, based on the pool boiling as given in Incropera et al. (2006), see above paragraph, in this study, the tested heat fluxes were less than 800 kW/m<sup>2</sup> and the wall superheat temperatures were less than 30°C, it can be inferred that the flow boiling in the three test sections seems to be dominated by nucleate boiling. Therefore, the effect of heat flux was found, as presented graphically in the previous section, especially at near zero quality.

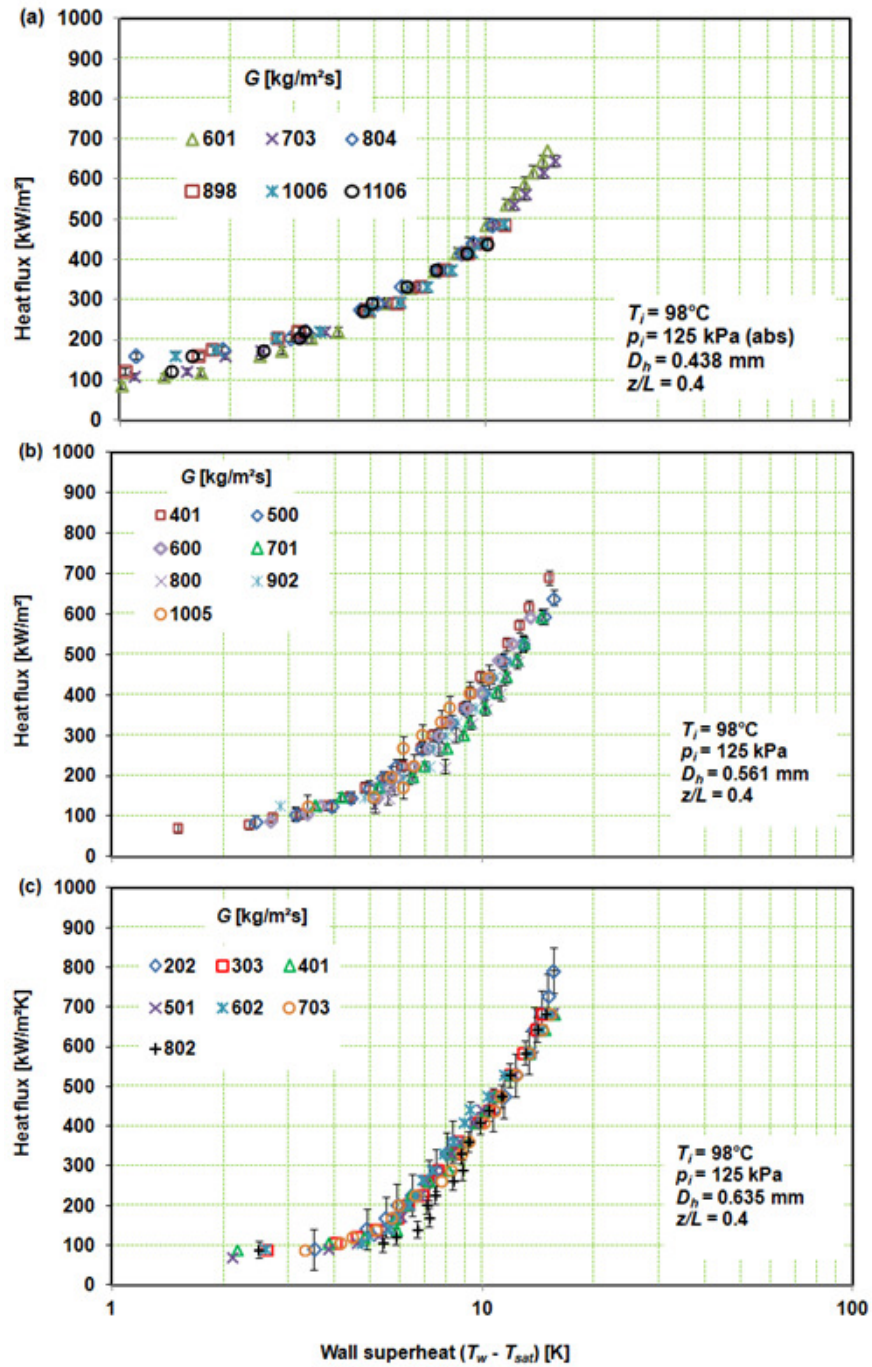


Figure 5.21 Effect of heat flux on the boiling curve at inlet temperature of  $98^\circ\text{C}$  and inlet pressure of 125 kPa (abs): (a)  $D_h = 0.438$  mm, (b)  $D_h = 0.561$  mm, (c)  $D_h = 0.635$  mm.

## 5.4 Heat transfer fluctuation

This is not the scope of the study, but this may be useful to see the heat transfer coefficient fluctuation. Since fluctuations occurred in flow boiling, together with inlet – outlet temperatures, inlet – outlet pressures, wall temperatures and mass flux, therefore examples of the heat transfer fluctuation for the three test sections at a constant value of mass flux and heat flux are presented. The data were recorded over 180 s (1800 data points), however in Fig. 5.22 the data are shown only for 20 s. The fluctuation data are plotted in graphical form for ease of interpretation. Figure 5.22(a) to (c) presents a set of heat transfer coefficient fluctuations for the 0.438 mm, 0.561 mm and 0.635 mm channels respectively, at a nominal mass flux of 600 kg/m<sup>2</sup>s, heat flux of about 200 kW/m<sup>2</sup>, inlet pressure of 125 kPa (abs) and inlet temperature of 98°C.

From the figure it can be noted that the effect of hydraulic diameter on the heat transfer fluctuations is not clear. For example, the biggest fluctuation of the local heat transfer coefficient obtained in each channel, as shown in Fig. 5.22, is approximately 3.4 kW/m<sup>2</sup>K (peak to peak) at the third thermocouple for the 0.438 mm channel, .4 kW/m<sup>2</sup>K at thermocouple five for the 0.635 mm channel (which is lower than that of the 0.438 mm) and 0.8 kW/m<sup>2</sup>K for the 0.561 mm channel. There is no indication of the sequent decrease or increase in the local heat transfer coefficient with a decrease in hydraulic diameter. Therefore, further investigation under different conditions is needed.

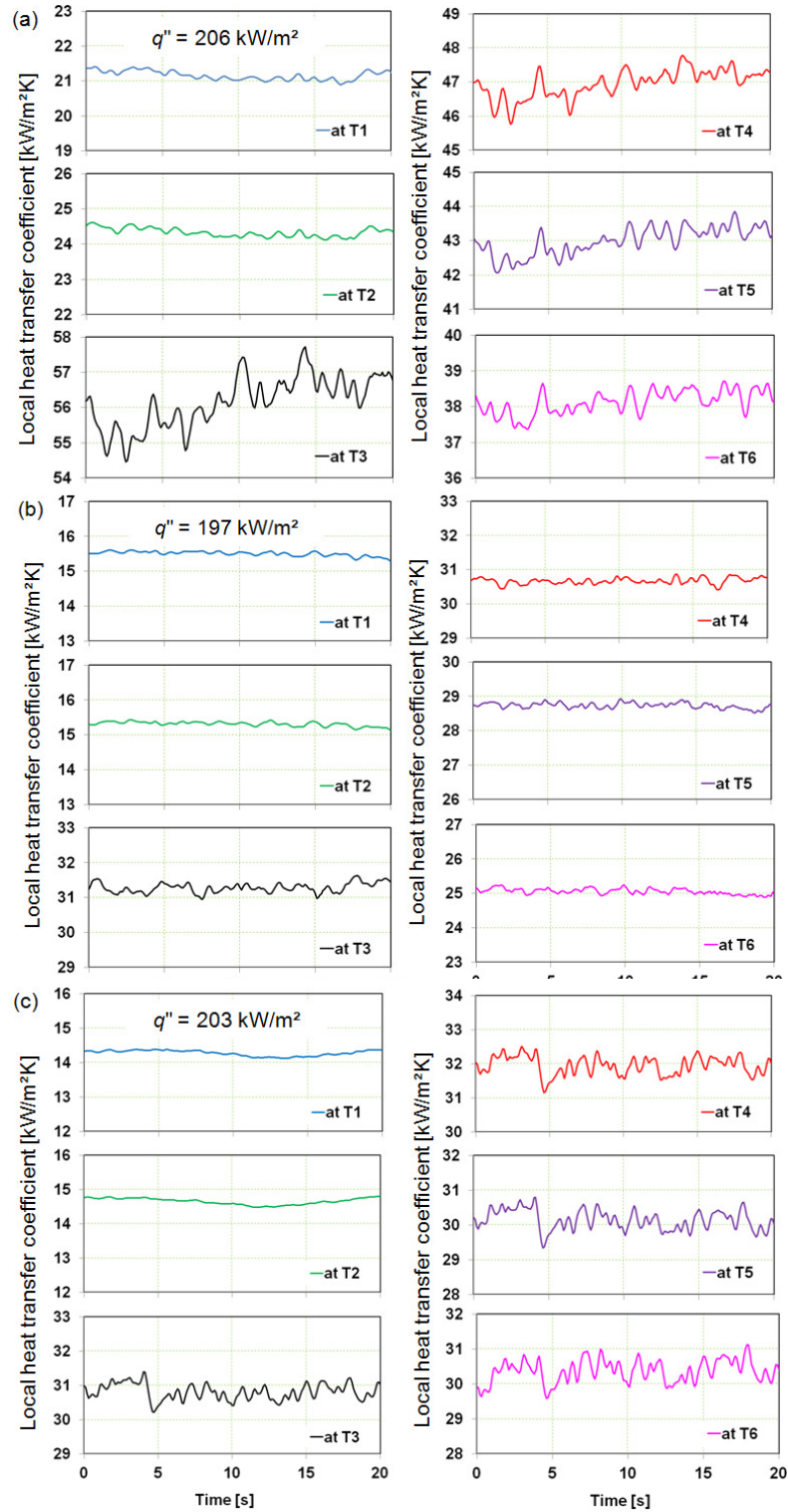


Figure 5.22 Fluctuation of local heat transfer coefficient at nominal mass flux of  $600 \text{ kg/m}^2\text{s}$ , inlet temperature and pressure of  $98^\circ\text{C}$  and  $125 \text{ kPa (abs)}$ : (a)  $D_h = 0.438 \text{ mm}$ , (b)  $D_h = 0.561 \text{ mm}$ , (c)  $D_h = 0.635 \text{ mm}$ .

## 5.5 Repeatability of measurements

The repeatability of the experimental results is an issue that may be raised in flow boiling studies particularly when the diameter becomes very small. As the size of channel decreases, accurate measurement and repeatability become increasingly difficult to achieve. Another factor possibly affecting repeatability is the difficulty in maintaining the condition of the heat transfer surface area. This is particularly the case for channels made of aluminium or copper. As is well known, the surfaces of such metals easily suffer fouling or deformation due to the thermal stress. When the former occurs the characteristics of the heat transfer may differ or become lower than when it was clean.

It is not the scope of the current study to investigate aging effects on the test sections, but it is considered important to know whether there is a day to day disparity in the measured local heat transfer coefficient. Hence the experiments were repeated for a single selected experimental condition for all test sections over a time period from two weeks to one month. Figure 5.23 presents the repeatability of the experiments at a nominal mass flux of  $600 \text{ kg/m}^2\text{s}$ , inlet temperature of  $98^\circ\text{C}$  and inlet pressure of  $125 \text{ kPa}$  (abs). The figure shows that the repeatability of measurement data is reasonable, especially at high heat fluxes. At low heat fluxes, repeatability is harder to achieve, which could be due to the onset of flow boiling generating larger fluctuations.

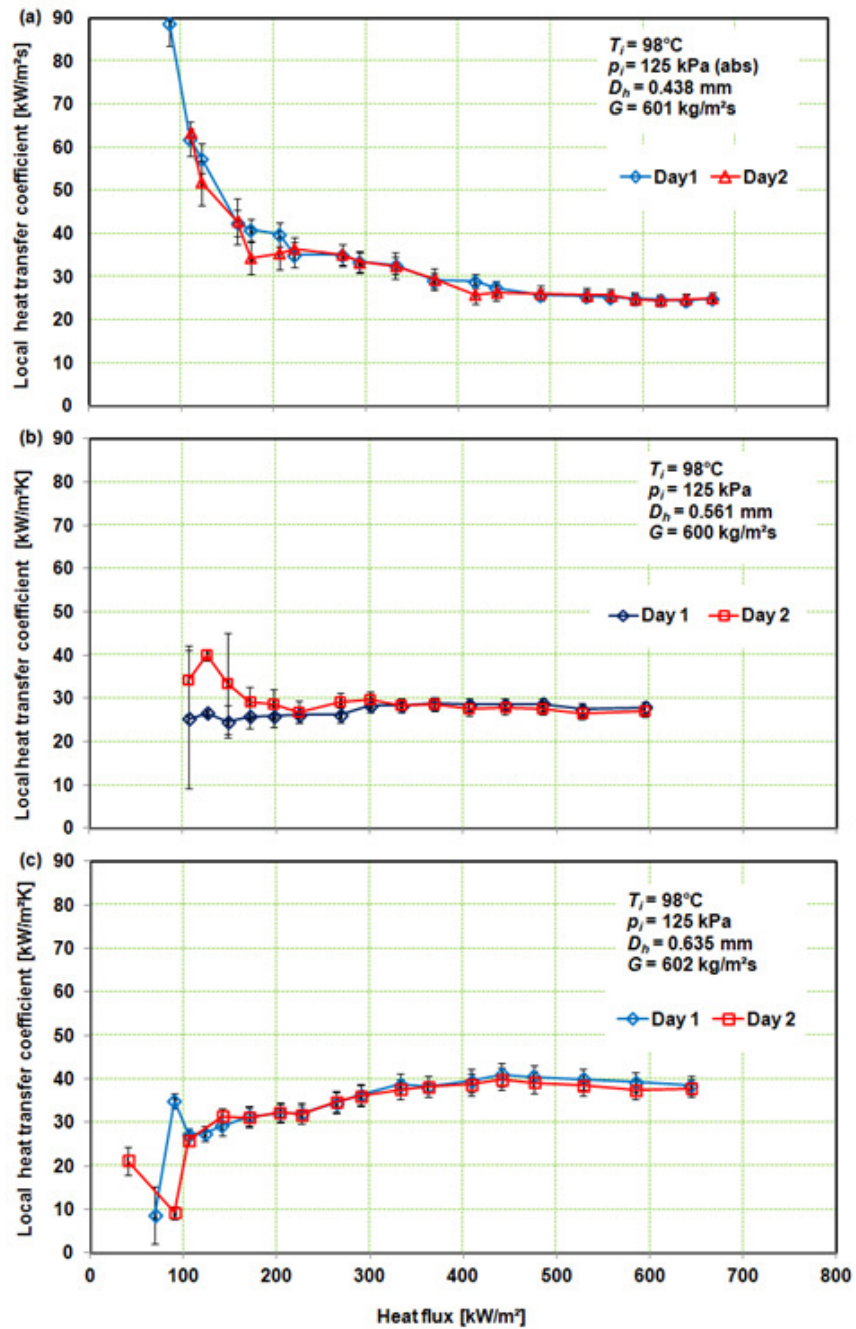


Figure 5.23 Repeatability of the local heat transfer measurement at a nominal mass flux of  $600\text{ kg/m}^2\text{s}$ , inlet pressure of  $125\text{ kPa}$ (abs) and inlet temperature of  $98^\circ\text{C}$  at  $z/L = 1$ : (a)  $D_h = 0.438\text{ mm}$ , (b)  $D_h = 0.561\text{ mm}$  and (c)  $D_h = 0.635\text{ mm}$ .

## 5.6 Comparison with flow boiling correlations

In this section, the experimental local heat transfer coefficients are compared with existing flow boiling heat transfer correlations, including correlations developed for macrochannels and mini/microchannels. The selected correlations are presented in Appendix A and the reason of choosing these correlations are given in Chapter 2.

### 5.6.1 Evaluation of macroscale correlations

A comparison of the experimental heat transfer coefficient with three widely used macroscale correlations developed for large diameter tubes has been performed and described in this section. The examined correlations include those of Shah (1982), Gungor and Winterton (1986) and Kandlikar (1990).

Figure 5.24 presents a comparison of experimental results with the macroscale correlations at a nominal mass flux of  $600 \text{ kg/m}^2\text{s}$ , at inlet temperature and pressure of  $98^\circ\text{C}$  and  $125 \text{ kPa}$  and at several heat fluxes. It should be noted that the experimental heat transfer coefficient data presented in Fig. 5.24 are calculated based on the temperature readings at near the outlet. From the figure, it is clear that all macroscale predictions increase almost linearly with heat flux. It indicates that the correlations developed for macroscale channels are strongly affected by the heat flux. The experimental heat transfer coefficient obtained in the  $0.561 \text{ mm}$  and  $0.635 \text{ mm}$  channels are nearly constant, whilst that obtained in the  $0.438 \text{ mm}$  channel decreases with an increase in the heat flux. The correlation of Kandlikar (1990) underestimates the experimental data for the  $0.561 \text{ mm}$  and  $0.635 \text{ mm}$  channels, whilst for the  $0.438 \text{ mm}$  channel underestimates the data at lower heat fluxes but over predicts the data at higher heat fluxes. Correlations of Shah (1982) and Gungor and Winterton (1987) always underestimate the data at lower heat fluxes but over predict the data at higher heat fluxes.

An analysis of the comparisons in more depth for all tested mass fluxes may be made via a MAE method, which can assess the accuracy of correlations in predicting the experimental data.

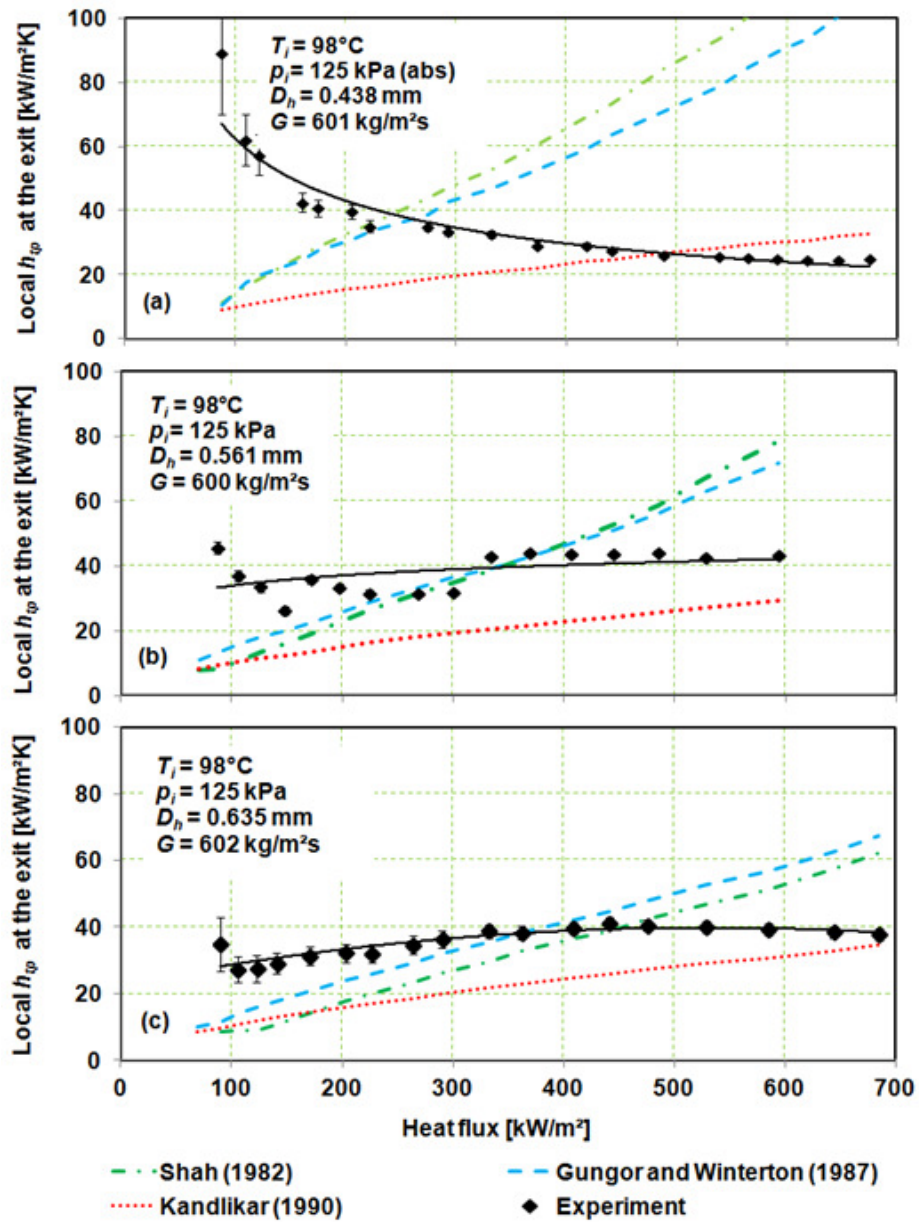


Figure 5.24 Experimental local heat transfer coefficient compared with macroscale predictions at a nominal mass flux of  $602 \text{ kg/m}^2\text{s}$ , inlet temperature of  $98^\circ\text{C}$  and inlet pressure of  $125 \text{ kPa (abs)}$ : (a)  $D_h = 0.438 \text{ mm}$ , (b)  $D_h = 0.561 \text{ mm}$  and (c)  $D_h = 0.635 \text{ mm}$ .

### Shah (1982)'s correlation

Shah (1982) selected nucleate and convective boiling terms for the total two-phase heat transfer coefficient. He found that the convective boiling depended only on the convective number  $Co$  rather than the Martinelli parameter ( $X$ ). On the other hand, the nucleate boiling was expressed only as a function of the boiling number  $Bo$ . Fig. 5.25 shows a comparison of the experimental data obtained in the three hydraulic diameter channels with the correlation proposed by Shah (1982). From the figure, it can be seen that the correlation of Shah (1982) cannot predict the experimental data accurately. It has MAEs of 86% for the 0.438 mm channel, 36.6% for the 0.561 mm channel and 47.4% for the 0.635 mm channel. A detail comparison is presented in Table 5.4.

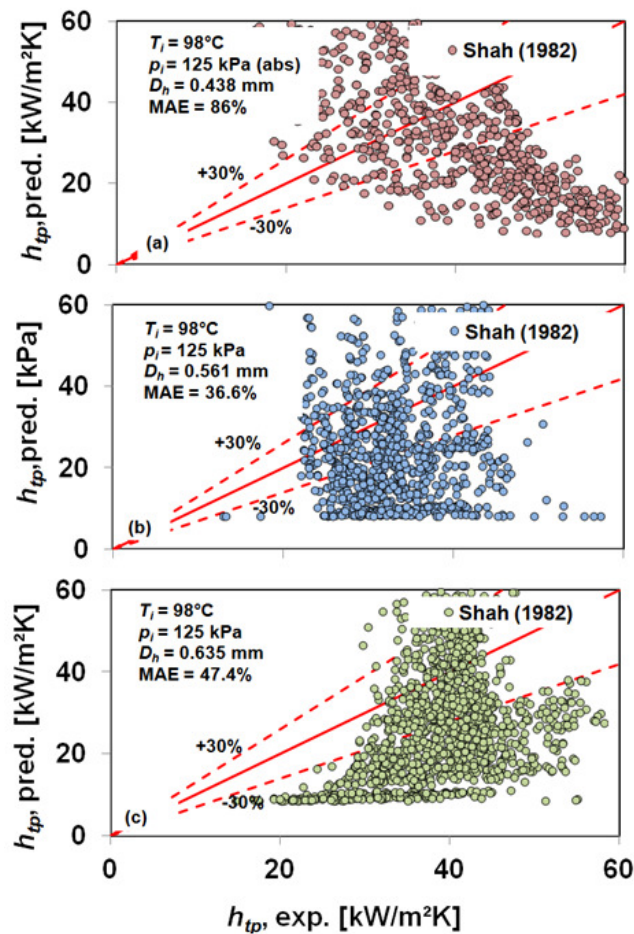


Figure 5.25 Comparison of experimental data with the correlation of Shah (1982): (a)  $D_h = 0.438$  mm, (b)  $D_h = 0.561$  mm and (c)  $D_h = 0.635$  mm channels.

### Gungor and Winterton (1987)'s correlation

Gungor and Winterton (1987) proposed a correlation based on 3700 data points for water, refrigerants and ethylene glycol. They modified the convective boiling enhancement factors ( $S$ ) to be a function of the Boiling number ( $Bo$ ) and ( $F$ ) to be a function of the Martinelli parameter ( $X$ ). Figure 5.26 presents the comparison of the experimental data with the correlation of Gungor and Winterton (1987). Similar to the correlation of Shah (1982), the correlation of Gungor and Winterton is also not accurate to predict the experimental data. The comparison results in MAEs of 70% for the 0.438 mm channel, 41.4% for the 0.561 mm channel and 47.3% for the 0.635 mm channel, see also Table 5.4.

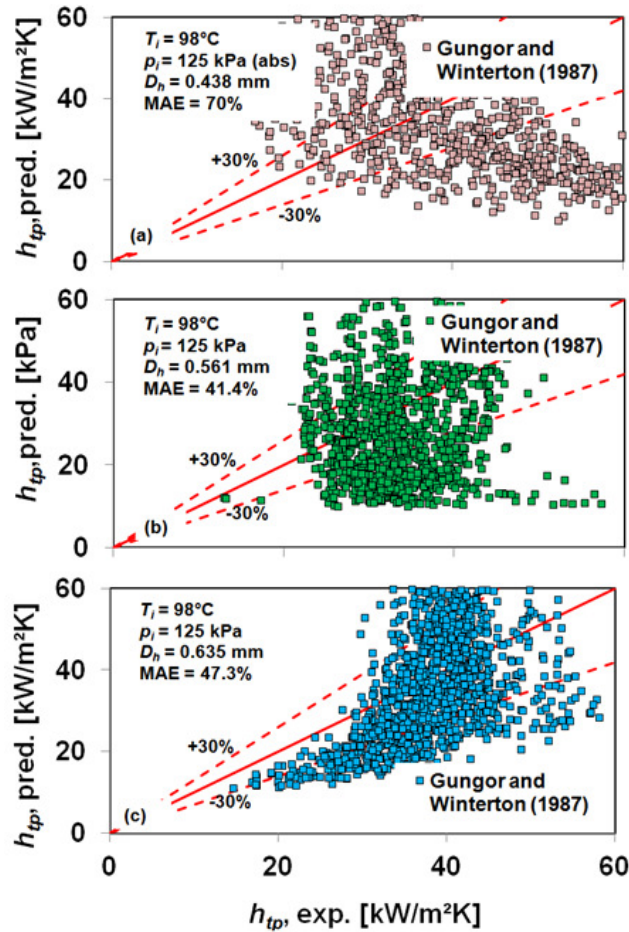


Figure 5.26 Comparison of experimental data with the correlation of Gungor and Winterton (1987): (a)  $D_h = 0.438$  mm, (b)  $D_h = 0.561$  mm and (c)  $D_h = 0.635$  mm channels.

### Kandlikar (1990)'s correlation

Kandlikar (1990) followed the same approach as Shah (1982) and proposed a general correlation for saturated flow boiling heat transfer in horizontal and vertical tubes. The correlation was developed based on a database consisting of 5264 data points including water and refrigerants,  $D = 4.6 - 32$  mm and vapour qualities up to 0.98. Kandlikar assumed that the contribution of nucleate and convective boiling mechanisms was noted by the convective number. When the convective number is greater than 0.65, the nucleate boiling is the dominant mechanism, but when  $Co$  is less than 0.65, convective boiling is the dominant mechanism.

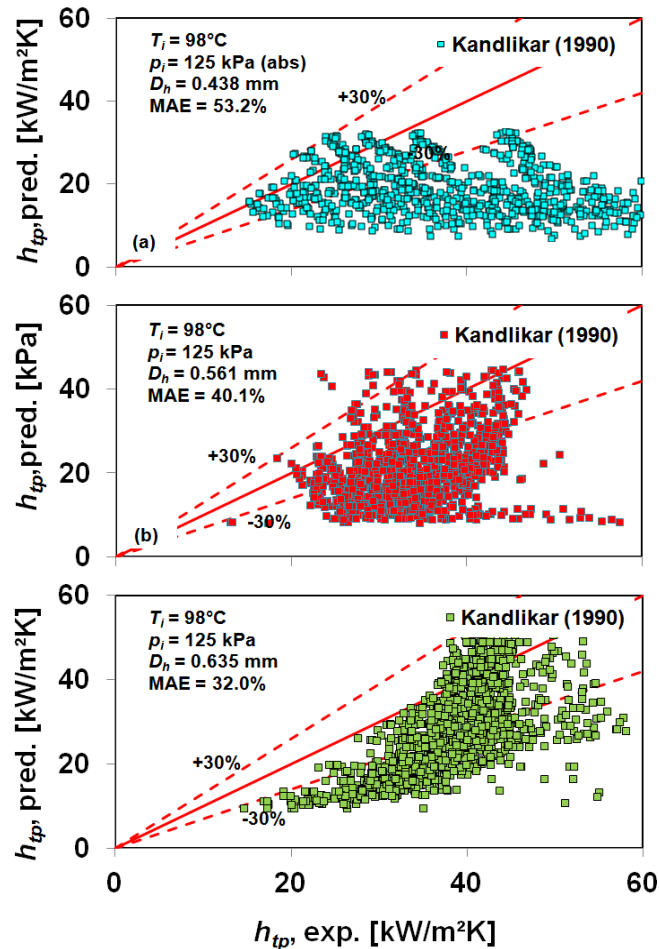


Figure 5.27 Comparison of experimental data with the correlation of Kandlikar (1990): (a)  $D_h = 0.438$  mm, (b)  $D_h = 0.561$  mm and (c)  $D_h = 0.635$  mm channels.

Kandlikar used the same dimensionless numbers as Shah namely the convection number and the boiling number to correlate the convective and nucleate boiling terms, respectively. The effect of fluid type was incorporated using a fluid dependent parameter ( $F_{fl}$ ) in the nucleate boiling term. This parameter works as a correction factor that accounts for all other parameters influencing nucleate boiling. Figure 5.27 compares the experimental data of heat transfer coefficient with the correlation of Kandlikar (19990). The correlation has MAEs of 53.2% for the 0.438 mm channel, 40.1% for the 0.561 mm channel and 32.0% for the 0.635 mm channel. A more detail comparison is provided in Table 5.4.

### 5.6.2 Evaluation of small to microscale correlations

A comparison of the experimental heat transfer coefficient with seven correlations developed for small to microchannels was conducted and discussed in this section. The tested correlations include those of Lazarek and Black (1982), Kew and Cornwell (1997), Yu et al. (2002), Warriar et al. (2002), Lee and Mudawar (2005), Sun and Mishima (2009) and Li and Wu (2010).

The trend of experimental data for the 0.438 mm decreases sharply with the heat flux at lower heat fluxes, then almost constant at higher heat fluxes. This could be due to the heat transfer mechanism. As the heat transfer coefficient was obtained at the thermocouple 6 (near the outlet), where the flow patterns were dominated by annular flow, so the heat transfer mechanism could be convective boiling. For other channels, at lower heat fluxes, the trends increase then at higher heat fluxes, the trends were almost independent on heat flux. The constant trends, similarly to that in the 0.438 mm channel, were due to the convective heat transfer. The trends of several correlations show increase at lower heat fluxes but are also almost constant at higher heat fluxes. However, correlations proposed by Warriar et al. (2002), Lee and Mudawar (2005) and Li and Wu (2010) are nearly constant. Figure 5.28 shows a comparison of experimental heat transfer coefficient data with the small to microscale correlations at a nominal mass flux of 600 kg/m<sup>2</sup>s, at inlet temperature and pressure of 98°C and 125 kPa and at several heat fluxes. Similar to Fig. 5.24, the experimental data presented in Fig. 5.28 were obtained by calculating the heat transfer coefficient based on temperature readings near the outlet. The correlation of Warriar et al. (2002) always underestimates the

experimental data for three channels. That was probably due to the correlations based on the single-phase four heated walls Nusselt number for fully developed flow which depended on the aspect ratio of the channel. For the 0.438 mm channel, however, the correlation is close to the experimental data at heat fluxes of 500 kW/m<sup>2</sup> and more. Similarly, the correlation of Lee and Mudawar (2005) is close to the experimental data at heat fluxes of above 500 kW/m<sup>2</sup> for the 0.438 mm channel, but underestimates the data at lower heat fluxes. For the 0.561 mm channel, the correlation agrees well with the experimental data at heat fluxes lower than 300 kW/m<sup>2</sup>, but underestimates the data at higher heat fluxes. For the 0.635 mm channel, the correlation agrees well with the experimental data at heat fluxes greater than 300 kW/m<sup>2</sup>, but over predicts the data at lower heat fluxes. The correlations of Lazarek and Black (1982), Kew and Cornwell (1997), Yu et al. (2002) and Sun and Mishima (2009) over predict the experimental data at higher heat fluxes, but underestimate the data at lower heat fluxes for the 0.438 mm and 0.635 mm channels. For the 0.561 mm channel, correlations of Lazarek and Black (1982), Kew and Cornwell (1997) and Yu et al. (2002) agree with the experimental data at heat fluxes of 150 kW/m<sup>2</sup> or greater. To have more detail comparisons, an MAE method is used and given in Figs. 5.29 to 5.36 for each correlation.

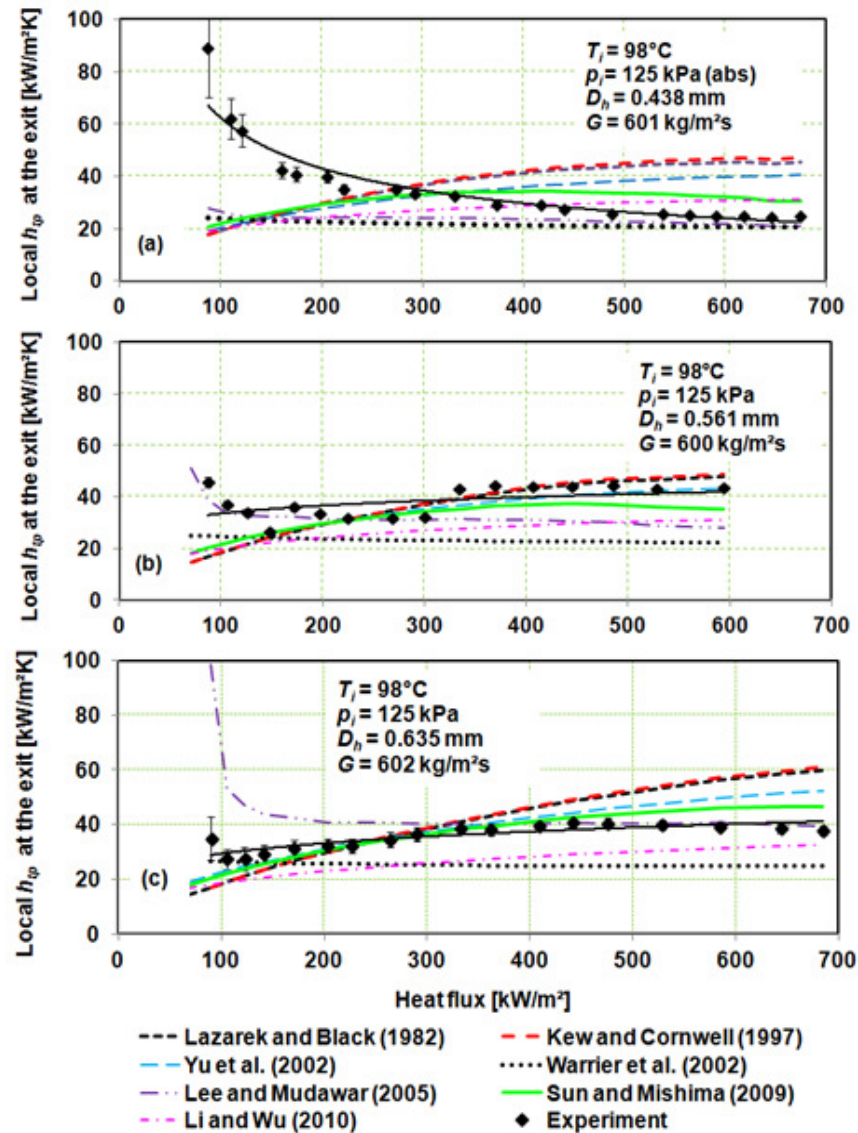


Figure 5.28 Experimental local heat transfer coefficient compared with small to microscale predictions at a nominal mass flux of  $600\text{ kg/m}^2\text{s}$ , inlet temperature of  $98^\circ\text{C}$  and inlet pressure of  $125\text{ kPa (abs)}$ : (a)  $D_h = 0.438\text{ mm}$ , (b)  $D_h = 0.561\text{ mm}$  and (c)  $D_h = 0.635\text{ mm}$ .

### Lazarek and Black (1982)'s correlation

As shown in the Appendix A, the correlation proposed by Lazarek and Black (1982) contains variables Reynolds number and Boiling number. This indicates that the correlation was intended to predict the experimental data which depended strongly on the Reynolds number and heat flux. The correlation was proposed for flow boiling of

refrigerant R113 in small tubes with an inner diameter of 3.1 mm. However, this correlation is selected to be compared with the experimental data because there was an effect of heat flux detected in this work. As shown in Fig. 5.29, the correlation gives MAEs of 45.7% for the 0.438 mm channel, 36.9% for the 0.561 mm channel and 22.7% for the 0.635 mm channel. From the MAE, it can be seen that as the hydraulic diameter decreases, the accuracy of the correlation decreases.

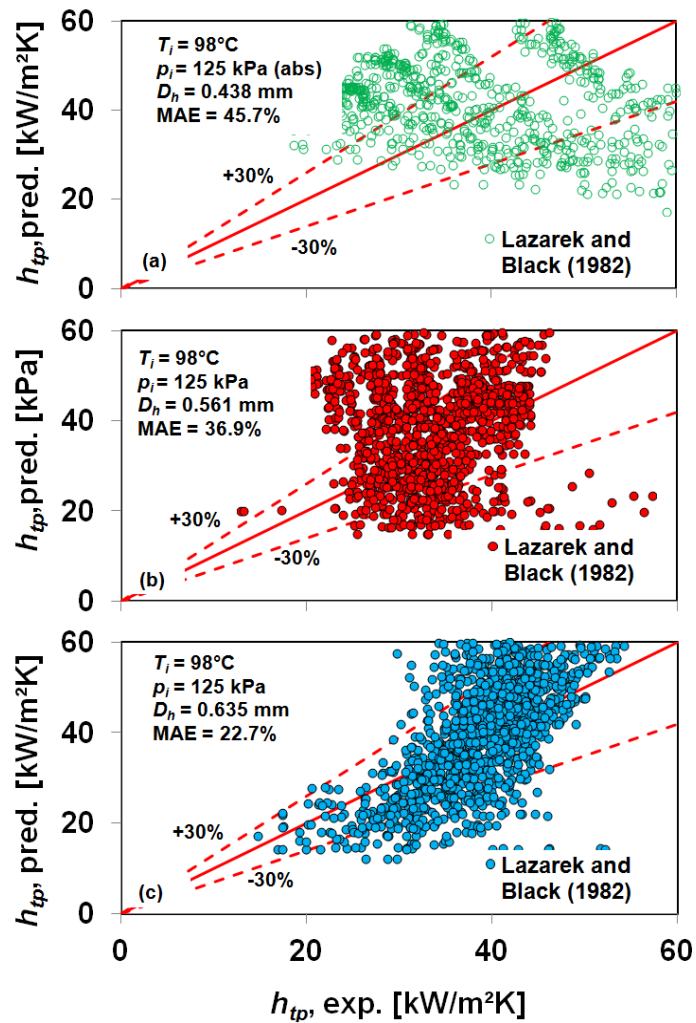


Figure 5.29 Comparison of experimental data with the correlation of Lazarek and Black (1982): (a)  $D_h = 0.438$  mm, (b)  $D_h = 0.561$  mm and (c)  $D_h = 0.635$  mm channels.

### Kew and Cornwell (1997)'s correlation

The correlation proposed by Kew and Cornwell was obtained by modifying the correlation of Lazarek and Black (1982). They multiplied the correlation of Lazarek and

Black by factor  $(1-x)^{-0.143}$  because they found the effect of quality. As the quality increased, the heat transfer coefficient increased, but at the mass flux of 1480 kg/m<sup>2</sup>s, it decreased with quality. The correlation was used by the authors to predict flow boiling heat transfer coefficient of R141b and water in tubes with diameters ranging from 1.39 to 3.39 mm. From the comparison, see Fig. 5.30, it shows that the correlation gives MAEs of 46.7% for the 0.438 mm channel, 37.4% for the 0.561 mm channel and 23.0% for the 0.635 mm channel. This correlations show less accurate than that of Lazarek and Black (1982), see Table 5.4 the MAE of Lazarek and Black is smaller than that of Kew and Cornwell. However, similar to that of Lazarek and Black, it demonstrates that as the hydraulic diameter decreases the accuracy of the correlation decreases too.

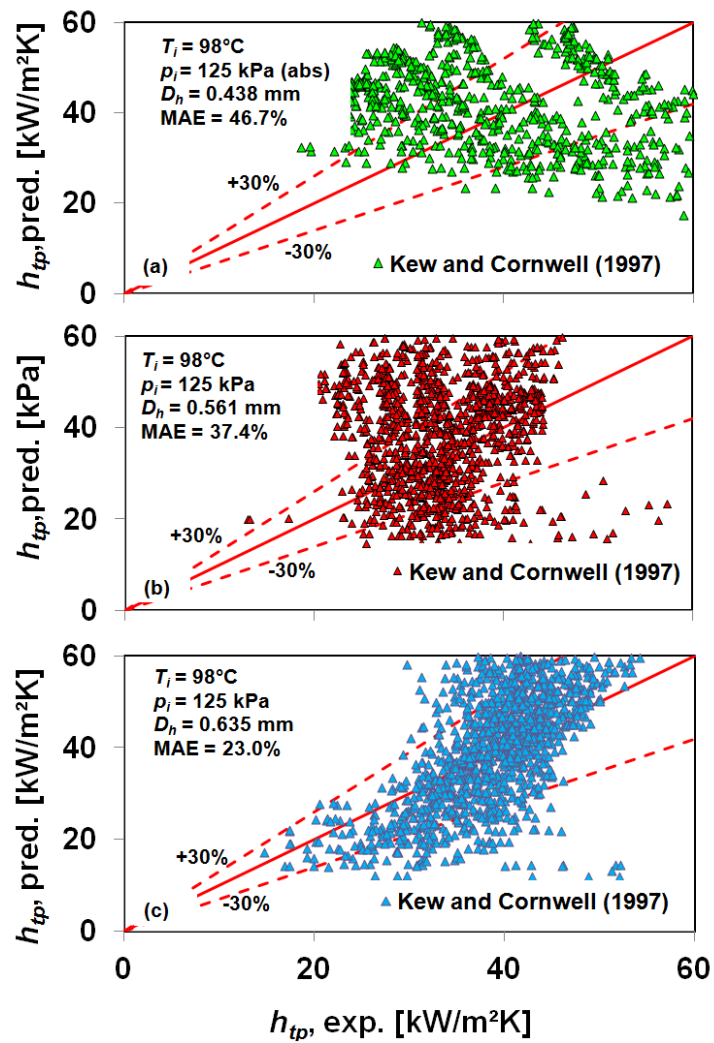


Figure 5.30 Comparison of experimental data with the correlation of Kew and Cornwell (1997): (a)  $D_h = 0.438 \text{ mm}$ , (b)  $D_h = 0.561 \text{ mm}$  and (c)  $D_h = 0.635 \text{ mm}$  channels.

### Yu et al. (2002)'s correlation

The correlation of Yu et al. (2002) was used to predict flow boiling of water in a horizontal tube with diameter of 2.98 mm. the correlation comprises Boiling number and Weber number. In terms of MAE, see Fig. 5.31, the correlation predicts the experimental data with MAEs of 38.2% for the 0.438 mm channel, 24.2% for the 0.561 mm channel and 14.1% for the 0.635 mm channel. Despite the simplicity, the correlation is more accurate to predict the experimental data, however, similar to the former correlations, the accuracy decreases as the hydraulic diameter decreases.

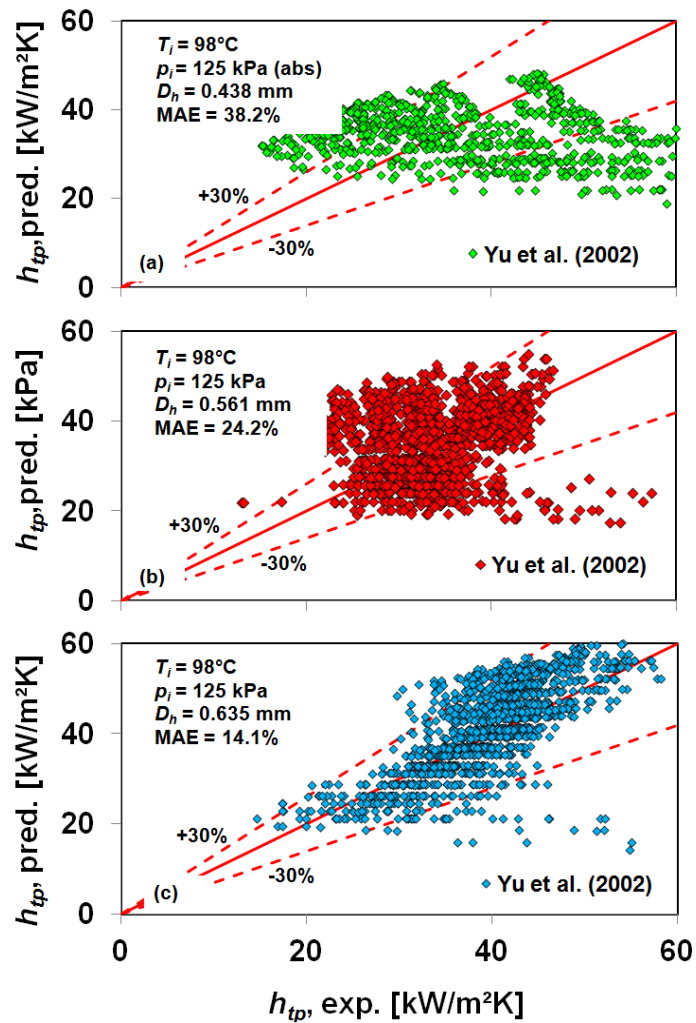


Figure 5.31 Comparison of experimental data with the correlation of Yu et al. (2002): (a)  $D_h = 0.438$  mm, (b)  $D_h = 0.561$  mm and (c)  $D_h = 0.635$  mm channels.

### Warrier et al. (2002)'s correlation

The correlation was developed to predict the data of saturated flow boiling of FC-84 in rectangular horizontal channel with a hydraulic diameter of 0.75 mm and uniform heat flux. The correlation consists of Boiling number and quality and based on single-phase Nusselt number for four heated walls. As shown in Fig. 5.32, the correlation can give MAEs of 41.7% for the 0.438 mm channel, 28.0% for the 0.561 mm channel and 29.8% for the 0.635 mm channel. Again, the correlation shows the decrease in accuracy as the hydraulic diameter decreases.

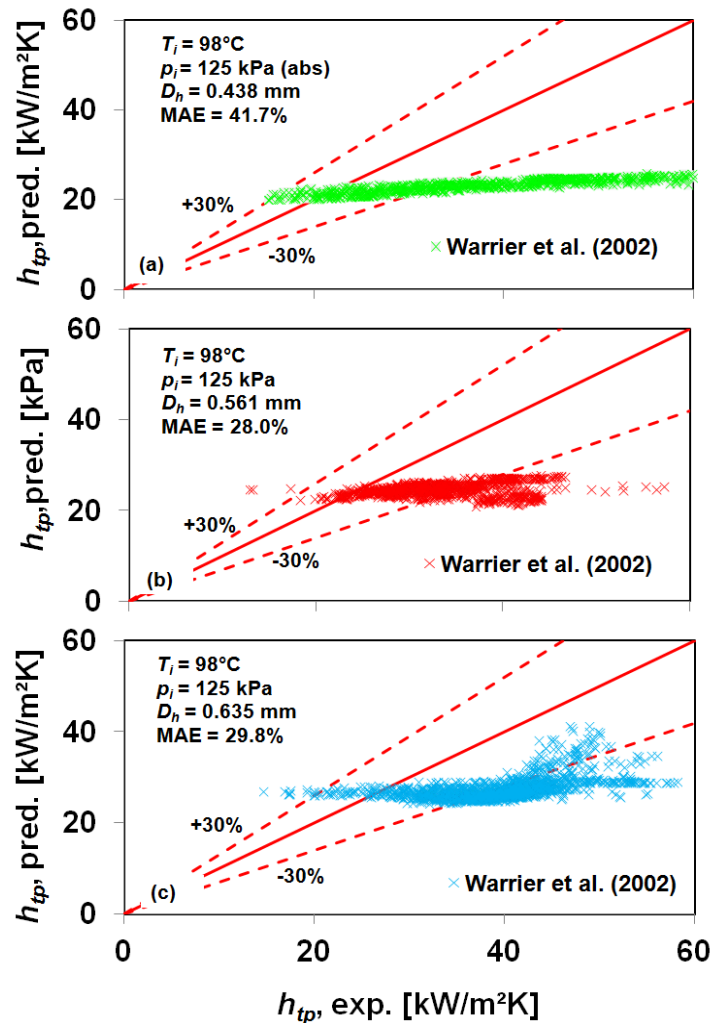


Figure 5.32 Comparison of experimental data with the correlation of Warrier et al. (2002): (a)  $D_h = 0.438$  mm, (b)  $D_h = 0.561$  mm and (c)  $D_h = 0.635$  mm channels.

### Lee and Mudawar (2005)'s correlation

Similar to that of the correlation proposed by Warriar et al. (2002), a correlation of Lee and Mudawar (2005) was also for flow boiling in rectangular channel and based on single-phase Nusselt number but for fluid types such as water and refrigerant R134a. This applied for a channel with a hydraulic diameter of 0.347 mm. The correlation can be seen in Appendix A and consist of Boiling number, Weber number and Martinelli parameter.

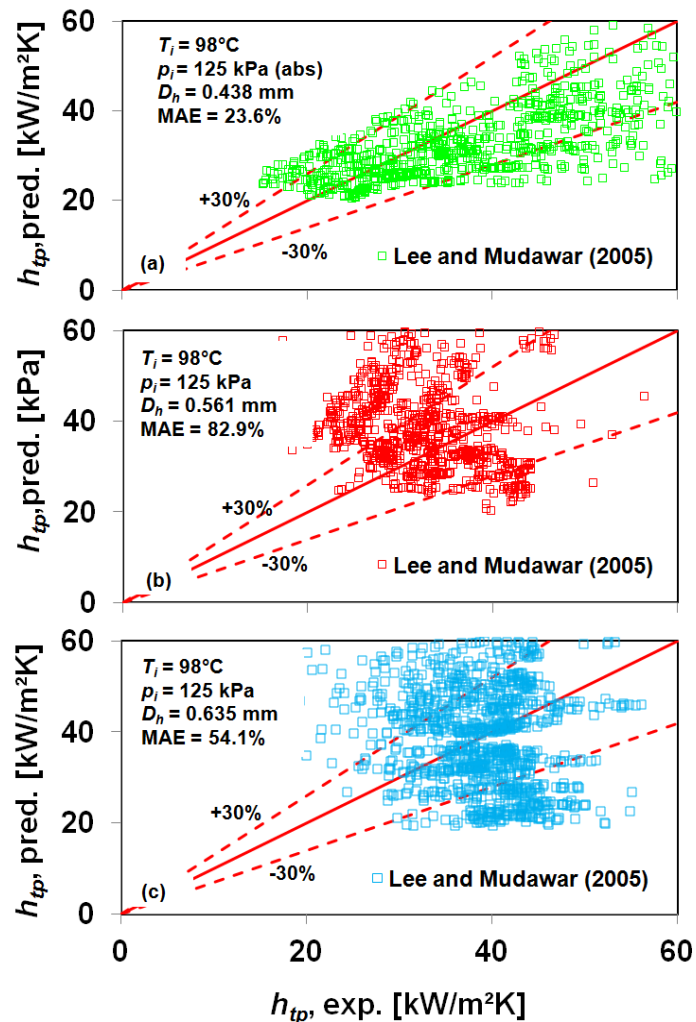


Figure 5.33 Comparison of experimental data with the correlation of Lee and Mudawar (2005): (a)  $D_h = 0.438$  mm, (b)  $D_h = 0.561$  mm and (c)  $D_h = 0.635$  mm channels.

From Fig. 5.33, the correlation results in MAEs of 23.6% for the 0.438 mm channel, 82.9% for the 0.561 mm channel and 54.1% for the 0.635 mm channel. The effect of

channel diameter on the accuracy of the correlation is not clear because the MAE is not in order with the decrease in hydraulic diameter.

### Sun and Mishima (2009)'s correlation

A correlation proposed by Sun and Mishima (2009) was intended for small to microchannels with diameters ranging from 0.21 to 6.05 mm and for 11 different fluid types. The correlation includes Reynolds number, Boiling number and Weber number and based on 2505 flow boiling data sets.

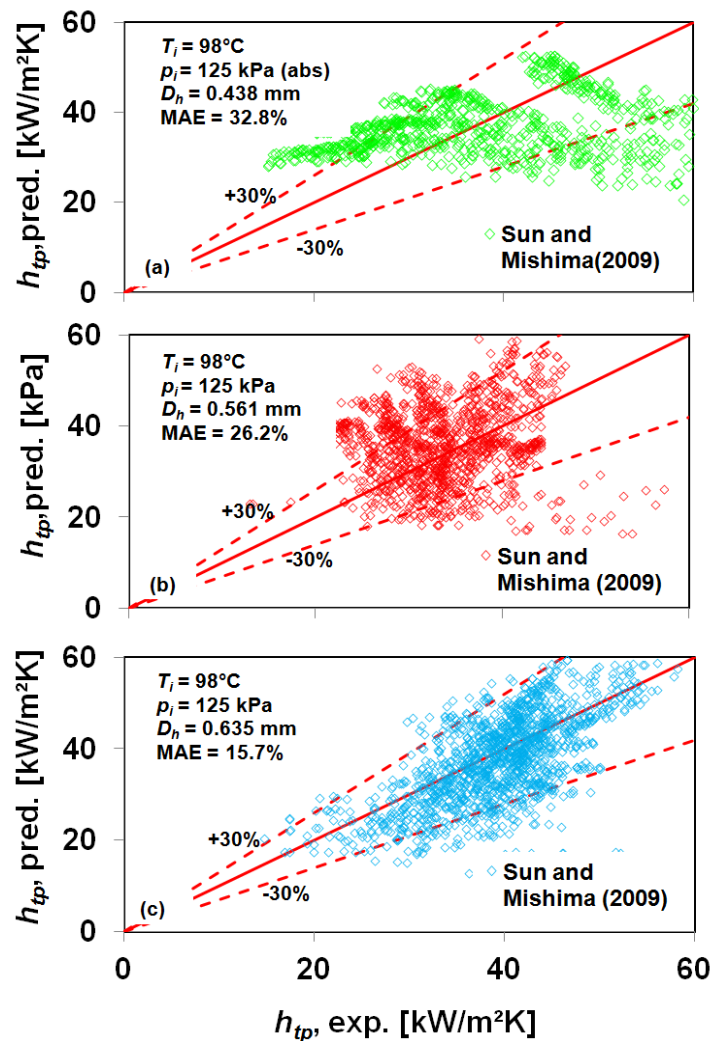


Figure 5.34 Comparison of experimental data with the correlation of Sun and Mishima (2009): (a)  $D_h = 0.438$  mm, (b)  $D_h = 0.561$  mm and (c)  $D_h = 0.635$  mm channels.

Figure 5.34 demonstrates that the correlation predicts the experimental data with MAEs of 32.8% for the 0.438 mm channel, 26.2% for the 0.561 mm channel and 15.7% for the 0.635 mm channel. A mode detail comparison is provided in Table 5.4.

### Li and Wu (2010)'s correlation

The correlation of Li and Wu (2010) was obtained least square regression method from 769 experimental data covering twelve fluid types and for flow boiling in tubes with diameters ranging from 0.148 to 3.25 mm. This correlation comprises of Boiling number, Bond number and Reynolds number.

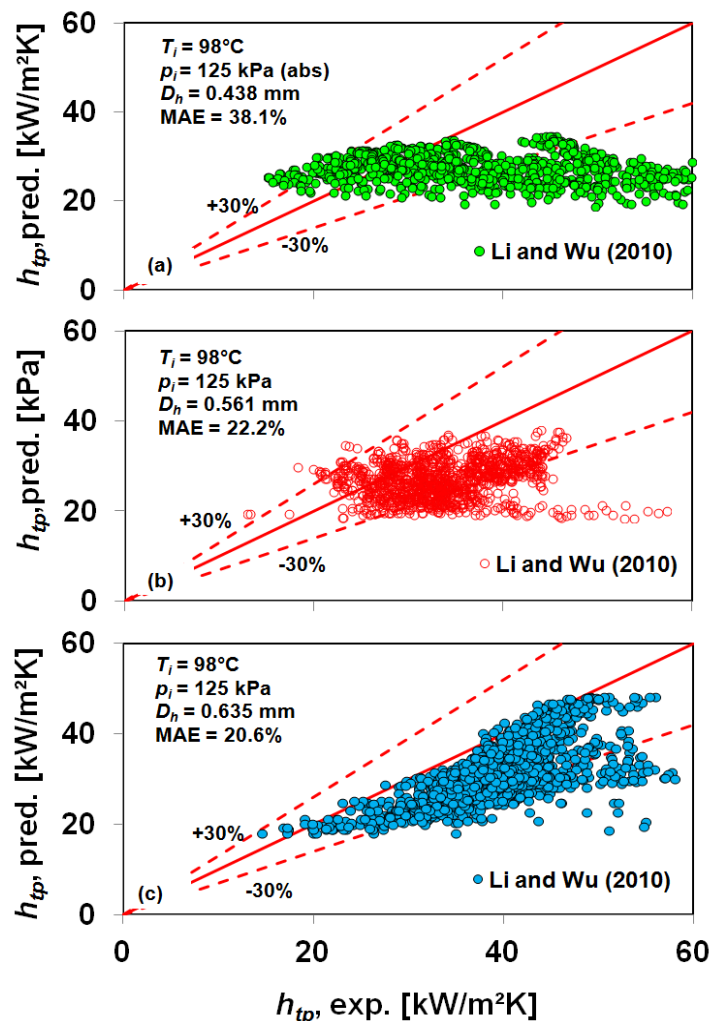


Figure 5.35 Comparison of experimental data with the correlation of Li and Wu (2010): (a)  $D_h = 0.438 \text{ mm}$ , (b)  $D_h = 0.561 \text{ mm}$  and (c)  $D_h = 0.635 \text{ mm}$  channels.

The comparison of experimental data with this correlation gives MAEs of 38.1% for the 0.438 mm channel, 22.2% for the 0.561 mm channel and 20.6% for the 0.635 mm channel. This correlation results in order of MAE with a decrease in hydraulic diameter. A more detail comparison can be seen in Table 5.4.

Table 5.4 Mean absolute error (MAE) and the percentage of data within the  $\pm 30\%$  error bands for all evaluated correlations.

Correlation	$D_h = 0.438$ mm		$D_h = 0.561$ mm		$D_h = 0.635$ mm	
	MAE %	$\beta$ %	MAE %	$\beta$ %	MAE %	$\beta$ %
Shah (1982)	86.0	17.5	36.6	50.5	47.4	30.3
Lazarek and Black (1982)	45.7	36	36.9	51.8	22.7	70.9
Gungor and Winterton (1987)	70	22.2	41.4	41.6	47.3	45.9
Kandlikar (1990)	53.2	22.7	40.1	31.2	32.0	44.0
Kew and Cornwell (1997)	46.7	35.4	37.4	51.6	23.0	70.2
Yu et al. (2002)	38.2	38.8	24.2	69.5	14.1	90.0
Warrier et al. (2002)	41.7	29.4	28.0	62.5	29.8	42.0
Lee and Mudawar (2005)	23.6	73	82.9	41.6	54.1	47.9
Sun and Mishima (2009)	32.8	50.1	26.2	66.1	15.7	87.6
Li and Wu (2010)	38.1	39.7	22.2	76.1	20.6	78.1

## **5.7 Summary**

Experimental flow patterns, flow pattern maps and heat transfer results in the three microchannel test sections have been presented and conclusions for this Chapter can be drawn in the following paragraphs.

### **5.7.1 Flow patterns and flow pattern maps**

The typical flow patterns observed in the three microchannel test sections are the same, namely bubbly, slug, churn and annular. Based on the observation location taken near the outlet, the flow patterns found were slug, churn and annular. The heat flux has a clear effect on the flow pattern, as the heat flux is increased, the flow patterns change, e.g. from bubbly to slug, from slug to churn and from churn to annular. However, the effect of mass flux on the pattern is not clear, see Table 5.2. There is no clear effect of size reduction on the flow pattern for these experimental conditions and channel dimensions, see Table 5.3. Existing flow pattern maps, e.g. Triplett et al. (1999), Hassan et al. (2005), Wang et al. (2011) and Chen et al. (2006) cannot predict well the experimental data. The flow pattern map proposed by Sobierska et al. (2006) in the form of mass flux versus quality successfully predicted the experimental data and it did not depend on the hydraulic diameter of the channel. The discrepancies between the observed flow patterns and published results could be due to the lack of agreed standards of flow pattern definition. In general, the flow patterns observed in this work are the same as those found at the macroscale.

### **5.7.2 Heat transfer characteristics**

The effect of heat flux on the local heat transfer coefficient is significant. However, as the mass flux and vapour quality increase the local heat transfer coefficient decreases for the 0.438 mm and 0.561 mm channels. The decrease in the local heat transfer coefficient with quality and mass flux was due to the high pressure drop. As the pressure drop increased, the local pressures decreased and the local saturation liquid temperatures decreased too. However, as the effect of heat flux on the local heat transfer coefficient is significant, then the mechanism of heat transfer is nucleate boiling. For the 0.635 mm channel, the effect of heat flux is clear but weakly affected by the mass flux and vapour quality, indicating that nucleate boiling was the dominant heat transfer mechanism. The effect of heat flux on the average heat transfer coefficient is not

significant for the 0.438 mm channel, but is significant for the 0.561 mm and 0.635 mm channels. A reduction in channel size increases the average heat transfer coefficient, over the range of heat fluxes lower than 500 kW/m<sup>2</sup>. The effect of hydraulic diameter on the heat transfer fluctuation is not clear and needs further investigation.

### **5.7.3 Comparisons with existing heat transfer coefficient correlations**

The experimental local heat transfer coefficient has been compared with existing published correlations available in the open literature. In general, the correlations are poor to predict the experimental data. Furthermore, as the size of the channel decreases, the data are difficult to predict. Therefore, the correlations predict the data with high MAEs ranging from 14.1% to 82.9%. From the comparisons, recommended correlations to be used are the correlation proposed by Lee and Mudawar (2005) for the 0.438 mm channel, the correlation of Li and Wu (2010) for the 0.561 mm channel and the correlation of Yu et al. (2002) for the 0.635 mm channel.

## Chapter 6

### Flow Boiling Pressure Drop: Results and Discussion

#### 6.1 Introduction

This chapter presents and discusses the experimental results for flow boiling pressure drop, together with examples of pressure fluctuation obtained in the three test sections. Basically, as stated in Chapter 2, the flow boiling pressure drop is affected by the mass flux, heat flux and size of the channel. However, the existing published data, as briefly reviewed in Chapter 2, are obtained from experiments using substantial differences in experimental conditions, working fluids and channel shapes/geometries, so that they are difficult to compare directly with each other. In this work, the uncertainty and influence of differences in the parameters investigated were reduced as much as possible. Firstly, the test sections covering three different hydraulic diameters, were made from the same material, and had the same geometry, namely the same depth and length. Secondly, identical experiments were performed on each test section, using the same working fluid (deionized water) and the same conditions, such as inlet pressure, inlet temperature, mass flux and heat flux.

An introduction to this Chapter is given in Section 6.1. Presentation and discussions of the two-phase pressure drop is provided in Section 6.2 and pressure and drop fluctuation is given and discussed in Section 6.3. Section 6.4 describes comparisons with existing two-phase flow pressure drop correlations and Section 6.5 is a brief chapter summary.

#### 6.2 Two-phase pressure drop

As the pressure gradient along the test section was assumed to be linear, particularly in calculating the local heat transfer coefficient, the inlet and outlet pressure played the most important roles in the flow boiling experiments. Hence, these two pressure sensors had to work properly and accurately. To ensure the inlet and outlet pressure transducers worked reliably, a friction factor test was conducted using a stainless steel tube with an inner diameter of 1.14 mm. This is shown in Fig. 4.1 in Chapter 4, and the results showed good agreement with the theory,  $fRe = 16$ .

### 6.2.1 Effect of hydraulic diameter on two-phase pressure drop

In the experiments, the inlet and outlet pressures were recorded directly and individually. Therefore, the experimental channel pressure drop was calculated by subtracting the measured outlet pressure from the measured inlet pressure. This is given by Eq. (3.2) in Chapter 3. However, since the channels were not equipped with a calming section, the pressure losses in the inlet and outlet plenums, due to the 90 degree turns and sudden contraction and enlargement, needed to be carefully considered. The inlet pressure loss can be estimated using Eq. (3.4) in Chapter 3 with a modification, rearranging it as

$$\Delta p_i = \frac{1}{2} \rho \bar{V}_p^2 K_{90} + \frac{1}{2} \rho \bar{V}_{ch}^2 K_c \quad (6.1)$$

The channel pressure drop was then obtained by subtracting the inlet pressure losses,  $\Delta p_i$  from the measured pressure drop and given by

$$\Delta p_{ch} = \Delta p_{meas} - \Delta p_i \quad (6.2)$$

The total channel pressure drop calculated using Eq. (6.2) may include the single-phase pressure drop particularly for the subcooled region, since the liquid entering the inlet channel is in a subcooled condition. To obtain the two-phase pressure drop, the single-phase pressure drop should be subtracted from the total channel pressure drop. The single-phase pressure drop existing in the subcooled region,  $\Delta p_{sp}$ , is calculated using Eq. (6.3) and the two-phase pressure drop,  $\Delta p_{tp}$ , is obtained using Eq. (6.4). It should be noted that the apparent friction factor,  $f_{app}$ , is given in Eq. (3.16) in Chapter 3.

$$\Delta p_{sp} = \frac{2f_{app}G^2}{\rho_l D_h} L_{sub} \quad (6.3)$$

$$\Delta p_{tp} = \Delta p_{ch} - \Delta p_{sp} \quad (6.4)$$

As demonstrated by many researchers, a decrease in channel size increases the pressure drop, whether for single-phase or two-phase flows. This is fairly obvious because the pressure drop varies inversely with the channel diameter. In single-phase flow

experiments, the decrease in hydraulic diameters from 0.635 mm to 0.561 mm and from 0.561 mm to 0.438 mm increased the pressure drops by approximately 35% and 91% respectively. In flow boiling experiments, decreasing the hydraulic diameters from 0.635 mm to 0.561 mm and from 0.561 mm to 0.438 mm increased the two-phase pressure drop by approximately 105% and 16% respectively, as shown in Fig. 6.1.

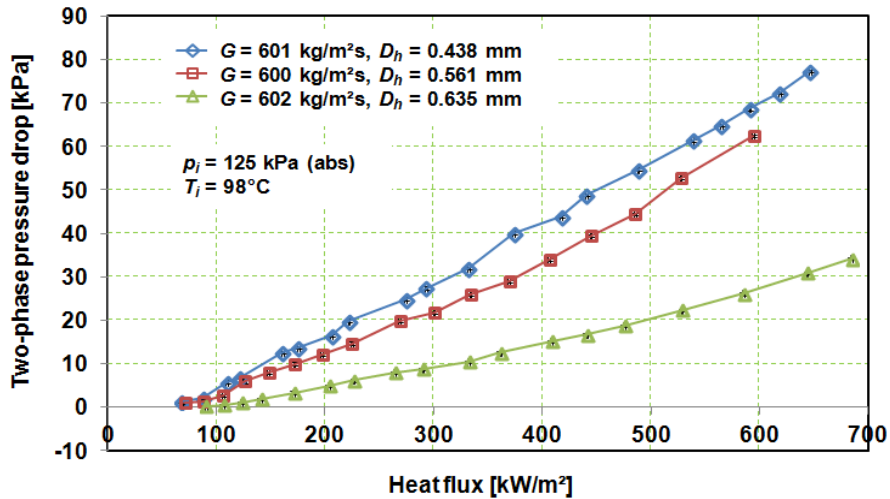


Figure 6.1 Two-phase pressure drop versus heat flux at almost the same mass flux for the 0.438 mm, 0.561 mm and 0.635 mm channels.

The difference in pressure drop obtained in the 0.438 mm and 0.561 mm channels is quite small which contradicts the results for single-phase flow. In single-phase flow for fully developed flow in a circular tube, the increase in pressure drop due to the decrease in diameter is approximately  $D^{-5}$ . The higher two-phase pressure drop for the 0.561 mm channel was probably due to the two components of pressure drop still increased in the range of tested heat fluxes; see Fig. 6.2(b). In the smallest test section,  $D_h = 0.438$  mm, the frictional pressure drop started to decrease at the heat flux of approximately 440 kW/m<sup>2</sup>, see Fig. 6.2(a), therefore the pressure drop slope for the 0.438 mm was only slightly higher than that of test section two. Thus, the effect of hydraulic diameter on the two-phase pressure drop is not proportional to  $D^{-5}$ , but also dependent on the contribution of the two components of pressure drop. When all components of pressure drop increase altogether, then the effect of hydraulic diameter on the two-phase pressure drop is big, e.g. the decrease of hydraulic diameter from 0.635 mm to 0.561 mm. From the above results, there is an indication that smaller diameter causes the frictional

pressure drop component to decrease earlier. This is due to the fact that at the same mass flux and heat flux, the smaller channel results in higher vapour quality, see explanations in Chapter 5. At higher vapour quality, the contribution of frictional pressure drop decreases because the influence of viscosity decreases. However, this needs further investigation, e.g. for smaller channel diameters, less than 0.4 mm.

As demonstrated by the results of Lockhart-Martinelli (1949), Qu and Mudawar (2003), Lee and Garimella (2008), and Saisorn and Wongwises (2008), the two-phase pressure drop is comprised of three components (for vertical channels) or two components (for horizontal channels). In this study, the channels were horizontal, so the two-phase pressure drop consisted of:

1. Accelerational pressure drop and
2. Frictional pressure drop.

The accelerational pressure drop was due to the movement and growth of bubbles, and estimated using the accelerational pressure drop equation of Mishima and Hibiki (1996). This involved the void fraction and flow quality at the outlet and is given by

$$\Delta p_a = G^2 v_l \left[ \frac{x_o^2}{\alpha_o} \left( \frac{v_g}{v_l} \right) + \frac{(1-x_o)^2}{1-\alpha_o} - 1 \right] \quad (6.5)$$

where  $\alpha_o$  is the void fraction, see Appendix A for more detail. Alternatively, it also can be predicted using correlations proposed by Lockhart-Martinelli (1949). However, that of Mishima & Hibiki (1996) was more accurate in predicting the two-phase pressure drop multiplier. For comparison purposes, both correlations were used.

The two-component pressure drop explained previously means that the experimental two-phase frictional pressure drop may be determined by subtracting the accelerational pressure drop from the calculated two-phase pressure drop. The varying contributions of the two components of two-phase pressure drops are presented in Fig. 6.2 as functions of heat flux. The frictional pressure drop increases with an increase in heat flux (in the range of quality up to 0.15) and then decreases, whilst the accelerational pressure drop continuously increases. This indicates that at higher heat fluxes or qualities in which the observed flow patterns are dominated by annular flows, the frictional pressure drop is

lower than the accelerational pressure drop. The possible reason is that as the vapour quality increases the mixed viscosity decreases. As a result, the friction force and hence the frictional pressure drop decrease. As explained in Chapter 4, in the smallest channel, at the same mass flux and heat flux, the quality is higher than that in the larger channels, as a result, the frictional pressure drop component turn to decrease earlier, see Fig. 6.2(a).

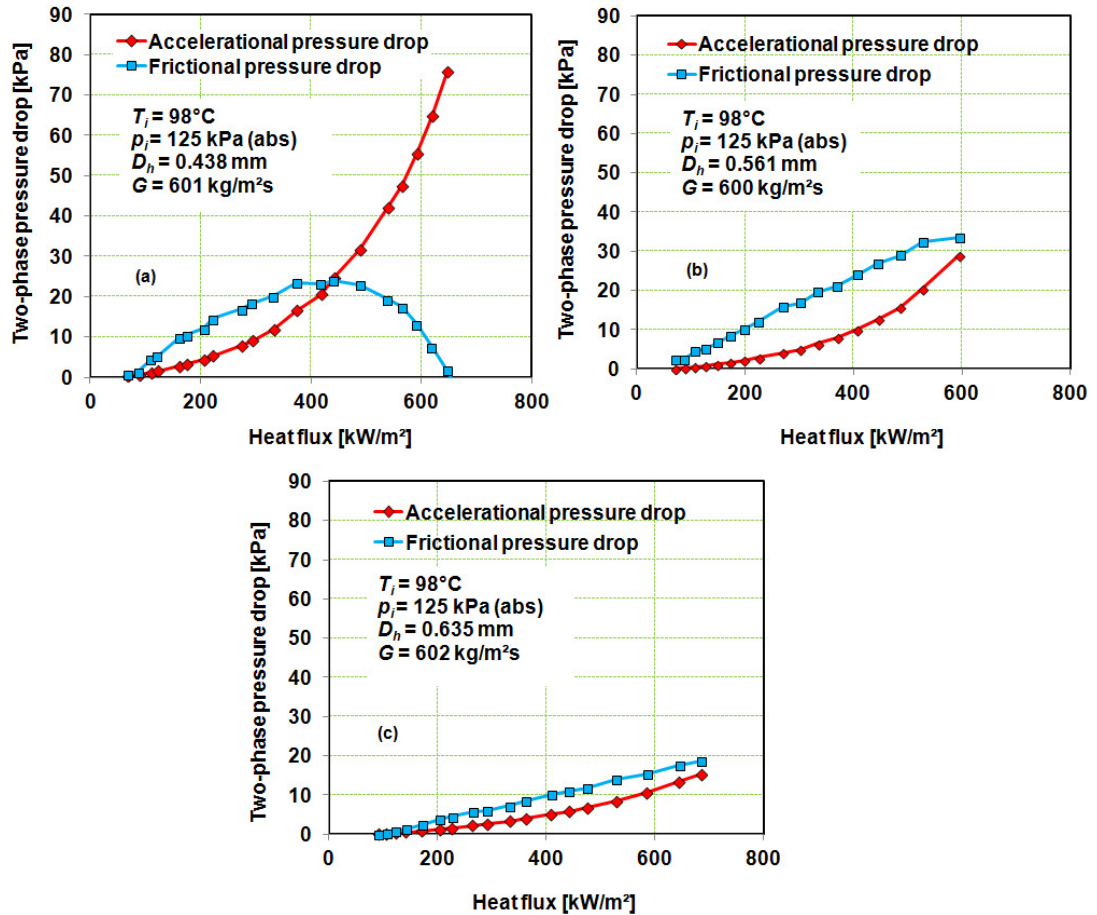


Figure 6.2 Accelerational and frictional pressure drops based on Eq. (6.5) at a nominal mass flux of  $600\text{ kg/m}^2\text{s}$  for the  $0.438\text{ mm}$ ,  $0.561\text{ mm}$  and  $0.635\text{ mm}$  channels.

In contrast, all correlations predict that the two components of pressure drop always increase with quality. Therefore, there is an inconsistency in using correlations for estimating the two components of experimental pressure drops. It suggested that the accelerational and frictional pressure drop correlations may need to be modified. Nevertheless, Mahmoud (2011), see Fig. 6.4 in his thesis, used the same approach to

obtain the experimental two-phase frictional pressure drop and the results showed the same trend as in this work. In Fig. 6.2(b) for the 0.438 mm channel, the frictional pressure drop just reaches the maximum value at the heat flux of approximately 600 kW/m<sup>2</sup> and thereafter it decreases. Differently for the 0.635 mm channel, all components of pressure drop increase as the heat flux increases; see Fig. 6.2(c). This can be inferred that as the hydraulic diameter decreases, the contribution of frictional pressure drop to the two-phase pressure drop become less dominant than the accelerational pressure drop, especially at high heat fluxes.

### 6.2.2 Effect of heat flux and mass flux on two-phase pressure drop

Figure 6.3 shows that the channel pressure drop is strongly dependent on the heat flux and mass flux. Similar trends of pressure drop were found for the 0.561 mm and 0.635 mm channels and consistent with those of a number of researchers, namely Tran et al. (2000), Qu and Mudawar (2003), Lee and Garimella (2008), Harrirchian and Garimella (2008) and Mahmoud (2011). However, due to many parameters which affect the pressure drop in flow boiling, e.g. heat flux, quality, void fraction, the pressure drop is not the same as that in fully developed single-phase flow.

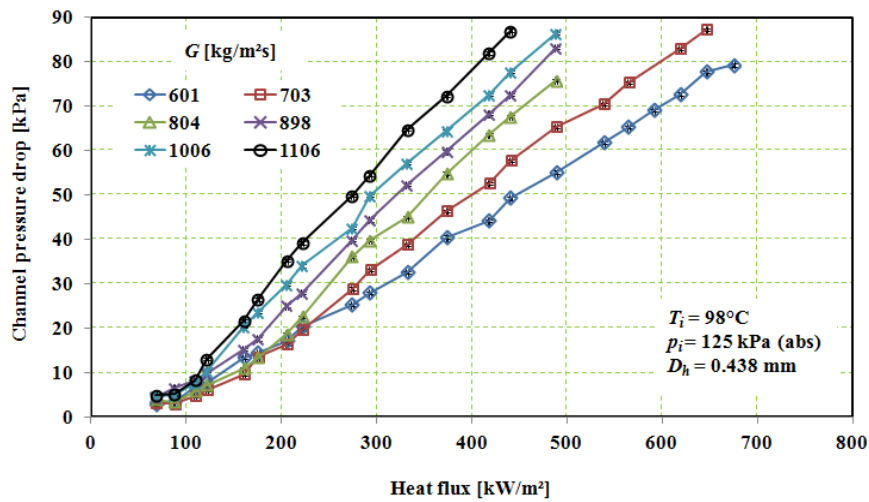


Figure 6.3 Total channel pressure drop of flow boiling in the 0.438 mm channel, showing effect of heat flux and mass flux.

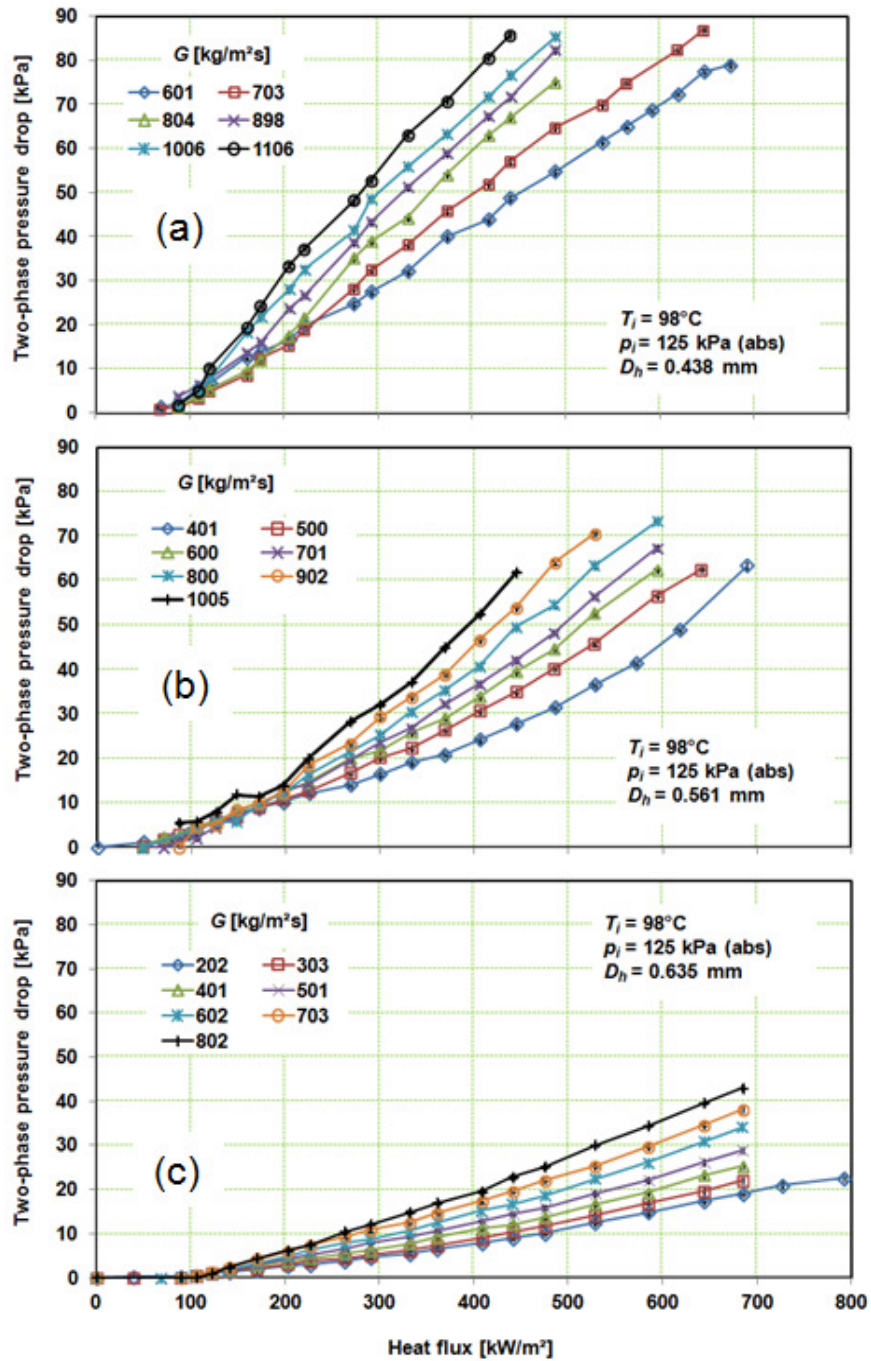


Figure 6.4 Effect of mass flux and heat flux on the two-phase pressure drop for the (a) 0.438 mm, (b) 0.561 mm and (c) 0.635 mm channels.

In Fig. 6.4, it can be seen that the two-phase pressure drop increases with heat flux for all test sections. This could be due to the decrease in the subcooled length with an increase in heat flux and more bubble formed at high heat fluxes. As the number of bubble increases, the flow becomes more restricted, therefore, the two-phase pressure drop increases. Furthermore, the two-phase pressure drop is slightly lower than the channel pressure drop becoming almost the same at high heat fluxes; see Fig. 6.5 for the 0.438 mm channel. This indicates that for high heat fluxes, the saturation region occupies almost the entire length of the channel.

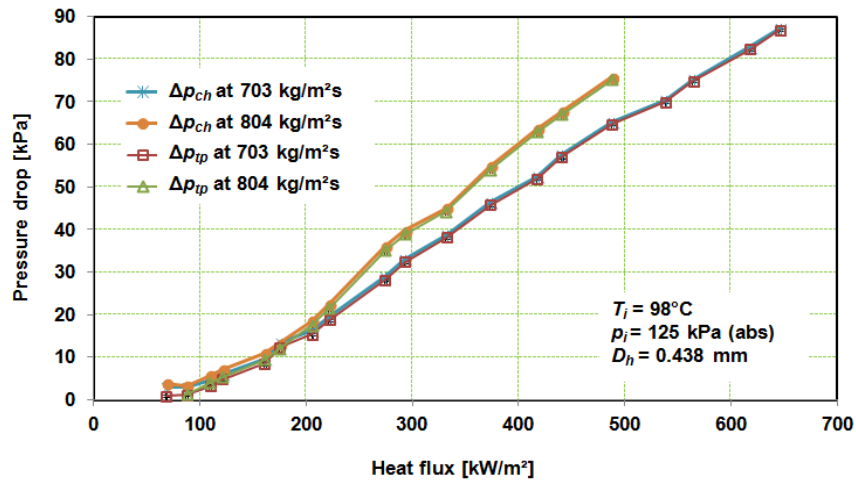


Figure 6.5 Channel and two-phase pressure drops at two different mass fluxes for the 0.438 mm channel.

The length of the saturation region can be estimated using Eq. (3.14) in Chapter 3, and a set of calculated saturation lengths is given in Fig. 6.6. The set, together with the complementary set of sub-cooled lengths, is plotted as a function of heat flux at a mass flux of 601 kg/m²s for the 0.438 mm channel. The figure shows that the length of the saturation region increases with an increase in heat flux. At a heat flux of 88 kW/m² and mass flux of 601 kg/m²s, the length of the subcooled region was 26.1 mm (42% of total length) and the saturation region was 35.9 mm (58% of total length). The corresponding single-phase and two-phase pressure drops were 1.24 kPa and 2.05 kPa respectively. At the highest heat flux of 675 kW/m², the length of the saturation region was 57.6 mm (92.9% of the total length) and the corresponding two-phase pressure drop was 78.9 kPa (99.6% of total channel pressure drop).

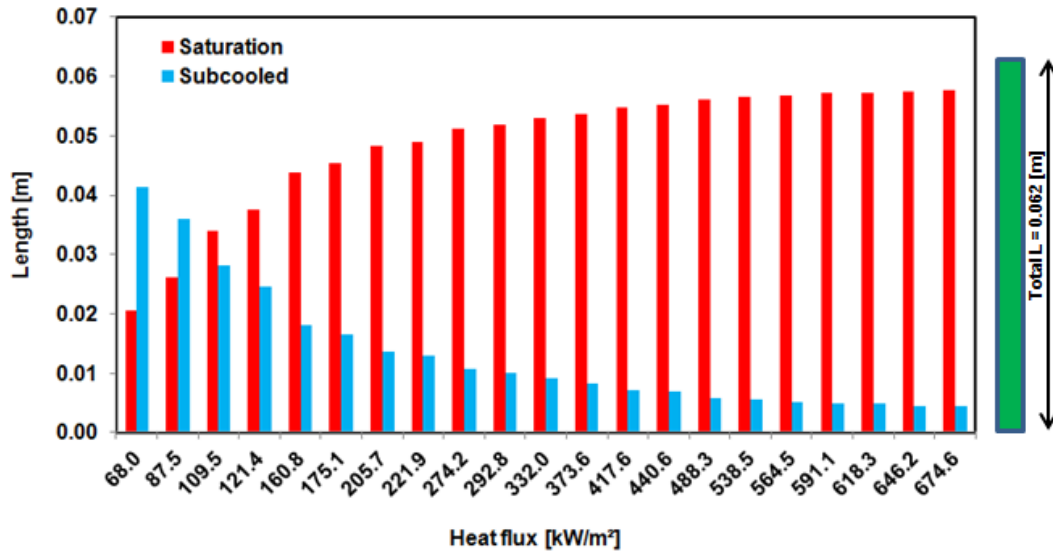


Figure 6.6 Subcooled and saturation lengths at the mass flux of 601 kg/m<sup>2</sup>s, inlet temperature of 98°C and inlet pressure of 125 kPa (abs) for the 0.438 mm channel.

In the same way as heat transfer, the two-phase pressure drop can be presented in the form of pressure drop versus quality. Fig. 6.7(a) to (c) presents the results for the three test sections. The figure shows that as the quality is increased, the two-phase pressure drop increases and the single-phase pressure drop decreases. This is consistent with results obtained by other researchers; Agostini et al. (2008), Wang et al. (2008) and Engineering Data Book III (Thome, 2004-2010). The increase in quality results in more bubble generation inside the test section, hence, increases the pressure drop. The dependence of two-phase pressure drop on mass flux is very clear. For example in Fig. 6.7(c) for the 0.635 mm channel, the slope of the two-phase pressure drop increases from approximately 58.4 kPa/unit quality at a mass flux of 202 kg/m<sup>2</sup>s, to about 437 kPa/unit quality at 802 kg/m<sup>2</sup>s.

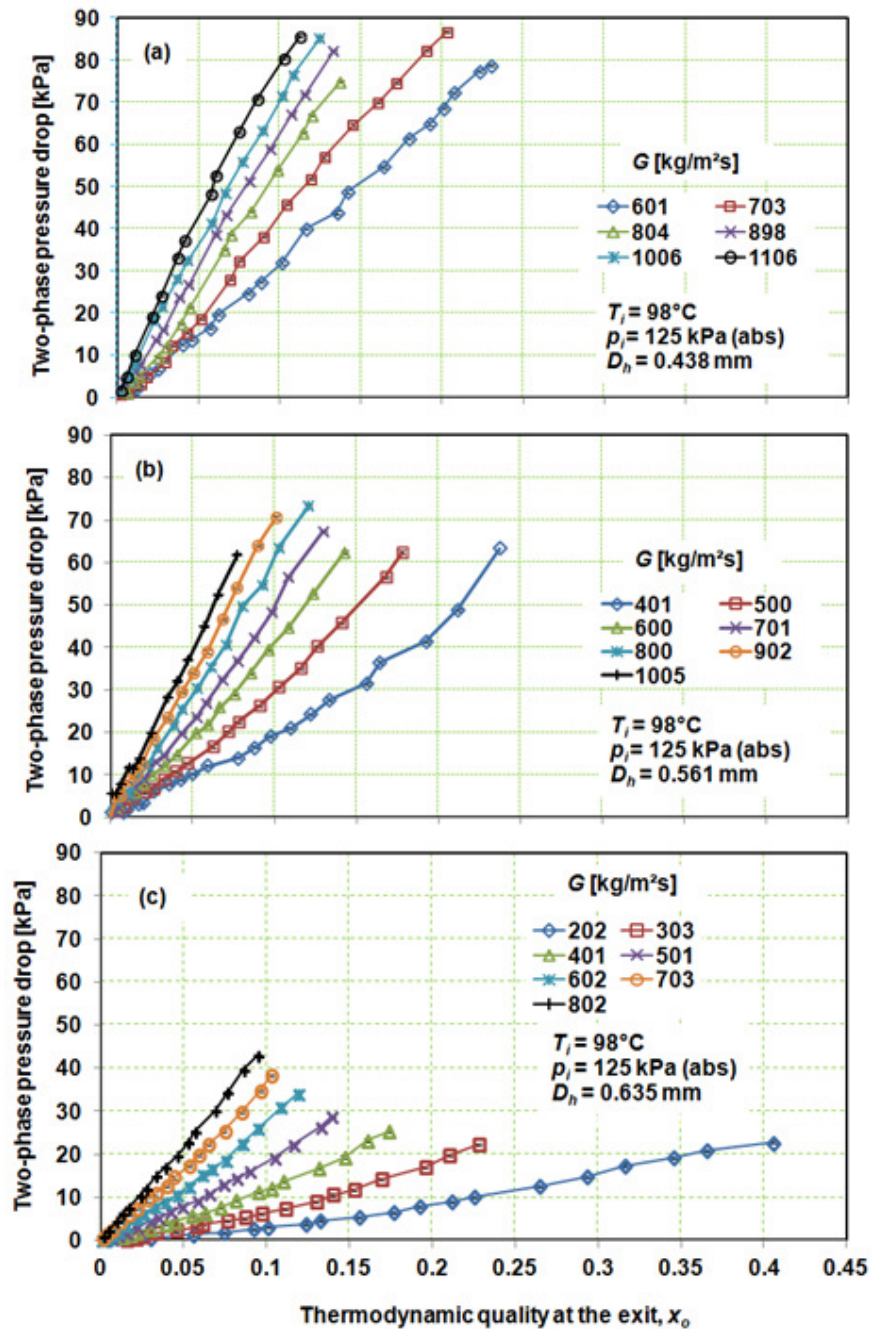


Figure 6.7 Two-phase pressure drop versus exit quality at the nominal mass flux of 600 kg/m<sup>2</sup>s, inlet temperature of 98°C and inlet pressure of 125 kPa obtained for the (a) 0.438 mm, (b) 0.561 mm and (c) 0.635 mm channels.

The two-phase pressure drop is also affected by the two-phase flow multiplier. Therefore, it is worthy presenting the experimental two-phase multiplier which can be estimated using Eq. (6.6) and the results are presented in Fig. 6.8.

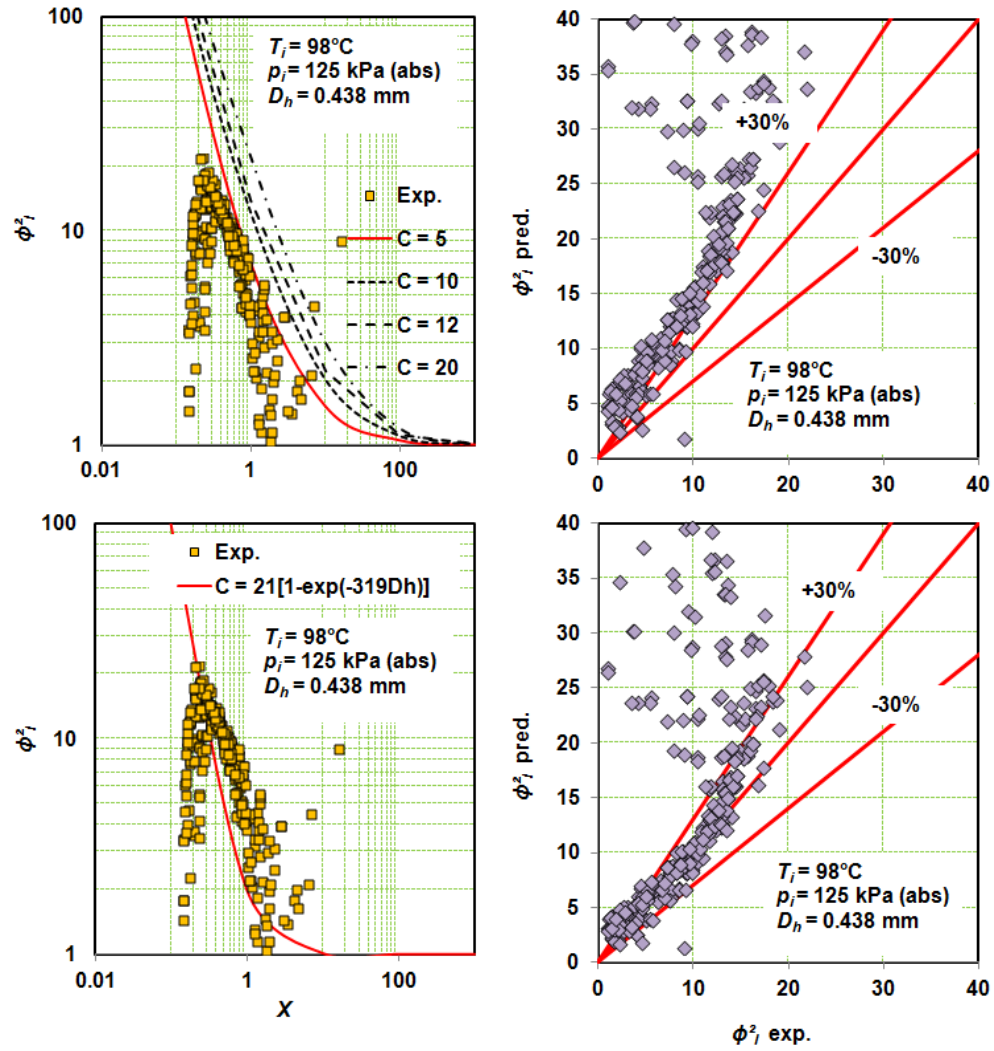


Figure 6.8 Experimental two-phase pressure drop multiplier for the 0.438 mm channel compared to predictions using correlations of: (a) Lockhart–Martinelli (1949) (b) Mishima & Hibiki (1996).

$$\Phi_l^2 = \frac{\Delta p_{tp,f}}{\Delta p_{sp}} \quad (6.6)$$

and the experimental Martinelli parameter is defined as

$$X^2 = \frac{\Delta p_{fl}}{\Delta p_{fg}} \quad (6.7)$$

Figure 6.8 shows that the experimental two-phase pressure drop multipliers are lower than those predicted using the Lockhart-Martinelli (1949) correlation. These lower values were also found by Lee and Lee (2008), see Fig. 4(d) of their paper, for their test section with a gap of 0.4 mm and a width of 20 mm. When the experimental two-phase multipliers are compared with predictions made using the correlation of Mishima & Hibiki (1996), a reasonable agreement is able to be achieved. This confirms that the Lockhart-Martinelli (1949) correlation results in overprediction of experimental data. The higher prediction of Lockhart-Martinelli (1949) was due to the constant  $C$ . The value of constant  $C$  used in Mishima and Hibiki (1996) is lower than that in Lockhart-Martinelli (1949), e.g. 2.74 for the 0.438 mm channel.

Similar to the local heat transfer coefficient, the pressure drop may relate to the flow patterns. On this occasion, some pressure drop values were correlated with observed flow patterns and are presented in Fig. 6.9 in the form of pressure drop versus superficial vapour velocity for the three test sections. The flow patterns given in the figure were observed near the outlet. From the figure, it can be seen that two-phase pressure drop increases with superficial vapour velocity. For the smallest test section the pressure drop lines are curved whereas for the largest test section they are almost linear. This indicates that as the hydraulic diameter decreases, the superficial vapour velocity increases at the same experimental conditions and the increase is faster than the increase in two-phase pressure drop. As a result, the two-phase pressure drop line shifts toward the right. Fig. 6.9 also shows that annular flow patterns in the largest test section start at a lower superficial vapour velocity than in the smallest test section. This is consistent with the explanation given in Chapter 5.

The effect of mass flux on the two-phase pressure drop at the same superficial gas velocity is not clear, at low mass fluxes the effect is significant but at higher mass fluxes is not. This could be due to the decrease in quality with the mass flux at the same superficial gas velocity; see Eq. (3.25) in Chapter 3.

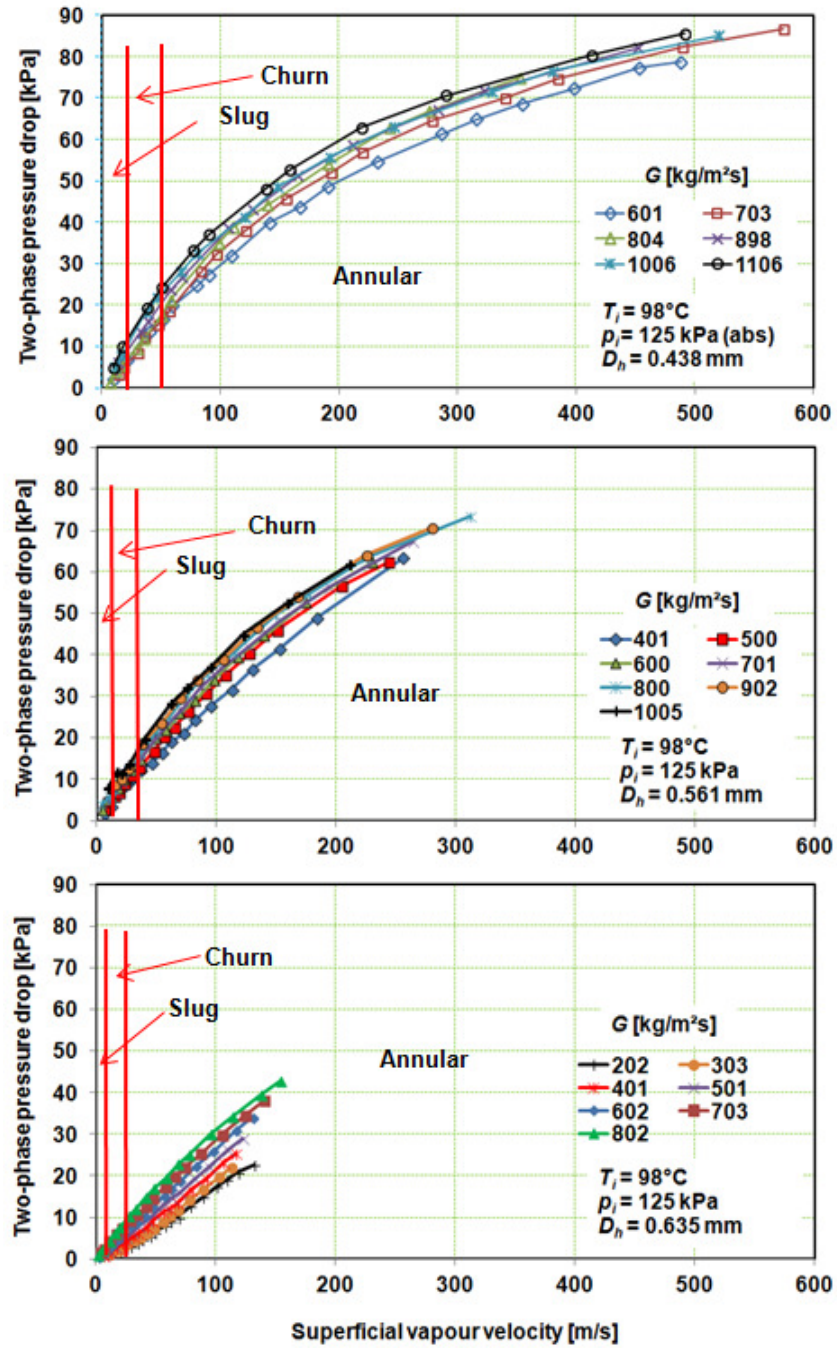


Figure 6.9 Two-phase pressure drops versus superficial velocity at inlet temperature and pressure of  $98^\circ\text{C}$  and  $125\text{ kPa (abs)}$  for the (a)  $0.438\text{ mm}$ , (b)  $0.561\text{ mm}$  and (c)  $0.635\text{ mm}$  channels. The corresponding flow patterns given on the graphs were flow patterns observed near the outlet.

### 6.3 Pressure and pressure drop fluctuation

As explained in the previous sub section, the pressure drop gradient was assumed to be linear along the test section. This assumption was also used in many published results, namely Qu and Mudawar (2003), Consolini & Thome (2009) and Mahmoud et al. (2011). This assumption means that all pressures are dependent on the inlet and outlet pressure measurements only. A sample set of pressure distributions based on the linear pressure gradient assumption and measurements is given in Fig. 6.10. From the figure it is clear that there is a significant difference of pressures based on the linear pressure distribution assumption and measurement. It indicates that the linear assumption of pressure distribution along the test section during flow boiling should be questioned. As the heat flux was increased, the deviation increased. For example, at the heat flux of 222 kW/m<sup>2</sup>, the deviation is negligible but at the heat flux of 563 kW/m<sup>2</sup>, the deviation is considerable. At the last heat flux, the deviations of pressure at pressure tapping three ( $z/L = 0.6$ ) and four ( $z/L = 0.8$ ) are approximately 20 kPa and 25 kPa. These differences give an incorrect estimation of heat transfer coefficients. Based on the linear pressure gradient assumption, at the heat flux of 563 kW/m<sup>2</sup>, the fluid saturation temperatures at  $z/L = 0.6$  and  $z/L = 0.8$  are 96 and 91°C, whilst based on the measurement they are 102 and 98°C. Wall temperatures at  $z/L = 0.6$  and 0.8 are 111.5 and 109.4°C. The heat transfer coefficients based on the linear pressure distribution assumption at those locations are 36.3 and 30.6 kW/m<sup>2</sup>, whilst based on the pressure measurement they are 59.3 and 49.4 kW/m<sup>2</sup>. The deviations of heat transfer calculation are then 38.8% and 38% respectively. However, as mentioned in Chapter 5, in this work, the linear pressure distribution assumption is used as the assumption was also used in many publications and the pressure distribution measurement need to be validated by a new operator using the same experimental conditions.

In addition, from Fig. 6.10, it can be seen that as the heat flux increased, so did the pressure drop; however, since the inlet pressure was kept constant, the outlet pressure or the system pressure has to decrease. Similarly, increasing the mass flux caused the pressure drop to increase, again requiring a decreased outlet pressure. This condition seemed to create more stable flow boiling because the flow behaviour was similar to being ‘sucked’ from the outlet (particularly when the outlet pressure was lower than the ambient pressure). Data of pressure and pressure drop fluctuation found in this work are

presented in Figs. 6.11 and 6.12 at the heat flux of 161 kW/m<sup>2</sup> and mass flux of 601 kg/m<sup>2</sup>s.

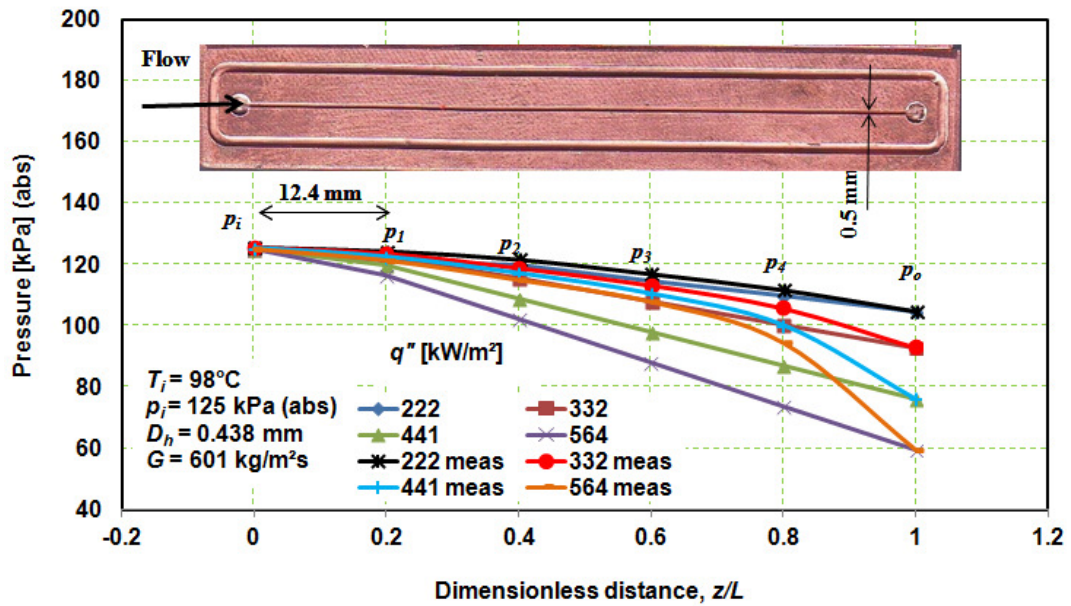


Figure 6.10 Pressure distribution along the test section based on the linear pressure distribution assumption and measurement, at a mass flux of 601 kg/m<sup>2</sup>s and several heat fluxes, for the 0.438 mm channel.

From Fig. 6.11 it can be noted that inlet and outlet pressures fluctuated between 24.36 and 25.2 kPa (0.84 kPa) and between 10.8 and 11.5 kPa (0.7 kPa) respectively. In addition, pressures at  $z/L$  of 0.2, 0.4, 0.6 and 0.8 fluctuated between 23.5 and 24.3 kPa, 22.5 and 23.3 kPa (0.8 kPa), 19.2 and 20.2 kPa (1 kPa), and 15.3 and 16.1 kPa (0.8 kPa) respectively. The largest fluctuation amplitude in pressure is 1 kPa measured at  $z/L$  of 0.4. The fluctuation of each pressure inside the test section does not show big deviations. This could be due to the low sensitivity of the pressure transducer (1 mV/kPa) and the existing bubble in the pressure tapping. The sensitivity affects the capability of pressure transducer to respond any fluctuations, whilst the bubble in the pressure tapping reduces the capability of pressure transducer to capture the fluctuation. In addition, all pressures seemed to fluctuate at almost the same phase.

The corresponding flow patterns observed for this condition, Fig. 6.11, were bubbly (near the inlet), churn (in the middle) and annular (near the outlet). From the flow

pattern view, it is not clear the deviation of fluctuation generated by a specific flow pattern. Therefore, the amplitude of fluctuation cannot be used to predict the flow pattern.

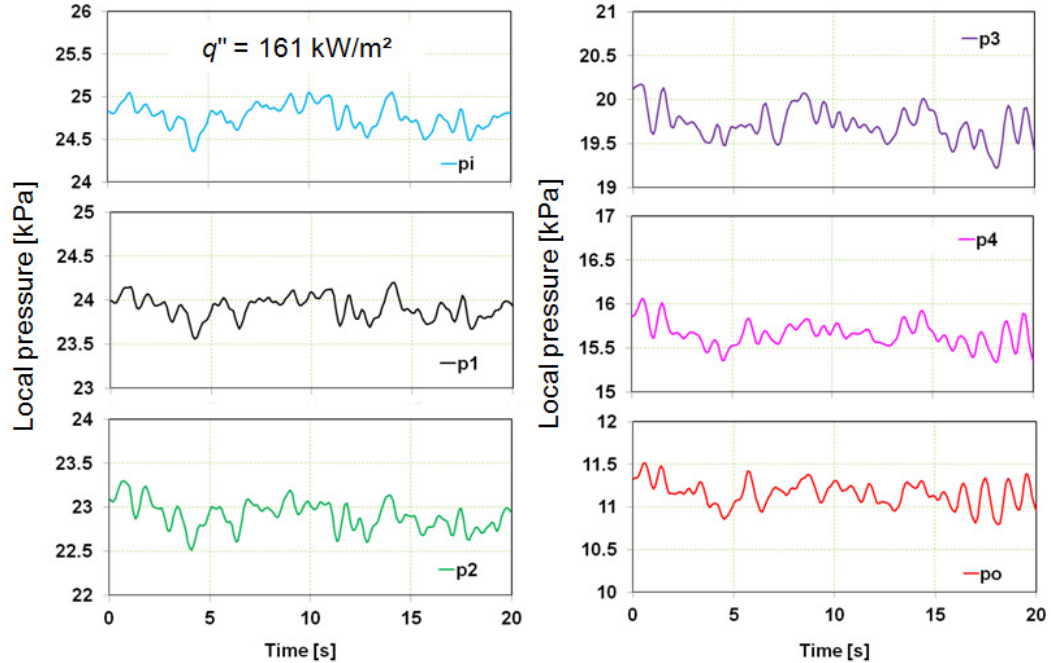


Figure 6.11 Pressure fluctuation at the mass flux of  $601 \text{ kg/m}^2\text{s}$ , heat flux of  $161 \text{ kW/m}^2$ , inlet temperature of  $98^\circ\text{C}$  and inlet pressure of  $125 \text{ kPa}$  (abs), for the  $0.438 \text{ mm}$  channel.

To identify the type of fluctuation usually researchers used pressure drop fluctuation and frequency, e.g. Brutin et al. (2003), Xu et al. (2005). Figure 6.12 presents the pressure drop fluctuation and frequency at the mass flux of  $601 \text{ kg/m}^2\text{s}$  and heat flux of  $161 \text{ kW/m}^2$  for the  $0.438 \text{ mm}$  channel. The pressure drop also fluctuated between  $13.3$  and  $13.9 \text{ kPa}$  ( $0.6 \text{ kPa}$ ) within  $20 \text{ s}$  observation. This fluctuation is small compared to that of Xu et al. (2005),  $0.8 - 6 \text{ kPa}$ .

A simple frequency analysis using dual channel spectral measurement provided in the LabView program was used in this work. The inputs to this program are time and pressure. These two signals come to the dual channel frequency analysis pallet and results in frequency and related amplitude, as shown in Fig. 6.12. The frequency of pressure drop fluctuation in Fig. 6.12 was found to be approximately  $1.05 \text{ Hz}$ .

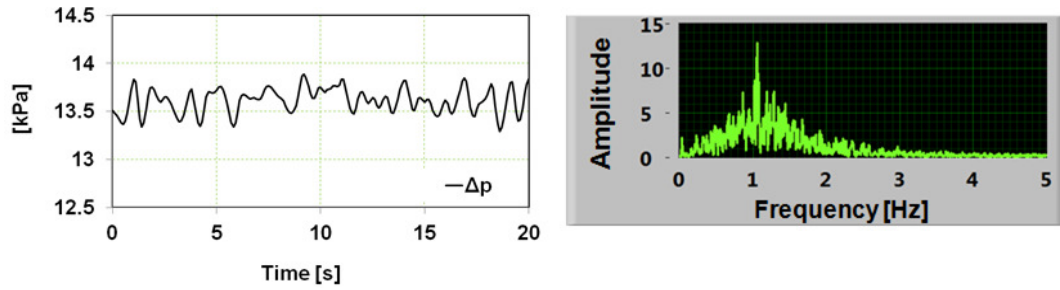


Figure 6.12 Pressure drop fluctuation and frequency at a mass flux of  $601 \text{ kg/m}^2\text{s}$  and heat flux of  $161 \text{ kW/m}^2$ , inlet temperature and pressure of  $98^\circ\text{C}$  and  $125 \text{ kPa}$  (abs) for the  $0.438 \text{ mm}$  channel.

Fig. 6.13 shows a similar plot to Fig. 6.11, for the same mass flux, but with a heat flux of  $222 \text{ kW/m}^2$ . From the figure, it can be seen that the inlet and outlet pressures fluctuated between  $24.5$  and  $25.9 \text{ kPa}$  ( $1.4 \text{ kPa}$ ) and between  $4$  and  $5.1 \text{ kPa}$  ( $1.1 \text{ kPa}$ ) respectively. Pressures at  $z/L$  of  $0.2$ ,  $0.4$ ,  $0.6$  and  $0.8$  fluctuated between  $23.1$  and  $24.6 \text{ kPa}$  ( $1.5 \text{ kPa}$ ),  $18.4$  and  $23 \text{ kPa}$  ( $4.6 \text{ kPa}$ ),  $16$  and  $17.3 \text{ kPa}$  ( $1.3 \text{ kPa}$ ), and  $10.8$  and  $12.6 \text{ kPa}$  ( $1.8 \text{ kPa}$ ) respectively. It may be noted that the pressure fluctuations here are larger than those at the heat flux of  $161 \text{ kW/m}^2$ . The largest fluctuation amplitude in this case is  $4.6 \text{ kPa}$  shown by pressure sensor 2 at  $z/L$  of  $0.4$ . The big amplitude of fluctuation could be due to the churn flow pattern, as the corresponding flow patterns observed were churn (near the inlet), churn (in the middle) and annular (near the outlet). Fig. 6.14 shows a similar plot to Fig. 6.12 for pressure drop fluctuation, but again with the heat flux of  $222 \text{ kW/m}^2$ , the fluctuation amplitude is about  $2.2 \text{ kPa}$  (peak to peak) with dominant frequencies of  $1.05 \text{ Hz}$ .

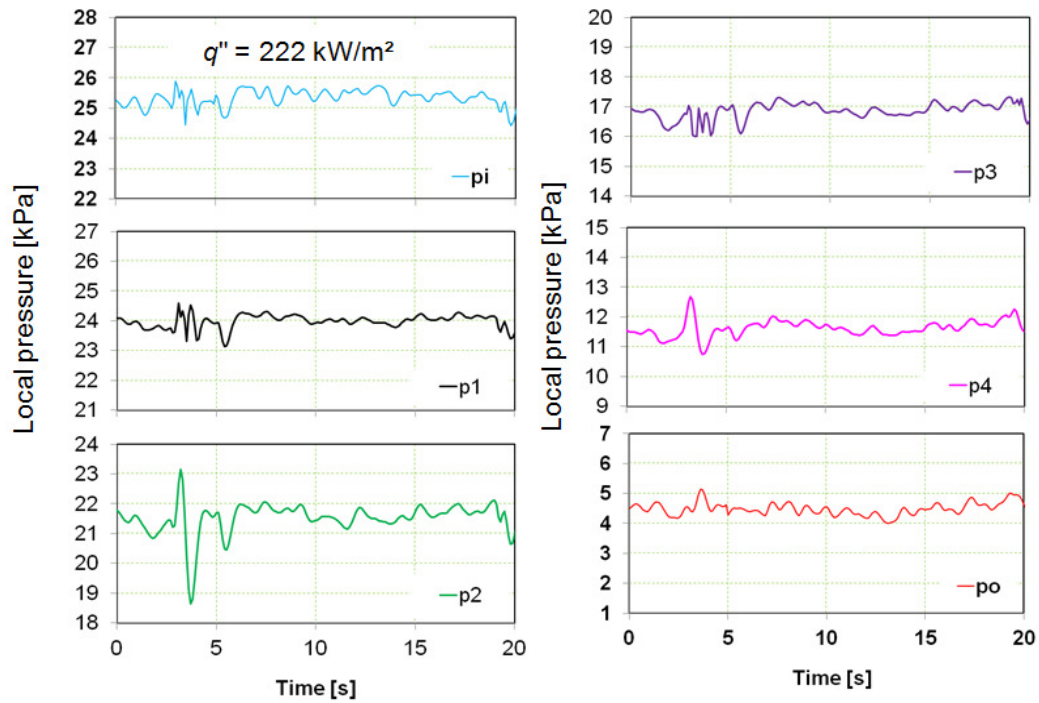


Figure 6.13 Pressure fluctuation at a mass flux of  $601 \text{ kg/m}^2\text{s}$  and heat flux of  $222 \text{ kW/m}^2$ , inlet temperature of  $98^\circ\text{C}$  and inlet pressure of  $125 \text{ kPa}$  (abs), for the  $0.438 \text{ mm}$  channel.

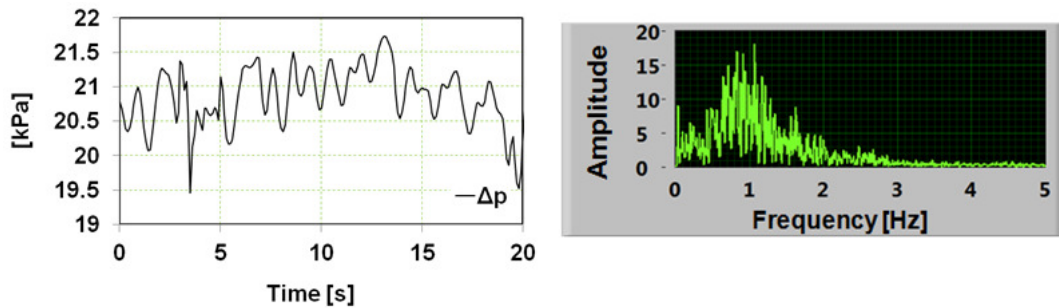


Figure 6.14 Pressure drop fluctuation and frequency at a mass flux of  $601 \text{ kg/m}^2\text{s}$  and heat flux of  $222 \text{ kW/m}^2$ , for the  $0.438 \text{ mm}$  channel.

A further set of fluctuations in pressure and pressure drop is shown in Fig. 6.15 and 6.16 to show the effect of a high heat flux of  $646 \text{ kW/m}^2$ . Again they are for the same mass flux of  $601 \text{ kg/m}^2\text{s}$ , and for the  $0.438 \text{ mm}$  channel. From Fig. 6.15 the inlet and outlet pressures fluctuate between  $25$  and  $25.8 \text{ kPa}$  ( $0.8 \text{ kPa}$ ) and between  $-52.7$  and  $-52$

kPa (0.7 kPa) respectively. Pressures at  $z/L$  of 0.2, 0.4, 0.6 and 0.8 fluctuated between 20.6 and 21.7 kPa (1.1 kPa), 13.7 and 14.6 kPa (0.9 kPa), 4.5 and 5.4 kPa (0.9 kPa), and -10.5 and -9.8 kPa (0.7 kPa) respectively. The largest amplitude fluctuation was registered by pressure sensor 1, at about 1.1 kPa. The above three pairs of pressure fluctuation data, show that the largest fluctuation occurs at the heat flux of 222 kW/m<sup>2</sup>. As the heat flux was increased the nucleation moved upstream and commenced between inlet and pressure sensor 1, or, further, near the inlet itself.

It is clear from Fig. 6.15 that the fluctuation in pressure reduces from lower to higher values of heat flux. This could be due to the high pressure drop or the nucleate boiling changed to evaporative boiling. This is consistent with the flow patterns observed at this condition. The corresponding flow patterns observed were churn (near the inlet), annular (in the middle) and annular (near the outlet). The fluctuation in pressure drop is presented in Fig. 6.16 at the same mass flux as for Figs.6.12 and 6.14 but with the yet higher heat flux of 646 kW/m<sup>2</sup>. The fluctuation has a frequency of 1 Hz and amplitudes varying between 77.2 and 78.5 kPa (1.3 kPa peak to peak) which is less than that at the heat flux of 222 kW/m<sup>2</sup> in Fig. 6.14.

Pressure drop fluctuation results for a higher hydraulic diameter forms the basis for Fig. 6.17. The data are for the 0.635 mm channel at a mass flux of 202 kg/m<sup>2</sup>s and heat flux of 226 kW/m<sup>2</sup>. Figure 6.16 shows that pressure drop fluctuates with irregular period and amplitude. The approximate maximum amplitude for the pressure drop is 0.6 kPa (peak to peak). With the experimental conditions stated in Fig. 6.17, the corresponding flow patterns were liquid (near the inlet), slug (in the middle) and annular (near the outlet).

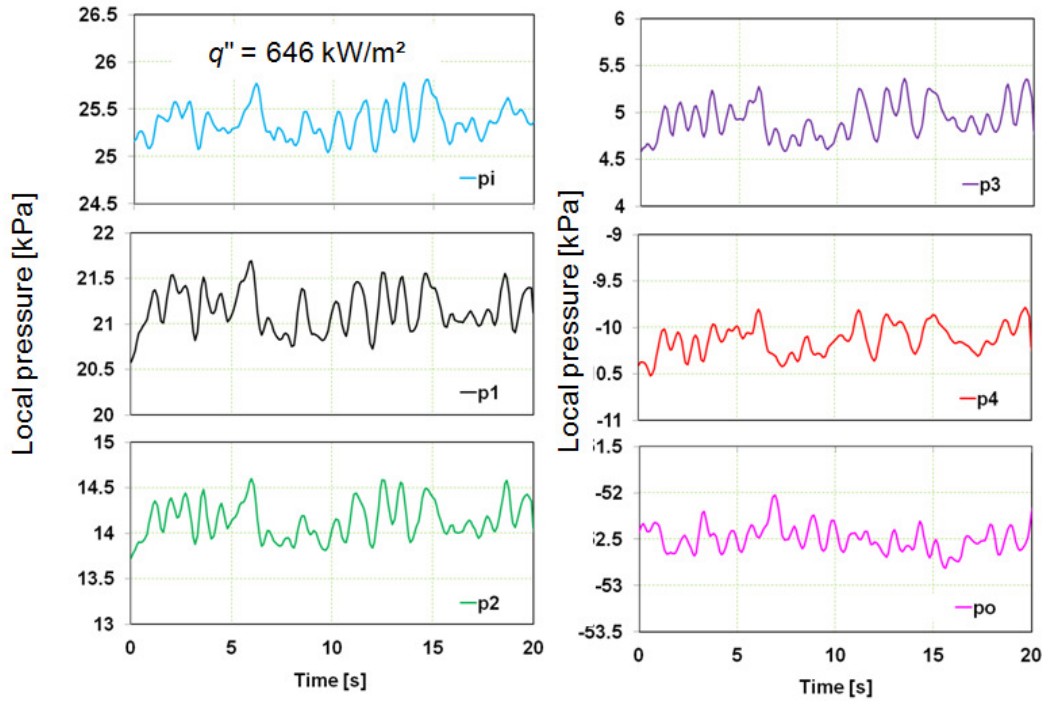


Figure 6.15 Pressure fluctuation at a mass flux of 601 kg/m<sup>2</sup>s and heat flux of 646 kW/m<sup>2</sup> and for the 0.438 mm channel.

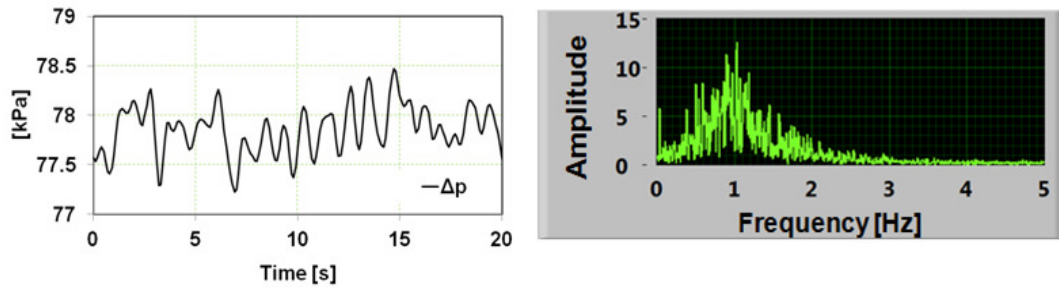


Figure 6.16 Pressure drop fluctuation and frequency at heat flux of 646 kW/m<sup>2</sup> and mass flux of 601 kg/m<sup>2</sup>s for the 0.438 mm channel.

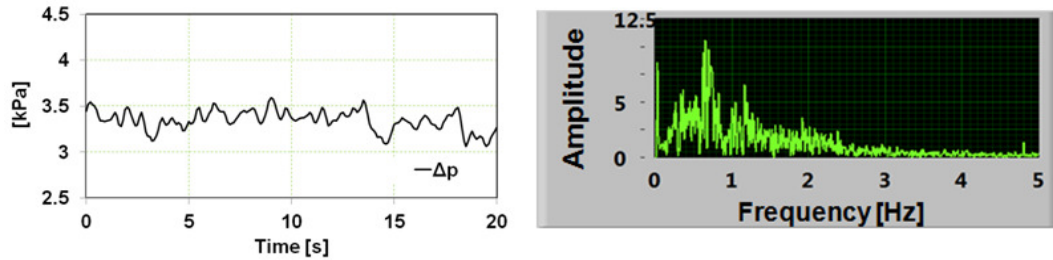


Figure 6.17 Pressure drop fluctuation and frequency obtained for the 0.635 mm at a mass flux of 202 kg/m<sup>2</sup>s and heat flux of 226 kW/m<sup>2</sup>.

Figure 6.18 shows pressure drop fluctuations for the three test section at a nominal mass flux of 700 kg/m<sup>2</sup>s and heat flux of 172 kW/m<sup>2</sup>, inlet temperature and pressure of 98°C and 125 kPa (abs). The pressure drop amplitude obtained in the 0.438 mm channel is approximately 0.8 kPa, in the 0.561 mm channel is about 0.8 kPa, and in the 0.635 mm channel is 0.7 kPa. Hence it can be concluded that at the same mass flux and heat flux, the fluctuation of pressure drop is almost the same for the three test section at the experimental conditions. The flow patterns observed in the 0.438 mm, 0.561 mm and 0.635 mm channels were bubbly-slug-annular, liquid-bubbly-slug and liquid-slug-churn. The pressure drop frequencies shown in Fig. 6.18 are 0.8 Hz for the 0.438 mm channel, 0.8 and 1 Hz for the 0.561 mm channel and 0.9 Hz for the 0.635 mm channel.

Zhang et al. (2009) classified flow instability, as represented by flow boiling fluctuations encountered in microchannels, into two groups: dynamic instability and static instability. Dynamic instability is the instability reflecting a feedback control process of combined parameters. As given by Boure et al. (1973) dynamic instability comprises instabilities due to pressure drop, density, acoustic oscillation and thermal effects. Static instability, on the other hand, is instability relating to the demand curve of pressure drop against mass flow rate which is generally termed excursion or Ledinegg instability. According to Brutin et al. (2003), pressure drop instability may be identified by large amplitude and frequencies ranging from 3.6 to 6.6 Hz. By comparison, Xu et al. (2005), when the period of pressure drop oscillation is approximately 117 s, corresponding to the frequency of 0.0085 Hz, and an amplitude of oscillation between -0.8 and 6 kPa, the flow instability is called LALPO (Long amplitude long period oscillation). Almost similar with those of Xu et al. (2005), Bogojevic et al. (2009) classified flow boiling instability into two groups. Firstly, it is called “HALF”, which is

noted by high amplitude and low frequency. This instability has a range of frequency between 0 to 3 Hz. Secondly, it is called “LAHF”, low amplitude high frequency. The later has frequencies ranging from 23 to 25 hz. However, in this study, such fluctuation was not observed.

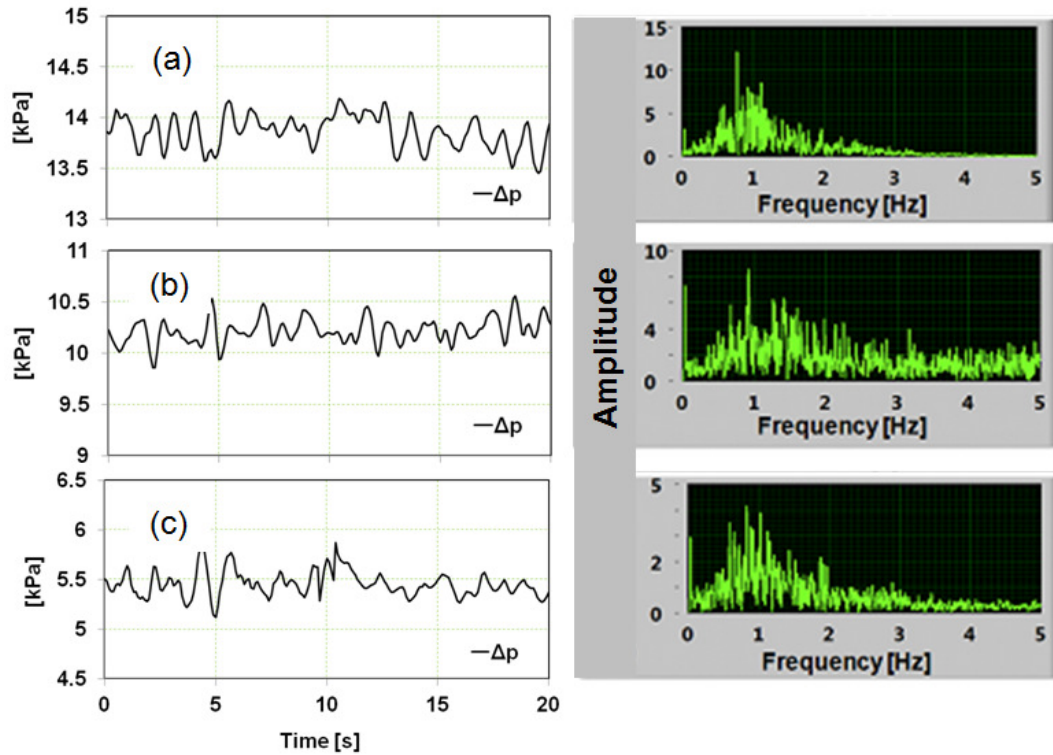


Figure 6.18 Pressure drop fluctuation and frequency at a nominal mass flux of 700 kg/m<sup>2</sup>s and heat flux of 172 kW/m<sup>2</sup>, inlet temperature and pressure of 98°C and 125 kPa (abs) for the (a) 0.438 mm, (b) 0.561 mm and (c) 0.635 mm channels.

Furthermore, Boure et al. (1973) explained instability in more detail. For a frequency of fluctuation of about 1 Hz, they identified the type of instability as density wave oscillation which was grouped within the fundamental dynamic instability, whereas when the frequency of oscillation was 0.1 Hz, the instability was called pressure drop oscillation, and included in the compound dynamic instability group. In Figs. 6.12, 6.14 and 6.16 the frequencies of the pressure drop fluctuation are 1.05 Hz, 1.05 Hz and 1 Hz respectively. In the context of the published data above it can be interpreted that the fluctuations found here were neither due to pressure drop instability nor Ledinegg instability, but density wave instability.

## 6.4 Comparison with existing correlations

The selected correlations are listed in Appendix A. They were proposed by Lockhart-Martinelli (1949), Mishima & Hibiki (1996), Yu et al (2002), Qu & Mudawar (2003), Lee & Lee (2008), Lee & Garimella (2008), and Homogenous flow model (1994). The latter (with a friction factor of 0.003) was taken from Qu and Mudawar (2003), who used the model to assess their own correlation and for comparison with their experimental data. Fig. 6.19(a), (b) and (c) presents examples of comparison with selected correlations at a nominal mass flux of 600 kg/m<sup>2</sup>s and for the 0.438 mm channel, 0.561 mm channel, and 0.635 mm channels respectively. From the figure, it is worth mentioning that as the channel size decreases, so does the accuracy of the correlations. The different hydraulic diameters used in the experiments may result in the identification of different suitable correlations.

Comparing experimental data with predictions using existing correlations allow the correlations to be tested and assessed using a mean absolute error (MAE) which is given by

$$\text{MAE} = \frac{1}{N} \sum_{j=1}^N \left| \frac{\Delta p_{\text{exp},j} - \Delta p_{\text{pred},j}}{\Delta p_{\text{exp},j}} \right| \times 100\% \quad (6.7)$$

MAE values are given in Table 6.1 for all existing correlations and for each channel size. The best correlations in terms of predictive ability are presented graphically in Figs. 6.20 - 6.22 with their MAE values.

From Table 6.1 and Figs. 6.20 to 6.22 respectively it is clear that the minimum MAE for the 0.438 mm channel is 34.5% obtained using the correlation of Mishima and Hibiki (1996), for the 0.561 mm channel is 25.9% attained using the correlation of Lee and Garimella (2008) and for the 0.635 mm channel is 31.5% obtained using the correlation of Mishima and Hibiki (1996).

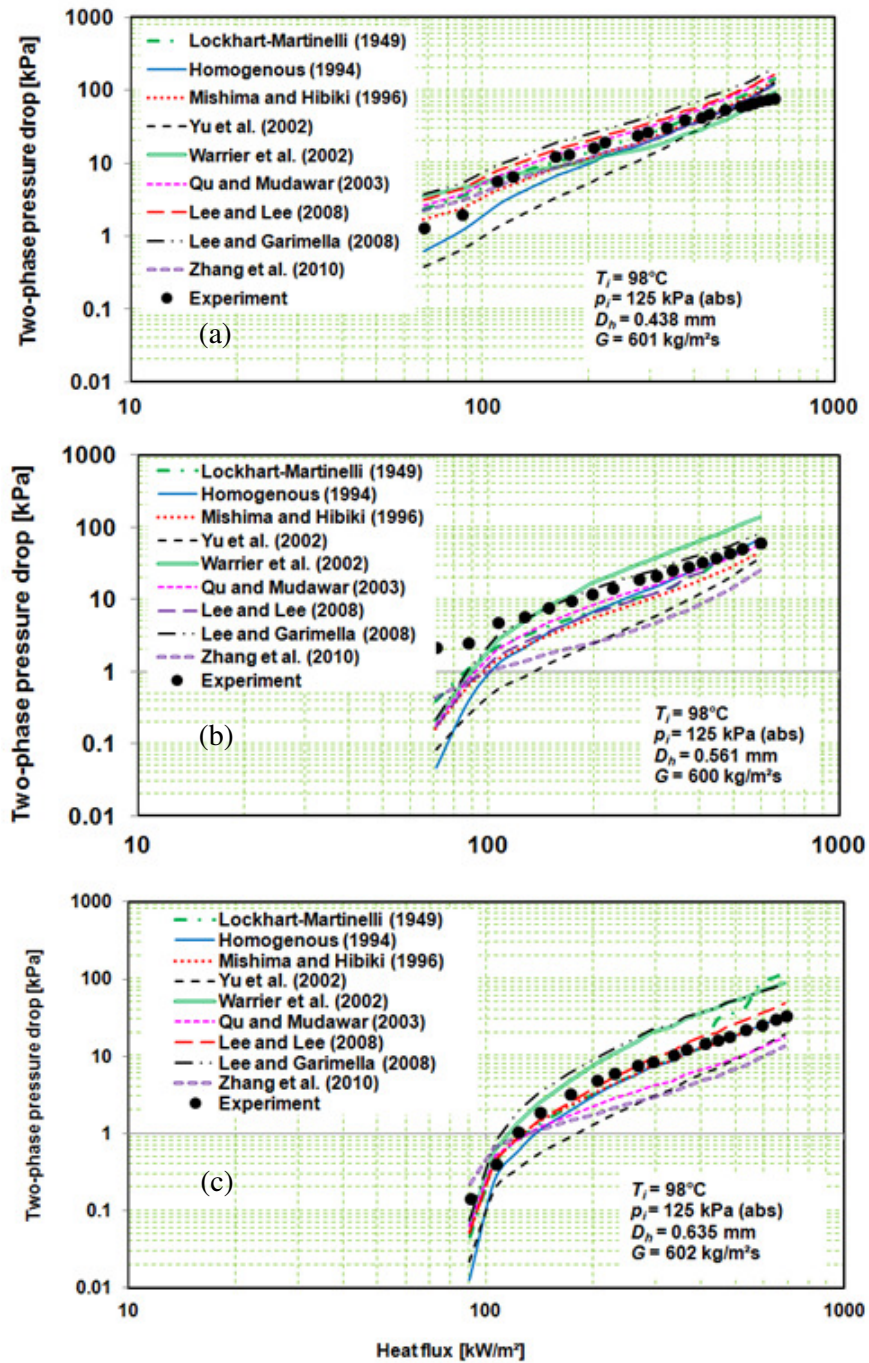


Figure 6.19 Comparison of the experimental data with selected correlations for the (a) 0.438 mm, (b) 0.561 mm and (c) 0.635 mm channels.

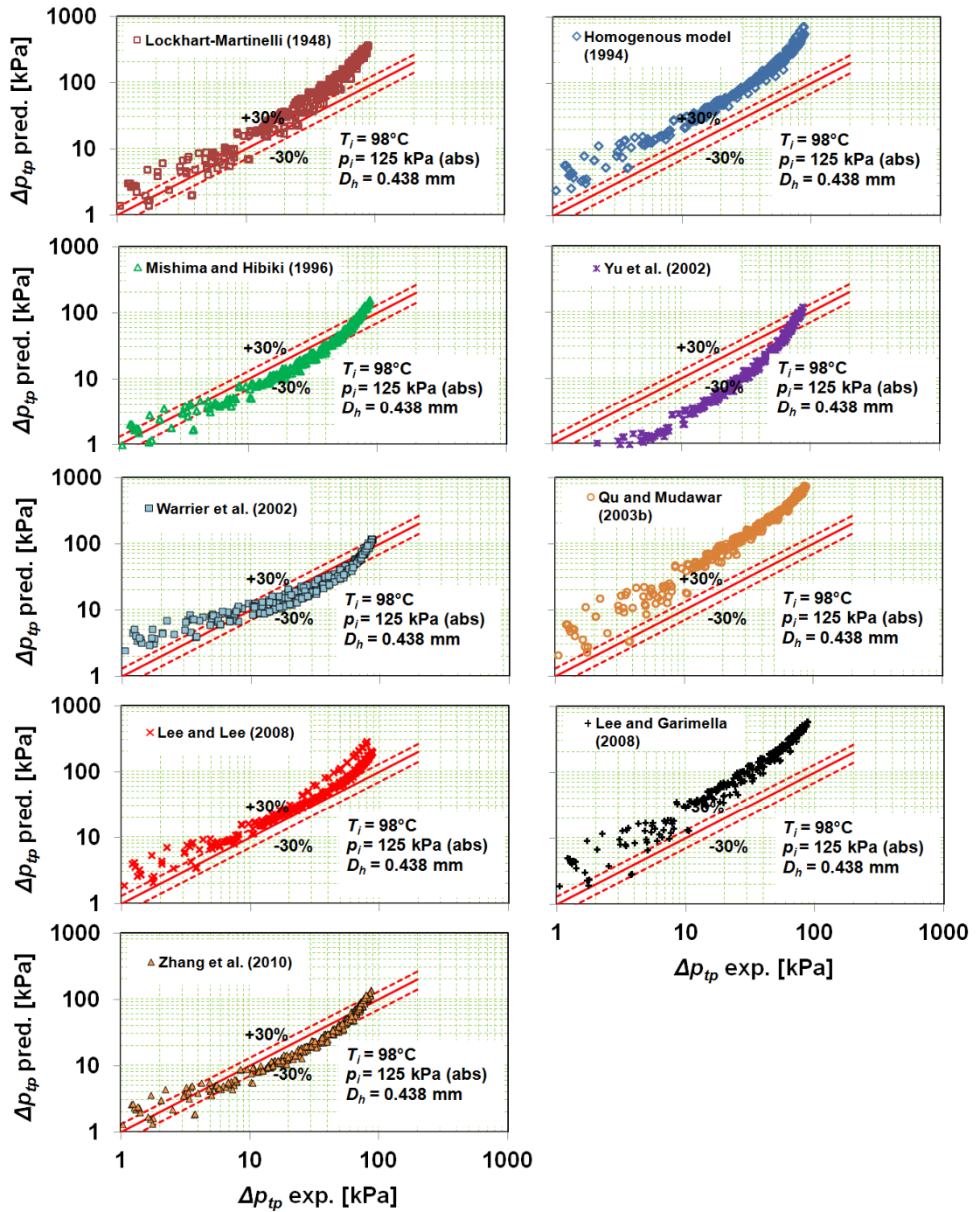


Figure 6.20 Comparison with correlations for the 0.438 mm.

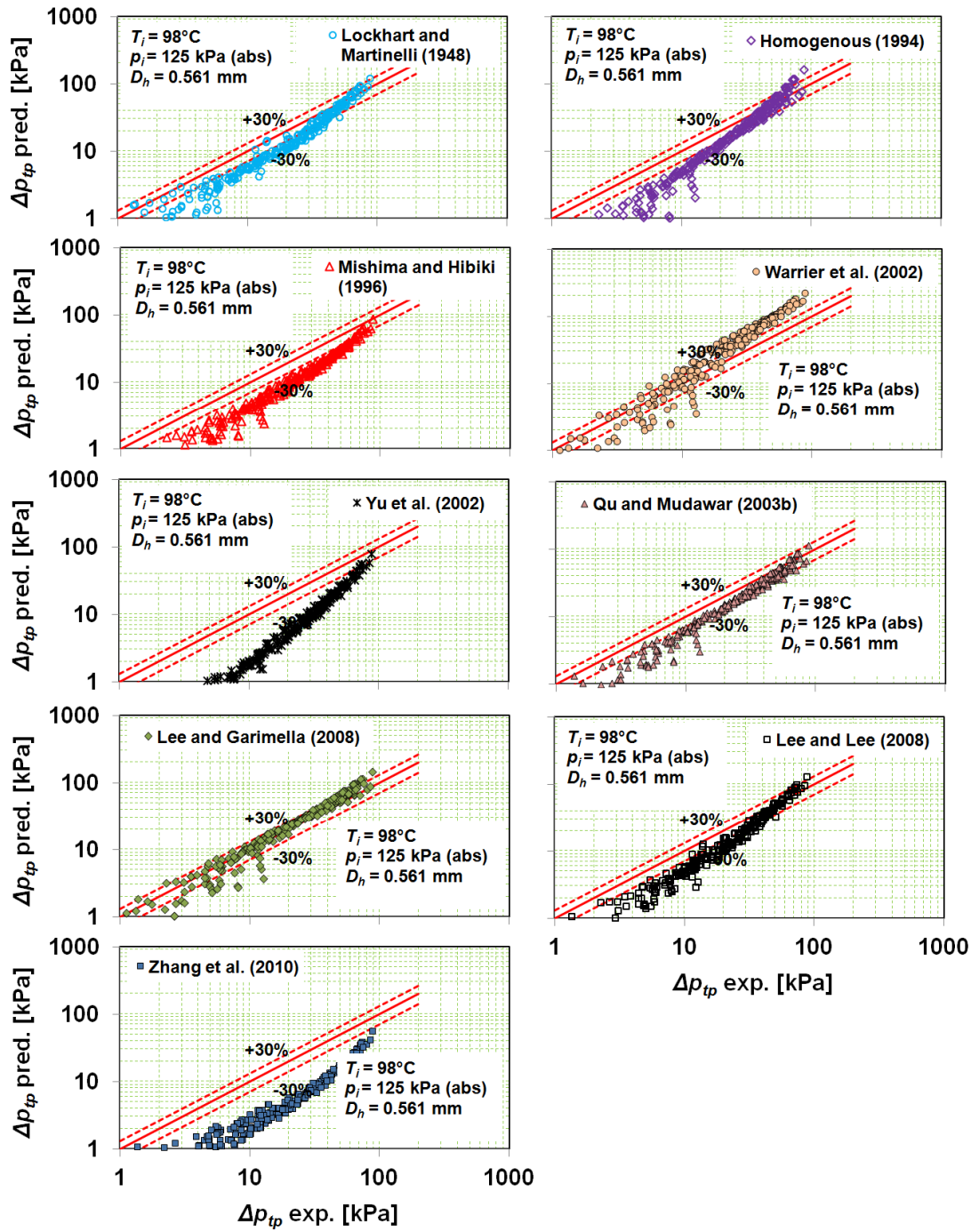


Figure 6.21 Comparison with correlations for the 0.561 mm.

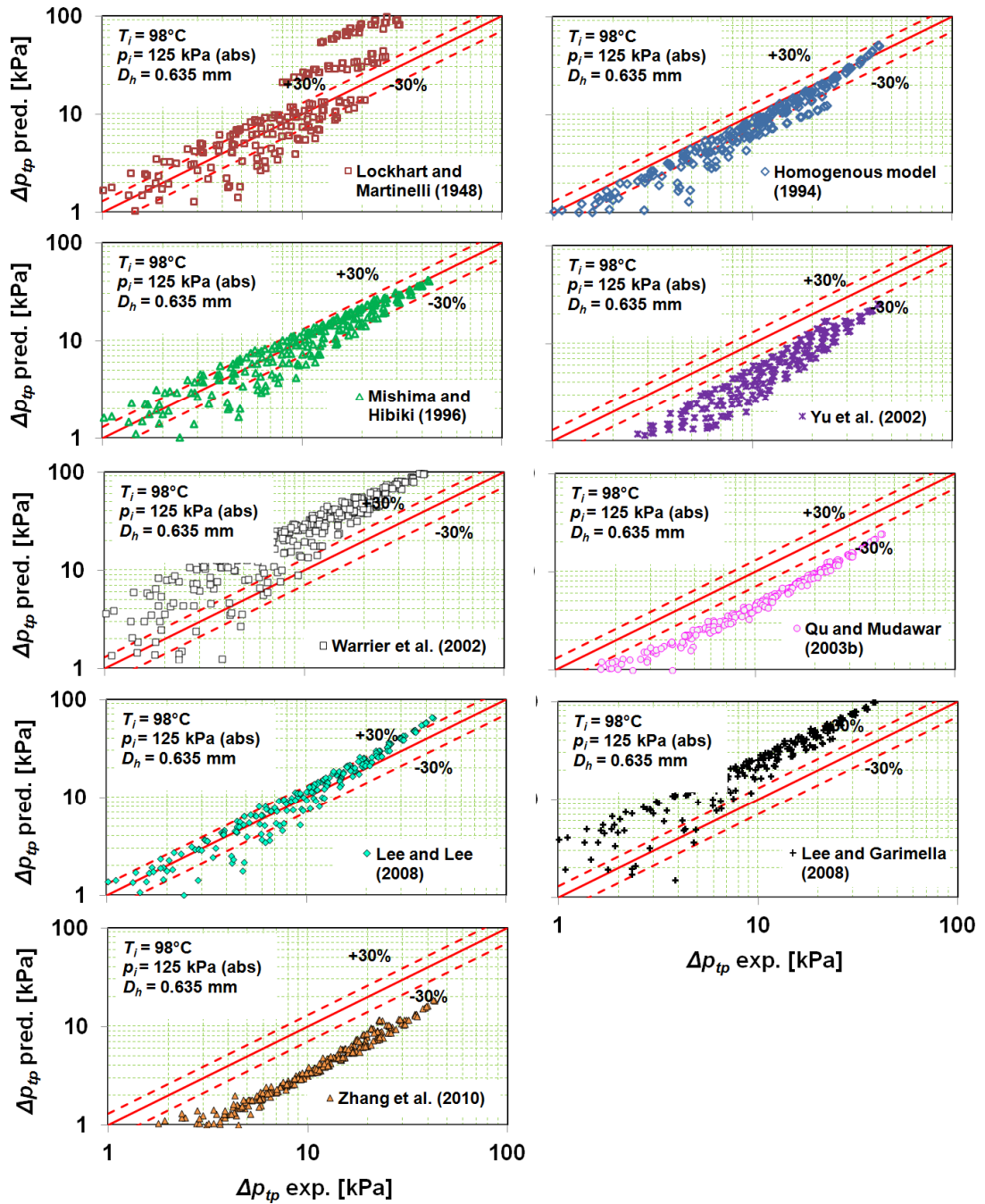


Figure 6.22 Comparison with correlations for the 0.635 mm.

Satisfying the criterion of ability of prediction within the 30% error bands are the correlations of Mishima and Hibiki (1996) for the 0.438 mm and 0.635 mm channels and Lee and Garimella (2008) for the 0.561 mm channel.

Table 6.1 MAE values of comparison with the existing correlations.

Correlation or reference	$D_h = 0.438$ mm		$D_h = 0.561$ mm		$D_h = 0.635$ mm	
	MAE [%]	$\beta$ [%]	MAE [%]	$\beta$ [%]	MAE [%]	$\beta$ [%]
Lockhart-Martinelli (1949)	128.7	13.5	33.2	40.0	121.2	30.4
Homogenous (1994)	272.0	0.33	41.0	36.3	29.1	62.0
Mishima and Hibiki (1996)	34.5	59.8	50.5	9.0	31.5	70.8
Yu et al. (2002)	52.9	22.1	70.0	2.2	57.3	2.9
Warrier et al. (2002)	48.4	59.4	56.5	22.7	163.6	6.7
Qu and Mudawar (2003b)	420.0	1.0	31.3	58.6	55.1	5.9
Lee and Lee (2008)	77.9	22.6	38.4	35.3	31.7	64.0
Lee and Garimella (2008)	295.5	1.65	25.9	70.7	160.6	5.9
Zhang et al. (2010)	35.5	65.0	71.7	0.36	64.3	4.4

## 6.5 Summary

Two-phase pressure drop experiments have been conducted using three different hydraulic diameter test sections (0.438 mm, 0.561 mm and 0.635 mm) with mass fluxes ranging from 200 to 1100 kg/m<sup>2</sup>s and heat fluxes from 79 to 973 kW/m<sup>2</sup>. The experiments were performed at a constant inlet temperature of 98°C (inlet subcooling 7 K) and a constant inlet pressure of 125 kPa (abs). Experimental results have been obtained and analyzed leading to conclusions as described in the following paragraphs.

The two-phase pressure drop increases with heat flux, mass flux and vapour quality. Increasing the heat flux results in increase bubble generation and quality, so that the flow has more restriction. As a result the pressure drop increases. In general, the two-phase pressure drop increases as the test section decreases. This is due to the fact that the pressure drop relates inversely to the channel hydraulic diameter.

The effect of hydraulic diameter on the pressure and pressure drop fluctuation is unclear but in general, as the hydraulic diameter decreases the pressure and pressure drop fluctuation decrease over the range of the experimental conditions. A higher pressure drop results in a smaller pressure fluctuation with a dominant frequency encountered of about 1 Hz, indicating that the fluctuation is due to the density wave oscillation.

Pressure drop data can be predicted using a number of correlations, as proposed by Mishima and Hibiki (1996) and Lee and Garimella (2008) with MAE values ranging from 25.9% to 34.5%. The recommended pressure drop prediction is the pressure drop correlation proposed by Mishima and Hibiki (1996). However, this recommendation is limited at experimental conditions: (i)  $q'' = 79$  to  $973$  kW/m<sup>2</sup>, (ii)  $\dot{m} = 200 - 1100$  kg/m<sup>2</sup>s, (iii)  $D_h = 0.438$  to  $0.635$  mm, (iv)  $p_i = 125$  kPa (abs) and  $T_i = 98^\circ\text{C}$  (inlet subcooled 7 K).

# Chapter 7

## Conclusions and Recommendations

### 7.1 Conclusions

Single-phase flow and flow boiling heat transfer and pressure drop in microchannels were investigated experimentally in the current study. Three test sections were used, made of free oxygen copper with hydraulic diameters of 0.438 mm, 0.561 mm and 0.635 mm. In single-phase flow experiments, the objective of the study was to identify the effect of fluid temperature and hydraulic diameter on the friction factor and to clarify the discrepancy of flow behaviour with the theory. In flow boiling experiments, the aims were to identify the effect of heat flux, mass flux, vapour quality and hydraulic diameter on the flow pattern and local & average heat transfer coefficient. In parallel with the heat transfer and pressure drop measurements, flow patterns were taken to assist in understanding and explaining the heat transfer results. They were observed at three locations, namely near the inlet, in the middle and near the outlet of the heated section, and recorded using a high speed camera. Additionally, a comprehensive exercise was conducted to compare the heat transfer and pressure drop results of the current study with predictions using existing heat transfer and pressure drop models and correlations. The conclusions that can be drawn from the present study are summarized below.

#### 7.1.1 Single-phase pressure drop and heat transfer

The experiments were performed at mass fluxes ranging from 278 to 5163 kg/m<sup>2</sup>s, at inlet temperatures of 30, 60 and 90°C (for pressure drop measurements) or 30°C (for heat transfer measurements) and at atmospheric pressure. The heat fluxes imposed were 146 – 537 kW/m<sup>2</sup>.

The conclusions are:

1. The effect of inlet temperature or fluid temperature on pressure drop was clear; pressure drop decreased as the fluid temperatures were increased.

2. The effect of fluid temperature on friction factor was not significant.
3. The effect of hydraulic diameter on pressure drop was significant.
4. The effect of hydraulic diameter on friction factor was insignificant.
5. The friction factors obtained in the three test sections were in reasonable agreement with developing flow theory.
6. The wall temperatures increased linearly at low mass fluxes but for high mass fluxes were almost constant.
7. The heat transfer coefficients were calculated using the uniform wall temperature method because of the nearly constant wall temperatures.
8. The heat transfer coefficients and Nusselt numbers depended on the Reynolds number both in laminar and turbulent flow.
9. The heat transfer coefficients and Nusselt numbers were higher than predicted by fully developed flow theory but in reasonable agreement with developing flow theory.
10. As the hydraulic diameter was decreased, the heat transfer coefficient increased. However Nusselt numbers seemed not to be affected by the hydraulic diameter.

### **7.1.2 Flow patterns**

The flow patterns were recorded in the present study at mass fluxes ranging from 200 to 1100 kg/m<sup>2</sup>s, heat fluxes from 79 to 793 kW/m<sup>2</sup>, and at inlet temperature and pressure of 98°C and 125 kPa (abs) respectively. The results demonstrated that:

1. The flow patterns observed in the 0.438 mm, 0.561 mm and 0.635 mm channels are bubbly, slug/confined, churn and annular.
2. Comparison of experimental data with available flow pattern maps indicates that there is reasonable agreement with the map proposed by Sobierska et al. (2006).
3. There is no clear effect of hydraulic diameter on the flow pattern at the same heat flux and mass flux for these experimental conditions.
4. The flow patterns change along the test section from near the inlet to the outlet at conditions of constant mass flux and heat flux.

5. The different flow patterns observed in the published results was mainly due to the lack of agreed standards of definitions of the patterns.
6. The length and locations of observation also support the deviation flow patterns observed in microchannels.
7. In general, in these experimental conditions, the flow patterns observed were the same as those obtained by the group, Chen et al. (2006) and those found in the conventional channels.

### **7.1.3 Heat transfer characteristics**

The local flow boiling heat transfer coefficient was determined experimentally for all test sections at the same conditions as those for flow pattern measurements and with inlet subcooling of  $\Delta T_{sub} \approx 7$  K and vapour qualities up to  $\approx 0.41$ . All measurements were recorded under steady conditions. The following conclusions can be drawn:

1. There was a significant effect of hydraulic diameter on the local heat transfer coefficient. For the 0.438 mm and 0.561 mm channels, the local heat transfer coefficient decreased with quality, whilst for the 0.635 mm channels the local heat transfer coefficient was almost independent of quality.
2. The decrease in local heat transfer coefficient with an increase in quality, for the 0.438 mm and 0.561 mm channels, was due to high pressure drops.
3. The highest local heat transfer coefficient was obtained for the 0.438 mm channel at near zero quality and the coincident flow patterns observed were slug flows.
4. For the three test sections, the effect of heat flux on the local heat transfer coefficient was significant, indicating that the nucleate boiling mechanism was dominant.
5. There was a strong effect of mass flux on the local heat transfer coefficient, particularly for the 0.438 mm and 0.561 mm channels. For the 0.635 mm channel the effect was not significant. The local heat transfer coefficient decreased with an increase in the mass flux, again due to high pressure drops.

6. When the local heat transfer coefficient was plotted versus dimensionless distance, the effect of heat flux on the local heat transfer coefficient was unclear.
7. The effect of hydraulic diameter on the local heat transfer coefficient at the same heat flux and mass flux was also unclear.
8. The effect of heat flux on the average heat transfer coefficient was significant for the 0.561 mm and 0.635 mm channels, but insignificant for the 0.438 mm channel.
9. The effect of hydraulic diameter on the average heat transfer coefficient was significant, in both subcooled and saturated conditions.
10. Several heat transfer coefficient correlations can be used for predicting the experimental data with MAEs ranging from 14.1% to 82.9%.
11. The heat transfer surface area seems to support the accurate measurement of heat transfer coefficient.

#### **7.1.4 Pressure drop**

The total flow boiling pressure drop in the three test sections has been measured at mass fluxes ranging from 200 to 1100 kg/m<sup>2</sup>s at atmospheric pressure. The results indicate that:

1. The two-phase pressure drop increases with increasing heat flux (exit quality), increasing mass flux and decreasing hydraulic diameter.
2. The contribution of the frictional pressure drop component to the total measured pressure drop was found to be the largest compared to the other components.
3. The accelerational pressure drop always increases with the heat flux or vapour quality.
4. Several correlations and models were evaluated. Results indicated that the Homogenous model (1994), Mishima & Hibiki (1996) and Lee and Garimella (2008) correlations are better than other correlations/models.

#### **7.2 Recommendations**

Based on the experiments conducted in the present study, the issues that require further investigations include the following:

- As the maximum quality obtained in the present study was only up to 0.4, it is recommended to extend the quality, e.g. 0.9. To achieve this needs a cover made of glass.
- The effect of hydraulic diameter on the local heat transfer coefficient and flow boiling fluctuation needs further investigation, e.g. different hydraulic diameters but the same aspect ratio and different experimental conditions.
- Work on synchronisation has not been performed; therefore it needs to be investigated.
- To avoid outlet pressure falling below the ambient pressure, the inlet pressure should be at least two bar absolute.
- Experiments using other fluids should be performed to clarify the trends of local heat transfer coefficient with fluid properties.

## References:

Agostini, B., Watel, B., Bontemps, A., and Thonon, B. Friction factor and heat transfer coefficient of R-134a liquid flow in minichannels. *Applied Thermal Engineering*, 22, pp. 1821 – 1834, 2002.

Agostini, B., Thome, J.R., Fabbri, M., Michel, B., Calmi, D., Kloter, U., High heat flux flow boiling in silicon multi channels Part I: Heat transfer characteristics of refrigerant R236fa, *Int. J. Heat Mass Transfer*, 51, pp. 5400 – 5414, 2008.

Akbar, M.K., Plummer, D.A., Ghiaasiaan, S.M., On gas-liquid two-phase flow regimes in microchannels, *Int. J. Multiphase Flow*, 29, pp. 855 – 865, 2003.

Akbari, M., Sinton, D., Bahrami, M., Pressure drop in rectangular microchannels as compared with theory based on arbitrary cross section, *J. Fluid Engineering*, 131, pp. 1 – 8, 2009.

Balasubramanian, P., Kandlikar, S.G., Experimental study of flow patterns, pressure drop, and flow instability in parallel rectangular minichannels, *Heat Transfer Engineering*, 26(3), pp. 20 – 27, 2005.

Bao, Z.Y., Fletcher, D.F., Haynes, B.S., Flow boiling heat transfer of Freon R11 and HCFC123 in narrow passages, *Int. J. Heat Mass Transfer*, 43, pp. 3347 – 3358, 2000.

Bavie`re, R., Le Person, S., Ayela, F., Favre-Marinet, M., An experimental study of water flow in smooth and rectangular micro-channels, Int. Conference on Microchannel and Minichannel, ASME Publication, 2004. In: Caney, N., Marty, P., Bigot, J., Friction losses and heat transfer of single phase in a mini channel, *Applied Thermal Engineering*, 27, pp. 1715 – 1721, 2007.

Bejan, A., *Convection Heat Transfer*, Third edition, John Wiley and Sons, Hoboken, New York, 2004.

Bogojevic, D., Sefiane, K., Walton, A.J., Lin, H., Cummins, G., Two-phase flow instabilities in a silicon microchannel heat sink, *Int. J. Heat Fluid Flow*, 30, pp. 854 – 867, 2009.

Boure, J.A., Bergles, A.E., Tong, L.S., Review of two-phase flow instability, *Nuclear Engineering and Design*, 25, pp. 165 – 192, 1973.

Brauner, N., Moalem-Maron, D., Identification of the range of small diameter conduits regarding two-phase flow pattern transitions, *International Communications Heat Mass Transfer*, 19, pp. 29 – 39, 1992.

Brutin, D., Topin, F., Tadrist, L., Experimental study of unsteady convective boiling in heated minichannels, *Int. J. Heat Mass Transfer*, 46, pp. 2957 – 2965, 2003.

Caney, N., Marty, P., Bigot, J., Friction losses and heat transfer of single phase in a mini channel, *Applied Thermal Engineering* 27, pp. 1715 – 1721, 2007.

Chen, W.L., Twu, M.C., and Pan, C., Gas-liquid two-phase flow in microchannels, *Int. J. Multiphase Flow*, 28, pp. 1235 – 1247, 2002.

Chen, L., Tian, Y.S., Karayiannis, T.G., The effect of tube diameter on vertical two-phase flow regimes in small tubes, *Int. J. Heat Mass Transfer*, 49, pp. 4220 – 4230, 2006.

Choi, S. B., Barron R. F., and Warrington, R. O., Fluid flow and heat transfer in microtubes, *ASME Micromechanical Sensors, Actuators and Systems*, DSC-vol. 32, 1991, In: Morini, G.L., Single-phase convective heat transfer in microchannels: a review of experimental results, *Int. J. Thermal Sciences*, 43, pp. 631 – 651, 2004.

Cho, H., Cho, K., Two-phase flow distribution and pressure drop in microchannel tubes under non heating and heating conditions, *Nanoscale and Microscale Thermophysical Engineering*, 10, pp. 233 – 247, 2006.

Coleman, H.W., Steele, W.G., *Experimentation, Validation, and Uncertainty Analysis for Engineers*, 3<sup>rd</sup> edition, John Wiley and Son, Inc., Hoboken, New Jersey, USA, 2009.

Coleman, J.W., Garimella, S., Characterization of two-phase flow patterns in small diameter round and rectangular tubes, *Int. J. Heat Mass Transfer*, 42, pp. 2869 – 2881, 1999.

Collier, J.G., Thome, J.R., *Convective Boiling and Condensation*, Chapter 2, 3<sup>rd</sup> edition, Oxford University Press Inc., New York, 1994.

Consolini, L., Thome, J.R., Microchannel flow boiling heat transfer of R134a, R236fa and R245fa, *Microfluid Nanofluid*, 6, pp. 731 – 746, 2009.

Costaschuck, D., Elsnab, J., Petersen, S., Klewicki, J.C., Ameel, T., Axial static pressure measurements of water flow in rectangular microchannel, *Exp. Fluids*, 43, pp. 907 – 916, Springer-Verlag, 2007.

Díaz, M.C., Boye, H., Hapke, I., Schmidt, J., Staate, Y., Zhekov, Z., Investigation of flow boiling in narrow channels by thermographic measurement of local wall temperatures, *Microfluidics and Nanofluidics*, 2(1), pp. 1 – 11, 2005.

Dittus, F.W., Boelter, L.M.K., Heat transfer in automobile radiators of tubular type, *Int. Comm. Heat Mass Transfer*, 12, pp. 3 – 22, 1930.

Gao, P., Person, S. L., Marinet, M. F., Scale effects on hydrodynamic and heat transfer in two dimensional mini and micro channel, *Int. J. Thermal Sciences*, 41, pp. 1017 – 1027, 2002.

Gedupudi, S., Kenning, D.B.R., Karayiannis, T.G., 1-D modeling of pressure fluctuation due to confined bubble growth during flow boiling in microchannel, 2<sup>nd</sup> Micro and Nano Flows conference, West London, UK, 2009.

Gnielinski, V., New equations for heat transfer in turbulent pipe and channel flow, *Int. Chemical Engineering*, 16, pp. 359 – 368, 1976.

Gungor, K. E. Winterton, R.H.S, Simplified general correlation for saturated and comparisons of correlations with data, *The Canadian Journal of Chemical Engineering*, 65(1), pp. 148 – 156, 1987.

Hager, W.H., Blasius: A life in research and education, *Experiments in Fluids*, 34, pp. 566 – 571, 2003.

Harrirchian, T., Garimella, S.V., Microchannel size effects on local flow boiling heat transfer to a dielectric fluid, *Int. J. Heat Mass Transfer*, 51, pp. 3724 – 3735, 2008.

Harrirchian, T., Grimella, S.V., The critical role of channel cross sectional area in microchannel flow boiling heat transfer, *Int. J. Multiphase Flow*, 35, pp. 904 – 913, 2009a.

Harrirchian, T. & Garimella, S.V., Effects of channel dimension, heat flux, and mass flux on flow boiling regimes in microchannels, *Int. J. Multiphase Flow*, 35(4), pp. 349 – 362, 2009b.

Harms, T.M., Kazmierczak, M.J., Gerner, F.M., Developing convective heat transfer in deep rectangular Microchannels, *Int. J. Heat Fluid Flow*, 20, pp. 149 – 157, 1999.

Hassan, I., Vailancourt, M., Pehlivan, K., Two-phase flow regime transitions in microchannels: A comparative experimental study, *Microscale Thermophysical Engineering*, 9(2), pp. 165 – 182, 2005.

Hayashi, S., Kasagi, N. & Suzuki, Y., The effects of inlet flow conditions on gas liquid two phase flow in a micro tube, *Proceedings of HT2007, 2007 ASME-JSME Thermal Engineering Summer Heat Transfer Conference*, Vancouver, British Columbia, Canada, July 8 – 12, 2007.

Hetsrony, G., Mosyak, A., Segal, Z., Pogrebnyak, E., Two-phase flow pattern in parallel micro-channels, *Int. J. Multiphase Flow* 29, pp. 341 – 360, 2003.

Hetsroni, G., Mosyak, A., Pogrebnyak, E., Segal, Z., Periodic boiling in parallel microchannels at low vapor quality, *Int. J. Multiphase Flow*, 32, pp. 1141 – 1159, 2006.

Hetsroni, G., Mosyak, A., Pogrebnyak, E., Segal, Z., Heat transfer of gas-liquid mixture in micro channel heat sink, *Int. J. Heat Mass Transfer*, 52, pp. 3963 – 3971, 2009.

Huo, X., Tian, Y.S. and Karayiannis, T. G. R134a Flow boiling heat transfer in small diameter tubes. *Advances in compact heat exchangers*, R.T. Edwards, Inc., 5, pp. 95 – 111, 2007.

<http://www.daftlogic.com/sandbox-google-maps-find-altitude.htm>.

<http://www.npl.co.uk/reference/faqs/>

<http://resource.npl.co.uk/pressure/pressure.html>

Huh, C., Kim, M.H., Pressure drop, boiling heat transfer and flow patterns during flow boiling in a single microchannel, *Heat Transfer Engineering*, 28(8-9), pp. 730 – 737, 2007.

Hwang, Y. W. and Kim, M. S., The pressure drop in microtubes and the correlation development, *Int. J Heat Mass Transfer*, 49, pp. 1804 – 1812, 2006.

Incropera, F.P., Dewitt, D.P., Bergman, T.L., Lavine, A.S., *Fundamental of heat and mass transfer*, Sixth Edition, John Wiley and Sons, USA, 2006.

Jiang, X. N., Zhou, Z. Y., Yao, J., Li, Y., Ye, X. Y., Micro fluid flows in micro channel, Pro. Transducer '95, Stockholm, Sweden, June 25-29, pp. 317 – 320, 1995.

Jiang, X.N., Zhou, Z.Y., Huang, X.Y., Liu, C.Y., Laminar flow through microchannels used for microscale cooling systems, IEEUCPMT Electronic Packaging Technology Conference, pp. 119 – 122, 1997.

Jiang, P.X., Fan, M.H., Si, G.S., Ren, Z.P., Thermal-hydraulic performance of small scale micro-channel and porous-media heat-exchangers, *Int. J. Heat and Mass Transfer*, 44, pp. 1039 – 1051, 2001.

Jiang, J., Hao, Y., Shi, M., Fluid flow and heat transfer characteristics in rectangular microchannel, *Heat Transfer-Asian Research*, 37, pp. 197 – 207, 2008.

Judy, J., Maynes, D., Webb, B. W., Characterization of frictional pressure drop for liquid flows through micro channel, *Int. J. Heat Mass Transfer*, 45(17), pp. 3477 – 3489, 2002.

Jung, J-Y., Kwak, H-Y., Fluid flow and heat transfer in microchannels with rectangular cross section, *Springer, Heat Mass Transfer*, 44, pp. 1041 – 1049, 2008.

Karayiannis, T.G., Shiferaw D., Kenning, D.B.R., Flow boiling in small- to micro- diameter tubes: experimental results and modelling, *ECI International Conference on Heat Transfer and Fluid Flow in Microscale*, Whistler, pp. 21 – 26, September 2008.

Karayiannis, T.G., Shiferaw, D., Kenning, D.B.R., Wadekar, V.V., Flow pattern and heat transfer for flow boiling in small to micro diameter tubes, *Heat Transfer Engineering*, 31(4), pp. 257 – 275, 2010.

Kandlikar, S. G., A general correlation for two-phase flow boiling heat transfer coefficient inside horizontal and vertical tubes, *Int. J. Heat Transfer*, 102, pp. 219 – 228, 1990.

Kandlikar, S.G., Joshi, S., Tian, S., Effect of channel roughness on heat transfer and fluid flow characteristics at low Reynolds numbers in small diameter tubes, *Proceedings of NHTC'01 35<sup>th</sup> National Heat Transfer Conference*, Anaheim, California, June 10 – 12, 2001.

Kandlikar S.G., Two-phase flow patterns, pressure drop, and heat transfer during boiling in minichannel flow passages of compact evaporators, *Heat Transfer Engineering*, 23(1), pp. 5 – 23, 2002.

Kandlikar, S.G., Grande, W.J., Evolution of microchannel flow passages—thermo hydraulic performance and fabrication technology, Proceedings of IMECE2002 ASME International Mechanical Engineering Congress & Exposition November 17-22, 2002, New Orleans, Louisiana.

Kandlikar, S.G., Joshi, S., Tian, S., Effect of surface roughness on heat transfer and fluid flow characteristics at low Reynolds numbers in small diameter tubes, *Heat Transfer Engineering*, 24 (3), pp.4 – 16, 2003.

Kandlikar, S.G., Kuan, W.K, Willistein, D.A, Borrelli, J., Stabilization of flow boiling in microchannels using pressure drop elements and fabricated nucleation site, *Int. J. Heat Mass Transfer*, 128, pp. 389 – 396, 2006.

Kays, W.M., London, A.L., *Compact Heat Exchanger*, 3<sup>rd</sup> edition, McGrawhill, New York, 1984.

Kawahara, A., Chung, P.M-Y., Kawaji, M., Investigation of two-phase flow patterns, void fraction and pressure drop in a micro-channel. *Int. J. Multiphase Flow*, 28(9), pp. 1411 – 1435, 2002.

Kenning, D.B.R., Yan, Y., Saturated flow boiling of water in a narrow channel: experimental investigation of local phenomena, *ICHEME Transaction A, Chemical Engineering Res. and Design*, 79, pp. 425 – 436, 2001.

Kenning, D.B.R., Wen, D.S., Das, K.S., Wilson, S.K., Confined growth of vapour bubble in capillary tube at initially uniform superheat: experiment and modeling, *Int. J. Heat Mass Transfer*, xx, pp. xxx-xxx, 2006.

Kew, P.A., Cornwell, K., Correlations for the prediction of boiling heat transfer in small diameter channels, *Applied Thermal Engineering*, 17(8-10), pp. 705 – 715, 1997.

Kohl, M.J., Abdel-Khalik, S.I., Jeter, S.M., Sadowski, D.L., An experimental investigation of microchannel flow with internal pressure measurements, *Int. J. Heat Mass Transfer*, 48, pp. 1518 – 1533, 2005.

Kuo, C.J., Peles, Y., Pressure effects on flow boiling instabilities in parallel microchannels, *Int. J. Heat Mass Transfer*, 52, pp. 271 – 280, 2009.

Lazarek, G.M., Black, S.H., Evaporative heat transfer, pressure drop and critical heat flux in a small tube with R113, *Int. J. Heat Mass transfer*, 25, pp. 945 – 960, 1982.

Lelea, D., Nishio, S., Takano, K., The experimental research on microtube heat transfer and fluid flow of distilled water, *Int. J. Heat Mass Transfer*, 47, pp. 2817 – 2830, 2004.

Lee, H.J., Lee, S.Y., Heat transfer correlation for boiling flows in small rectangular horizontal channels with low aspect ratios, *Int. J. Multiphase Flow*, 27, pp. 2043 – 2062, 2001.

Lee, C.Y., Lee, S.Y., Pressure drop of two-phase plug flow in round mini-channels: Influence of surface wettability, *Exp. Thermal and Fluid Science*, 32, pp. 1716 – 1722, 2008.

Lee, P.S., Garimella, S.V., Liu, D., Investigation of heat transfer in rectangular microchannels, *Int. J. Heat Mass Transferr*, 48, pp. 1688 – 1704, 2005.

Lee, P.S., Garimella, S.V., Saturated flow boiling heat transfer and pressure drop in silicon microchannel arrays, *Int. J. Heat Mass Transfer*, 51, pp. 789 – 806, 2008.

Lee, J., Mudawar, I., Two-phase flow in high-heat-flux micro-channel heat sink for refrigeration cooling application: Part II Heat transfer characteristics, *Int. J. Heat Mass Transfer*, 48, pp. 941 – 955, 2005.

Lee, J., Mudawar, I., Fluid flow and heat transfer characteristics of low temperature two-phase micro-channel heat sinks-Part 2. Subcooled boiling pressure drop and heat transfer, *Int. J. Heat Mass Transfer*, 51, pp. 4327-4341, 2008.

Lee, J., and Mudawar, I., Low temperature two phase microchannel cooling for high heat flux thermal management of defense electronic, *IEEE Transaction on Component and Packaging Technology*, 32(2), June, 2009.

Li, Z-H., and Cui, H-H., Experiments about simple liquid flows in microtubes, 1<sup>st</sup> International Conference on Microchannels and Minichannels, April 21 – 23, Rochester, New York, USA, 2003.

Li, W., Wu, Z., A general correlation for evaporative heat transfer in micro/mini-channels, *Int. J. of Heat Mass Transfer*, 53, pp. 1778 – 1787, 2010.

Li, Z., He, Y.L., Tang, G.H., Tao, W.Q., Experimental and numerical studies of liquid flow and heat transfer in microtubes, *Int. J. Heat Mass Transfer*, 50, pp. 3447 – 3460, 2007.

Lin, S., Kew, P.A., Cornwell, K., Flow boiling of refrigerant R141B in small tubes, *Trans IChemE*, 79, Part A, pp. 417 – 424, 2001.

Lin, T.Y., Kandlikar, S.G., An experimental investigation of structure roughness on heat transfer during single-phase liquid flow at microscale, 3<sup>rd</sup> Micro and Nano Flows Conference, Thessaloniki, Greece, 22 – 24 August, 2011.

Lockhart, R.W., Martinelli, R.C., Proposed correlation of data for isothermal two-phase, two-component flow in pipes, *Chemical Engineering Process*, 45(1), pp. 39 – 48, 1949.

Lu, C.T., Pan, C., Stabilization of flow boiling in microchannel heat sinks with a diverging cross-section design, *J. Micromech. Microeng.*, 18 , pp. 1 – 13, 2008.

Mahendale, S.S., Jacobi, A.M., Shah, R.K., Fluid flow and heat transfer at micro and meso scale with application to heat exchanger design, *Applied Mechanics Reviews*, 53(7), pp. 175 – 193, 2000.

Mahmoud, M.M., *Flow Boiling of R134a in Vertical Mini-diameter Tubes*, PhD Thesis, Brunel University, UK, 2011.

Mala, G. M., Li, D., and Dale, J. D., Heat transfer and fluid flow in microchannels. *Int. J. Heat Mass Transfer*, 40(13), pp. 3079 – 3088, 1997.

Mala, G.M., Li, D., Flow characteristics of water in microtubes, *Int. J. Heat Fluid Flow*, 20, pp. 142 – 148, 1999.

Mahmoud, M.M., Kenning, D.B.R., Karayiannis, T.G., Single and two phase heat transfer and pressure drop in a 0.52 mm vertical metallic tube, Seventh International Conference on Enhanced, Compact and Ultra Compact Heat Exchanger: From Microscale Phenomena to Industrial Applications, CHE 2009.

Maranzana, G., Perry, I., Maillet, D., Mini and microchannels: influence of axial conduction in the walls. *Int. J. Heat Mass Transfer*, 47, pp. 3993 – 4004, 2004.

McQuillan, K.W., Whalley, P.B., Flow pattern in vertical two phase flow, *Int. J. Multiphase Flow*, 11(2), pp. 161 – 175, 1985.

Mishan, Y., Mosyak, A., Pogrebnyak, E., Hetsroi, G., Effect of developing flow and thermal regimes on momentum and heat transfer in micro scale heat sinks, *Int. J. Heat Mass Transfer*, 50, pp. 3100 – 3114, 2007.

Mishima, K., Hibiki, T., Nishihara, H., Some Characteristics of Gas–liquid Flow in Narrow Rectangular Ducts, *Int. J. Multiphase Flow*, 19(1), pp. 115 – 124, 1993.

Mishima, K., Hibiki, T., Some characteristics of air-water two-phase flow in small diameter vertical tubes, *Int. J. Multiphase Flow*, 22(4), pp. 703 – 712, 1996.

Morini, G.L., Single-phase convective heat transfer in microchannels: a review of experimental results, *Int. J. Thermal Sciences*, 43, pp. 631 – 651, 2004.

Mudawar, I., Assessment of high heat flux thermal management schemes. *Transactions on Components and Packaging Technologies*, 24(2), pp. 122 – 140, 2001.

Mukherjee, A., Kandlikar, S.G., The effect of inlet constriction on bubble growth during flow boiling in microchannels, *Int. J. Heat Mass Transfer*, 52, pp. 5204 – 5212, 2009.

Naphon, P., Wiriyaart, S., Liquid cooling in the mini-rectangular fin heat sink with and without thermoelectric, *International Communications in Heat and Mass Transfer*, 36, pp. 166 – 171, 2009.

Papautsky, I., Brazzle, J., Ameen, T., Frazier, A., B., Laminar fluid behavior in micro channel using micro polar fluid theory, *Sensors and Actuator*, 73, pp. 101 – 108, 1999.

Peng, X.F., Wang, B.X., Forced convection and boiling characteristics in microchannel, *Heat transfer* 1998, Proc. of 11<sup>th</sup> IHTC, Korea, 1, pp. 371 – 390, 1998.

Peng, X.F., Hu, H.Y., Wang, B.X., Flow boiling through V-shape microchannels, *Exp. Heat Transfer*, 11(1), pp. 87 – 100, 1998.

Pfahler, J., Harley, J., Bau, H., Liquid transport in micron and sub micron channel, *sensor and actuator*, A21-A23, pp. 43 – 434, 1990.

Pfund, D., Rector, D., Shekarriz, A., Pressure drop measurements in a microchannel, *Fluid Mechanic and Transport Phenomena*, 46(8), pp. 1496 – 1507, 2000.

Phillips, R.J., *Forced Convection, Liquid Cooled, Microchannel Heat Sinks*, MS Thesis Department of Mechanical Engineering, Massachusetts Institute of Technology, Cambridge Chapter 2, p. 70, 1987.

Qu, W., Mala, G.M., Li, D., Pressure-driven water flows in trapezoidal silicon microchannels, *Int. J. Heat Mass Transfer*, 43, pp. 353 – 364, 2000.

Qu, W., Mudawar, I., Transport phenomena in two-phase microchannels heat sinks, *Proceedings of IMECE2002*, ASME International Mechanical Engineering Congress & Exposition, November 17-22, New Orleans, Louisiana, 2002.

Qu, W., Mudawar, I., Measurement and prediction of pressure drop in two-phase microchannel heat sinks, *Int. J. Heat Mass Transfer*, 46, pp. 2737-2753, 2003a.

Qu, W., Mudawar, I., Flow boiling heat transfer in two-phase microchannel heat sinks-I. Experimental investigation and assessment of correlation methods, *Int. J. Heat Mass Transfer*, 46, pp. 2755 – 2771, 2003b.

Qu, W., Yoon, S.M., Mudawar, I., Two-phase flow and heat transfer in rectangular microchannels, *Int. J. Electronics Packaging*, 126, pp. 288 – 300, 2004.

Ren, L., Qu, W., Li, D., Interfacial electrokinetics effects on liquids flow in microchannels, *Int. J. Heat Mass Transfer*, 44, pp. 3125 – 3134, 2001.

Revellin, R., Dupont, V., Ursenbacher, T., Thome, J.R. and Zun, I., Characterization of diabatic two phase flows in microchannels: Flow parameter results for R134a in a 0.5 mm channel, *Int. J. Multiphase Flow*, 32, pp. 755 – 774, 2006.

Ribatski, G., Wojtan, L., & Thome, J. R., An analysis of experimental data and prediction methods for two-phase frictional pressure drop and flow boiling heat transfer in micro-scale channels. *Experimental Thermal and Fluid Science*, 31, pp. 1 – 19, 2006.

Rosa, P., Karayiannis, T. G., and Collins, M. W., Single-phase heat transfer in microchannels: the importance of scaling effects, *Applied Thermal Engineering*, 29(17-18), pp. 3447 – 3468, 2009.

Saitoh S., H. Daiguji, Hihara, E. Effect of tube diameter on boiling heat transfer of R134a in horizontal small-diameter tubes, *Int. J. Heat Mass Transfer*, 48, pp. 4973 – 4984, 2005.

Saisorn, S. and Wongwises, S., The effects of channel diameter on flow pattern, void fraction and pressure drop of two phase air-water flow in circular microchannels, *Experimental Thermal and Fluid Science*, 34(4), pp. 454 – 462, 2010.

Shah, R. K., A correlation for laminar hydrodynamics entry length solution for circular and non circular ducts, *J. Fluids Engineering*, 100, pp. 177 – 179, 1978.

Shah, M.M., Chart correlation for saturated boiling heat transfer: equations and further study, *ASHRAE Transactions*, 88, pp. 185 – 196, 1982.

Shah, R.K. and Sekulić, D.P. *Fundamentals of Heat Exchanger Design*, John Wiley & Sons Inc., 2003.

Shah, R.K., London, A.L., *Laminar flow forced convection in ducts*, Supplement 1 to Advances in Heat Transfer, Academic Press New York, 1978.

Shen, S., Xu, J.L., Zhou, J.J., Chen, Y., Flow and heat transfer in microchannels with rough wall surface, *Energy Conversion and Management*, 47, pp. 1311 – 1325, 2006.

Sieder, E.N., Tate, G.E., Heat transfer and pressure drop of liquids in tubes, *Industrial and Engineering Chemistry*, 28, pp. 1429 – 1435, 1936.

Silverio, V., Moreira, A.L.N., Pressure drop and heat convection in single-phase fully-developed, laminar flow in microchannels of diverse cross section, 5<sup>th</sup> European Thermal Science Conference, the Nederland, 2008.

Sing, S.G., Bhide, R.R., Duttgupta, S.P., Puranik, B.P., Agrawal, A., Two phase flow pressure drop characteristics in trapezoidal silicon microchannels, *IEEE Transaction on components and packaging technology*, 32(4), pp. 887 – 900, 2009.

Sobierska, E., Kulenovic, R., Mertz, R., Groll, M., Experimental results of flow boiling of water in a vertical microchannel, *Exp. Thermal and Fluid Sci.* 31, pp. 111 – 119, 2006.

Sowinski, J., Dziubinski, Experimental study on gas-viscous liquid mixture flow regimes and transition criteria in vertical narrow rectangular channels, *World Academy of Science, Engineering and Technology*, 23, pp. 1 – 4, 2008.

Steinke, M. E., Kandlikar, S. G., Single-phase liquid friction factors in microchannel, *Int. J. Thermal Science*, 45, pp. 1073 – 1083, 2006.

Steinke, M.S., Kandlikar, S.G., Magerlein, J.H., Colgan, E.G., Raisanen, A.D., Development of an experimental facility for investigating single-phase liquid flow in microchannels, *Heat Transfer Engineering*, 27, pp. 41 – 52, 2006.

Sumith, B., Kaminaga, F., Matsumura, K., Saturated flow boiling of water in a vertical small diameter tube, *Exp. Thermal Fluid Science*, 27, pp. 789 – 801, 2003.

Sun, L., Mishima, K., An evaluation of prediction methods for saturated flow boiling heat transfer in mini-channels, *Int. J. Heat Mass Transfer*, 52, pp. 5323 – 5329, 2009.

Tiselj, I., Hetsroni, G., Mavko, K., Mosyak, A., Pogrebnyak, E., Segal, Z., Effect of axial conduction on the heat transfer in micro-channels, *Int. J. Heat Mass Transfer*, 47, pp. 2551–2565, 2004.

Thome, J.R., *Engineering Data Book III*, Engineering Thermal Innovation, Chapter 13, Walverine Tube Inc., Switzerland, 2004 – 2010.

Toh, K.C., Chen, X.Y., Chai, J.C., Numerical computation of fluid flow and heat transfer in microchannels, *Int. J. Heat Mass Transfer*, 45, pp. 5133 – 5141, 2002.

Tran, T.N., Wambsganss, M.W., France, D.M., Small circular and rectangular channel boiling with two refrigerants, *Int. J. Multiphase Flow*, 22, pp. 485 – 493, 1996.

Tran, T.N., Chyu, M.C., Wambsganss, M.W., France, D.M., Two phase pressure drop of refrigerant during flow boiling in small channels: an experimental investigation and correlation development, *Int. J. Multiphase Flow*, 26, pp. 1739 – 1754, 2000.

Tukerman, D.B., Pease, R.F.W., High performance heat sinking for VSLI, *IEEE Electron Device Lett.* EDL2, 126 – 129, 1981.

Triplett, A.K., Ghiaasiaan, S.M., Abdel-Khalik, S.I., Sadowski, D.L., Gas-liquid two-phase flow in microchannels, Part I: Two-phase flow patterns. *Int. J. Multiphase Flow*, 25, pp. 377 – 394, 1999.

Urbanek, W., Zemel, J.N., Bau, H.H., An investigation of temperature dependence of Poiseuille numbers in microchannel flow, *J. Micromech. Microeng.*, 3, pp. 206 – 208, 1993.

Venkatesan, M., Das, S.K., Balakrishnan, A.R., Effect of tube diameter on two-phase flow patterns in mini tubes, *The Canadian Journal of Chemical Engineering*, 88, pp. 936 – 944, 2010.

Vlasie, C., Macchi, H., Guilpart, J., Agostini, B., Flow boiling in small diameter channels, *Int. J. Refrigeration*, 27, pp. 191 – 201, 2004.

Wambsganss, M.W., Jendrzejczyk, J.A., France, D.M., Two-phase flow pattern and transitions in a small, horizontal, rectangular channel, *Int. J. Multiphase Flow*, 17(3), pp. 327 – 342, 1991.

Wambsganss, M.W., France, D.M., Jendrzejczyk, J.A., Tran, T.N., Boiling heat transfer in a horizontal small-diameter tube, *ASME, J. Heat Transfer*, 115, pp. 963 – 972, 1993.

Wang, B.X., Peng, F.X., Experimental investigation on liquid forced convection heat transfer through microchannel, *Int. J. Heat Mass Transfer*, 37, pp. 73 – 82, 1994.

Wang, H., Wang, Y., Influence of three-dimensional wall roughness on the laminar flow in microtube, *Int. J. Heat Fluid Flow*, 28, pp. 220 – 228, 2007.

Wang, G., Cheng, P., Wu, H., Unstable and stable flow boiling in parallel microchannels and in a single microchannel, *Int. J. Heat Mass Transfer*, 50, pp. 4297 – 4310, 2007.

Wang, G., Cheng, P., Bergles, A.E., Effects of inlet/outlet configuration on flow boiling instability in parallel microchannels, *Int. J. Heat Mass Transfer*, 51, pp. 2267 – 2281, 2008.

Wang, G., Hao, L., Cheng, P., A four-zone model for saturated flow boiling in a microchannel of rectangular cross-section, *Int. J. Heat Mass Transfer*, 53, pp. 3439 – 3448, 2010.

Wang, J., Huang, Y., Wang, Y., Photographic study on two phase flow patterns of water in a single side heated narrow rectangular microchannel, *ASME J. Engineering for Gas Turbines and Power*, 133, pp. 1 – 5, 2011.

Wang, Y., Sefiane, K., Effects of heat flux, vapour quality, channel hydraulic diameter on flow boiling heat transfer in variable aspect ratio micro-channels using transparent heating, *Int. J. Heat Mass Transfer*, 55, pp. 2235 – 2243, 2012.

Warrier, G.R., Dhir, V.K., Momoda, L.A., Heat transfer and pressure drop in narrow rectangular channels, *Exp. Thermal Fluid Sci.*, 26, pp. 53 – 64, 2002.

Watel, B., Review of Saturated Flow Boiling in Small Passages of Compact Heat Exchangers, *Int. J. Thermal Sci.*, 42, pp. 107 – 140, 2003.

Wen, D.S., Yan, Y., Kenning, D.B.R., Saturated flow boiling of water in a narrow channel: time-averaged heat transfer coefficients and correlations, *Applied Thermal Engineering*, 24, pp. 1207 – 1223, 2004.

Wilding, P., Pfahler, J., Bau, H. H., Zemel, N. J., Kricka, L. J., Manipulation and flow of biological fluids in straight channel micro machined in silicon, *J. Clinical Chemistry*, 40(1), pp. 43 – 47, 1994.

Wilmarth, T, Ishii, M, Two-phase flow regimes in narrow rectangular vertical and horizontal channels hr. *J. Hear Mass Transfer*, 37(12), pp. 1749 – 1758, 1994.

Wu, P., Little, W. A., Measurement of friction factor for the flow of gases in very fine channel used for micro miniature Joule-Thomson refrigerator, *Cryogenic*, (5), pp. 273 – 277, 1983.

Wu, H.Y., Cheng, P., Boiling instability in parallel silicon microchannels at different heat flux, *Int. J. Heat Mass Transfer*, 47, pp. 3631 – 3641, 2004.

Wu, H.Y., Cheng, P., Wang, H., Pressure drop and flow boiling instability in silicon microchannel heat sinks, *J. Micromech. Microeng*, 16, pp. 2138 – 2146, 2006.

Xiong, R., Chung, J.N., An experimental study of the size effect on adiabatic gas-liquid two-phase flow patterns and void fraction in microchannels, *Physics of Fluids*, 19(3), pp. 1 – 8, 2007.

Xu, J.L., Cheng, P., Zhao, T.S., Gas-liquid two-phase flow regimes in rectangular channels with mini/micro gaps, *Int. J. Multiphase Flow*, 25, pp. 411 – 432, 1999.

Xu, B., Ooi, K.T., Wong, N.T., Choi, W.K., Experimental investigation of flow friction for liquid flow in microchannels, *Int. Comm. Heat Mass Transfer*, 27(8), pp. 1165 – 1176, 2000.

Xu, J., Zhou, J., Gan, Y., Static and dynamic flow instability of a parallel microchannel heat sink at high heat fluxes, *Energy Conversion and Management*, 46, pp. 313 – 334, 2005.

Xu, J., Liu, G., Zhang, W., Li, Q., Wang, B., Seed bubbles stabilize flow and heat transfer in parallel microchannels, *Int. J. Multiphase Flow*, 35, pp. 773 – 790, 2009.

Yen, T.H., Kasagi, N., Suzuki, Y., Forced convective boiling heat transfer in microtubes at low mass and heat fluxes, *Int. J. Multiphase Flow*, 29, pp. 1771 – 1792, 2003.

Yin, J.M., Bullard, C.W., Hrnjak, P.S., Single phase pressure drop measurements in a microchannel heat exchanger, *Heat Transfer Engineering*, 23, pp. 3 – 12, Taylor and Francis, 2002.

Yue, J., Chen, G., Yuan, Q., Pressure drops of single and two phase flows through T type microchannel mixer, *J. Chemical Engineering*, 102, pp. 11 – 24, 2004.

Yun, R., Heo, J.H., Kim, Y., Evaporative heat transfer and pressure drop of R410A in microchannels, *Int. J. Refrigeration*, 29(1), pp. 92 – 100, 2006.

Yu, W., France, D. M., Wambsganss, M.W., Hull, J.R., Two-phase pressure drop, boiling heat transfer, and critical heat flux to water in a small-diameter horizontal tube, *Int. J. Multiphase Flow*, 28, pp. 927 – 941, 2002.

Zhang, L., Wang, E.N., Goodson, K.E., Kenny, T.W., Phase change phenomena in silicon microchannels, *Int. J. Heat Mass Transfer*, 48, pp. 1572 – 1582, 2005.

Zhang, T., Tong, T., Chang, J.Y., Peles, Y., Prasher, R., Jensen, M.K., Wen, J.T., Phelan, P., Ledinegg instability in microchannels, *Int. J. Heat Mass Transfer*, 52, pp. 5661 – 5674, 2009.

Zhang, W., Hibiki, T., Mishima, K., Correlations of two-phase pressure drop and void fraction in min-channel, *Int. J. Heat Mass Transfer*, 53, pp: 453 – 465, 2010.

Zhao, T.S., Bi, Q.C., Co-current air-water two-phase flow patterns in vertical triangular microchannels, *Int. J. Multiphase Flow*, 27, pp. 765 – 782, 2001.

Zu, Y.Q., Gedupudi, S., Yan, Y.Y., Karayianis, T.G., Kenning, D.B.R., Numerical simulation and experimental observation of confined bubble growth during flow boiling in microchannel with rectangular cross section of high aspect ratio, ICNMM, Pohang, South Korea, 2009.

# APPENDICES

## A. Selected correlations for the study

The experimental results of the present work are compared with the theory or correlations listed in this appendix and the comparison results are presented in Chapter 4 for single-phase flow data, Chapter 5 for flow boiling heat transfer data and Chapter 6 for flow boiling pressure drop data.

### 1. Single-phase friction factor correlations

The single-phase conventional friction factor theory and correlations are used for comparison with the experimental data and are listed in Table A.1.

Table A.1 Selected friction factor theory and correlations.

Reference	Friction factor correlation	Applicability
Shah and London (1978)	$f_{FD} = \frac{24}{\text{Re}} \left( \frac{1 - 1.3553\beta + 1.9467\beta^2}{-1.7012\beta^3 + 0.9564\beta^4 - 0.2537\beta^5} \right)$ $\beta = \frac{W}{H} \text{ or } \beta = \frac{H}{W}, \text{ in general } \beta = \frac{\text{Theshortside}}{\text{Thelongside}}$ $\text{Re} = \frac{\rho \bar{V} D_h}{\mu}$	For laminar fully developed flow, $\text{Re} \leq 2000$ , non circular conduits with aspect ratios of up to 1, macroscale conduits.
Shah (1978)	$f_{app} = \frac{3.44}{\text{Re} \sqrt{L^*}} + \frac{(f \text{Re})_{FD} + \frac{K(\infty)}{4L^*} - \frac{3.44}{\sqrt{L^*}}}{\text{Re} \left( 1 + \frac{C}{L^{*2}} \right)}$ $K(\infty) = 0.6611 + 1.1182\beta + 2.1758\beta^2 - 5.8322\beta^3 + 4.4683\beta^4 - 1.1553\beta^5$ $L^* = \frac{L}{\text{Re} D_h}; C = 0.000029 - 0.00029$	For laminar developing flow, $\text{Re} \leq 2000$ , rectangular conduits with aspect ratios ranging from 0 to 1, macroscale conduits.

Hager (2003)	Blasius correlation: $f = 0.079 \text{Re}^{-0.25}$	For fully developed turbulent flow in circular tubes, macroscale tubes, $\text{Re} \geq 3000$
Phillips (1987)	$f_{app} = \left( 0.0929 + \frac{1.01612}{L/D_h} \right) \text{Re}^* \left( -0.268 - \frac{0.3293}{L/D_h} \right)$ $\text{Re}^* = \text{Re} \left[ \frac{2}{3} + \frac{11}{24\beta} (2 - 1/\beta) \right]$	For developing turbulent flow in rectangular conduits, $\text{Re} \geq 3000$ , macroscale conduits.

## 2. Single-phase flow heat transfer correlations

Previous researchers elucidated that in microchannels the heat transfer was higher than that in macroscales. In macroscale sizes, the Nusselt number is constant 4.36 for fully developed flow in circular ducts for uniform heat flux (3.66 for uniform wall temperature) or dependent on the aspect ratio for non circular ducts, e.g. 3.61 for constant heat flux (2.98 for uniform temperature) for aspect ratio of 1 (Incropera et al., 2006).

Table A.2 Selected Nusselt number correlations.

Reference	Nusselt number correlation	Applicability
Dittus and Boelter (1930)	Dittus-Boelter's correlation: $\text{Nu} = 0.023 \text{Re}^{0.8} \text{Pr}^{0.4}$	For fully developed turbulent flow in circular conduits for heating process, macroscale conduits, $\text{Re} \geq 3000$ , $0.6 \leq \text{Pr} \leq 160$
Sieder and Tate (1936)	Sieder and Tate's correlation	For flow in entry region round ducts, laminar and turbulent.

	$\text{Nu}_D = 1.86 \left( \frac{\text{RePr}D}{L} \right)^{1/3} \left( \frac{\mu}{\mu_s} \right)^{0.14}$	
Gnielinski (1976)	Gnielinski's correlation: $\text{Nu} = \frac{(f/2)(\text{Re}-1000)\text{Pr}}{1+12.7(f/2)^{1/2}(\text{Pr}^{2/3}-1)}$ $f = 0.25(0.79 \ln \text{Re} - 1.64)^{-2}$	For fully developed turbulent flow in circular conduits, $\text{Re} \geq 3000$ , $0.5 \leq \text{Pr} \leq 2000$
Shah and London (1978)	$\text{Nu}_T = 43.2\beta^6 - 137.8\beta^5 + 181.6\beta^4 - 133.3\beta^3 + 62.32\beta^2 - 17.77\beta + 4.861$  $\text{Nu} = 5.212L^{*-0.15}; \beta = 0.228$ $\text{Nu} = 4.541L^{*-0.18}; \beta = 0.39$ $\text{Nu} = 4.017L^{*-0.21}; \beta = 0.78$ $L^* = \frac{L}{\text{RePr}D_h}$	For laminar fully developed flow, $\text{Re} \leq 2000$ , uniform wall temperature, in rectangular channel, three heated walls, macroscale channels, adopted from Table 43 with a standard deviation of 0.0006.  For simultaneously developing flow region in rectangular conduits, adopted from Table 52, $L^* > 0.016$ $\text{Pr} = 0.72$
Choi et al. (1991)	$\text{Nu} = \begin{cases} 0.000972 \text{Re}^{1.17} \text{Pr}^{1/3} \\ 3.82 \times 10^{-6} \text{Re}^{1.96} \text{Pr}^{1/3} \end{cases}$	For flow in tubes: $\text{Re} < 2000$ $2500 < \text{Re} < 20000$
Bejan (2004)	$\text{Nu} = C'(L/\text{Re}D_h \text{Pr})^{-0.5}$	For laminar developing flow for non circular conduits, $\text{Re} \leq 2000$ , macroscale conduits.

### 3. Flow boiling heat transfer correlations

Since the microchannel was introduced by Tukerman and Pease (1989), many correlations, modeling, numerical and simulation for flow boiling in microchannels have been developed intensively. An important feature that is often overlooked in comparing the correlations is the trend of heat transfer coefficient versus quality. The heat transfer coefficient can increase, remain constant, or decrease with quality, depending on two parameters – Boiling number,  $Bo = q'' / Gh_{fg}$  and liquid to vapour density ratio ( $\rho_f / \rho_g$ ), see Kandlikar (1999). However, no correlation/modeling could be used for predicting the experimental data adequately.

Table A.3 Selected flow boiling heat transfer correlations.

Reference	Heat transfer coefficient correlation	Application
Shah (1982)	$Co = \left( \frac{1-x}{x} \right)^{0.8} \left( \frac{\rho_g}{\rho_L} \right)^{0.5}$ $\frac{h_{cb}}{h_l} = \frac{1.8}{Co^{0.8}}$ <p>For <math>Co &gt; 1</math>:</p> $\frac{h_{nb}}{h_L} = \begin{cases} 230Bo^{0.5} & Bo > 0.0003 \\ 1 + 46Bo^{0.5} & Bo < 0.0003 \end{cases}$ <p>For <math>0.1 &lt; Co &lt; 1</math>:</p> $\frac{h_{nb}}{h_L} = FBo^{0.5} \exp(2.74Co - 0.1)$ $F = \begin{cases} 14.7 & Bo > 0.0011 \\ 15.43 & Bo < 0.0011 \end{cases}$	Based on 780 data points.

	<p>For <math>N_{Co} &lt; 0.1</math>:</p> $\frac{h_{nb}}{h_L} = FBo^{0.5} \exp(2.74Co - 0.15)$ $h_l = 0.023 Re_l^{0.8} Pr_l^{0.4} \frac{k_l}{D}$ $Bo = \frac{q''}{Gh_{lg}}$	
Lazarek and Black (1982)	$h_{tp} = \frac{k_l}{D} 30 Re_l^{0.857} Bo^{0.714}$ $Re_l = \frac{G(1-x)D}{\mu_l}$	<p>Saturated flow boiling in small channels, <math>ID = 3.1</math> mm.</p> <p>Working fluid : R113</p> <p><math>q'' = 14 - 380</math> kW/m<sup>2</sup></p> <p><math>G = 125 - 750</math> kg/m<sup>2</sup>s</p> <p><math>Re = 860 - 5500</math></p> <p><math>Bo = (2.3 - 76) \times 10^{-4}</math></p> <p>Pressure: 130 - 410 kPa.</p>
Gungor and Winterton (1987)	$h_{tp} = (SS_2 + FF_2)h_{sp}$ $S = 1 + 3000 Bo^{0.86}$ $F = 1.12 \left( \frac{x}{1-x} \right)^{0.75} \left( \frac{\rho_l}{\rho_g} \right)^{0.41}$ $S_2 = \begin{cases} Fr_l^{0.1-2Fr_l} & \text{for horizontal and } Fr_l < 0.05 \\ 1 & \text{otherwise} \end{cases}$ $F_2 = \begin{cases} Fr_l^{1/2} & \text{if horizontal and } Fr_l < 0.05 \\ 1 & \text{otherwise} \end{cases}$	<p>Saturated flow boiling in horizontal and vertical conduits, based on 3600 data points, covering working fluids: R11, R12, R22, R113, R114 and Water.</p>

	$Fr = \frac{G^2}{\rho^2 g D_h}$																			
Kandlikar (1990)	<p>Smooth tubes:</p> $h_l = 0.023 \text{ Re}_l^{0.8} \text{ Pr}_l^{0.4} \frac{k_l}{D}$ $\frac{h_{tp}}{h_l} = C_1 Co^{C_2} (25 Fr_l)^{C_3} + C_4 Bo^{C_4} F_{fl}$ $Co = \left( \frac{1-x}{x} \right)^{0.8} \left( \frac{\rho_g}{\rho_l} \right)^{0.5}$ <p><math>Co &lt; 0.65</math> convective boiling.  <math>Co &gt; 0.65</math> nucleate boiling.</p> <table border="1"> <thead> <tr> <th></th> <th><math>Co &lt; 0.65</math></th> <th><math>Co &gt; 0.65</math></th> </tr> </thead> <tbody> <tr> <td><math>C_1</math></td> <td>1.136</td> <td>0.6683</td> </tr> <tr> <td><math>C_2</math></td> <td>-0.9</td> <td>-0.2</td> </tr> <tr> <td><math>C_3</math></td> <td>667.2</td> <td>1058</td> </tr> <tr> <td><math>C_4</math></td> <td>0.7</td> <td>0.7</td> </tr> <tr> <td><math>C_5</math></td> <td>0.3</td> <td>0.3</td> </tr> </tbody> </table>		$Co < 0.65$	$Co > 0.65$	$C_1$	1.136	0.6683	$C_2$	-0.9	-0.2	$C_3$	667.2	1058	$C_4$	0.7	0.7	$C_5$	0.3	0.3	<p>Saturated flow boiling of water and refrigerant:</p> <p>Water: <math>F_{fl} = 1</math>  R11: <math>F_{fl} = 1.3</math>  R12: <math>F_{fl} = 1.5</math>  R22: <math>F_{fl} = 2.2</math>  R113: <math>F_{fl} = 1.3</math>  R134a: <math>F_{fl} = 1.63</math>  R152a: <math>F_{fl} = 1.1</math></p> <p><math>G = 13</math> to <math>8179 \text{ kg/m}^2\text{s}</math>  <math>q'' = 0.03</math> to <math>228 \text{ W/cm}^2</math>  <math>Bo = 0.03 \times 10^{-4}</math> to <math>46.5 \times 10^{-4}</math>.</p> <p>Pressure: <math>0.4</math> to <math>64.2 \text{ bar}</math>  <math>ID = 4 - 32 \text{ mm}</math>.  <math>x = 0.001</math> to <math>0.987</math></p>
	$Co < 0.65$	$Co > 0.65$																		
$C_1$	1.136	0.6683																		
$C_2$	-0.9	-0.2																		
$C_3$	667.2	1058																		
$C_4$	0.7	0.7																		
$C_5$	0.3	0.3																		
Kew and Cornwell (1997)	$h_{tp} = \frac{k_l}{D} 30 \text{ Re}_l^{0.857} Bo^{0.714} (1-x)^{-0.143}$	<p>Flow boiling of R141b and water in horizontal tubes with diameters ranging from <math>1.36</math> to <math>3.69 \text{ mm}</math>.</p>																		

Warrier et al. (2002)	$h_{sp} = Eh_{sp}$ $h_{sp} = Nu_4 \frac{k_l}{D_h}$ $E = 1 + 6Bo^{1/16} - 5.3(1 - 855Bo)x^{0.65}$ $Nu_4 = 8.235 \left( \begin{array}{l} 1 - 2.042\beta + 3.767\beta^2 \\ - 2.477\beta^3 + 5.361\beta^4 - 0.186\beta^5 \end{array} \right)$	For saturated flow boiling of FC-84 in rectangular parallel channels with a hydraulic diameter of 0.75 mm, horizontal position and uniform heat flux, heated from the top and bottom of channels.
Yu et al. (2002)	$h_{sp} = 6.4 \times 10^6 (Bo^2 We_l)^{0.27} \left( \frac{v_g}{v_l} \right)^{-0.2}$ $We_l = \frac{v_l G^2 D}{\mu_l};$	For subcooled flow boiling of water in horizontal pipes with an inner diameter of 2.98 mm at inlet temperatures up to 80 °C, Pressure: 200 kPa $G = 50 - 200 \text{ kg/m}^2\text{s}$ $x = 0.15$ to 1
Sun-Mishima (2009)	$h_{sp} = \frac{6 Re_l^{1.05} Bo^{0.54}}{We_l^{0.191} (\rho_l / \rho_g)^{0.142}} \frac{k_l}{D}$	For saturated flow boiling, based on 2505 data points for 11 liquids covering diameters ranging from 0.21 to 6.05 mm.
Lee and	For $x = 0 - 0.05$	For saturated flow

<p>Mudawar (2005)</p>	$h_{tp} = 3.856X^{0.267}h_{sp}$ $h_{sp} = Nu_3 \frac{k_l}{D_h} \text{ or } h_{sp} = Nu_4 \frac{k_l}{D_h}$ $Nu_3 = 8.235 \left( \begin{array}{l} 1 - 1.883\beta + 3.767\beta^2 \\ - 5.814\beta^3 + 5.361\beta^4 \\ - 2\beta^5 \end{array} \right)$ $X_{vv} = \left( \frac{\mu_l}{\mu_g} \right)^{0.5} \left( \frac{1-x}{x} \right)^{0.5} \left( \frac{v_l}{v_g} \right)^{0.5}$ $X_{vt} = \left( \frac{f_l Re_g^{0.25}}{0.079} \right)^{0.5} \left( \frac{1-x}{x} \right)^{0.5} \left( \frac{v_l}{v_g} \right)^{0.5}$ $Re_g = \frac{Gx D_h}{\mu_g}$ <p>For <math>x = 0.05 - 0.55</math></p> $h_{tp} = 436.48 Bo^{0.522} We_l^{0.351} X^{0.665} h_{sp}$	<p>boiling in rectangular channels, <math>D_h = 0.347</math> mm.</p> <p>Working fluids: water and R134a.</p>
<p>Li and Wu (2010)</p>	$h_{tp} = 334 Bo^{0.3} (Bd Re_l^{0.36})^{0.4} \frac{k_l}{D}$ $Bd = \frac{g \Delta \rho D_h^2}{\sigma}$	<p>769 data points <math>D = 0.148 - 3.25</math> mm 12 different fluids</p>

#### 4. Pressure drop correlation

There are many correlations for flow boiling pressure drop which mainly consist of pressure drop due to friction, acceleration and gravity. For horizontal channels the effect of gravity is

negligible. Table A.4 shows the selected correlations which are used for comparison in this work. The correlations include macro and microscale correlations for water and refrigerant.

Table A.4 Selected two-phase pressure drop correlations.

Reference	Pressure drop correlation	Application
Lockhart-Martinelli (1949)	$\Delta p_a = G^2 v_l \left[ \frac{x_o^2 \left( \frac{v_g}{v_l} \right)}{\alpha_o} + \frac{(1-x_o)^2}{1-\alpha_o} - 1 \right]$ $\alpha_o = 1 - \frac{1}{\sqrt{1 + \frac{C}{X} + \frac{1}{X^2}}}$ $\phi_l^2 = 1 + \frac{C}{X_{vv}} + \frac{1}{X_{vv}^2}$ $X_{vv} = \left( \frac{\mu_l}{\mu_g} \right)^{0.5} \left( \frac{1-x}{x} \right)^{0.5} \left( \frac{v_l}{v_g} \right)^{0.5}$ $X_{vt} = \left( \frac{f_l \text{Re}_g^{0.25}}{0.079} \right)^{0.5} \left( \frac{1-x}{x} \right) \left( \frac{v_l}{v_g} \right)^{0.5}$ $\Delta p_f = \frac{L_{tp}}{x_o} \int_0^{x_o} \frac{2 f_l G^2 (1-x)^2 v_l}{D_h} \phi_l^2 dx$ $f_l \text{Re}_l = 24 \left( \begin{array}{l} 1 - 1.3553 \beta + 1.9467 \beta^2 - 1.7012 \beta^3 \\ + 0.9564 \beta^4 - 0.2537 \beta^5 \end{array} \right)$ $\text{Re}_l = \frac{G(1-x)D_h}{\mu_l}; \text{Re}_g = \frac{GxD_h}{\mu_g}$	<p>For two-phase flow in tubes with constants:</p> <p>C = 5 (laminar liquid – laminar vapour).</p> <p>C = 12 (laminar liquid – turbulent vapour).</p> <p>C = 10 (turbulent liquid – laminar vapour).</p> <p>C = 20 (turbulent liquid – turbulent vapour).</p> <p>Working fluids: air-water, benzene, kerosene, oils.</p> <p>Tube with diameters of 0.0586 to 1.017 in.</p>
Homogenous model, Collier and Thome (1994)	$\Delta p_{tp} = \Delta p_f + \Delta p_a$ $\Delta p_a = G^2 v_{lg} x_o$	<p>For steam-water mixture flow, laminar and turbulent, circular horizontal channels</p> <p><math>\dot{m} = 1.9 \times 10^{-3} - 51.1 \times</math></p>

	$\Delta p_f = \frac{2f_l L G^2 v_l}{D_h} \left[ 1 + \frac{x_o}{2} \left( \frac{v_{lg}}{v_l} \right) \right]$ $f_l = 0.0035$	$10^{-3}$ kg/s Pressure = 1 bar – critical pressure $x = 0.01 - 1$
Mishima and Hibiki (1996)	$\Delta p_f = \frac{L_{tp}}{x_o} \int_0^{x_o} \frac{2f_l G^2 (1-x)^2 v_l}{D_h} \phi_l^2 dx$ $\Delta p_a = G^2 v_l \left[ \frac{x_o^2}{\alpha_o} \left( \frac{v_g}{v_l} \right) + \frac{(1-x_o)^2}{1-\alpha_o} - 1 \right]$ $\alpha_o = \frac{1}{1 + \frac{1-x_o}{x_o} \left( \frac{v_l}{v_g} \right)^{2/3}}$ $C = 21 \left[ 1 - e^{-319 D_h} \right]$ $\phi_l^2 = 1 + \frac{C}{X_{vv}} + \frac{1}{X_{vv}^2}$ $X_{vv} = \left( \frac{\mu_l}{\mu_g} \right)^{0.5} \left( \frac{1-x}{x} \right)^{0.5} \left( \frac{v_l}{v_g} \right)^{0.5}$	For two-phase flow in vertical and horizontal tubes and rectangular channels. Working fluids: Air-water $Re_g = 177 - 9580$ . $Re_l = 542 - 3720$ . $D = 1.05 - 4$ mm $U_{gs} = 0.071 - 49.4$ m/s $U_{ls} = 0.071 - 2.33$ m/s
Yu et al (2002)	$\Delta p_f = \frac{L_{tp}}{x_o} \int_0^{x_o} \frac{2f_l G^2 (1-x)^2 v_l}{D_h} \phi_l^2 dx$ $\Delta p_a = G^2 v_l \left[ \frac{x_o^2}{\alpha_o} \left( \frac{v_g}{v_l} \right) + \frac{(1-x_o)^2}{1-\alpha_o} - 1 \right]$ $\phi_l^2 = \frac{1}{X_{vt}^{1.9}}$	For water subcooled boiling with inlet temperature up to 80 °C, Pressure: 200 kPa. $G = 50 - 200$ kg/m <sup>2</sup> s. $x_e = 0.15$ to 1.

	$X_{vt} = (f_l \text{Re}_g^{0.2} / 0.046)^{0.5} \left[ \left( \frac{1-x}{x} \right) \left( \frac{v_l}{v_g} \right)^{0.5} \right]$ $\text{Re}_g = \frac{Gx D_h}{\mu_g}$	Horizontal pipe $ID = 2.98$ mm.
Warrier et al. (2002)	$\frac{\Delta P_f}{\Delta P_a} = \frac{\int_0^{x_o} \frac{2f_l G^2 (1-x)^2 v_l}{D_h} \phi_l^2 dx}{G^2 v_l \left[ \frac{x_o^2}{\alpha_o} \left( \frac{v_g}{v_l} \right) + \frac{(1-x_o)^2}{1-\alpha_o} - 1 \right]}$ $\phi_l^2 = \left( 1 + \frac{C}{X_{vv}} + \frac{1}{X_{vv}^2} \right)$ $C = 2 \left[ 1 - \exp(-319 D_h) \right] (0.0041 G + 0.0613)$ $f_l \text{Re}_l = 24 \left( \begin{array}{l} 1 - 1.3553\beta + 1.9467\beta^2 \\ -1.7012\beta^3 + 0.9564\beta^4 \\ -0.2537\beta^5 \end{array} \right)$ $X_{vv} = \left( \frac{\mu_l}{\mu_g} \right)^{0.5} \left( \frac{1-x}{x} \right)^{0.5} \left( \frac{v_l}{v_g} \right)^{0.5}$ $\alpha = \frac{G^2 \int_0^{x_o} \frac{2f_l G^2 (1-x)^2 v_l}{D_h} \phi_l^2 dx}{G^2 v_l \left[ \frac{x_o^2}{\alpha_o} \left( \frac{v_g}{v_l} \right) + \frac{(1-x_o)^2}{1-\alpha_o} - 1 \right]}$	Saturated flow boiling in rectangular channel, $D_h = 0.75$ mm Working fluid: FC-84
Qu and Mudawar (2003b)	$\Delta p_f = \frac{L_{tp}}{x_o} \int_0^{x_o} \frac{2f_l G^2 (1-x)^2 v_l}{D_h} \phi_l^2 dx$ $\phi_l^2 = 1 + \frac{C}{X_{vv}} + \frac{1}{X_{vv}^2}$ $C = 2 \left[ 1 - \exp(-319 D_h) \right] (0.0041 G + 0.0613)$ $f_l \text{Re}_l = 24 \left( \begin{array}{l} 1 - 1.3553\beta + 1.9467\beta^2 \\ -1.7012\beta^3 + 0.9564\beta^4 \\ -0.2537\beta^5 \end{array} \right)$ $X_{vv} = \left( \frac{\mu_l}{\mu_g} \right)^{0.5} \left( \frac{1-x}{x} \right)^{0.5} \left( \frac{v_l}{v_g} \right)^{0.5}$ $\Delta p_a = G^2 v_l \left[ \frac{x_o^2}{\alpha_o} \left( \frac{v_g}{v_l} \right) + \frac{(1-x_o)^2}{1-\alpha_o} - 1 \right]$	For subcooled flow boiling of water in microchannel with hydraulic diameter of 349 $\mu\text{m}$ , $q'' = 40\text{-}130$ W/cm <sup>2</sup> Tin = 30 and 60 °C, G = 135 – 402 kg/m <sup>2</sup> s, MAE 12.4%.
Lee and Lee (2008)	$\Delta p_f = \frac{L_{tp}}{x_o} \int_0^{x_o} \frac{2f_l G^2 (1-x)^2 v_l}{D_h} \phi_l^2 dx$ $\Delta p_a = G^2 v_l \left[ \frac{x_o^2}{\alpha_o} \left( \frac{v_g}{v_l} \right) + \frac{(1-x_o)^2}{1-\alpha_o} - 1 \right]$	For two-phase flow in horizontal rectangular channels. Gap $H$ : 0.4 to 4 mm. $W = 20$ mm.

	$\phi_l^2 = 1 + \frac{C}{X_{vt}} + \frac{1}{X_{vt}^2}$ $X_{vt} = \left( \frac{f_l \text{Re}_g^{0.25}}{0.079} \right)^{0.5} \left( \frac{1-x}{x} \right) \left( \frac{v_l}{v_g} \right)^{0.5}$ $f_l \text{Re}_l = 24 \begin{pmatrix} 1 - 1.3553\beta + 1.9467\beta^2 \\ -1.7012\beta^3 + 0.9564\beta^4 \\ -0.2537\beta^5 \end{pmatrix}$ $C = 0.06185 \text{Re}_{lo}^{0.726}$ $\text{Re}_{lo} = GD_h / \mu_l$	<p>Working fluids: air-water.</p> <p><math>\text{Re}_{lo} = 175 - 17700</math>.</p>
<p>Lee and Garimella (2008)</p>	$\Delta p_f = \frac{L_{tp}}{x_o} \int_0^{x_o} \frac{2f_l G^2 (1-x)^2 v_l}{D_h} \phi_l^2 dx$ $\phi_l^2 = 1 + \frac{C}{X_{vv}} + \frac{1}{X_{vv}^2}$ $X_{vv} = \left( \frac{\mu_l}{\mu_g} \right)^{0.5} \left( \frac{1-x}{x} \right)^{0.5} \left( \frac{v_l}{v_g} \right)^{0.5}$ $\Delta p_a = G^2 v_l \left[ \frac{x_o^2}{\alpha_o} \left( \frac{v_g}{v_l} \right) + \frac{(1-x_o)^2}{1-\alpha_o} - 1 \right]$ $C = 2566G^{0.5466} D_h^{0.8819} (1 - \exp(-319D_h))$	<p>For saturated flow boiling of deionized water in parallel microchannel,</p> <p><math>T_i = 90.6</math> to <math>95.1^\circ\text{C}</math></p> <p><math>Q = 46</math> to <math>126</math> (ml/min)</p> <p><math>q'' = 10 - 340</math> (W/cm<sup>2</sup>),</p> <p><math>D_h = 162.55</math> to <math>571</math> <math>\mu\text{m}</math>,</p> <p>MAE = 11.4% to predict their test data.</p>
<p>Zhang et al. (2010)</p>	$\Delta P_f = \frac{G^2}{1 + 0.28X} \int_0^x \left[ \frac{f_l}{X} + \frac{1}{X^2} \right] \phi_l^2 dx$ $\phi_l^2 = \left( \frac{f_l}{X} + \frac{1}{X^2} \right) \left( \frac{D_h \rho_l}{2\sigma} \right)^{0.5} \left( \frac{1-x}{x} \right)$ $C = 24 \left[ 1 - \exp\left( -\frac{\rho_l}{\rho_g} \right) \right] \left( \frac{0.358}{X} \right)$ $La = \left[ \frac{\rho_l}{\rho_g} \right] \left( \frac{\rho_l}{\rho_g} \right)^{0.5} \left( \frac{G}{D} \right)$ $\Delta P = G^2 \int_0^x \left[ \alpha \rho_g + (1-\alpha) \rho_l \right] dx$ $\Delta P_a = \frac{G^2}{x} \left[ \frac{\alpha_o}{\rho_l} + \frac{1-\alpha_o}{\rho_g} \right] - 1$ $\alpha = \frac{\rho_l}{\rho_l + \frac{\rho_g}{1 + 0.28X}}$	<p>For adiabatic gas-liquid flow, adiabatic liquid-vapour flow and flow boiling in circular and rectangular, vertical and horizontal conduits with diameters ranging from</p>

		0.0146 to 6.25 mm and Ref $\leq$ 2000, Reg $\leq$ 2000.
--	--	--

## B. Sensor calibration results

As explained in Chapter 3, calibrations were obtained before used for measuring the variables in the experiments. The sensors included pressure sensors, thermocouples, Coriolis flowmeter, barometer and power meter. All uncertainties obtained in the calibration have been given in Chapter 3. This appendix presents the calibration data in graphical form together with calibration equations derived from the data.

### 1. Pressure sensor calibration

Pressure sensors comprised one reference pressure, six local pressure sensors and one additional pressure sensor. The type and specification of the pressure sensors also have been provided in Chapter 3. A picture of the reference pressure is presented in Fig. B.1 and the reference pressure calibration results are shown in Fig. B.2.



Figure B.1 A photograph of the reference pressure sensor.

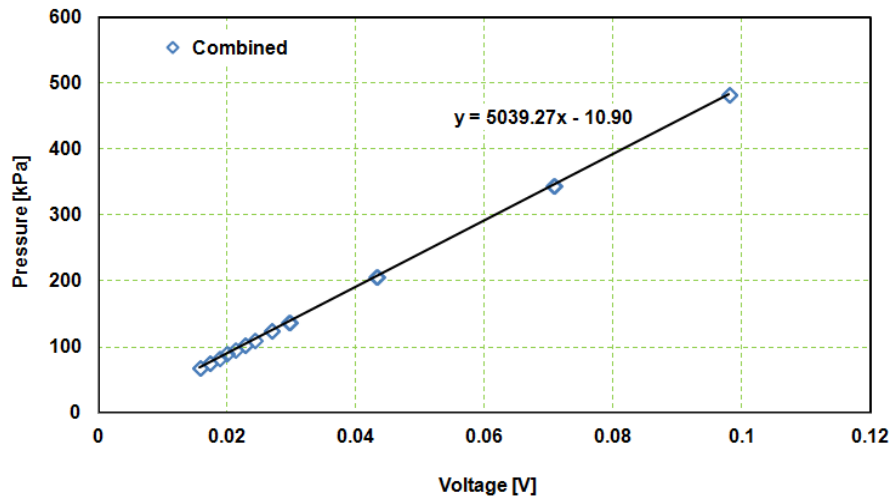


Figure B.2 Reference pressure (Druck pressure transducer) calibration results.

There were six local pressure sensors installed along the test section. They were calibrated against the water manometer and reference pressure (Druck pressure sensor). The image of the sensors is presented in Fig. B.3 and the calibration results are given in Fig. B.4 and Fig. B.5. In flow boiling experiments, the outlet pressure at high mass fluxes especially for the 0.438 mm and 0.561 mm channels was lower than the ambient pressure, therefore, the outlet pressure was replaced using a new pressure sensor model Pi6010P with a range of measurements of -1 to 1.6 bar and an accuracy of  $\pm 0.4$  kPa (calibration).

Honeywell differential pressure sensor:

Type : PCC26.

Pressure range: 0 – 15 psi.

Output: 0 - 10 Vdc.

Accuracy:  $\pm 0.25\%$

Operating temperature:  $-40^{\circ}\text{C}$  to  $85^{\circ}\text{C}$ .

Repeatability and hysteresis:  $\pm 0.2\%$  FS.



Transducer type : Pi6010P (supplied by Applied Measurements Ltd, Aldermarston, Berks, UK).

Pressure range: -1 to 1.6 bar (gauge).

Span: 10 Vdc.

Accuracy:  $\pm 0.4$  kPa (calibration).



Figure B.3 Local pressure sensors.

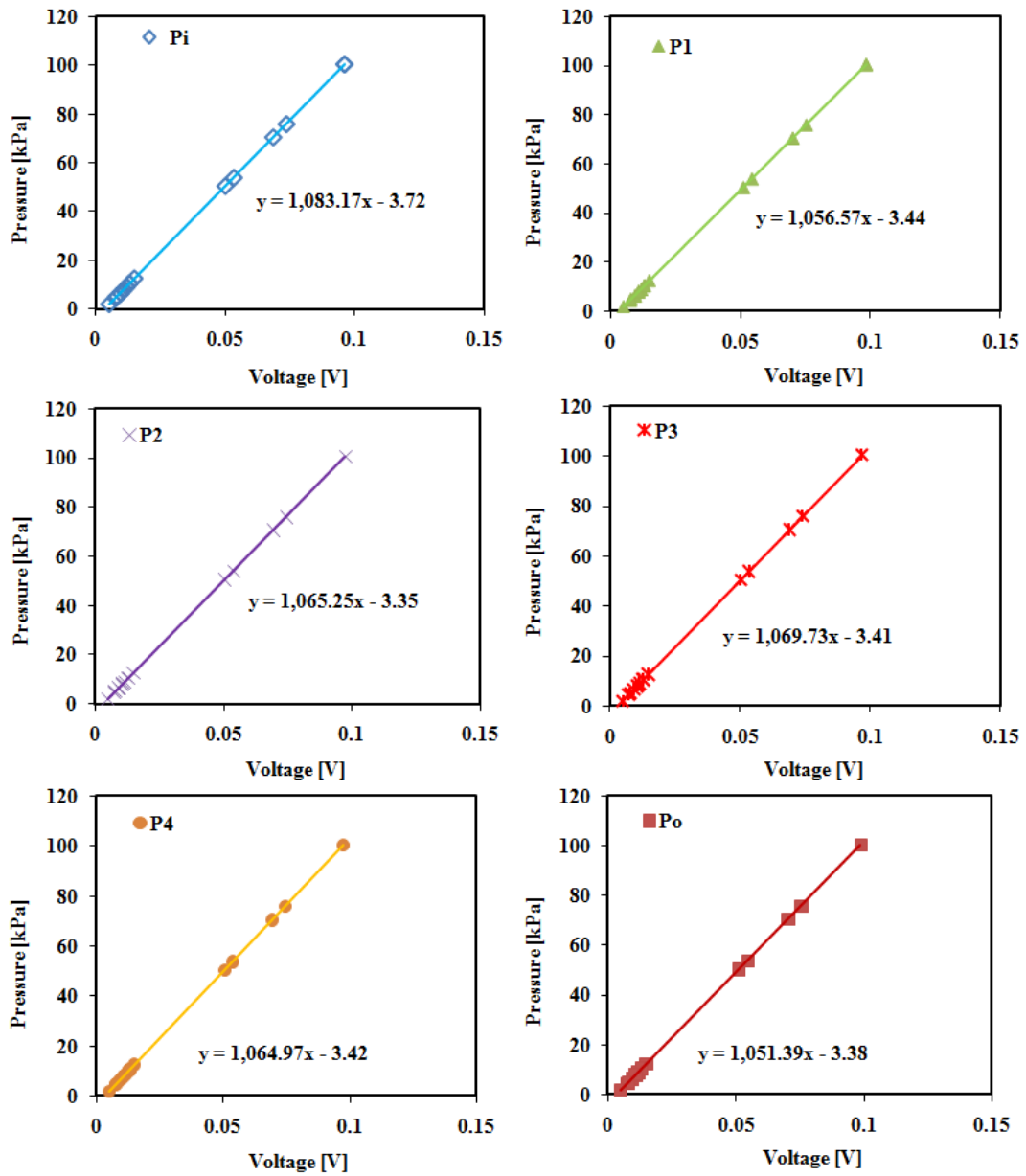


Figure B.4 Local pressure transducer calibration results.

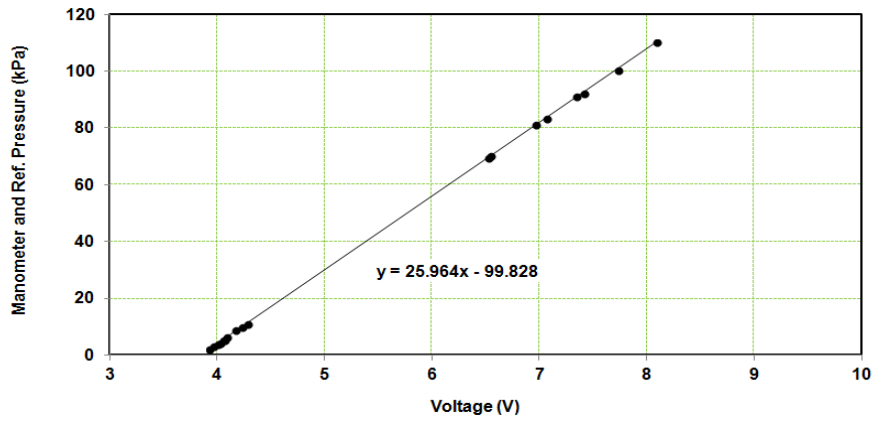


Figure B.5 Local pressure transducer (Pi6010P) calibration results.

## 2. Barometer calibration

Cole Parmer digital barometer (Model EW-99760-00) with an accuracy of  $\pm 5$  mbar and range of measurement of 795 to 1050 mbar used for measuring ambient pressure during performing flow boiling experiments was compared to a Fortin mercury barometer (mmHg). The calibration curves are presented in Fig. B.6.

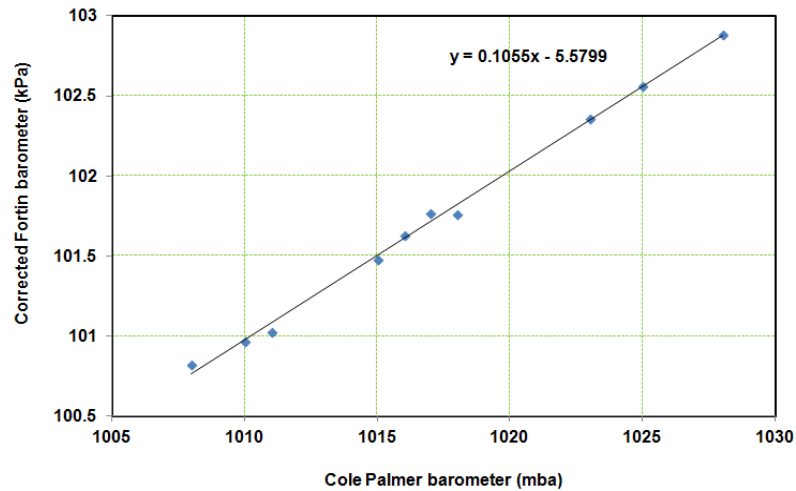


Figure B.6 Comparison of Cole Parmer digital barometer reading with the corrected Fortin mercury barometer (kPa).

### 3. Coriolis flowmeter calibration

A Micro Motion Coriolis mass flowmeter comprising an Elite sensor (Model CMF010M323NB) and a transmitter (Model RFT9739E) was used for measuring the flow rate of the fluid and was calibrated using a collection and weighing method. The calibration results are presented in Fig. B.7.

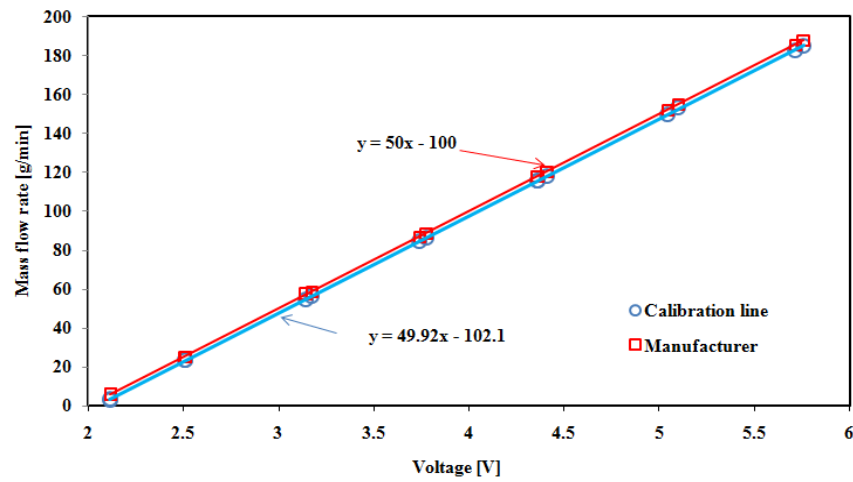


Figure B.7 Coriolis flowmeter calibration results.

### 4. Digital multimeter calibrations

Two digital multimeters (Black Star, model 3225 MP) were used to measure the alternating current and voltage of the supply to the cartridge heater inserted in the microchannel test section. These meters have five AC voltage and six AC current measuring ranges of 200 mV to 750 V and 200  $\mu$ A to 10 A respectively. The stated accuracy of this meter is 0.25% of reading. One of the multimeters was calibrated against a Fluke 5500A multi-function calibrator by Optical Test & Calibration Ltd and the results are presented in Fig. B.8.

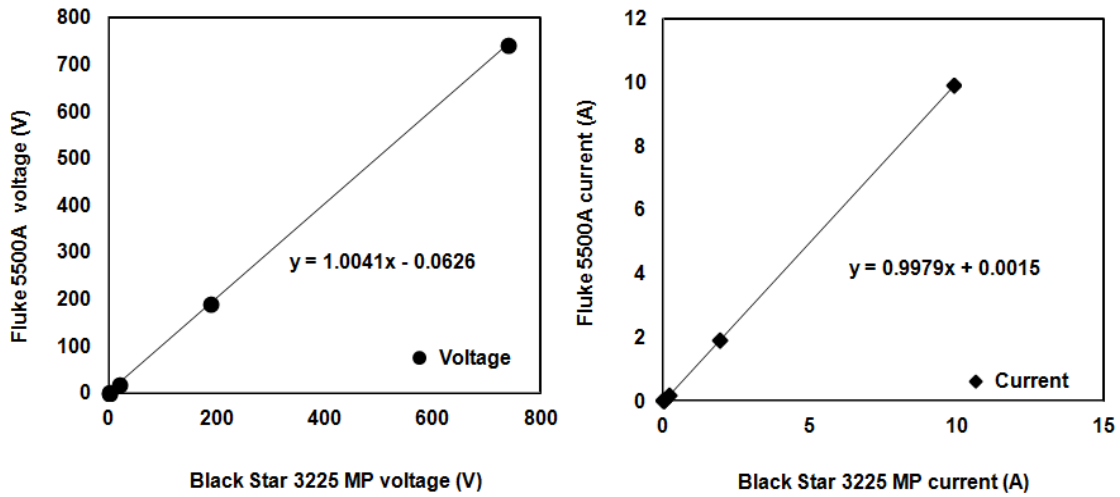


Figure B.8 Power meter calibration curves.

## 5. Thermocouple calibration

Eight thermocouples were inserted into the test sections for measuring: (i) inlet fluid temperature, (ii) outlet fluid temperature, and (iii) six wall temperatures along the microchannel. They were calibrated against a precision thermometer with a platinum thermometer in stirred constant temperature liquid bath. The results are presented in Fig. B.9.

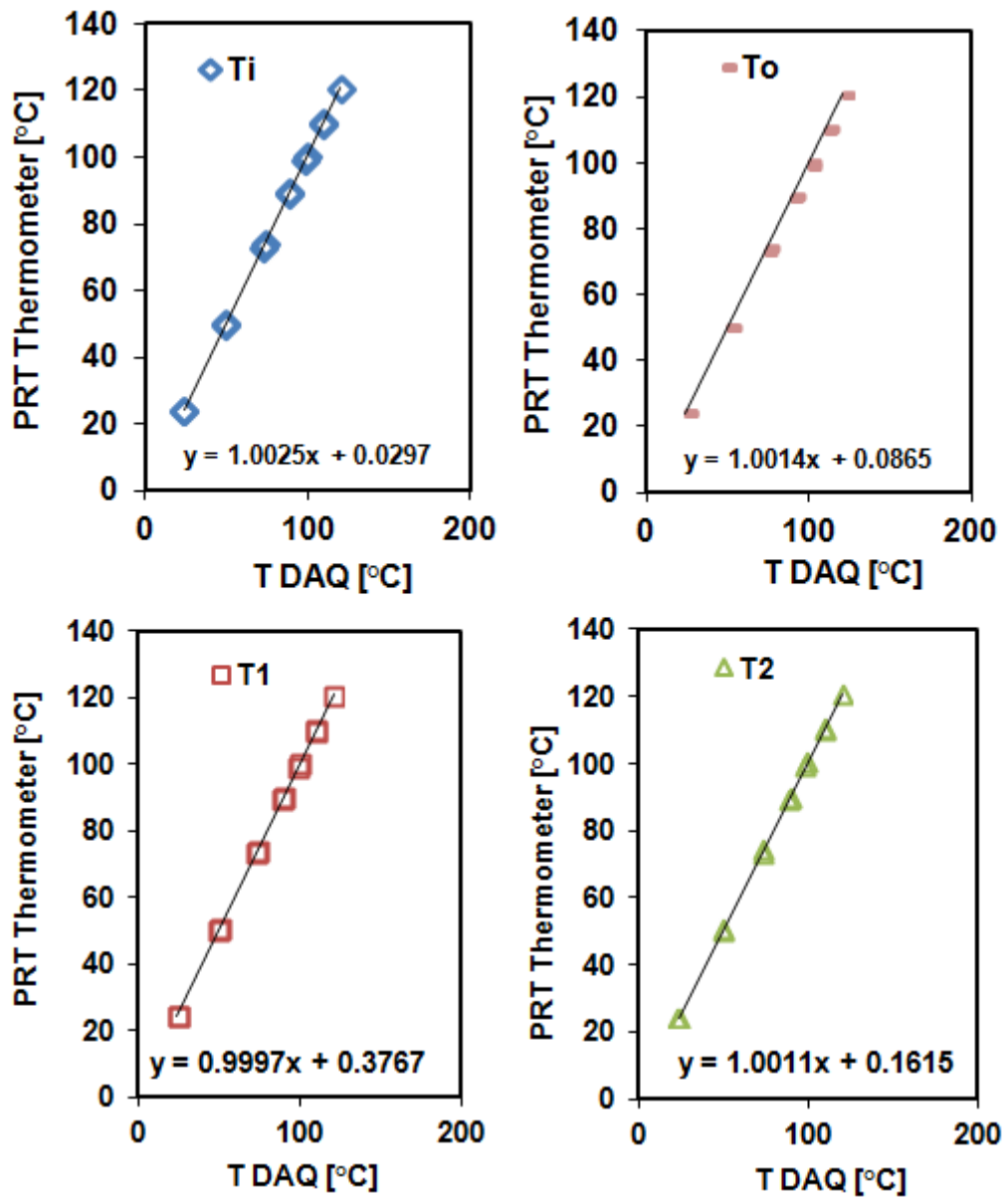


Figure B.9a Thermocouple calibration results.

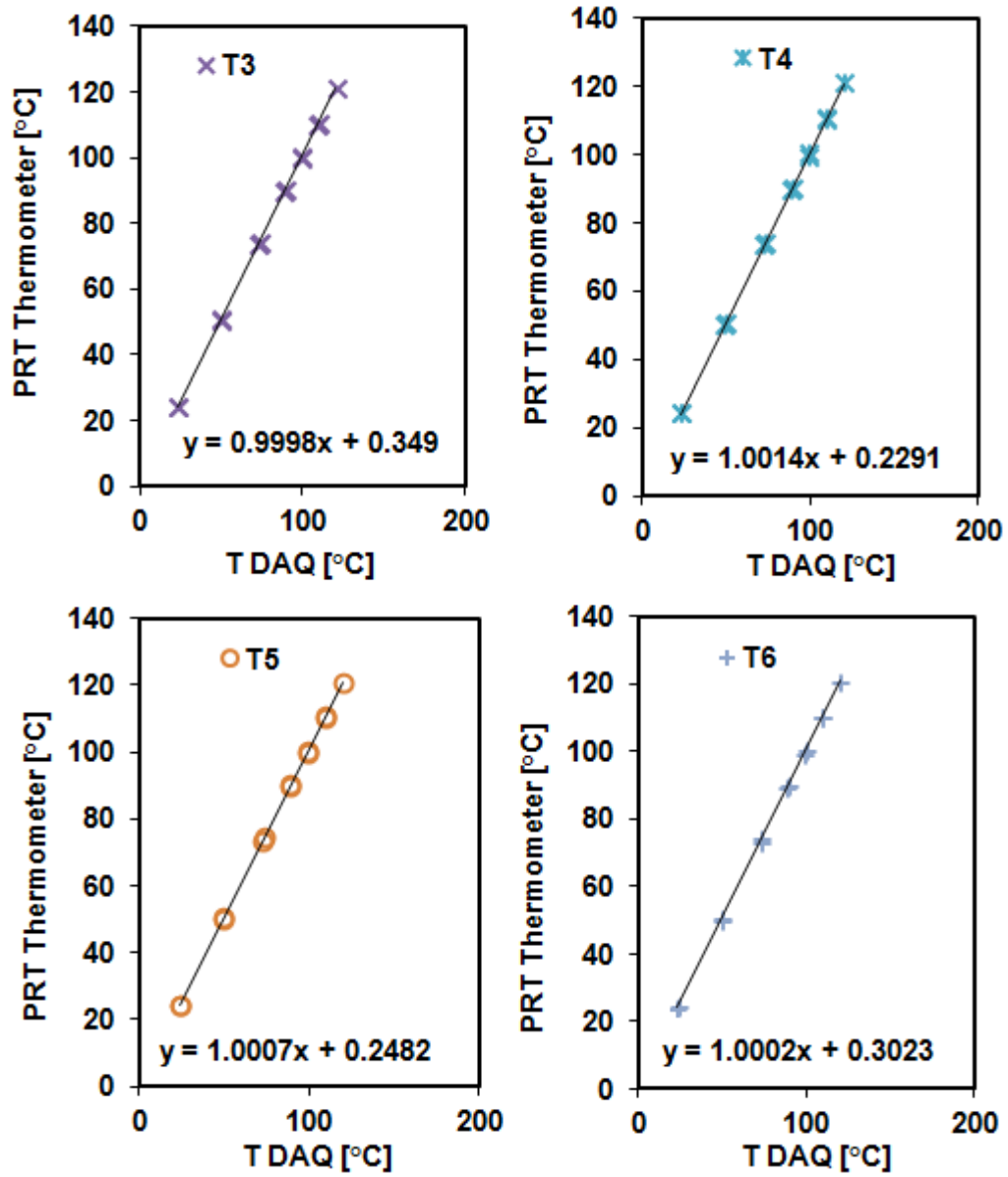


Figure B.9b Thermocouple calibration results.

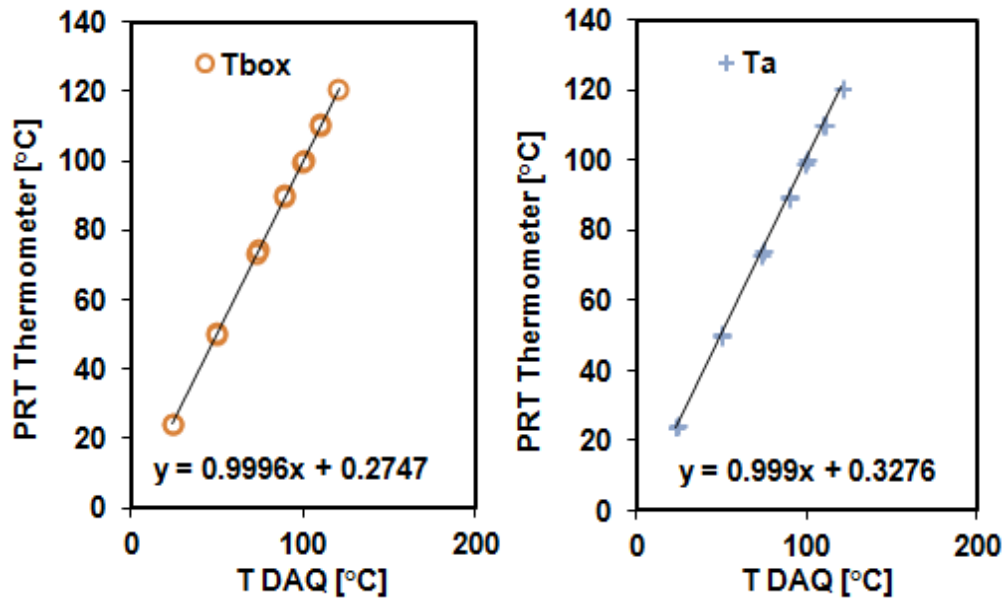


Figure B.9c Thermocouple calibration results.

### C. Test section design

As there is no criterion to choose a size or geometry of a microchannel and adequate correlation, choosing any sizes and geometries of channel is still useful. In our group there was a single bubble flow boiling model proposed by Gedupudi et al. (2009) applied for a rectangular microchannel with a width of 1.5 mm and depth of 0.39 mm. Therefore, the original channel size chosen is: 0.39 mm deep, 1.5 mm wide and 62 mm long. Whilst other sizes in this work were made to identify disparity results with channel widths. The main purpose to choose the size was actually to validate the modeling using a synchronization method; however, due to the technical problem the synchronization work could not be performed.

## C.1 Simulation

Prior to manufacturing the test sections, a simple simulation using fluent was performed to see a contour of temperature distribution on the body of test section block and estimate the heat loss. Nevertheless, in the simulation, the actual construction of the test section was simplified in order to be easier in executing the fluent program. Also, only the channel with a width of 1.71 mm was simulated. The main objective of the simulation is to obtain what size of the copper block which has the smallest heat loss to the ambient. The simulation was performed in two different set up. Firstly, there is no flow on the test section, but there is a convective heat transfer rate from the channel slot to the ambient whilst other surfaces are perfectly insulated. Secondly, there is flow on the channel slot. Thus, the boundary conditions are as follows:

A. For the simulation without fluid flow:

1. On the channel surface, a convective heat transfer coefficient of  $1.5 \text{ kW/m}^2\text{K}$  was applied.
2. The ambient temperature was 300 K.
3. Heat source was assumed to be constant, e.g.  $30 \text{ kW/m}^2$  located on the contact surface between copper block and cartridge heater.
4. All surfaces of the copper block were assumed to be adiabatic.
5. Constant properties and steady state condition.
6. The test section model is shown in Fig. C.1.

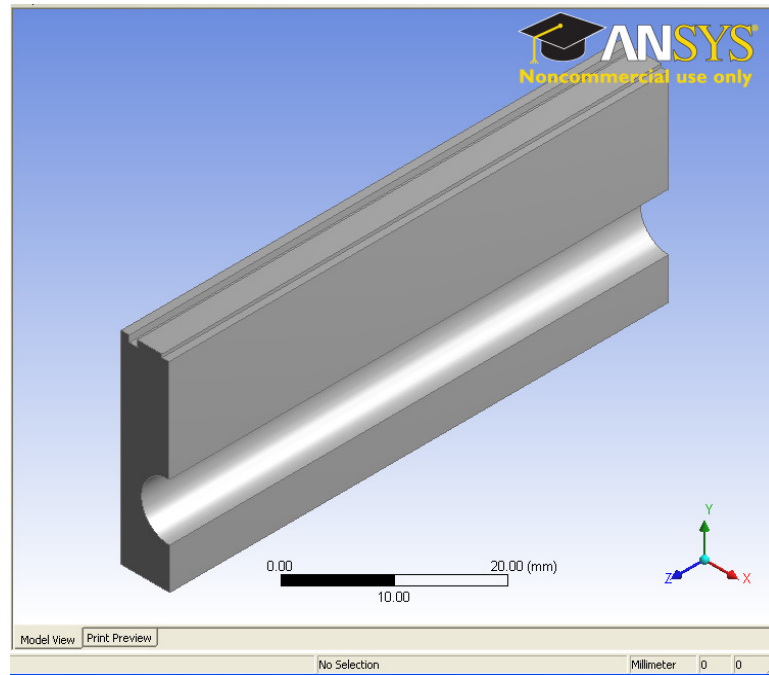


Figure C.1 Model of the test section.

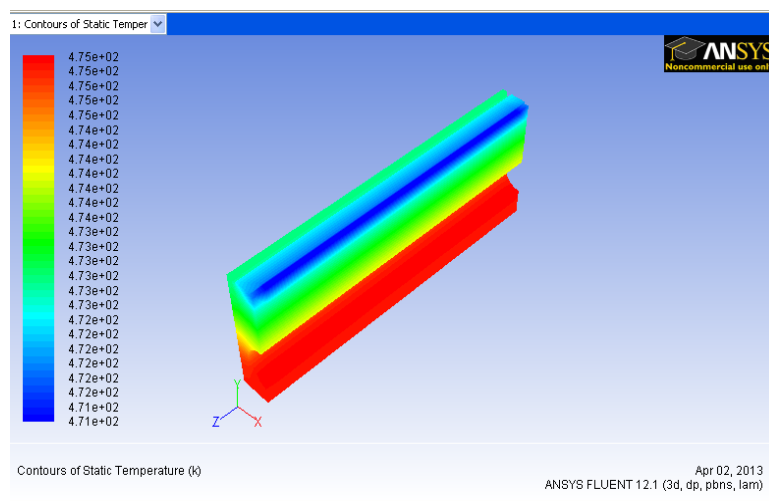


Figure C.2 Contours of temperature distribution on the copper body of the test section, isometric view.

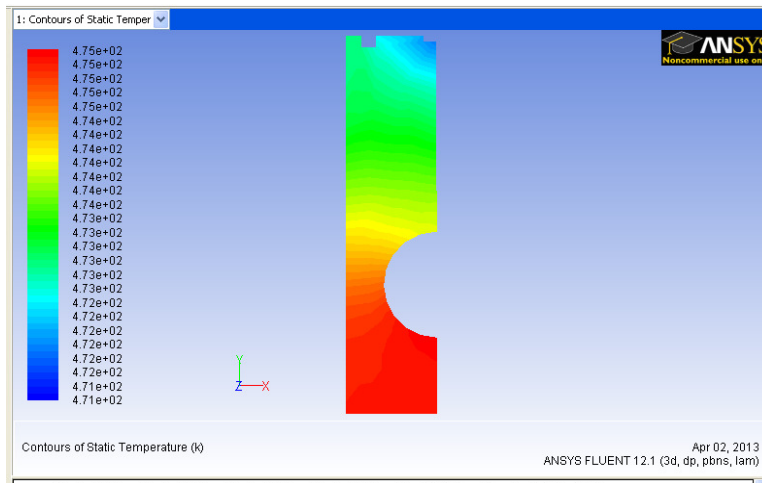


Figure C.3 Contours of temperature distribution, cross section view and in the middle of body.

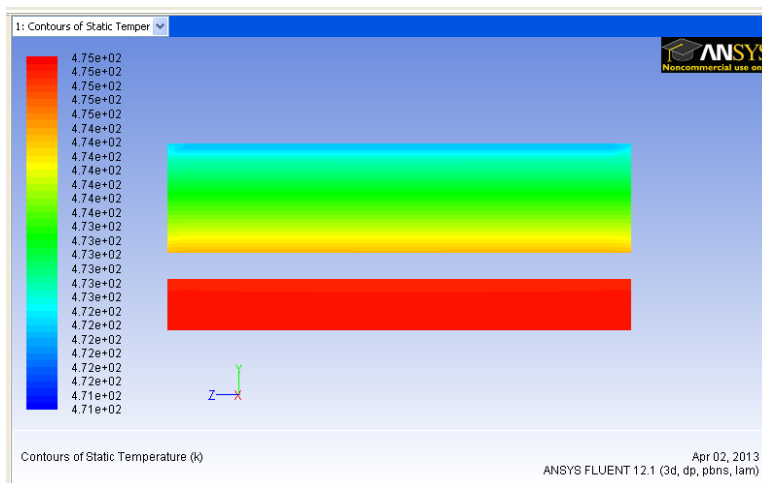


Figure C.4 Contour of temperature distribution along the body of the test section.

After the boundary conditions were input into the dialog box, then the simulation can be run and results can be obtained. For the model with an overall size of 25 high, 12 wide and 62 long, the temperature counters can be attained and presented in Fig. C.2 – C.4. As shown in the figures, that the temperature distribution decreases from the location near the cartridge heater to the channel base. The red area is the hottest part, whilst the blue area is the coldest one. The hot area

is located below the cartridge heater where the heat cannot flow to the bottom of the body due to adiabatic conditions, whilst the blue area is located around the channel slot where the convective heat transfer is assumed to be available. Isothermal lines on the body are also seen clearly, especially in the region of contour transitions. Near the channel base, the isothermal lines seem to circle the channel slot, whilst in the area lower than that, the wall temperatures seem to be uniform. In the contour transition region, red – yellow – green area, the isothermal lines increase from the cartridge heater surface to the end wall of the test section.

B. Simulation with flow; the boundary conditions are:

1. A uniform heat flux is applied on the cartridge heater surface, e.g.  $30 \text{ kW/m}^2$ .
2. The ambient temperature is 300 K.
3. Outlet pressure is 0 kPa (gauge).
4. Heat transfer coefficient of air contacting the outer wall of test section is assumed to be  $10 \text{ W/m}^2 \text{ K}$ .
5. Shape factor of radiation is assumed to be 1.
6. Inlet temperature is 300 K.
7. Fluid velocity is assumed to be constant along the test section, e.g. 1 m/s, 2 m/s and 5 m/s.
8. Constant channel material properties and steady state condition.
9. Three test section models are used: (a) two different sizes of rectangular copper block (25 mm x 12 mm x 62 mm and 50 mm x 12 mm 62 mm), (b) a cone copper block with a height of 25 mm, width of 12 mm on the top and 18 mm on the bottom and length of 62 mm.

The results in the form of temperature contours are presented in Figs. C.5 – C.8 and the heat losses estimated using Fluent and calculation are given in Table C.1.

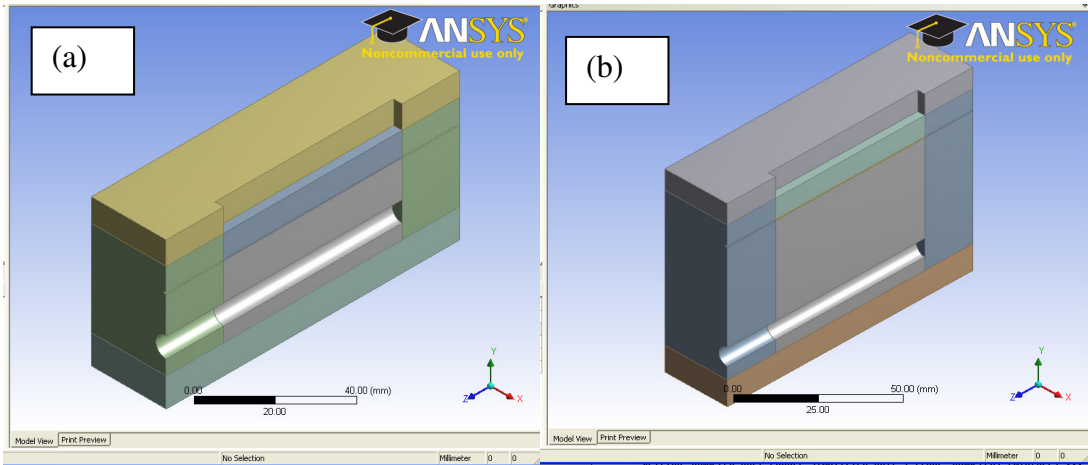


Figure C.5 Model for the rectangular copper block: (a) 25 mm high, (b) 50 mm high.

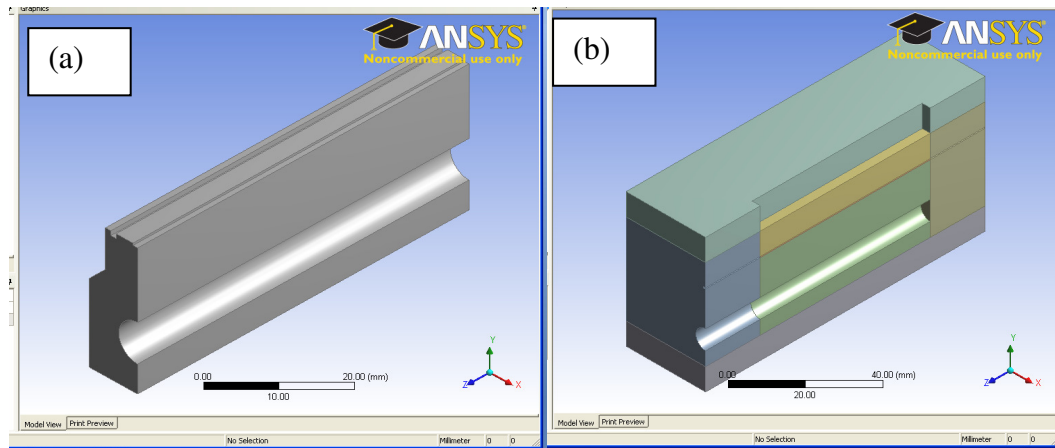


Figure C.6 Model for the cone copper block: (a) before insulated, (b) after insulated.

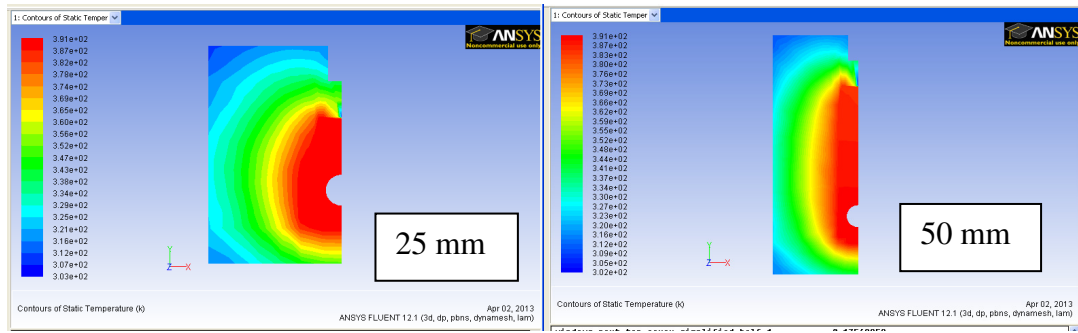


Figure C.7 Contours of wall temperatures (cross section view) for the 25 mm high and 50 mm high copper blocks at the fluid velocity of 1 m/s.

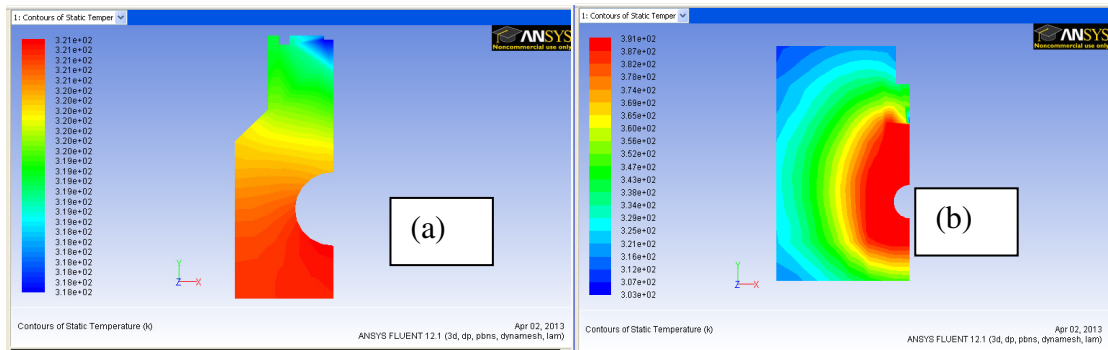


Figure C.8 Contours of wall temperatures (cross section view) for the cone copper block; (a) without flow, (b) at the fluid velocity of 1 m/s.

From Figs. C.3 and C.8(a), it is clear that the rectangular copper block at the same conditions and without flow results in higher wall temperatures compared with the cone copper block. Whilst from Figs. C.7 and C.8(b) at the same fluid velocity of 1 m/s and conditions, all models result in the same maximum temperature of about 391 K. Nevertheless, when the heat loss is taken into account, the smallest rectangular copper block is the best, because it results in lower heat losses, see Table C.1.

Table C.1 Comparison of heat losses estimated using Fluent with the calculation.

Shape	Height [mm]	Fluid velocity [m/s]	Heat input rate [W]	Heat loss rate Fluent [W]	$T_o$ [K]	Calculated heat loss rate [W]
Rectangular	25	1	20.3	2.1	313.0	2.27
	25	2	20.3	1.92	306.6	1.97
	25	5	20.3	1.83	302.7	1.54
	50	1	20.3	4.99	311.0	5.04
	50	2	20.3	4.85	305.6	4.75
	50	5	20.3	4.77	302.2	5.02
Cone	25	1	20.3	3.96	311.8	3.93
	25	2	20.3	3.85	305.9	3.91
	25	5	20.3	3.62	302.4	3.63

From the simulation results, it is recommended to design a test section with an overall dimension of 25 mm high, 12 mm wide and 72 mm long.

## C.2 Technical drawings

The technical drawings were created using SolidWork version 9 which was provided by Brunel University and are shown below.

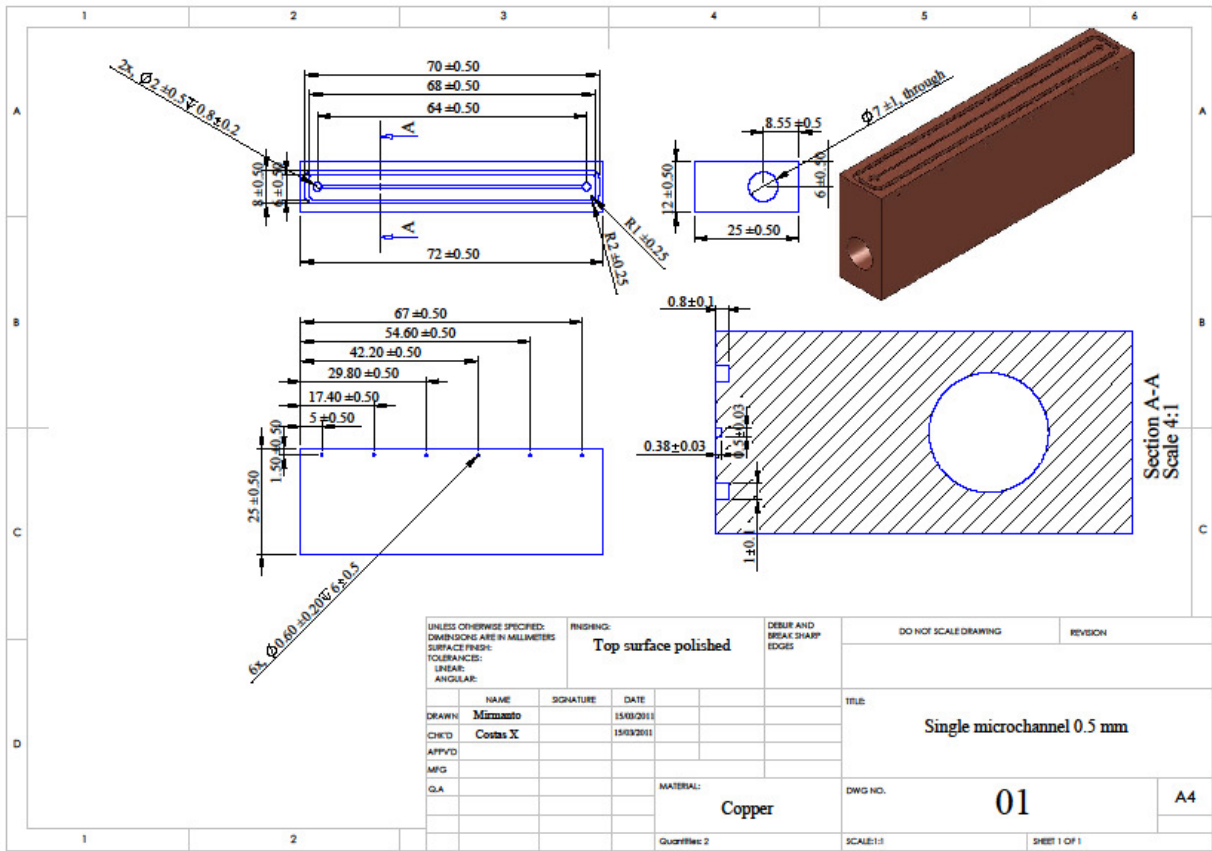


Figure C.9 Test section with a width of 0.5 mm.

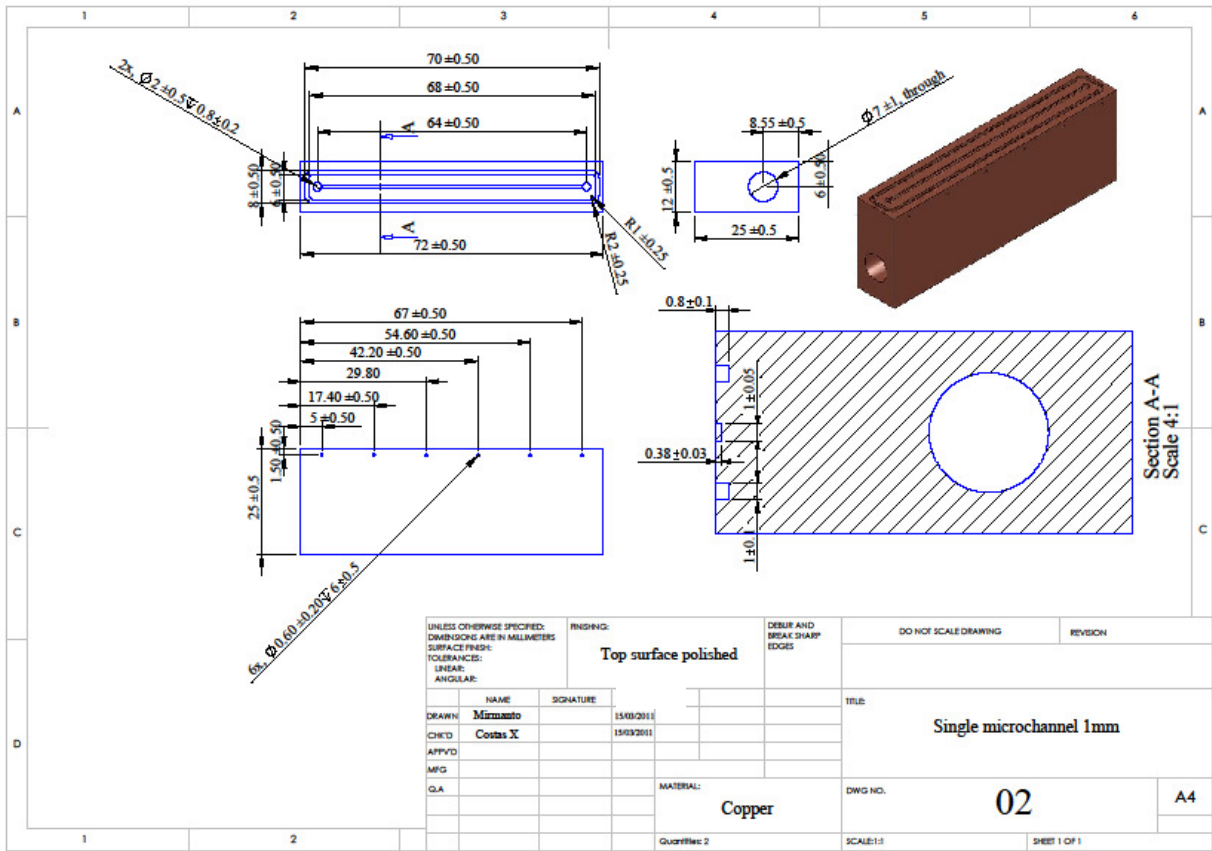


Figure C.10 Test section with a width of 1 mm.

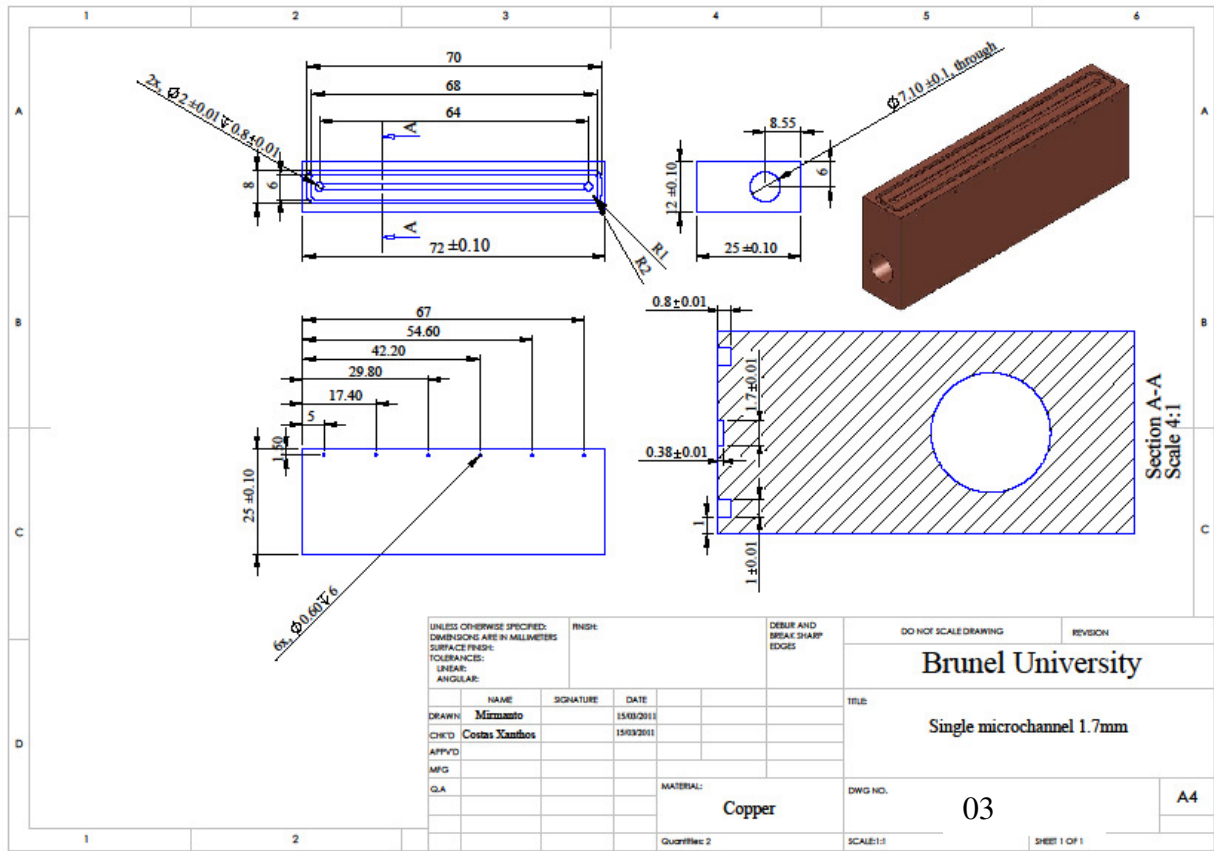


Figure C.11 Test section with a width of 1.7 mm.

## D. Uncertainty analysis

Uncertainty can be defined as an estimate of the interval,  $\mu$ , or range that contains an error in the experimental measurement or result. The total error in a measurement is the difference between the measured value and the true value, which is the sum of the systematic or bias errors and the random or precision errors. Systematic errors are those fixed errors that do not vary during a measurement. Errors in the measuring instruments can be reduced by calibration, but errors due to imperfect calibration standards or methods, calibration equation errors, and installation or

environmental effect remain. Random errors result from unsteady influences that cause scatter in measurements and the associated uncertainty and can be reduced by taking multiple readings over an appropriate time interval. The random uncertainty of a measured variable is then estimated using statistical analysis, assuming that the distribution of the readings follows a normal and Gaussian distribution. Following Coleman and Steele (2009), the random uncertainty of a measured variable,  $X$ , is estimated as the standard deviation,  $S_x$ , of a sample of  $N$  measurements of the variable,  $X$ , calculated as follows::

$$S_x = \sqrt{\frac{1}{N-1} \sum_{i=1}^N (X_i - \bar{X})^2} \quad (\text{D.1})$$

$$\bar{X} = \frac{1}{N} \sum_{i=1}^N X_i \quad (\text{D.2})$$

where  $\bar{X}$  is the mean value of the sample population.

By contrast, the systematic uncertainty of a measured variable,  $X$ , is calculated as the root sum (RSS) given by Eq. (D.3).

$$B_x = \sqrt{\sum_{k=1}^M (B_x)_k^2} \quad (\text{D.3})$$

Where  $(B_x)_k$  is the  $k^{\text{th}}$  of the elemental systematic uncertainties  $(B_x)_1, (B_x)_2, (B_x)_3, \dots, (B_x)_M$ , estimated from, for example calibration data and instrument specifications given by the manufacturers.

According to the ISO guide (1993) cited in Coleman and Steele (2009), the overall uncertainties,  $U$ , of a measured variable with a 95% confidence level is given by

$$U = t_{95\%} u_c \quad (\text{D.4})$$

where  $t_{95\%}$  is the value from the  $t$  distribution that gives a 95% confidence level and  $u_c$  is the combined uncertainty (systematic and random uncertainties) given by Eq. (D.5).

$$u_c = \sqrt{B_x^2 + S_x^2} \quad (\text{D.5})$$

For an experimental result  $r$ , defined by Eq. (D.6) which is a function of  $j$  measured variables  $X_i$ , the propagated error can be calculated using Eq. (D.7).

$$r = r(X_1, X_2, \dots, X_j) \quad (\text{D.6})$$

$$U_r = \sqrt{\left(\frac{\partial r}{\partial X_1}\right)^2 U_{X_1}^2 + \left(\frac{\partial r}{\partial X_2}\right)^2 U_{X_2}^2 + \dots + \left(\frac{\partial r}{\partial X_j}\right)^2 U_{X_j}^2} \quad (\text{D.7})$$

Equation (D.7) gives the absolute uncertainty,  $U_r$ , in the result. It can also be written in the dimensionless form shown in Eq. (D.8), to give the relative uncertainty,  $U_r/r$  of the result, as follows:

$$\frac{U_r}{r} = \sqrt{\left(\frac{X_1}{r} \frac{\partial r}{\partial X_1}\right)^2 \left(\frac{U_{X_1}}{X_1}\right)^2 + \left(\frac{X_2}{r} \frac{\partial r}{\partial X_2}\right)^2 \left(\frac{U_{X_2}}{X_2}\right)^2 + \dots + \left(\frac{X_j}{r} \frac{\partial r}{\partial X_j}\right)^2 \left(\frac{U_{X_j}}{X_j}\right)^2} \quad (\text{D.8})$$

The above approach was used to carry out the propagated uncertainty analysis for all parameters. The uncertainties of measuring instruments and sensors are summarized in Table. D.1.

Table D.1 Uncertainties of experimental measurements.

Parameter	Measuring instrument	Uncertainty, (95% confidence level)
Channel depth	Microscope	$\pm 0.002$ mm
Channel width	SEM	$\pm 0.002$ mm
Channel length	Vernier Calliper	$\pm 0.4$ mm
AC voltage	Multimeter	$\pm 0.03$ V, (Calibration certificate)
AC current	Multimeter	$\pm 0.01$ A, (Calibration certificate)
Mass flow rate	Coriolis flow meter	$\pm 0.6$ g/min (Calibration)
Pressures	Differential pressure transducers	$\pm 0.2$ kPa, (Calibration)
Temperatures	K type thermocouple	$\pm 0.2$ K, (Calibration)

#### D.1 Channel geometry uncertainties

- a. The hydraulic diameter,  $D_h$ , of the rectangular cross-sectional channels is calculated using Eq. (D.9), where the channel width,  $W$ , and height,  $H$ , are measured quantities as given in Table D.1. The propagated uncertainty in  $D_h$  is obtained from Eq. (D.10) or (D.11).

$$D_h = \frac{2WH}{W + H} \quad (\text{D.9})$$

$$U_{D_h} = \left[ \left( \frac{\partial D_h}{\partial W} \right)^2 U_W^2 + \left( \frac{\partial D_h}{\partial H} \right)^2 U_H^2 \right]^{0.5} \quad (\text{D.10})$$

$$\frac{U_{D_h}}{D_h} = \sqrt{\left(\frac{H}{W+H} \frac{U_W}{W}\right)^2 + \left(\frac{W}{W+H} \frac{U_H}{H}\right)^2} \quad (\text{D.11})$$

- b. Similarly, the cross sectional area,  $A_c$ , of the channel and the propagated uncertainty in  $A_c$  can be found using Eq. (D.12) to (D.15).

$$A_c = WH \quad (\text{D.12})$$

$$U_{A_c} = \left[ \left(\frac{\partial A_c}{\partial W}\right)^2 U_W^2 + \left(\frac{\partial A_c}{\partial H}\right)^2 U_H^2 \right]^{0.5} \quad (\text{D.13})$$

$$U_{A_c} = \sqrt{(H)^2 U_W^2 + (W)^2 U_H^2} \quad (\text{D.14})$$

$$\frac{U_{A_c}}{A_c} = \sqrt{\left(\frac{U_W}{W}\right)^2 + \left(\frac{U_H}{H}\right)^2} \quad (\text{D.15})$$

- c. The heat transfer area,  $A_{ht}$ , and the propagated uncertainty in  $A_{ht}$  can be calculated from Eq. (D.16) and (D.17).

$$A_{ht} = (2H+W)L \quad (\text{D.16})$$

$$\frac{U_{A_{ht}}}{A_{ht}} = \sqrt{\left(\frac{2U_H}{(2H+W)}\right)^2 + \left(\frac{U_W}{(2H+W)}\right)^2 + \left(\frac{U_L}{L}\right)^2} \quad (\text{D.17})$$

- d. The aspect ratio of the rectangular channel  $\beta = H/W$  is affected by the uncertainties in channel width and depth. The propagated uncertainty in the aspect ratio,  $U_\beta$ , is given by

$$\frac{U_\beta}{\beta} = \sqrt{\left(\frac{U_H}{H}\right)^2 + \left(\frac{U_W}{W}\right)^2} \quad (\text{D.18})$$

### D.2 Mass flux uncertainty

The mass flux is defined by Eq. (D.19), as the measured mass flow rate derived by the cross-sectional area of the test section. Hence, the propagated uncertainty in  $G$  can be calculated by applying Eq. (D.20).

$$G = \frac{\dot{m}}{A_c} \quad (\text{D.19})$$

$$\frac{U_G}{G} = \sqrt{\left(\frac{U_{\dot{m}}}{\dot{m}}\right)^2 + \left(\frac{U_{A_c}}{A_c}\right)^2} \quad (\text{D.20})$$

### D.3 Heat flux uncertainty

The uncertainty in the channel wall heat flux is due to the uncertainties in determining the heat removed by the fluid ( $q_{rem}$ ) and the heat transfer area. The rate of heat removal by the fluid is determined by applying Eq. (3.7) or Eq. (D.21) and the heat flux can be calculated using Eq. (3.8). However, the experimental heat loss measurements show that the average rate of heat loss from the test section is approximately 6.8% of the electrical input power. Then the rate of heat removal by the fluid can be estimated as

$$q_{rem} = \dot{m}C_p(T_o - T_i) = VI - q_{loss} = 0.93VI \quad (\text{D.21})$$

Then the uncertainty in the rate of heat removal by the fluid is:

$$\frac{U_{q_{rem}}}{q_{rem}} = \sqrt{\left(\frac{U_V}{V}\right)^2 + \left(\frac{U_I}{I}\right)^2} \quad (\text{D.22})$$

and the uncertainty in the heat flux is then given by

$$\frac{U_{q''}}{q''} = \sqrt{\left(\frac{U_{q_{rem}}}{q_{rem}}\right)^2 + \left(\frac{U_{A_{ht}}}{A_{ht}}\right)^2} \quad (\text{D.23})$$

#### D.4 Uncertainties in heat transfer coefficient and Nusselt number for single-phase flow

It is necessary to distinguish between the heat transfer coefficient for single-phase flow and that for two-phase flow. As the wall temperature distribution was found to be reasonable uniform in the single-phase flow experiments, the heat transfer coefficient is calculated using a logarithmic mean temperature difference (LMTD) method, as in Eq. (3.9). Appreciating that  $\Delta T = T_o - T_i$ ,  $\Delta T_i = T_w - T_i$ ,  $\Delta T_o = T_w - T_o$ , the uncertainty in heat transfer coefficient for single-phase flow may be formulated as

$$\frac{U_{\bar{h}}}{\bar{h}} = \sqrt{\left(\frac{U_{q''}}{q''}\right)^2 + \left(\frac{U_{\Delta T_{lm}}}{\Delta T_{lm}}\right)^2} \quad (\text{D.24})$$

where the uncertainty in  $\Delta T_{lm}$  is:

$$\frac{U_{\Delta T_{lm}}}{\Delta T_{lm}} = \sqrt{\left(\frac{U_{\Delta T}}{\Delta T}\right)^2 + \left(\frac{U_{LN}}{LN}\right)^2} \quad (\text{D.25})$$

and the uncertainty of  $U_{\Delta T} = U_{\Delta T_i} = U_{\Delta T_o} = 0.3 \text{ K}$ ,  $LN$  is equal to  $\ln \frac{\Delta T_i}{\Delta T_o}$ , and the uncertainty of  $LN$ ,  $U_{LN}/LN$ , is derived as:

$$\frac{U_{LN}}{LN} = \sqrt{\left(\frac{U_{\Delta T_i}}{\Delta T_i \ln \frac{\Delta T_i}{\Delta T_o}}\right)^2 + \left(\frac{-U_{\Delta T_o}}{\Delta T_o \ln \frac{\Delta T_i}{\Delta T_o}}\right)^2} \quad (\text{D.26})$$

The experimental Nusselt number can be obtained using Eq. (3.11) and the uncertainty in the Nusselt number is expressed as

$$\frac{U_{\bar{Nu}}}{\bar{Nu}} = \sqrt{\left(\frac{U_{\bar{h}}}{\bar{h}}\right)^2 + \left(\frac{U_{D_h}}{D_h}\right)^2} \quad (\text{D.27})$$

Any uncertainty in evaluating the fluid thermal conductivity is assumed to be negligible.

#### D.5 Uncertainties in the Fanning friction factor and Poiseuille number

Prior to deriving the uncertainties in the friction factor and Poiseuille number, the uncertainty in the measured pressure drop,  $U_{\Delta p_{meas}}$  should be obtained. This can be determined using Eq. (D.28).

$$\frac{U_{\Delta p_{meas}}}{\Delta p_{meas}} = \sqrt{\left(\frac{U_{p_i}}{p_i - p_o}\right)^2 + \left(\frac{U_{p_o}}{p_i - p_o}\right)^2} \quad (\text{D.28})$$

In the current study, the channel pressure drop is equal to the measured pressure drop minus the entry and exit pressure losses. Hence, the uncertainty in the channel pressure drop is given by

$$U_{\Delta p_{ch}} = \sqrt{(U_{\Delta p_{meas}})^2 + (U_{\Delta p_c})^2 + (U_{\Delta p_e})^2 + 2(U_{\Delta p_{90}})^2} \quad (D.29)$$

Equation (3.5) can be rearranged as follows:

$$f_{ch} = \frac{\Delta p_{ch} D_h}{2L\rho\bar{V}_{ch}^2} = \frac{\rho\Delta p_{ch} D_h A_c^2}{2L\dot{m}^2} \quad (D.30)$$

According to Eq. (D.30), the uncertainty in the Fanning friction factor is derived from the uncertainties in channel pressure drop, hydraulic diameter, cross sectional area, mass flow rate and test section length. Thus, the propagated uncertainty of the friction factor can be calculated as:

$$\frac{U_{f_{ch}}}{f_{ch}} = \sqrt{\left(\frac{U_{\Delta p_{ch}}}{\Delta p_{ch}}\right)^2 + \left(\frac{U_{D_h}}{D_h}\right)^2 + \left(\frac{2U_{A_c}}{A_c}\right)^2 + \left(\frac{U_L}{L}\right)^2 + \left(\frac{2U_{\dot{m}}}{\dot{m}}\right)^2} \quad (D.31)$$

The Poiseuille number uncertainty is generated by the uncertainties in Fanning friction factor and Reynolds number, therefore, the Reynolds number uncertainty should be determined first. This is achieved by obtaining firstly the Reynolds number from Eq. (D.32) and then its uncertainty by applying Eq. (D.33).

$$\text{Re} = \rho\bar{V}_{ch} D_h / \mu = \frac{2\dot{m}}{\mu(W+H)} \quad (D.32)$$

$$\frac{U_{\text{Re}}}{\text{Re}} = \sqrt{\left(\frac{U_{\dot{m}}}{\dot{m}}\right)^2 + \left(\frac{U_W}{W+H}\right)^2 + \left(\frac{U_H}{W+H}\right)^2} \quad (D.33)$$

Hence, the uncertainty of the Poiseuille number can be obtained from Eq. (D.34).

$$\frac{U_{Po}}{Po} = \sqrt{\left(\frac{U_{f_{ch}}}{f_{ch}}\right)^2 + \left(\frac{U_{Re}}{Re}\right)^2} \quad (D.34)$$

#### D.6 Flow boiling pressure drop uncertainty

In the flow boiling experiments, the channel pressure drop is determined as

$$\Delta p_{ch} = \Delta p_{meas} - \Delta p_c - \Delta p_{90} \quad (D.35)$$

Hence, the uncertainty in the channel pressure drop is given by

$$U_{\Delta p_{ch}} = \sqrt{(U_{\Delta p_{meas}})^2 + (U_{\Delta p_c})^2 + (U_{\Delta p_{90}})^2} \quad (D.36)$$

The pressure drop in the subcooled flow boiling region is given by

$$\Delta p_{sp} = \frac{2f_{app}G^2}{\rho_l D_h} L_{sub} \quad (D.37)$$

Consequently, the subcooled pressure drop uncertainty is expressed as

$$\frac{U_{\Delta p_{sp}}}{\Delta p_{sp}} = \sqrt{\left(\frac{2U_G}{G}\right)^2 + \left(\frac{U_{L_{sub}}}{L_{sub}}\right)^2 + \left(\frac{U_{D_h}}{D_h}\right)^2} \quad (D.38)$$

The two-phase pressure drop is defined by subtracting the single-phase pressure drop from the channel pressure drop (see Eq. (3.20)), and the uncertainty in the two-phase pressure drop is expressed as

$$\frac{U_{\Delta p_{tp}}}{\Delta p_{tp}} = \sqrt{\left(\frac{U_{\Delta p_{ch}}}{\Delta p_{ch} - \Delta p_{sp}}\right)^2 + \left(\frac{U_{\Delta p_{sp}}}{\Delta p_{ch} - \Delta p_{sp}}\right)^2} \quad (\text{D.39})$$

#### D.7 Local flow boiling heat transfer coefficient uncertainty

In the flow boiling experiments, the wall heat flux was assumed to be uniform along the channel. The local heat transfer coefficient is obtained from Eq. (3.21) and the uncertainty in the local heat transfer coefficient is given by

$$\frac{U_{h_p(z)}}{h_p(z)} = \sqrt{\left(\frac{U_{q''}}{q''}\right)^2 + \left(\frac{U_{T_w}}{T_w - T_{sat}(z)}\right)^2} \quad (\text{D.40})$$

#### D.8 Local enthalpy uncertainty

The local specific enthalpy comprises of enthalpy of liquid in the inlet (obtainable from the saturation water table at the corresponding temperature and pressure) and the local heat rate with a length of  $z$ . The enthalpy of liquid in the inlet is considered to be negligibly small; therefore the uncertainty of local enthalpy is given by

$$U_{i(z)} = \sqrt{\left(\frac{(2H+W)z}{\dot{m}} U_{q''}\right)^2 + \left(\frac{2q''z}{\dot{m}} U_H\right)^2 + \left(\frac{q''z}{\dot{m}} U_w\right)^2 + \left(\frac{q''(2H+W)}{\dot{m}} U_z\right)^2 + \left(\frac{q''(2H+W)z}{\dot{m}^2} U_{\dot{m}}\right)^2} \quad (\text{D.41})$$

#### D.9 Local vapour quality uncertainty

The local saturation enthalpies for liquid  $i_l(z)$ , and evaporation,  $i_{lg}(z)$ , can be found in the saturation water table at the corresponding local saturation temperature and pressure, and therefore their uncertainties are negligibly small. As a result, the uncertainty in local quality is

$$U_{x(z)} = \frac{U_{i(z)}}{i_{lg}(z)} \quad (\text{D.42})$$

#### D.10 Subcooled length uncertainty

Since the lengths of the subcooled and saturated regions affect the heat transfer coefficient in the flow boiling experiments, it is worth deriving the uncertainties in the subcooled and saturated lengths. However, the saturation length is equal to the difference between the total length and the subcooled length. The uncertainty in the subcooled length is expressed as

$$\frac{U_{L_{sub}}}{L_{sub}} = \sqrt{\left(\frac{U_{\dot{m}}}{\dot{m}}\right)^2 + \left(\frac{-U_{T_i}}{T_{sat}(z) - T_i}\right)^2 + \left(\frac{-U_{q''}}{q''}\right)^2 + \left(\frac{-2U_H}{2H + W}\right)^2 + \left(\frac{-U_W}{2H + W}\right)^2} \quad (\text{D.43})$$

The uncertainty in the two-phase length is then given by

$$U_{L_{tp}} = \sqrt{(U_L)^2 + (U_{L_{sub}})^2} \quad (\text{D.44})$$

#### D.11 Superficial velocity uncertainty

The vapour and liquid superficial velocities can be found from Eq. (3.25) and (3.26) and the uncertainty in vapour superficial velocity is given by

$$\frac{U_{J_g}}{J_g} = \sqrt{\left(\frac{U_G}{G}\right)^2 + \left(\frac{U_{x(z)}}{x(z)}\right)^2} \quad (\text{D.45})$$

The uncertainty of liquid superficial velocity is expressed as

$$\frac{U_{J_g}}{J_g} = \sqrt{\left(\frac{U_G}{G}\right)^2 + \left(\frac{U_{x(z)}}{(1-x(z))}\right)^2} \quad (\text{D.46})$$

The range of measurements and the uncertainties for the single-phase experiments are shown in Table D.2 for Test sections 1, 2 and 3.

Table D.2 Experimental conditions and uncertainties for single-phase experiments.

	Value/Range	Uncertainty
Channel width, $W$ [mm]	0.5, 1, 1.71	$\pm 0.12\%$
Channel depth, $H$ [mm]	0.39	$\pm 0.51\%$
Channel length, $L$ [mm]	62.0	$\pm 0.44\%$
Hydraulic diameter, $D_h$ [mm]	0.438, 0.561, 0.635	$\pm 0.34, 0.37, 0.42\%$
Heat transfer area, $A_{ht}$ [mm <sup>2</sup> ]	79.4, 110.4, 154	$\pm 0.49, 0.47, 0.66\%$
Mass flux, $G$ [kg/m <sup>2</sup> s]	278 – 5163	$\pm 2 - 7.3\%$
Heat flux, $q''$ [kW/m <sup>2</sup> ]	146 – 537	$\pm 4 - 11\%$
Inlet temperature, $T_i$ [°C]	30 – 90	$\pm 0.2$ K
Outlet temperature, $T_o$ [°C]	30 – 95	$\pm 0.2$ K
Pressure drop, $\Delta P_{ch}$ [kPa]	1.5 – 82	$\pm 0.11 - 26\%$
Channel friction factor, $f_{ch}$	0.012 – 0.057	$\pm 4 - 34\%$
Poiseuille number, $f_{ch} \text{Re}$	23 – 99	$\pm 4.4 - 37\%$
Average heat transfer coefficient, $\bar{h}$ [kW/m <sup>2</sup> K]	6.2 – 53	$\pm 6.3 - 17.2\%$

Average Nusselt number, $\overline{Nu}$	6.2 – 48	$\pm 6.3 - 17.2\%$
---	----------	--------------------

The ranges of measurements and uncertainties for flow boiling experiments are presented in Table D.3, for the three different hydraulic diameters.

Table D.3 Experimental conditions and uncertainties for flow boiling experiments.

	Value/Range	Uncertainty
Channel width, $W$ [mm]	0.5, 1, 1.71	$\pm 0.12\%$
Channel depth, $H$ [mm]	0.39	$\pm 0.51\%$
Channel length, $L$ [mm]	62.0	$\pm 0.44\%$
Hydraulic diameter, $D_h$ [mm]	0.438, 0.561, 0.635	$\pm 0.34, 0.37, 0.42\%$
Heat transfer area, $A_{ht}$ [mm <sup>2</sup> ]	79.4, 110.4, 154	$\pm 0.49, 0.47, 0.66\%$
Mass flux, $G$ [kg/m <sup>2</sup> s]	200 – 1100	$\pm 2 - 8.8\%$
Inlet pressure, $p_i$ [kPa](abs)	123 – 126.9	$\pm 0.2$ [kPa]
Outlet pressure, $p_o$ [kPa](abs)	38 – 125.4	$\pm 0.4$ [kPa]
Heat flux, $q''$ [kW/m <sup>2</sup> ]	79 – 793	$\pm 5.6 - 3.4\%$
Inlet temperature, $T_i$ [°C]	97 – 98.9	$\pm 0.2$ [K]
Outlet temperature, $T_o$ [°C]	74.2 – 98.9	$\pm 0.2$ [K]
Local heat transfer coefficient, $h(z)$ [kW/m <sup>2</sup> K]	13 – 65	$\pm 4 - 6\%$
Vapour quality, $x(z)$	0 – 0.41	$\pm 0 - 8.5\%$

## **Publications**

### **A. Conference**

- [1] Mirmanto, D B R Kenning, J S Lewis and T G Karayiannis, Pressure drop and heat transfer characteristics for single-phase developing flow of water in rectangular microchannels, Proceedings of the 6<sup>th</sup> European Thermal Sciences Conference, Eurotherm 12, Poitiers – Futuroscope, FRANCE, September 04 - 07, 2012.
  
- [2] Mirmanto, John Lewis, Tassos Karayiannis, Flow patterns and heat transfer measurements for flow boiling of water in a rectangular microchannel, Proceedings of the 3rd European Conference on Microfluidics, Microfluidics 2012, Heidelberg, December 3-5, 2012.
  
- [3] Mirmanto, J S Lewis, T G Karayiannis, Flow boiling of water in three different hydraulic diameter rectangular microchannels, submitted to the 13<sup>th</sup> UK Heat Transfer Conference, UKHTC 2013, Imperial College London, 2 – 3 September, 2013.

### **B. Journal**

- [1] Mirmanto, D B R Kenning, J S Lewis and T G Karayiannis, Pressure drop and heat transfer characteristics for single-phase developing flow of water in rectangular microchannels, Journal of Physics: Conference Series 395 (2012) 012085 doi:10.1088/1742-6596/395/1/01285, pp. 1 – 13, 2012.
  
- [2] Mirmanto, John Lewis, Tassos Karayiannis, Flow patterns and heat transfer measurements for flow boiling of water in a rectangular microchannel, submitted to Journal Microsystem Technologies.